NASA CONTRACTOR REPORT

NASA CR-2637

INVESTIGATION OF A BEARINGLESS HELICOPTER ROTOR CONCEPT HAVING A COMPOSITE PRIMARY STRUCTURE

Richard L. Bielawa, Marvin C. Cheney, Jr., and Richard C. Novak

Prepared by
UNITED TECHNOLOGIES RESEARCH CENTER
East Hartford, Conn. 06108
for Langley Research Center
and U.S. Army Air Mobility R&D Laboratory

NATIONAL AERONAUTICS AND SPACE ADMINISTRATION • WASHINGTON, D. C. • OCTOBER 1976

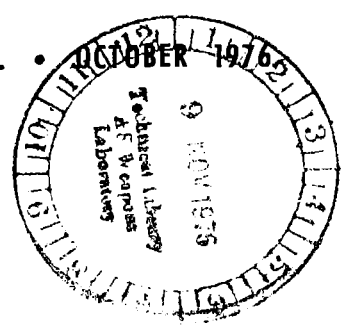

1. Report No.	2. Government Accession No.	3. Recipient's
NASA CR-2637		

4. Title and Subtitle	5. Report Date
Investigation of a Bearingless Helicopter Rotor Concept Having a Composite Primary Structure	October 1976
	6. Performing Organization Code

7. Author(s)	8. Performing Organization Report No.
Richard L. Bielawa, Marvin C. Cheney, Jr., and Richard C. Novak	R76-911209-47
	10. Work Unit No.
9. Performing Organization Name and Address	
United Technologies Research Center East Hartford, CT 06108	11. Contract or Grant No. NAS 1-10960
	13. Type of Report and Period Covered Contractor Report
12. Sponsoring Agency Name and Address	14. Army Project No.
National Aeronautics and Space Administration Washington, DC 20546 and U.S. Army Air Mobility R&D Laboratory Moffett Field, CA 94035	1F161102AH45

15. Supplementary Notes

The contract research effort that led to the results in this report was financially supported by USAAMRDL-Langley Directorate

This is a final report and complements NASA CR-2638 Technical Monitor: Carl E. Swindlehurst, Jr.

16. Abstract

Experimental and analytical investigations were conducted to evaluate a bearingless helicopter rotor concept (CBR) made possible through the use of the specialized nonisotropic properties of composite materials. The investigation was focused on four principal areas which were expected to answer important questions regarding the feasibility of this concept. First, an examination of material properties was made to establish moduli, ultimate strength, and fatigue characteristics of unidirectional graphite/epoxy, the composite material selected for this application. The results confirmed the high bending modulus and strengths and low shear modulus expected of this material, and demonstrated fatigue properties in torsion which make this material ideally suited for the CBR application. Second, a dynamically scaled model was fabricated and tested in the low speed wind tunnel to explore the aeroelastic characteristic of the CBR and to explore various concepts relative to the method of blade pitch control. Two basic control configurations were tested, one in which pitch-flap coupling could occur and another which eliminated all coupling. It was found that both systems could be operated successfully at simulated speeds of 180 knots; however, the configuration with coupling present revealed a potential for undesirable aeroelastic responses. The uncoupled configuration behaved generally as a conventional hingeless rotor and was stable for all conditions tested. Another decoupled rotor configuration was extensively analyzed, but was not tested due to scaling difficulties. Third, a preliminary design of a full-scale rotor was conducted to establish full-scale requirements and to show that no significant problems would be encountered in the manufacture of a CBR blade. Finally, an aeroelastic computer program was developed to simulate the unique CBR blade structure and operating environment. This analysis was then employed to examine the stability characteristics of a full-scale design under various flight conditions and under conditions where material properties were degraded due to possible flaws in fabrication or partial failures in operation. This study revealed no dynamic problems for the conditions investigated, has confirmed that significant reductions in rotor system complexity and weight can be achieved with the CBR, and further, that graphite/epoxy is ideally suited for the special requirements of the CBR.

17. Key Words (Suggested by Author(s))	18. Distribution Statement
Composite materials, Wind tunnel tests, Bearingless rotors, Helicopter rotor design, Rotor aeroelastic stability, Stresses and loads, Rotor configurations	Unclassified - Unlimited Subject Category 05

19. Security Classif. (of this report)	20. Security Classif. (of this page)	21. No. of Pages	22. Price*
Unclassified	Unclassified	248	$8.75

*For sale by the National Technical Information Service, Springfield, Virginia 22161

PREFACE

The purpose of this contract was to perform an investigation of a bearingless helicopter rotor concept having a composite primary structure. The results of this investigation are presented in two separate reports. The one herein contains the results of graphite/epoxy fatigue tests, wind tunnel experiments, correlation studies, and a preliminary design of a full scale helicopter rotor. The companion report, NASA CR-2638 presents the mathematical derivation of and program user's manual for the aeroelastic analysis used to generate most of the analytical results presented herein.

The project was managed by Mr. M. C. Cheney. The composite material investigation was performed by Mr. R. C. Novak. The detailed design and fabrication of the model rotor was performed by Mr. Cheney and Mr. E. D. Bellinger, and the experimental data were acquired by Messrs. Bellinger and B. W. Goepner. Development of the aeroelastic analysis, generation of the correlation results, and the aeroelastic analysis calculations of the full-scale design were performed by Dr. R. L. Bielawa. Design of the full-scale blade configurations was performed by Mr. J. A. Longobardi of the Sikorsky Aircraft Division with assistance from Dr. L. E. Greenwald of UTRC. Assistance in the management of the experimental test program was provided by Mr. A. J. Landgrebe.

Note that all original data was recorded in English units and subsequently converted to metric units. A table is presented to facilitate conversion of data back to English units should it be desired.

TABLE OF CONTENTS

TABLE OF CONTENTS (Cont'd)

INVESTIGATION OF A BEARINGLESS HELICOPTER ROTOR CONCEPT HAVING A COMPOSITE PRIMARY STRUCTURE

Richard L. Bielawa,
Marvin C. Cheney, Jr., and
Richard C. Novak
United Technologies Research Center

SUMMARY

Experimental and analytical investigations were conducted at the United Technologies Research Center (UTRC) to evaluate a bearingless helicopter rotor concept (CBR) made possible through the use of the specialized nonisotropic properties of composite materials. The investigation was focused on four principal areas which were expected to answer important questions regarding the feasibility of this concept. First, an examination of material properties was made to establish moduli, ultimate strength, and fatigue characteristics of unidirectional graphite/epoxy, the composite material selected for this application. The results confirmed the high bending modulus and strengths and low shear modulus expected of this material, and demonstrated fatigue properties in torsion which make this material ideally suited for the CBR application. Second, a dynamically scaled model was fabricated and tested in the UTRC low speed wind tunnel to explore the aeroelastic characteristics of the CBR and to explore various concepts relative to the method of blade pitch control. Two basic control configurations were tested, one in which pitch-flap coupling could occur (cantilever torque tube design) and another which eliminated all coupling (pinned-pinned torque tube design). It was found that both systems could be operated sucessfully at simulated speeds of 180 knots; however, the configuration with coupling present revealed a potential for undesirable aeroelstic responses. The uncoupled configuration behaved generally as a conventional hingeless rotor and was stable for all conditions tested. Another decoupled rotor configuration (snubber torque tube design) was extensively analyzed, but was not tested due to scaling difficulties. Third, a preliminary design of a full-scale rotor was conducted to establish full-scale requirements and to show that no significant problems would be encountered in the manufacture of a CBR blade. Finally, an aeroelastic computer program was developed to simulate the unique CBR blade structure and operating environment. This analysis was then employed to examine the stability characteristics of the full-scale snubber torque tube design under various flight conditions and under conditions where material properties were degraded due to possible flaws in fabrication or partial failures in operation. This study revealed no dynamic problems for the conditions investigated, has confirmed that significant reductions in rotor system complexity and weight can be achieved with the CBR, and further, that graphite/epoxy is ideally suited for the special requirements of the CBR.

A description of the aeroelastic analysis developed under this contract along with detailed procedures for its use is presented separately in NASA CR-2638 (Ref. 1).

INTRODUCTION

Fully articulated rotors have successfully powered rotary wing aircraft since their inception and have brought the helicopter to its present unique position in the field of air transportation. However, high cost and maintenance requirements, primarily related to complicated hub mechanisms, have restricted the growth of the helicopter. Hingeless rotors sought to reduce these requirements by simplifying the hub through the elimination of the flapping and lagging hinges; however, current designs (Refs. 2 through 4) still have not significantly reduced weight and cost since feathering bearings have been used to provide pitch control and heavy structure has been necessary to react centrifugal loads.

The study of a new rotor concept designed to eliminate all hinges and bearings through a specialized use of fiber reinforced composite materials, was initiated at the United Technologies Research Center (UTRC) in 1968. This concept utilized a finite length of unidirectional composite material, with its attendant low shear modulus, in place of the feathering bearings of conventional hingeless rotors. This "flexbeam" member is carried through the center region to retain an opposing blade, thus eliminating individual blade retention hardware and resulting in a simple, low weight, low profile hub requiring little or no maintenance. The encouraging results obtained from the early work at UTRC led to a research contract jointly sponsored by the NASA Langley Research Center and the US Army Air Mobility Research and Development Laboratory. It is the results of this contract that are reported herein. The objective of this research was to assess the general feasibility of this rotor system, called the Composite Bearingless Rotor (CBR) through a series of experimental and analytical investigations. It was the purpose of these investigations to explore all aspects of the rotor system, from the viewpoints of basic material properties, stability characteristics, wind tunnel verification of rotor performance and dynamics, and full-scale design requirements. There were fundamental questions regarding the durability of unidirectional composite materials when utilized in the unconventional manner required of this design, that is, with imposed oscillatory motions about the weakened shear axis where the fibers are not loaded in their respective axial directions. Another potential problem area which required study was the effect a time varying twisted beam might have on the blade response. In effect, the inboard blade structure varies with collective and cyclic pitch potentially influencing the in-plane and out-of-plane stiffness characteristics. The problem of inputting control deflections by means of a torque tube at a finite distance outboard of the hub also had to be considered, as well as pitch-flap and pitch-lag coupling phenomena which may result from motions of this control torque tube. Finally, the problem of applying the technology developed and the experience

gained in the model scale investigations to full-scale rotors had to be addressed. The task of eventually reducing these results to practice is, in the final analysis, the ultimate test of the success of a new concept.

A review of the CBR concept and a summary of a portion of the results obtained during the course of the contract were presented at the American Helicopter Society National Forum in 1972 (Ref. 5).

LIST OF SYMBOLS

a	aerodynamic section lift curve slope, $(\text{deg})^{-1}$
A_{1_s}, B_{1_s}	longitudinal and lateral cyclic pitch angles, respectively, applied at the swash-plate, deg
b	number of blades
c	blade or flexbeam section chord, m
c_ℓ, c_d, $c_{m_{c/4}}$	airfoil section lift, drag and pitching moment about quarter chord aerodynamic coefficients, respectively
c_{d_o}	airfoil section drag aerodynamic coefficient at angle-of-attack for zero lift
C_D	rotor drag coefficient, $D/\rho\pi R^2(\Omega R)^2$
C_L	rotor lift coefficient, $L/\rho\pi R^2(\Omega R)^2$
C_{PF}	rotor propulsive force coefficient, $PF/\rho\pi R^2(\Omega R)^2$
C_{PM}	pitching moment coefficient, $M_y/\rho\pi R^3(\Omega R)^2$
C_Q	rotor torque coefficient, $Q/\rho\pi R^3(\Omega R)^2$
C_{RM}	rolling moment coefficient, $M_x/\rho\pi R^3(\Omega R)^2$
C_T	rotor thrust coefficient, $T/\rho\pi R^2(\Omega R)^2$
C_Y	lateral force coefficient, $Y/\rho\pi R^2(\Omega R)^2$
D	rotor drag, N; or plate bending stiffness, $Et^3/12(1-\upsilon^2)$, Nm
e	radial coordinate of the blade offset point
E	Young's (bending) modulus of elasticity, N/m^2
EI_E, EI_F	blade bending stiffnesses for edgewise and flatwise flexing, respectively, Nm^2

ΔEI	difference in blade bending stiffnesses, $EI_E - EI_F$, Nm^2
f_s	torsion shear stress, MN/m^2
F_{PR}	push rod load, positive in compression, N
G	shear modulus of elasticity, N/m^2
GJ	torsional stiffness, Nm^2
I/c	section modulus, m^3
I_x'	torsional inertia distribution, kg m^2/m
k_A	radius of gyration of tension load carrying portion of section, m
L	rotor lift, N
M_E, M_F	blade edgewise and flatwise bending moments, respectively, positive forward and upper fibers in compression, Nm
M_x, M_y	rotor aerodynamic roll and pitch moments, positive port and nose edges up, respectively, Nm
M_θ	torsion moment, positive for radially increasing resultant twist rate, Nm
PF	rotor propulsive force, positive in direction of flight, N
nP	n times rotor frequency, Ω
Q	rotor torque, Nm
r	blade (nondimensional) radial station, x_5/R
R	rotor radius, m
$\bar{R}$	ratio of full scale rotor radius to model rotor radius
[S]	aerodynamic static stability matrix

t	blade or flexbeam section thickness, m
T	rotor thrust, N
$[T]$	rotor aerodynamic trim matrix
U	local aerodynamic section air velocity, m/sec
V	forward flight speed of rotor, m/sec
w'	blade mass distribution, kg/m
x_5	spanwise location, m
y_5, z_5	blade (nondimensional) inplane and out-of-plane elastic deformations, respectively
Y	rotor lateral force, positive to starboard, N
α	airfoil section angle of attack, deg
α_s	rotor shaft angle, positive is nose-up deflection of plane of rotation relative to tunnel air velocity, deg
β	fiber alignment angle for composite materials, deg (see figure 1)
γ_{w_i}, γ_{v_k}, γ_{θ_j}	uncoupled vibratory mode shapes for i^{th} flatwise bending, k^{th} edgewise bending and j^{th} torsion modes, respectively
δ_3	effective flapping hinge orientation angle producing pitch-flap coupling, deg
γ_{equ}	blade equivalent mass ratio, $pacR/\int_0^1 w'(\gamma_{w_1})^2 dr$
ζ	ratio of damping level to critical value
θ	blade collective control angle experimentally measured at swash-plate or other remote location, deg
θ_{w_i}	automatic blade pitch change per unit deflection in the i^{th} flatwise bending mode

$\theta_{.75R}$	blade collective angle as measured at 0.75 station, deg
θ_1	blade linear twist angle defined by twist rate of aerodynamic portion, positive for root pitch less than tip pitch, deg
$\Delta\theta_{.75R}$, ΔA_{1_s}, ΔB_{1_s}, $\Delta\alpha_s$	perturbations in collective, longitudinal and lateral cyclic, and rotor shaft angles, respectively, deg
λ, λ_o	uniform rotor inflow ratio, also eigenvalue, as appropriate
λ_{1_c}, λ_{1_s}	first harmonic cosine and sine components of radially linear rotor inflow, as defined by Glauert
μ	advance ratio, $V\cos\alpha_s/\Omega R$
ν	Poisson's ratio
ρ	air density, kg/m^3
σ	rotor solidity, $bc/\pi R$; real part of eigenvalue, or modal equivalent characteristic exponent
σ_E, σ_F	blade edgewise and flatwise bending stresses, respectively, positive for leading edge and upper surface in compression, MN/m^2
τ	torsional shear stress, N/m^2
ψ	blade azimuth angle measured from downstream position, deg
ω	blade natural frequency (for uncoupled or coupled mode); imaginary part of eigenvalue; or identified modal frequency, as appropriate, Hz
$\bar{\omega}_{w_i}$, $\bar{\omega}_{v_k}$, $\bar{\omega}_{\theta_j}$	blade (nondimensional) natural frequencies for ith flatwise bending, kth edgewise bending and jth torsion uncoupled natural modes, respectively

Ω	rotor stational speed, rad/sec
$\bar{\Omega}$	ratio of full scale rotor rotational speed to model rotor rotational speed

Subscripts

$(\ )_e$	due to elastic effects
$(\ )_{FB}$	for flexbeam
$(\ )_{FS}$	full scale
$(\ )_f$	final value
$(\ )_i$	initial value
$(\ )_{MS}$	model scale
$(\ )_{nom}$	for nominal configuration
$(\ )_{subcr.}$	for subcritical design configuration (i.e. $\bar{\omega}_{v_1} > 1$)
$(\ )_{supercr.}$	for supercritical design configuration (i.e. $\bar{\omega}_{v_1} \leq 1$)
$(\ )_{TRIM}$	trimmed conditions
$(\ )_{TT}$	for torque tube

Superscripts

$(\bar{\ })$	nondimensionlization by combinations of R and Ω
$(^*)$	differentiation with respect to ψ
$(\ )'$	differentiation with respect to r

CONCEPT DESCRIPTION

The Composite Bearingless Rotor (CBR) evolved as a result of the unique application of fiber reinforced composite materials. The nonisotropic nature of unidirectional composites, generally considered an undesirable feature, yields a structure which was decidedly softer in torsion than in a direction which loads the fibers axially. By employing a finite length of this material, torsional deflections can be achieved to satisfy the pitch angle change requirements of a helicopter rotor while providing sufficient stiffness in the in-plane and out-of-plane directions to satisfy hingeless rotor frequency requirements.

A comparison of the modulus characteristics of fiber-reinforced composites and metals is given in Fig. 1 where Young's modulus, E, is plotted versus shear modulus, G. The variations, or trade-offs, of E and G for composite materials can be achieved by adjustments in the alignment of the fibers relative to the spanwise axis of the structure denoted by β in Fig. 1. The shaded area represents a boron composite where the left end corresponds to material with unidirectional fibers ($\beta = 0$) producing high bending modulus and low shear modulus, and the right end of the shaded area corresponds to a material with all fibers aligned ± 45 deg giving maximum shear modulus. The E and G values between these extremeties are achieved by alignment angles between 0 deg and 45 deg or by combinations of unidirectional and cross plies. Values are shown for several metals which demonstrate the increasing trend of shear modulus with Young's modulus. This is typical of isotropic materials which have a fairly constant value of E/G of approximately 2.5 as shown by the straight line in Fig. 1. Composite materials can have the opposite trend - decreasing G with increasing E which is the key to the use of these materials in the bearingless rotor concept.

A schematic of the basic components of the CBR are shown in Fig. 2. The blade spars consist of unidirectional composite material as shown in Fig. 2a, where, for a 4-bladed rotor, two single lengths are used, one for each set of opposing blades. The 4-bladed system simply consists of intersecting the two spars as shown in the figure. The dimensions of the spar are dictated by the edgewise and flatwise frequency requirements and the required torsional properties over the inboard, or flexbeam, portion of the blade. The aerodynamic cover is assembled from approximately the 25 percent radial position to the tip. This cover would normally be constructed of composite material with 45 deg fiber alignment to give maximum torsional stiffness. The cover is then bonded to the spar through a foam filler or honeycomb resulting in a torsionally stiff blade over the outer 75 percent as shown in Fig. 2b. The inner 25 percent, the flexbeam, remains soft in torsion, and it is this portion of

the blade that is elastically twisted to achieve collective and cyclic pitch control. The remainder of the rotor assembly consists of the control torque tube which is cantilivered inboard from the 25 percent station, Fig. 2c, and the two plates which make up the hub, Fig. 2d. Because of the carry-through feature of the blades, minimal hub retention hardware is required resulting in an extremely simple hub design.

There can be several variations to the CBR concept which are not depicted in the sketches in Fig. 2. For example, it may not be necessary to extend the unidirectional spar over the full blade span. A conventional blade design could be employed and joined to the outboard end of the flexbeam. Also, dynamic considerations may require more or less fixity on either the inboard or outboard end of the torque tube than is inherent in the cantilevered design shown for concept illustration purposes in Fig. 2. For example, the inboard end of such a cantilevered torque tube could be additionally attached to the flexbeam by means of a "snubber" which would allow relative feathering motion but suppress relative translational motion. Various such alternative torque tube configurations are described in detail in subsequent portions of this study.

Controls to the rotor are applied through a swash plate in a conventional manner. The dynamic response characteristics are generally similar to hingeless rotors operating today, particularly for the snubber design where nearly all blade pitch coupling is eliminated. These response characteristics are almost entirely dependent upon the fundamental bending frequencies which can be tailored to any desired values without affecting the basic CBR concept.

COMPOSITE MATERIAL INVESTIGATION

As discussed previously, the bearingless composite rotor concept is heavily dependent on the unique elastic properties of the materials as well as their fatigue characteristics. As a result, high priority was placed on a composite material investigation to define modulus characteristics, measure static strengths, and determine fatigue properties.

The fatigue performance of advanced resin matrix composites is generally considered to be a plus when the materials are compared with metals. The bulk of the supporting evidence for this conclusion is based on testing performed under conditions in which the reinforcing fibers carried the applied load (Refs. 6 through 8). Thus, since the fibers behave in an elastic manner, it is not suprising that the fatigue performance of the composites has been found to be good. However, the bearingless rotor concept relies on the fatigue performance of the composite structure under combined bending and torsion loading conditions. Under these circumstances the composite response is not necessarily elastic over all load ranges, and the matrix resin strength or the resin-fiber interfacial bond strength becomes very important to the performance of the system.

The following sections describe the materials and test procedures used in an experimental program to study the pertinent static and fatigue properties of the composites, and a brief discussion of the test results.

Experimental Approach

All specimens consisted of HTS (high tensile strength) graphite fiber in a matrix of Fiberite X-05 epoxy. Preimpregnated tape (prepreg) was purchased at various intervals in the program to provide information on the repeatability of material properties from lot to lot. The specimens were fabricated from 12 plies of prepreg and cured at 325°F under .55 MN/m^2 (80 psi). The finished specimen sheets were 2.5 mm (0.10 in.) thick with a fiber content of approximately 60 percent. The fatigue test specimens were cut to either 2.54 cm or 1.27 cm (one inch or one-half inch) widths and approximately fifteen cm (six inches) in length. The tests consisted of static flexure and interlaminar shear, flexure and torsion fatigue, and combined flexure/torsion fatigue which simulated combined blade flatwise, edgewise, and torsional deflections. Static 4-point flexure tests were conducted at a span-to-depth ratio of 32:1. Interlaminar shear strength was measured in a 3-point bend test at a span-to-depth ratio of 4:1. The fatigue tests were conducted using a VISHAY variable throw cam driven by a

1120 watt (1.5 hp) electric motor at 3600 rpm as shown in Fig. 3. The specimens were run to 10^7 cycles, and the post-test moduli were compared to the pre-test moduli to determine possible material degradation.

Results and Discussion

Static Properties - The results of the static property measurements are presented in Table II. With the exception of the flexural strength of the Lot 1D-52 1B, the data exhibited fairly low scatter and fell within the expected range. The apparent low strengths of that lot were due to a low filament volume fraction (50 percent) in the composites which were tested. This was also reflected in the somewhat lower bending modulus for the material.

The pertinent points brought out by the static data are the verification of the required high E/G ratio (~25) and the demonstration of static shear and bending strengths which are significantly higher than the design stresses for a typical bearingless rotor application.

Fatigue Properties - The results of the pure bending fatigue and pure torsion fatigue are graphically presented in Figs. 4 and 5, respectively. As mentioned previously the performance of the materials was measured by reductions in the shear stiffness, G, and the bending stiffness, E, because the specimens did not suffer complete fracture as metals do under fatigue loading. Rather, the failure mode was in the form of cracks through the resin matrix which gradually reduced the section modulus of the specimen. An example of the cracking which was observed is shown in Fig. 6 which is a photomicrograph of a specimen subjected to a vibratory torsional stress of ± 52.7 MN/m^2 (7650 psi) for 5×10^6 cycles. The graphite filaments appear as light circles which are surrounded by the epoxy matrix. The small crack can be seen to propagate from interface to interface through the matrix. There is no evidence of broken filaments.

Since no precipitous stiffness reduction was evident from these results it was difficult to establish a failure criterion. Accordingly, the stress corresponding to a nominal 10 percent reduction in modulus was tentatively selected as the endurance limit. Considerably more fatique testing would be necessary before a firm endurance limit could be established. The vibratory stresses corresponding to the 10 percent criterion are estimated from Figs. 4 and 5 at 758 MN/m^2 (110,000 psi) for bending and 48 MN/m^2 (7000 psi) for shear.

Because the vibratory stresses are present in combined form in the bearingless rotor, a series of combined bending/torsion fatigue tests was conducted to determine if the material responded in a predictable manner based on the pure bending and torsion results. In addition, some tests were performed with a steady axial load to simulate the centrifugal force present in an actual blade.

The combined stress state was produced by using a setup similar to that shown in Fig. 3 except the specimen was positioned off the center of rotation of the fixture, producing a combination of bending and twisting. Steady tension was initially provided by dead weight loading of a cable attached to the end of the specimen by friction clamps. Later this was replaced by a hydraulic cylinder. Several testing trials were conducted before satisfactory results were achieved.

The results of these tests are summarized in Table III. In general, the data indicate that the effects of combined loading were slightly more severe than would be predicted based on the simple loading results discussed previously. This may have been related to test effects such as indicated for specimen KC1-6. Nevertheless, with the exception of specimen KC4-2, the specimens were capable of sustaining a total bending stress of approximately 669 MN/m^2 (97,000 psi) for 10^7 cycles with 10 percent reduction in modulus. This compares favorably with the 758 MN/m^2 (110,000 psi) endurance limit found for pure bending, given the stochastic nature of fatigue.

MODEL ROTOR TESTS

Test Facility and Equipment

Wind Tunnel - The tests were conducted in the United Technologies Corporation 1.22- x 1.83-m subsonic wind tunnel which has a closed return, closed throat circuit and operates with a maximum test section velocity and Reynolds number of 44.7 m/sec and 2.89 x 10^6 per m, respectively. Static pressure in the irregular octagonal test section is atmospheric.

Small-Scale Rotor Test Rig - The rotor test rig employed in this program is shown in Fig. 7. It was designed primarily for exploratory testing of small-scale rotors in the 1.22- x 1.83-m subsonic wind tunnel. Power to the rotor is supplied by direct drive from a 40 hp, variable-speed electric motor. The motor and rotor force measuring system were mounted outside the tunnel above the test section. Rotor thrust, drag and torque were measured by means of strain-gaged bending beams. A 25-unit slip-ring assembly mounted on the rotor drive shaft provided a signal transfer point for measuring blade stresses and bending loads.

Model Rotor Description

Both 2- and 4- bladed dynamically scaled model rotors were tested in hover and forward flight to demonstrate the viability of the composite bearingless rotor concept. The blade design parameters for the two torque tube configurations are presented in Table IV. A photograph of a 4-blade rotor installed in the wind tunnel for forward flight test conditions is shown in Fig. 7. The elements comprising the flexbeams and the pinned and cantilever torque tube configurations are shown in Figs. 8 and 9, respectively.

The model rotor blades were fabricated as integral sets of opposing blade pairs. Each such blade pair set utilized a common primary structural bending element comprised of unidirectional graphite filaments, continuous from tip to (opposite) tip, cast in an epoxy matrix. Furthermore, each rotor blade in turn consisted of two main spanwise sections starting from the blade root offset (rotor hub). The first spanwise section comprised the flexbeam-torque tube region and the second made up the outer blade region. The details of the flexbeam and two torque tube configurations are shown in Figs. 8 and 9. The flexbeam, which was the inboard portion of the centrifugal and bending load carrying member, had zero pretwist, spanned the radial region from 0.05 to 0.33R and had a cross sectional chord to thickness ratio of approximately 7.2.

Outboard of the flexbeam, additional model spar components consisted of the graphite/epoxy material encased in aluminum 0.254 mm thick to produce the model scale torsional stiffness. Lead tape 0.127 mm thick was used to scale mass and inertias, and balsa wood was used to form the NACA 0012 airfoil. A protective wrap of 0.064 mm mylar was shrunk fit to the balsa to provide an aerodynamically clean and uniform surface. Figure 10 illustrates the juxtaposition of the various elements of the outboard blade cross section.

The blade chord was constant at 0.039 m from the 0.33 R station to the tip. The blade was preconed 2 deg to alleviate the steady bending stress due to rotor thrust at a $C_T/\sigma = 0.08$. The model blade spanwise distributions of weight, flatwise stiffness, edgewise stiffness, torsional stiffness, torsional inertia and the spar radius of gyration are plotted in Figs. 11 and 12 for both pinned and cantilevered torque tube configurations. Using the blade section properties shown in Figs. 11 and 12, the uncoupled model blade (vacuum) natural frequencies and mode shapes were calculated using the United Technologies Corporation Uncoupled Mode Blade Natural Frequency computer program. These are shown in Figs. 13 through 16 and are given in Table IV for the nominal tip speed conditions of 99.1 m/sec. The flatwise and edgewise bending modes (Figs. 15 and 16) show the typical character of a cantilevered beam with zero deflections and slope at the blade root offset.

As stated above, two torque tube configurations were tested on the CBR blades. The pinned-pinned torque tube configuration, shown in Fig. 8, consisted of a pitch arm, feathering bearing, universal joint, 0.635 cm OD-0.089 cm wall thickness 303 stainless steel tubing, a flexible coupling and blade attachment. This torque tube allowed no pitch-flap coupling because the universal joint and flexible coupling transmitted only pitch moments to the blade and eliminated any blade bending feedback (pitch-flap coupling) to the pushrod. The root end of the pinned-pinned torque tube was attached to the hub so that the blade centrifugal load was not significantly affected by the torque tube.

The cantilevered torque tube configuration shown in Fig. 9, consisted of a 0.953 cm OD - 0.124 cm wall thickness 6065-T6 aluminum tubing bonded to two 2.54 cm square 6065-T6 aluminum plates. These plates, together with their connecting clamping screws, were used to effect attachment to the blade at the 0.31 R spanwise station. As shown in Fig. 9, the cantilevered torque tube is mounted in its trailing edge position. It could also be mounted in a leading edge position. Since the cantilevered torque tube to blade attachment point was fixed at the 0.31 R station, pitch-flap coupling was changeable only by attaching the pitch link at various of the radial points on the torque tube as shown in Fig. 9.

Scaling Factors

To apply the model scale data presented herein to a full-scale rotor of the same design, an appropriate scale factor must be applied to the parameter being scaled. A summary of these scale factors is given in Table V.

Test Data

Test Conditions - Wind tunnel test conditions were selected to encompass a range of advance ratios, and thrust coefficients typical of contemporary helicopter operation. Advance ratios of 0, 0.1, 0.25, 0.35 and 0.47 were tested at the nominal tip speed over a range of shaft angles and collective pitches. Except where specifically required for derivative data, the cyclic A_{1_s} and B_{1_s} control angles were adjusted at each test point to approximately null out the first harmonics of inboard flatwise bending stress. Hovering data were taken within the tunnel test section at 107.7 percent, 100 percent, 92.3 percent and 76.9 percent nominal tip speed of 99.1 m/sec for blades configured with the pinned-pinned torque tube and with the cantilevered torque tube incorporating various available pitch-flap couplings. In particular, those cantilevered torque tube configurations selected included push-rod attachment points at 0.060 R and 0.080 R for trailing edge attachment and at 0.070 R and 0.091 R for leading edge attachment. These four push-rod attachment configurations define equivalent (geometric) δ_3 angles, relative to the first flatwise bending mode, of 48.1°, 33.2°, -41.5° and -23.0°, respectively. A summary of the forward flight test conditions is given in Table VI.

Test Data Acquisition and Reduction - The rotor data obtained during the test consisted of rotor performance (thrust, drag, and torque) and blade stresses (flatwise, edgewise, and torsional). The thrust, drag and torque data, obtained from self-balancing potentiometers, were corrected for tares and reduced to coefficient form (C_L/σ, C_D/σ and C_Q/σ) using the measured shaft angles (hub plane angles of attack) with appropriate corrections. Flexbeam flatwise and edgewise dynamic stress, blade outboard flatwise bending moment, and flexbeam torsion moment (or alternately, twist deflection) data were obtained from various strain gages and numerically calculated from visicorder output. These strain gages were located as follows: flatwise and edgewise bending gages were located near the blade root at 6 percent span, a flatwise bending gage was located outboard of the torque tube attachment point at 42 percent span and a torsion gage was located on the flexbeam at 17 percent span. The bending stress and moment calibrations were conducted by applying bending moments and dividing by the appropriate I/c's. Additionally, the directly calculable stresses and moments due to gravity were subtracted out. The flexbeam torsion gage output was similarly calibrated by applying a torque with the torque tube in place but with the pitch link disconnected.

Nominally, collective and cyclic pitch control angles were obtained from the outputs of potentiometers geared to the swash-plate drive motors. A cross-check on the pitch control angles was afforded by taking the mean and first harmonic cosine and sine components of the flexbeam torsion gage output. For the pinned-pinned torque tube configuration the potentiometer measurements of control angle correlated reasonably well with the torsion gage measurements; whatever discrepancies present were most probably due to flexibility in the flexible coupling and/or slop between the feathering cuff and its retention bolt (see Fig. 8). For the cantilevered torque tube configuration, however, the potentiometer outputs were inherently incapable of giving accurate measurements of the effective control angles due to the substantial washout caused by flexbeam bending flexibility. Hence, the potentiometer measured values of control angle used to identify the various performance and stress data must be considered to be only "indicated" or "swash-plate" values and not effective control angles.

Rotor angle of attack was obtained by first measuring the geometric tilt angle of the shaft relative to the tunnel test section and then subtracting that tilt angle required, at each advance ratio, to null the thrust when all control angles are set to zero. For advance ratios of 0.25, 0.35, and 0.47, the tilt angles so required were 0.3 deg, 0.7 deg and 1.0 deg, respectively. The source of this zero thrust angle of tilt is the blockage caused by the rotor rig. Thus, this angle of attack correction is only approximate since a finite rotor thrust would necessarily change the rotor drag (or alternately, the propulsive force) which would in turn vary the blockage. However, an assessment of the variation of this blockage with rotor thrust was beyond the capabilities of tunnel instrumentation and the zero thrust tilt angle corrections were used throughout.

Accuracy of Data - The estimated accuracies with which the parameters determining a given test condition could be set or determined are as follows:

Parameter	Accuracy
Swash plate (Indicated Control Angle)	± 0.2 deg
Tip Speed	± 0.3 m/sec
Shaft Angle	± 0.05 deg
Tunnel Speed	± 0.3 m/sec
Air Temperature	± 2°F

The static data repeatability for thrust, drag, and torque was derived from repeated calibrations of the strain gages made while determining the calibration derivatives for conversion of strain gage units (SGU's) into forces or moments. The dynamic data repeatability was established by considering the range of C_L/σ, C_D/σ and C_Q/σ measurements observed from consecutive test points. The mean range was established and related to the standard deviation using the procedures outlined in Ref. 9. The results for the accuracy of the thrust drag and torque measurements are given below:

Thrust, Drag and Torque Accuracy

Static Repeatability	Dynamic Repeatability
Thrust: ± 0.068 N	± 0.002 C_L/σ
Drag: ± 0.091 N	± 0.004 C_D/σ
Torque: ± 0.0138 Nm	± 0.003 C_Q/σ

The estimated accuracies of the dynamic data which were acquired on the recording oscillograph are the following:

Parameter	Accuracy
Flatwise Bending Stress (r = 0.06 R)	± 0.14 MN/m^2
Edgewise Bending Stress (r = 0.06 R)	± 0.14 MN/m^2
Flatwise Bending Moment (r = 0.42 R)	± 0.00043 Nm
Flexbeam Torsion (r = 0.17 R)	± 0.00043 Nm ± 0.1 deg

Experimental Results

The experimental results presented herein consist of hover performance (Figs. 17 through 22), forward flight performance (Figs. 23 through 33), vibratory stresses (Figs. 34 through 42), and control derivatives (Table VII and Figs. 43 through 47). Within each category the results for the pinned-pinned torque tube are presented first, followed by those for the cantilevered torque tube with various of the four tested push-rod attachment locations. Since the pinned-pinned torque tube configuration is inherently free of any geometrically induced pitch-flap coupling effects, the results obtained for this configuration provide a good standard for evaluating the results obtained

with the cantilevered torque tube configurations. All performance results are presented in the form of nondimensional force and torque coefficients divided by solidity. The vibratory stress (and bending moment) results are presented in the form of 1/2 peak-to-peak (PTP) values. The "performance" control derivative results are presented in the form of tables of numerically calculated derivatives. The "stress" control derivative results are presented in the form of (azimuthal) time-histories of blade stress and their perturbations due to perturbations in the control angles.

Hover Performance - Figures 17 through 21 show for each torque tube configuration the parametric variations in C_T/σ and C_Q/σ with collective pitch angle for each of four (4) tip speeds. Figure 17, which presents the results for the pinned-pinned torque tube, shows typical rotor characteristics for variations in both collective angle and tip speed. Since the pinned-pinned torque tube is inherently devoid of any pitch-flap coupling, these results provide a convenient basis for interpreting the results for the various cantilevered torque tube configurations which exhibit substantial pitch-flap coupling. Some scatter is seen in the torque coefficients at zero pitch and at the higher pitch settings. Variations in the effective pitch-flap coupling which the various push-rod attachment locations on the cantilevered torque tube configurations produce are amply shown in Figs. 18 through 21. The effective pitch-flap coupling for a hingeless rotor must necessarily be determined from the geometry of the elastically deflected blade. The variations in performance characteristics with tip speed for the cantilevered torque tube configurations demonstrate that this geometry is significantly influenced by the blade's centrifugal force field.

For those cantilevered torque tube configurations with trailing edge attachment (Figs. 18 and 20), the effects of control washout, due to flexbeam bending flexibility and negative (flap up-pitch down) pitch-flap coupling, are seen in the consistently higher collective angles required to obtain any given performance point. However, for those configurations with leading-edge attachment (Figs. 19 and 21) the effects of positive pitch-flap coupling when combined with the washout characteristics of flexbeam bending flexibility, are seen to produce initially a control washout at low collective angles, which diminishes at the higher angles. This can be seen by comparing thrust levels at low collective pitch settings on Figs. 19 and 21 with those on Fig. 17 for the pinned-pinned case. The latter case is seen to produce higher C_T/σ for the same θ at low values of θ, but at the higher θ's the C_T/σ values are similar. This trend is also seen in Fig. 22 where the pitch-flap coupling characteristics of the cantilevered torque tube on hovering performance are summarized. For either type of cantilivered torque tube attachment (leading- or trailing-edge) there is a washout due to flexbeam bending flexibility. That is, any finite push-rod load will not only twist the flexbeam, but bend

it as well, due to the relatively long load path for the push-rod shear load. Thus, for unit push-rod load, less of the total strain energy must necessarily be stored in torsion with less resulting flexbeam torsional deflection. Added to this initial washout due to flexbeam bending is the automatic pitch change due to the geometry of the elastically deflected blade (pitch-flap coupling), which is either positive or negative as the push-rod attachment point is ahead or aft of the feathering axis, respectively. For those configurations tested, the cantilevered torque tube generally produced a net washout of the inputted swash-plate collective angle relative to the behavior of the pinned-pinned torque tube.

Forward Flight Performance - In a similar manner to the hovering performance results, the forward flight performance results are shown in Figs. 23 through 33. For each torque tube configuration C_L/σ, C_D/σ, and C_Q/σ are shown for parametric variations in rotor angle of attack, collective angles, and advance ratio. Figures 23, 24, and 25 present the performance results for the pinned-pinned torque tube at advance ratios of .25, .35, and .47, respectively. Included in these figures are performance results for another model rotor similar in size, geometry, and twist and tested in the same facility at similar test conditions. This model rotor, however, was of semi-articulated type (flap hinges, but no lag hinges or cyclic pitch) and was fabricated with very high torsional rigidity ($\omega_{\theta_1} \approx 22$ P). A description of this semi-articulated model and its performance results are presented in Ref. 10. Selected performance results for this semi-articulated rotor are included in these figures to show what effect, if any, might result from the elastic characteristics peculiar to bearingless rotors. The semi-articulated rotor results presented in these figures are cross-plotted values to obtain results at the three advance ratios of .25, .35, and .45, and for tip-path angles of attack. This data manipulation was required to approximate more closely the bearingless rotor model conditions wherein, because of the deliberate nulling of hub moments, the shaft angle of attack coincided with the tip-path plane angle of attack.

Figures 23, 24, and 25 show that the cross plotted results for the semi-articulated model rotor generally agree quite well with the bearingless rotor results. Some descrepancies in collective pitch could arise due to the accuracy with which collective pitch could be set and with which the tip-path plane can be measured in the case of the flapping rotor results. The pinned-pinned torque tube configuration performance results of these three figures can be used, in a like manner as those for hovering performance, as a basis for interpreting the cantilevered torque tube configuration results.

Figures 26 through 29 show the forward flight performance results for the cantilevered torque tube configured model at an advance ratio of 0.25 for each of the four selected push-rod attachment locations. Comparison of

these figures with the corresponding results for the pinned-pinned torque tube configuration (Fig. 23) shows a reinforcement and extension of the hovering performance results: that a significant amount of control angle washout occurs with the cantilevered torque tube configurations. Furthermore, also in repetition of the hovering performance results, the two trailing edge attachment configurations have more washout at the higher collective angles than do those configurations with leading edge attachment. Figures 30 and 31 present similar cantilevered torque tube forward flight performance results for an advance ratio of .35, for two of the selected push-rod attachment points. Figures 32 and 33 then present corresponding results for an advance ratio of .47. In all these figures the same general findings as discussed above are reinforced.

Vibratory Stresses - Figures 34, 35, and 36 present 1/2 PTP values of inboard flatwise bending stresses, inboard edgewise bending stresses and outboard flatwise bending moments, respectively, for the model with the pinned-pinned torque tube. Note that these metric system stresses can be converted to the English system using Table I. General observations to be made from these data are (1) that the 1/2 PTP bending moments and stresses are monotonic increasing functions of advance ratio, (2) that the flatwise bending stresses and moments are monotonic increasing fuctions of blade loading, C_T/σ, (3) that edgewise bending stresses not only increase faster with blade loading than do flatwise stresses, but appear to achieve minimum values at finite values of blade loading, and (4) that the stresses are relatively insensitive to the means by which blade loading is achieved (collective angle vs. shaft angle of attack). Figures 37, 38 and 39 present corresponding 1/2 PTP bending stress and moment results for the model rotor configured with the cantilevered torque tube and with one of the trailing edge push-rod attachment locations. Similarly, Figs. 40, 41, and 42 present 1/2 PTP bending stress and moment results for one of the leading edge push-rod attachment locations. Observations which can be made from these figures, when compared with corresponding pinned-pinned torque tube results and with each other are: (1) that the inboard vibratory flatwise stresses for the cantilevered torque tube configurations showed stronger dependency upon blade loading than did those for the pinned-pinned torque tube, (2) that the cantilevered torque tube cases showed considerable 0.5 P oscillatory behavior at the higher advance ratio ($\mu = 0.47$), (3) that, for the cantilevered torque tube configuration with trailing edge push-rod attachment, the vibratory stresses were sensitive not only to C_T/σ, but independently to collective angle as well, (4) that, at the low blade loadings, inboard stresses for the cantilevered torque tube configurations were less than those for the pinned-pinned torque tube configuration, but that the reverse was true for the outboard flatwise bending moments, and (5) that the edgewise stresses for both torque tube configurations showed close qualitative agreement with variations in blade loading. An important characteristic of

the cantilevered torque tube configurations is that the (vibratory) push-rod load directly contributes to the total vibratory bending stresses in the flexbeam. Thus, it is not unreasonable to find that the vibratory bending stresses should be independently affected by blade control angle. The source of the 0.5 P oscillations is unknown, but the results of the correlation study suggest that the rotor may have been in a once every other revolution retreating blade stall condition, perhaps precipitated by the inherently soft torsion system for cantilevered torque tube configurations.

Control Angle Derivatives - For selected trimmed test conditions all rotor control angles (A_{1_s}, B_{1_s}, $\theta_{.75}$ and α_s) were independently perturbed to obtain the variations in performance and stresses due to variations in these control angles. Table VII summarizes the performance perturbation results in the form of partial derivatives of the measured load coefficients (divided by solidity) with respect to each of the control angles. These results again demonstrate the loss of control power experienced with the cantilevered torque tube configurations relative to the pinned-pinned torque tube configuration. Also shown in this table is that in this advance ratio range the lift coefficient/solidity derivatives are monotonic increasing functions of advance ratio. This table further corroborates Fig. 22 in showing that the cantilevered torque tube configuration with leading edge push-rod attachment has significantly more control power than does that with trailing edge attachment. This is consistent with the fact that the geometric pitch-flap coupling for the leading edge attachment configuration is positive (destabilizing) whereas that for the trailing edge attachment configuration is negative (stabilizing). Geometric pitch-flap coupling is defined herein as that calculated using pitch horn and mode shape geometry and discounting the washout due to flexbeam flexibility effects. The difference in pitch-flap coupling values for the two cantilevered torque tube configurations is also seen in the difference in sign for the lift coefficient derivative with respect to longitudinal cyclic, $\partial (C_L/\sigma)/\partial A_{1_s}$

The stress pertubation results are given in Figs. 43 through 47 for the same torque tube configurations and conditions given in Table VII. These figures each present the time-histories over one azimuthal revolution of inboard flatwise and edgewise bending stresses for the trimmed and plus and minus perturbations of control angles. Most notably these figures show that the variations of edgewise bending stresses with perturbations in control angles are generally small relative to those for flatwise bending stresses. The only case showing significant variations in this stress is the .35 advance ratio case for the cantilevered torque tube with leading-edge push-rod attachment location (Figs. 47a through 47d). Less obvious from these figures is the result that the variations in these stresses appear to be predominantly first harmonic. Furthermore, some cases (Figs. 44a, 44d, 46d,

47b, 37d) show significant differences in amplitude of variation for the plus and minus control angle pertubation, this would indicate nonlinear functional relationships of these stresses to the control angles.

CORRELATION RESULTS AND ANALYSIS VALIDATION

Time-histories of stresses and accompanying performance data for selected runs from the experimental model tests were used as correlation data for validation of the rotor aeroelastic analysis (computer program G400, described in Ref. 1). Discussion of the details of the test model and of the experimental wind tunnel test procedures are contained in a previous section. This section discusses the correlation and analysis validation study which consisted of (1) selection of appropriate experimental test cases for correlation, (2) formulation of valid ground rules for meaningful correlation and modification of the analysis to comply with them, and (3) actual validation of the analysis by applying it to the experimental test data. The following subsections discuss these component tasks.

Selection of Correlation Cases

A total of twelve (12) test cases were selected for the purpose of program validation. The major criterion for selection was to give a range of blade loadings (C_L/σ), advance ratios, and shaft angles representative of realistic full-scale flight conditions. In addition, cases were specifically chosen to substantiate the operation of the program within limited parameter variation. Two cases were chosen at substantially the same blade loading, advance ratio, and shaft angle but with two and four blades, respectively, to establish, if possible, the independence of program correlation to number of blades. Where possible, both pinned-pinned and cantilevered torque tube configured cases were chosen at comparable load conditions, to validate program operation for each of these optional dynamic configurations. Within the cantilevered torque tube configured cases, both leading- and trailing-edge push-rod attachment location cases were selected. Finally, since most experimental cases were run with the hub moments (i.e., 1P flatwise stresses) very close to zero, two cases were selected from a run with perturbations in control angles to show the isolated effect of substantial hub moment. All of the twelve correlation cases used for the program validation are summarized in Table VIII.

It is to be noted in this table that the pinned-pinned torque tube had essentially zero pitch-flat/edge coupling for all modes, whereas the cantilevered torque tube configuration demonstrated significant (geometric) pitch-flat coupling. Because of the existence of a "wobble mode" (rigid body torsion coupled with flatwise bending through the flexbeam bending flexibility)

for this configuration, actual pitch-flat coupling is dynamically phase lagged and modulated from the geometric value (see Ref. 1). The geometric shaft angles listed must be interpreted and used with reference to the zero lift hub angles of attack; for advance ratios of .25, .35, and .47 the zero lift hub angles-of-attack were, repsectively: -0.3, -0.7 and -1.0 degree. Finally, the control angles indicated in this table are those as best estimated from the considerations discussed in the following subsection.

Ground Rules for Establishing Correlation

In establishing the proper basis for correlation, it became apparent that the following factors had to be considered:

1. Using the data of Table VI, it can be shown that, for the outer 25 percent span of the blades, the various flight conditions tested defined a Reynolds number range of 80,400 to 422,000 and a corresponding Mach number range of .081 to .428. For this Reynolds number range and considering the clean airfoil construction used on the model blades, boundary layer transition can be expected to strongly affect the airfoil characteristics. Indeed, Ref. 10 shows, for a rotor operating in this test condition - Reynolds number range, that: a) the advancing blade sections are exclusively laminar, b) the low Reynolds number retreating blade sections are predominantly turbulent, and c) the extent of transition is a strong monotonically increasing function of blade loading.

2. Reliable NACA 0012 airfoil data in the operating Reynolds number range for these model tests are almost nonexistent. Extrapolation of existing (turbulent boundary layer) NACA 0012 airfoil data into the low Reynolds number range thus becomes more of an expeditious procedure than an accurate estimate.

3. Because the bearingless rotor is a hingeless rotor, substantial 1P stresses can easily be generated from 1P blade angles-of-attack. Furthermore, these 1P stresses are generally capable of masking and/or diminishing the higher harmonic content of the stresses.

4. Several sources of error in the measurement of the 1P blade angles-of-attack exist:

a. Blade control angles were measured primarily at the nonrotating portions of the swash-plate by means of potentiometers. These measurements inherently lack the ability to account for torsional flexibilities in the control angle load path above the swash plate. Potential sources of such flexibility include the swash plate itself and, for the pinned-pinned torque tube configuration the bushing for the inboard retention bolt and the Thomas coupling at the outboard end. While these latter flexibilities were lacking for the cantilevered torque tube, the bending flexibility of the spar provided a mechanism for considerable "washout" of the inputted control angle (see Ref. 1 for a discussion of this flexibility). This represented a significant problem in determining the actual blade angle under rotating conditions for the cantilevered torque tube configuration.

b. Reference signals from the potentiometers for the zero values of control angles could at best, be obtained only indirectly: at zero rotor speed using an inclinometer or, at nominal rotor speed, using thrust measurements.

c. The effective rotor (hub) angle-of-attack could only be estimated from the measured geometric angle-of-attack and the "zero thrust" angle-of-attack, i.e., the geometric angle needed to null the thrust. This latter quantity essentially represents the vertical deflection of the trimmed flow caused by model blockage. At nonzero thrusts, however, both blockage effects and tunnel-floor reflection effects would be expected to increase. These two effects are, furthermore, extremely difficult to measure or estimate and no attempt was made to do so.

d. It is likely that significant 1P components of inflow exist within the test section. Beyond any possible tunnel swirl (existing in the absence of the test model) a mechanism exists for asymmetric flow conditions: the motor torque which is imparted to the air by the rotor creates, in effect, a differential lateral blockage. That is, the equivalent drag center for the rotor model is laterally displaced from the tunnel plane of symmetry.

The above four items are all probably present to some extent, some greater than others. Their uncertainties are attributable to the expense and/or a lack of practical method of reliably and accurately measuring these effects. However, these effects are not considered influential in achieving the primary objective of this study which is to evaluate the overall feasibility of the Composite Bearingless Rotor.

5. Measurement of rotor thrust is relatively reliable and accurate; repetitive reference signals for zero thrust were easily obtained resulting in good calibrations.

6. The effects of blade pitch angle and structural twist of the flexbeam (resulting from pitch angle) on edgewise loading and edgewise coupling with flatwise should be significant based upon the order of magnitude of terms in the coupled edgewise bending response equation. Hence, the actual blade pitch angles should be as closely duplicated in the analysis as possible.

A consideration of these factors led to the following selected procedures for correlation:

1. The airfoil characteristics to be used as input to the aeroelastic analysis were estimated from the results of numerous previous aerodynamic studies made of rotors tested in this wind tunnel. Zero variation in Mach number (and, equivalently, Reynolds number) was assumed and a typical angle of attack variation in c_ℓ, c_d, $c_{m_{c/4}}$ was assumed. Based upon known stall boundaries for similar rotors tested in this facility (see Ref. 10) a lift stall airfoil section angle of attack of 11 degrees was assumed, with a gradual stall behavior above this angle. Drag coefficient variation with angle-of-attack was selected to best simulate various measured rotor drag and torque measurements. Moment coefficient was selected from low Reynolds number two-dimensional data available at UTRC. These assumed airfoil characteristics are plotted in Fig. 48. At best, they are a coarse approximation and represent the most probable impediment to accurate correlation; this is especially true for the drag coefficient upon which the edgewise stress is so dependent.

2. Meaningful stress correlations could be best made if the analysis were first run in a trimming mode wherein the calculated thrust and first harmonics of flatwise stresses were appropriately forced to agree with the measured values (actual measured thrust and null values for first harmonics of inboard flatwise stress). The aeroelastic analysis was thereby modified: (1) to trim on hub pitching and rolling moments as determined by first harmonics of blade root flatwise stresses, and (2) to effect the trim calculation by varying the zeroth and the first cosine and sine harmonic components of a generalized Glauert (momentum) inflow model (see Ref. 1) keeping control angles fixed.

3. For the pinned-pinned torque tube configuration, flexbeam torsion strain gage data were used to determine control angles. For the

cantilevered torque tube configuration, however, wherein substantial torsion flexibility and pitch-flat bending coupling effects obscure the torsion strain gage signals, the swash-plate potentiometer data were used, and a rigid-body torsion (wobble) mode was included in the analysis.

4. It is assumed that the primary purpose of the correlation study is to validate the aeroelastic analysis in so far as it adequately simulates the primary characteristics peculiar to the bearingless rotor. Therefore, although the analysis has provision for using variable (vorticity induced) inflow and unsteady (dynamic stall) aerodynamics, it was decided to use a more conventional inflow description (generalized Glauert using momentum considerations) and the usual quasi-static airloads formulation. This decision was further justified in that first, the variable inflow would be expected to affect only the higher harmonics of stress at the cost of significantly increased computation. Secondly, since the static airfoil characteristics were known only approximately, the inclusion of unsteady data was unwarranted. These two simplifying approximations should be kept in mind in the discussion of the results of applying the analysis, which follows.

Application of Test Results to Analysis Validation

Using the parameters defining the twelve correlation cases given in Table VIII together with the considerations discussed in the above subsection, the rotor aeroelastic analysis was run to simulate these test conditions. The results of these correlation runs are given in Table IX, and Figs. 49 through 86. For each of the twelve correlation cases, the analysis was first run without a trim calculation using the control angles listed in Table VIII, and then with the modified trim calculation wherein rotor lift and first harmonics of flatwise stress at the root were matched to the experimental values. The trim was obtained by maintaining the control angles at the experimental values and varying the generalized Glauert momentum coefficients, λ_o λ_{1_c}, and λ_{1_s}. In each figure the experimental values, and analytic values with and without trim are presented.

The performance correlation results are given in Table IX. Specifically, the rotor lift, drag, and torque coefficients (per solidity) for each of the twelve correlation cases are listed for the experimental, analytical (non-trimmed), and analytic (trimmed) results, respectively. The conventional (uniform) and generalized Glauert momentum inflow ratios, being aerodynamic idealizations, pertain only to the analytic result cases, as appropriate.

Comparison of the experimental results with the nontrimmed analytic results shows that, indeed, the nontrimmed analytic performance results are considerably in disagreement with the experimental performance results. However, comparison of the experimental results with the trimmed analytic results shows substantial improvement in the drag correlation and moderate improvement in torque. The corresponding lift results are, of course, essentially identical by virtue of the trim calculation. As was discussed in the above experimental model test results section the experimental accuracy limits on the lift, drag, and torque coefficient (per solidity) were, respectively, ±.002, ±.004 and ±.003. Hence, it is reasonable that correlation is seen to be best for the higher rotor loaded test cases; with the exception of the drag results for case 72.06 the trimmed analytical results correlate to within the experimental accuracies given above.

The stress time-history correlation results are shown in Figs. 49 through 86. These results consist of time histories of blade flatwise and edgewise stresses at the spar root (r = .06 R) and blade flatwise moment at a span of .42 R, which is somewhat outboard of the torque tube to flexbeam juncture (r = .31 R). For the four cantilevered torque tube cases, results are additionally presented for the flexbeam torsional stresses equivalently expressed in terms of flexbeam twist deflection. The results for the twelve cases defined in Table VIII are presented sequentially in the figures, and each of the four Roman numerically designated groups in Table VIII are discussed separately below.

As with the performance correlation results, stress time-histories are presented each for the experimental, analytic (nontrimmed) and analytic (trimmed) results.

Group I - Effect of Number of Blades - Since the aeroelastic analysis used in this study assumes hub rigidity and momentum inflow, it is inherently independent of numbers of blades. Hence the time-histories presented in Figs. 49 through 54 mainly show the effect of number of blades upon the experimental results for the pinned-pinned torque tube configuration. The effect of number of blades is essentially aerodynamic and, hence, it is reasonable to expect that the results found for one torque tube configuration would apply to both. Case 25.03 (Figs. 49 through 51) and case 87.08 (Figs. 52 through 54) are both at approximately the same flight conditions as defined by advance ratio, blade thrust loading, and control and hub angles. The lowest advance ratio (μ = .25) was chosen to accentuate the aerodynamic differences. From comparisons of Figs. 49, 50 and 51 respectively, with Figs. 52, 53 and 54 the following observations can be made.

1. The qualitative features of the experimental stresses and moments

(peak-to-peak levels and phase angles) are relatively insensitive to number of blades.

2. The four-bladed (case 87.08) stress time histories show greater harmonic content than the two-bladed case time histories. This should reasonably follow from the increased variable inflow due to the wake vorticity of the two additional blades.

3. The nontrimmed analytic root flatwise bending stresses show substantial lack of correlation with the experimental values.

4. The effect of trimming is to greatly improve the root flatwise bending stress correlation. In general, the phasing and harmonic content (mostly second) are well simulated.

5. The trimmed analytic root edgewise bending stress results show moderate improvement over those for the untrimmed analytic results. The main improvement appears to be in the phasings of the first harmonic contents; the first harmonic amplitudes do not agree well for these cases.

Group II - Pinned-Pinned Torque Tube Configuration, Flight Condition Variation - Time history results for cases 22.03, 22.04, 21.05 and 22.05 are shown in Figs. 55 through 66, and show the effects of limited flight condition variation upon correlation for the pinned-pinned torque tube configuration. The importance of this torque tube configuration to the correlation study is that it is virtually free of any complicating pitch-flap coupling characteristics in contrast to the albeit mechanically simpler cantilevered torque tube configuration.

In general, the correlation results for these four pinned-pinned torque tube cases show characteristics similar to those observed and discussed above: While the untrimmed analytic results correlate very poorly, the effect of trimming is to give relatively good correlation. Specific observations which can be drawn from the trimmed analytic results of Groups I and II combined are as follows:

1. Root flatwise stresses (Figs. 49, 52, 55, 58, 61 and 64): The predicted second and higher harmonic contents and phasings are generally in good agreement with experiment. Correlation is poorest at the low advance ratio cases where the observed increased higher harmonic content is not simulated; correlation of harmonic content is consistently excellent at the two higher advance ratios. The mean or zeroth harmonic stresses do not consistently correlate well, however.

2. Root edgewise stresses (Figs. 50, 53, 56, 59, 62, and 65): These stresses are both observed and calculated to be predominantly 1P and the predicted values show moderate agreement in amplitude and phase with experiment. The predicted values are generally smaller in PTP amplitude than, and are phased more in advance of, experimental. These cases represent concurrent variations in both blade loading and advance ratio. Comparison of the results shows that the azimuthal maximum and minimum points of the 1P component appear to be sensitive to these two parameters. While not shown in these correlative experimental results, the effect of blade loading change at constant advance ratio was examined using harmonic analyses of stresses at other flight conditions. There, it was consistently seen that at a given advance ratio the phasing of the 1P content of the edgewise stress was monotonically advanced (i.e., maximum stresses occur at an earlier azimuth angle) with increasing blade loading or equivalently, with mean airfoil angle-of-attack. Thus, since the cases of Group II are also at monotonically decreasing blade loadings, the trend of 1P edgewise stress phasing seen in these correlation cases is consistent. Although the analytic edgewise stresses are, as noted, generally phased in advance of the experimental results, the combined blade loading-advance ratio trend appears to be reasonably well correlated. More will be said on this topic of 1P edgewise stress phase angle below in the discussion of the next group of correlation cases.

3. Blade outboard bending moment (Figs. 51, 54, 57, 60, 63, and 66): Despite a substantial variation in advance ratio and blade loading the experimental results show the remarkable similarity that the responses are predominantly 1P, 3P, and 4P, and the peak-to-peak values and general azimuthal signature are all invariant. The theoretical results show a similar qualitative behavior in that there is no significant PTP variation with these parameters either. The analytic PTP values however are consistently less than the experimental values as a result of the analytic results being predominantly only 1P, 2P, and 3P.

Group III - Effect of Hub Moments - Because of the proximity of the first edgewise mode frequency to 1P ($\bar{\omega}_{v_1} = 1.35$), the low inherent damping of this mode and the potential for significant elastic coupling of edgewise bending with flatwise bending due to twist, it is reasonable to allow that blade edgewise 1P stresses might be a function of 1P flatwise bending, or equivalently rotor hub moment. Since the aeroelastic analysis predicts zero elastic coupling of flatwise and edgewise bending due to twist a further test of the analysis is to compare analytically predicted edgewise stress responses with experimental ones to detect this coupling, if present. In order to isolate this effect correlation was attempted with cases 11.05 and 11.06 which differ by 1.3 degrees of B_{1_s} as shown in Table VIII. Case 11.05 is essentially a zero hub

moment (zero 1P flatwise bending) case whereas significant 1P flatwise bending is present in case 11.06 as is shown by contrasting Figs. 67 and 69. Figures 68 and 70 show the corresponding edgewise stresses for these two conditions. It can readily be seen that, although the analytic results show a substantially advanced phase angle from the experimental results, the PTP edgewise stresses and the neglibility of 1P flatwise bending upon edgewise bending are well correlated. As was discusssed in the Group II results the phasing of the 1P edgewise stresses appears to be a strong function of some combination of blade loading, or equivalently, mean blade section angle of attack and of advance ratio. Indeed, cases 11.05 and 11.06 being low disk loading cases, show a relatively retarded 1P phase angle and are thus consistent with this general trend discussed earlier.

Group IV - Cantilevered Torque Tube Configuration, Flight Condition Variation- Unlike the pinned-pinned torque tube, the cantilevered torque tube introduces a significant degree of elastic coupling between flatwise bending and rigid body feathering. The primary resulting coupled mode is referred herein as the "wobble" mode. Direct consequences of this coupling are: a) control angle "washout" wherein swash-plate input angles, considerably larger than those for a pinned-pinned configuration, are required to achieve comparable performance and/or trim, b) general inability to eliminate pitch-flat coupling for more than one bending mode at a time, c) resulting pitch-flat couplings manifesting dynamic amplifications and phase lags due to the impedance characteristics of the wobble mode, and d) a relatively "soft" torsion system with the potential for coupling with all the major lower frequency modes.

A mathematical requirement for the successful modeling of this elastic coupling is the ability to calculate the force-deflection characteristics of the flexbeam-torque tube assembly at the push-rod attachment point. That is, the out-of-plane deflection of this attachment point accruing from blade flexbeam bending flexibility and due to a parallel directed unit load at that point must be accurately calculated. Reference 1 describes some of the details involved in this calculation, which is an internal portion of the aeroelastic analysis and uses transfer matrix techniques. This calculation was satisfactorily validated experimentally by measuring the flexibility of a statically mounted blade spar (flexbeam) loaded in tension to simulate the centrifugal load. For the nominal condition, a flexibility of .440 mm/N was calculated versus a measured value of .414 mm/N for the blade spar with an equivalent static torsion load. The use of this flexibility for modeling the elastic restraint and "dynamic" pitch-flat coupling of the wobble-mode is also described in Ref. 1.

The time-histories, shown in Figs. 71 through 86, present the correlative results for the cases of Group IV. Specifically, they show comparisions between

experiment and theory for limited variations in flight conditions and pitch-flat coupling, as determined by push-rod/torque tube attachment point location. In addition to those stress and moment quantities similarly shown for the pinned-pinned torque tube configuration, flexbeam torsion deflection results are also presented. The torsional rigidity of the pinned-pinned torque tube configuration discussed above in Groups I, II, and III was relatively high ($\bar{\omega}_{\theta_1} = 6.0P$). Hence, the flexbeam was effectively uncoupled in torsion so that its torsion stress, or equivalently, elastic twist was substantially determined by the swash-plate input angles. Indeed, the time-histories of the flexbeam torsion deflections for the pinned-pinned torque tube cases were regularly sinusoidal and consequently used to establish the effective control input angles. Because of their regularity, formal presentation of these time-histories would have been superfluous and was consequently omitted. In the case of the cantilevered torque tube, however, the torsion system was relatively soft, owing to the inclusion of flatwise bending flexibility in the effective torsion restraint. The time-histories of flexbeam elastic twist, in this case, became multi-harmonic; superimposed on the 1/rev character due to swash-plate inputs were the multi-harmonic responses of the wobble-mode. Thus, the flexbeam torsion traces ceased to be a source of input calibration and, moreover, became an additional correlative quantity. Specific observations to be drawn from the trimmed analytic results of Group IV are as follows:

1. Blade root flatwise bending stress (Figs. 71, 75, 79, and 83): The predicted results follow the same trends observed for the pinned-pinned torque tube. In general, the low advance ratio ($\mu = .25$) results underpredict the 3P (and higher) results, but the higher advance ratio ($\mu = 0.47$) results are in excellent agreement. The mean value is also well correlated but not consistent.

2. Blade root edgewise bending stress (Figs. 72, 76, 80 and 84): Again the predicted results follow the same trends observed for the pinned-pinned torque tube. The predominantly 1P PTP amplitude is underpredicted and phased in advance of the experiment.

3. Blade outboard bending moment (Figs. 73, 77, 81 and 85): Whereas the lower advance ratio results are seen to parallel the results for the pinned-pinned torque tube, the predicted harmonic results for the higher advance ratio case are in very good agreement with the experiment.

4. Flexbeam torsion deflection (Figs. 74, 78, 82 and 86): The predicted results are predominantly 1P and correlate the 1P in amplitude and phase excellently. It should be noted that these time-histories each represent the sum of collective and cyclic swash-plate inputs together with the substantial wash-out due to mean and 1P wobble mode responses, as reference to Table VIII

shows. The higher harmonics (mainly 2P, 3P, and 4P) seen in the experimental results are not well simulated; this is consistent with the underprediction of both 3P root flatwise bending and 1P root edgewise bending whose product would thus constitute an underpredicted 4P torsion response.

5. Subharmonics of case 73.08 (Figs. 83 thru 86): These figures each show two experimental time histories for the plotted azimuthal period of 360 deg.: these multiple traces each represent the two halves of time histories which repeat in a regular fashion with an azimuthal period of 720 deg. Thus, the responses are manifesting (stable) 0.5P subharmonic characteristics. Examination of the experimental portion of these figures shows that:

a) The experimental 0.5P subharmonic content is most dominant in the blade root flatwise and edgewise bending responses.

b) The experimental flatwise bending stresses (Fig. 83) show the greatest degree of dissimilarity between revs on the retreating to aft portion of the disk. The dissimilarity is one primarily in level and secondarily of phase, since the maximum and minimum points occur at approximately the same azimuth angles.

c) The dissimilarity of edgewise bending stresses (Fig. 84) between revs is mainly one of phasing; the transition from maximum stress to minimum is either lagged or advanced between revolutions, again on the retreating to aft portions of the disk.

d) On the aft, advancing to leading portions of the disk the experimental flatwise bending and torsion responses both show a dissimilarity between revs in 2P amplitude with the phasing virtually unchanged.

The above results can be interpreted to a certain extent by noting that in Fig. 83, on the retreating side for revolution no. 1, the flatwise bending response is unable to sustain the increased 2P response amplitude shown on the advancing side. Moreover, at an azimuth of approximately 225 degrees, the rev. no. 1 appears to demonstrate a stalled characteristic. Furthermore, examination of Figs. 84 and 85, respectively, show for the rev. no. 1 portions of the responses, that at the forward portion of the disk the blade concurrently has an increased aft lag rate and an increased pitch angle, both conductive to stall. The analytic predictions on the other hand show a similar stalled characteristic. Indeed, although not shown, examination of the details of blade angle of attack distribution for this analytic case show the blade to be mildly (quasi-statically) stalled over the azimuthal sector defined from 230 degrees to 330 degrees. Thus, it would appear probable that a principal source of the experimental 0.5P subharmonic response is a subharmonic stalling

of the blade on the retreating side. It is likely that this stalling is aggravated by the subharmonic increase in 2P torsional responses which are a probable result first of the higher coupling of torsion with the flatwise bending responses, which themselves are mainly 2P, and second, the greater susceptibility of blade torsion to (relatively) low frequency excitation due to the increased torsional flexibility of this torque tube configuration.

Correlation Study Evaluation & Comments

Based upon the details of the correlation cases discussed above and recalling both the experimental limitations and the assumed aerodynamic simplifications, it is generally concluded that the aeroelastic analysis predicts blade bending and torsion responses consistent with rotor performance with reasonable accuracy. It is furthermore concluded that the analysis is suitable for the aeroelastic analysis of the full scale design. Other more specific comments to be made concerning analysis correlation are as follows:

1. It is likely that the analysis was run with inaccurately defined flight condition parameters for several of the correlation cases in that the analysis of some of the correlation cases (87.08, 22.04, 21.05, and 73.08) achieved exceptionally good correlation for all stress and moment variables.

2. Correlation tended to improve with advance ratio. This trend is most likely due to the known reduction of variable inflow effects with speed.

3. Best correlation was achieved with inboard flatwise stress. The most probable reason for this is that this variable is so strongly a function of lifting airloads which are the most linear and can thus most accurately be approximated.

4. Actual one-to-one correlation of edgewise stress both in magnitude and phase was only moderate. However, the trends of edgewise stress with parametric variation were duplicated with reasonable accuracy. Since the edgewise stresses were predominantly one per rev it is most likely that the edgewise stresses were governed mainly by aerodynamic drag forces. It is therefore likely that the only moderate correlation of edgewise stresses is due to the coarseness of the assumed model airfoil drag characteristics.

5. Correlation of the predominantly one/rev flexbeam torsion stresses for the cantilevered torque tube was excellent. Higher harmonics of this torsion stress were consistently underpredicted, however.

6. The 0.5P subharmonic responses of case 73.08 were not successfully simulated. One probable reason for this discrepancy is that the model rotor appeared to be stalling every other revolution and was therefore a strongly aerodynamic phenomenon requiring accurate airfoil drag data which wasn't available.

7. The analysis accurately predicted a minimal influence of 1P flatwise bending on edgewise stresses.

8. The analysis correlated well in a passive sense in that it did not predict unstable motion for any case which was observed to be stable.

FULL SCALE DESIGN

The primary objective of conducting a preliminary full-scale design as part of this feasibility study were 1) to enable an experienced rotor designer to examine the practical aspects of the CBR from the viewpoint of fabrication and total system requirements, and 2) to provide realistic blade mass and stiffness characteristics for use in the aeroelastic analysis discussed in a later section of this report. The specific rotor size was not of particular importance. It was believed, however, that a relatively large rotor would be of greater significance since there has been a general concern over the ability to scale up relatively small hingeless rotors (diameters less than 12m (40 ft)) for large helicopter applications. An S-61 size aircraft was selected having a 4-bladed rotor with a diameter of 18.9 m (62 ft), chord of .58 m (1.9 ft), and a design tip speed of 198 m/sec (650 ft/sec). Initially, blade frequencies typical of conventional hingeless rotors were selected, i.e., first mode flatwise frequency slightly greater than one-per-rev and first edgewise frequency between one-per-rev and two-per-rev. It was felt that such a design would be relatively free of instabilities and the aeroelastic analysis could focus exclusively on the dynamic characteristics associated with the CBR and not be influenced by unrelated dynamic phenomena of hingeless rotors. Two designs were considered, one having a cantilevered control torque tube, and the other having a control torque tube with a "snubber" support at the root end to eliminate pitch coupling associated with flapwise motions of the torque tube. The decision to include the snubber design was influenced primarily by an early wind tunnel investigation in which adverse coupling was experienced under certain low tip speed operating conditions. Although the test was exploratory in nature and the coupling arising from an unrealistic off-design operating condition, it demonstrated the potential for undesirable coupling in the cantilever torque tube design which should be thoroughly evaluated before proceeding to full-scale development. It was thus decided that both torque tube concepts be configured so that preliminary design information would be available for each.

A comprehensive aeroelastic analysis of the full-scale design is presented in a later section, and in this analysis only the "snubber" design is studied. The extent of this study was such that only one design could be so investigated, and it was decided that the first generation CBR to reach flight status would probably be of the snubber design -- the minimum risk approach. However, both designs were evaluated in the model wind tunnel program.

Several composite materials were available that could possibly satisfy the stiffness requirements of the CBR. Most notable were fiberglass, boron/epoxy, graphite/epoxy. From the standpoint of cost, fiberglass was the obvious choice; however, due to its lower bending modulus, an increased flexbeam

cross-section would be required to achieve the desired frequencies. This would also necessitate an increase in flexbeam length since its torsional stiffness would go up due to the larger cross-section. The shear modulus of fiberglass is approximately equivalent to that of graphite/epoxy so that no benefit in reduced torsional stiffness can be realized in using fiberglass with low bending modulus. Graphite/epoxy was selected over the boron/epoxy primarily due to its lower cost and greater machinability. It was also favored because of the experience gained in its use during the initial studies and experiments conducted in developing the CBR concept.

The design features of both the cantilever and the snubber torque tube configurations are described in the following paragraphs.

Cantilever Torque Tube Design

The general layout of the cantilever torque tube design is shown in Fig. 87. The initial requirements that set the basic spar dimensions were a first flatwise mode frequency between 1.05 P and 1.10 P to ensure good handling qualities, a first mode edgewise frequency greater than 1.25 P to provide adequate separation from the primary edgewise excitation frequency of 1 P, and a flexbeam torsional stiffness sufficiently low so as not to exceed the push-rod design loads or the control actuator limits. The flatwise and edgewise frequencies are determined primarily by the flexbeam thickness and chord dimensions. The torsional stiffness is determined primarily by the flexbeam thickness and length. The flexbeam that satisfied these requirements was 2.44 m (96 in.) in length, tapered in chord from 0.305 m (12 in.) at the hub (Station 15) to 0.203 m (8 in.) at Station 111, and tapered in thickness from 3.05 cm (1.2 in.) to 2.54 cm (1.0 in.) over this same span. The flexbeam could either be joined to the blade at Station 111 by means of a conventional bolted joint or carried through to the tip forming the primary structure of the entire blade. The decision to carry through to the tip or have a joint at Station 111 depends upon composite materials manufacturing facilities, transportability requirements, and blade folding requirements. The design selected for this study was of the continuous spar type where the spar carried from the tip of one blade through to the tip of the opposing blade. The chord dimension of the outboard spar was maintained at the value at Station 111 (0.203 m); however, the reduced flatwise stiffness contribution required of the outboard spar allowed the thickness to be tapered from 2.54 cm (1.0 in.) to 0.64 cm (0.25 in.).

The blade cover is comprised of graphite/epoxy with $\pm$ 45 deg fiber alignment to provide maximum torsional stiffness. The skin thickness was set at 0.102 cm (0.040 in.) which was sufficient to provide a fixed root torsional frequency of greater than 5 P. The leading edge is protected with a steel/nickel plated abrasion strip and extends from the outboard end of the torque

tube to the blade tip cap. A small abrasion strip also covers the leading edge of the tip cap. Nomex honeycomb is used to fill the cavity between the spar and cover and structurally bonded to both to form a blade which is relatively rigid in torsion. The leading edge incorporates a molded counterweight consisting of lead shot and adhesive to mass balance the blade at the quarter chord.

The torque tube is cantilevered from Station 111 inboard to station 19. The torque requires not only high torsional rigidity to transmit control input to the flexbeam but also requires high flatwise bending stiffness to prevent large bending deflections caused by the pushrod loads. To accomplish these requirements both + 45 deg plies and 0 deg plies are laminated resulting in a maximum skin thickness of 1.52 cm (.6 in.) at the juncture tapering to 0.25 cm at Station 19. The thickness also tapers to 0.25 cm at the leading and trailing edges of the torque tube. In order to accommodate a total pitch travel of -10 deg to +35 deg and to allow for the bending deflection of the torque tube under the maximum push rod load a total thickness of 43.2 cm (17 in.) was required.

The flexbeam design was initiated by prescribing that the flexbeam cyclic shear stress not exceed the design allowables under maximum cyclic pitch condition. The allowable stress was set at 24 MN/m^2 (3500 psi). This level was established from the fatigue tests reported in a separate section of this report, wherein an average fatigue limit of 48 MN/m^2 (7000 psi) (defined as a 10 percent reduction in modulus after 10^7 cycles) was measured. Applying a safety factor of 2 gives the design limit of 24 MN/m^2. The cyclic pitch required at the trimmed high speed condition of 170 kn was approximately 10 deg. A conservative value of 15 deg was selected to include maneuvers. Using the midflexbeam station as representative, the stress is calculated from the following equation

$$f_s = \frac{tG\theta}{\ell}$$

where t and ℓ are the flexbeam thickness and length, respectively. Solving for flexbeam length,

$$\ell = \frac{tG\theta}{f_s} = \frac{0.0279 \times 6207 \times 0.262}{24} = 1.89 \text{ m } (74 \text{ in.})$$

Further conservatism was added by extending the length to 2.44 m (96 in.) to cover possible stress concentrations and variations in G. For this flexbeam length the calculated maximum cyclic stress at the midpoint is 18.6 MN/m^2 (2700 psi), well below the fatigue limit.

To minimize the steady torsional stress in the flexbeam a built-in twist of 13.5 deg was used. This represents an average collective pitch estimated for a typical helicopter mission. The built-in twist is incorporated during the material layup of the flexbeam where the actual mold in which the beam is cured is twisted to the required angle prior to layup. The aerodynamic twist rate of the outboard portion of the blade is -4 deg, and the airfoil section NACA 0012. If desired, the twist and airfoil section could be easily modified in the mold designs for the spar and skin; however, for the purposes of this feasibility study conventional airfoil and twist were used.

A preliminary aeroelastic analysis, performed after the preliminary design study, revealed lowly damped coupling between several bending modes and the rigid body torsion mode (wobble mode acting about pushrod support point) at a high forward speed condition. This condition was improved with the addition of an 11.35 kg (25 lb) tip weight.

The blade mass and stiffness characteristics are given in Figs. 88 thru 90 and torque tube and flexbeam information is given in Figs. 91 thru 93. A summary of the blade uncoupled natural frequencies is presented in Figs. 94 and 95. It should be noted that these figures contain results for both subcritical and supercritical designs. These represent the two configurations studied in the aeroelastic analysis and refer to the frequency placement of the first edgewise mode. A subcritical designation represents a first edgewise frequency of greater than the rotational frequency and is the design described in this section. The supercritical represents an edgewise frequency less than rotational frequency. The decision to examine the superciritical case was made following the completion of the full-scale design effort described in this section. Further discussion of the supercritical case is presented in the Aeroelastic Analysis Section.

Snubber Torque Tube Design

The layout for the snubber torque tube design is shown in Fig. 96. The general design features of this configuration are identically equivalent to those of the cantilever design except for the torque tube characteristics. In this design an additional support point is provided for the torque tube. In addition to the juncture at the outboard end of the flexbeam and the attachment point of the push rod, an elastomeric snubber is incorporated at the inboard end of the torque tube and bonded to it and the flexbeam. With such a three point support essentially all pitch coupling due to flapping is eliminated. In this design the torque tube is not required to transmit bending moments, only torsional moments, and thus only ±45 deg fibers are used. The skin thickness is constant at 0.25 cm (0.1 in.). Also, to achieve the condition of low bending moments in the torque tube, the total thickness of the torque tube at the juncture is reduced to that of the blade itself and the

fiber angles are increased beyond ± 45 deg to affect a reduction in bending modulus at this point. The resulting structure remains relatively high in torsional stiffness but reduced significantly in flatwise bending stiffness. The total torque tube thickness at Station 19 to accommodate the 45 deg pitch requirement is 38.6 cm (15.2 in.). The structural and frequency information presented in Figs. 88 to 94 also apply to the snubber torque design.

The total blade weight amounted to 120 kg (265 lb) and the hub plates 145 kg (320 lb). In comparing CBR weight with a conventional articulated rotor of the same diameter and solidity, an additional 45.4 kg (100 lb) are added to account for a somewhat larger shaft to accommodate the larger hub moment capability. This results in a total rotor weight plus added shaft weight of 671 kg (1480 lb) which is approximately 23 percent less than the articulated rotor.

AEROELASTIC ANALYSIS OF FULL-SCALE DESIGN

Selection of Configuration Details and Variants

The specific component structural elements of the full-scale design were sized by the fundamental requirements of strength (torque tube and flexbeam), and by satisfying basic vibrational characteristics (i.e., absence of integral harmonic resonances). Variants of the basic design, however satisfactory they might be on the basis of these fundamental requirements, must show satisfactory performance in a variety of more comprehensive aeroelastic categories. In addition, even within the confines of the basic design, as defined in the previous section, considerable latitude exists in the proper selection of various details which could profoundly affect the aeroelastic characteristics. Consequently, a proper design analysis should include an investigation of the effects of parametric variation of these details. To satisfy these requirements the general aeroelastic analysis described in Reference 1 and validated in the correlation section of this report was employed. This section presents the results of applying this analysis in its various specific categories to variants of the full-scale rotor design. More specifically, two basic nominal blade designs were selected: one, a subcritical configuration wherein the uncoupled first edgewise modal frequency was set near to 1.3P and the other, a supercritical case wherein the edgewise frequency was set near to 0.8P. The former value was selected for subcritical operation as it provided adequate separation from 1P and 2P and generally represented the state-of-the-art. The latter value was selected as being a conservative value from an air resonance standpoint based upon the results of References 11 and 12.

As was discussed in the previous section, although two different torque tube configurations were designed, only the snubber design was used herein. The nominal torque tube properties for the snubber design are shown in Figures 91 and 92 and compared with those for the cantilevered design in Figure 91. Initial aeroelastic calculations showed that, for the supercritical design, the nominal torque tube stiffnesses raised the effective (coupled) first edgewise modal frequency to 0.88P. Indeed, calculated time history responses indicated "excessive" 1P edgewise responses for this configuration. Consequently, the supercritical design was reconfigured with flatwise and edgewise torque tube stiffnesses equal to 25 percent of the nominal values as used in the subcritical design. This reduction in stiffness lowered the effective first edgewise frequency to 0.81P. In addition, whereas the nominal push-rod radial attachment point of 21 in. is used for the subcritical design, a value of 19 in. is used for the supercritical design. This value was selected to eliminate all significant amounts of geometric pitch-flat and pitch-edge coupling from the supercritical design. Conventional NACA 0012 airfoil data

were used with an incremental drag coefficient of 0.002 to account for operational surface roughness. The built-in precone and prelead angles were assumed to be 3.5 degrees and zero, respectively. In both rotor configurations three (3) flatwise, two (2) edgewise, and one (1) torsion (uncoupled) modes were assumed for the blade elastic description. A structural damping equivalent critical damping ratio of 0.015 was assumed for the edgewise modes. Except where noted, the full redundant analysis capability of the aeroelastic analysis (as described in Reference 1) was utilized. The following subsections will describe, in turn, the results of the eigensolution analysis, the choice and calculation of the basic trim cases, aerodynamic stability derivatives, transient responses due to partial material failure, the effects of unsteady aerodynamics, and the results of blade transient stability analyses of both the cantilevered torque tube configured test model rotor and the full-scale design.

Eigensolutions

The eigensolutions of interest that are available are the "vacuum" and "nonvacuum" calculations wherein the perturbational airloads are, respectively, neglected and included. The "vacuum" eigensolutions are useful in establishing coupled modal frequencies and mode shapes due to such coupling effects as blade control pitch angle, twist, precone and prelead angles, torque tube stiffnesses, section mass and tension center offsets and structural damping. Such eigensolution information is most useful for insuring against integral harmonic resonances. The "nonvacuum" eigensolutions are useful for identifying flutter and/or aeromechanical instability characteristics in hover, and for providing a crude indicator of stability trends in forward flight. The nonvacuum eigensolution considered herein is of the "frozen azimuth" type wherein the periodicity of the equation coefficients defining the mass, damping and stiffness matrices is neglected. Such an analysis is thus incapable of accurately identifying stability levels of rotors in forward flight. While recourse could have been made to extending the nonvacuum eigensolution to a Floquet theory type analysis, such as are alternatively described in References 13, 14, and 15, the time-history solution of the fully nonlinear formulation was deemed intrinsically more accurate and relevant to the stability analysis of a trimmed, realistically configured rotor blade design. A more detailed description of this stability analysis is contained below in a subsequent subsection. The remainder of this subsection describes first, the results of using the vacuum eigensolution to obtain coupled frequency and mode shape information with limited parameter variation and second, the results of using the nonvaccum eigensolution for a series of hovering flight conditions.

Using the vacuum eigensolution, the effects of tip speed, collective angle and torque tube stiffness variations on the coupled frequencies and mode shapes were determined for the two basic blade designs (subcritical and supercritical). For each of these designs the above three parametric variations

were made about the nominal conditions defined by a tip speed of 198 m/sec, a collective angle of 12 deg and the snubber torque tube stiffnesses shown in Figure 92.

Coupled (Vacuum) Modal Frequencies - The effects of the parametric variations on the coupled modal frequencies are shown in Figures 97 through 99 for the subcritical design and Figures 100 through 102 for the supercritical design. These results were obtained by disregarding all aerodynamic terms in the general eigensolution. Figure 97 shows for the subcritical design the effect of tip speed variation on the coupling of the primitive "uncoupled" modal frequencies (those shown in Figures 94 and 95). Not unexpectedly, the intersection point of the second flatwise (2F) mode with the first edgewise (1E) mode at a tip speed of approximately 75 m/sec shown in Figure 95 becomes two diverging branches at that tip speed as shown in Figure 97. At such a point each branch is characterized by comparable amounts of both (2F) and (1E) modal content. At the nominal rotor speed the original (1E) branch has become predominantly (2F). Note that in all the coupled frequency figures, the predominant modal contributors to the coupled modes at the high end of the parameter scale are shown in parentheses, in order of decreasing percent contribution. Of significance is the result that the first edgewise mode (1E) contributes to such a large degree to both the second and third coupled flatwise modes. In addition, Figures 98 and 101 both show that for the collective pitch angle range most typical of helicopter operation all modes except the third coupled flatwise mode are reasonably well separated from integral harmonics. Since flatwise modes are relatively well damped and 5P excitations of this mode are low, the close proximity of this modal frequency to 5P is not considered critical.

Coupled (Vacuum) Mode Shapes - Due to the variety of coupling mechanisms considered in the analysis (pitch angle, twist, coning, structural damping, etc.), even in the absence of aerodynamic loads the coupled mode shape components are generally nonuniformly phased. That is, there is no point in the oscillation cycle of any vibrating coupled mode wherein all portions of the blade concurrently have zero kinetic (or, alternatively potential) energy. Hence, coupled mode shape information must include, in addition to the usual component deflection distributions, the concurrent component velocity distributions as well.

Presented in each of the Figures 103 through 106, and for each of the six (6) coupled frequencies typically shown in the preceding figures (97 through 102), are the spanwise distributions of modal deflection and (nondimensional) velocity in each of three (3) components of motion for $\theta_{.75R}$ = 0 deg and 12 deg. The components of motion so depicted are inplane and out-of-plane translation (y_5 and z_5, respectively), and torsion (θ). Variation of the coupled mode shapes with the other parameters (tip speed and torque tube bending stiffnesses) was found to be qualitatively quite similar

to the variations with collective angle. Results for the subcritical design at 0 and 12 deg collective angle are shown in Figures 103 and 104, respectively, and the results for the supercritical design are shown in Figures 105 and 106.

A comparison of the zero collective cases (Figures 103 and 105) shows two main dissimilarities: (1) the $\overset{*}{y}_5$ and $\overset{*}{z}_5$ velocities associated with the respective coupled (1F) and (1E) modes are oppositely phased for the two rotor types, (2) the presence of significant pitch-flat coupling for the subcritical rotor design and negligible amounts for the supercritical one is reflected in the respective amounts (or absence) of torsion motion in the coupled flatwise modes. Note that the torsional components of these coupled modes shown in Figure 103 clearly demonstrate the locally exaggerated torsional flexing of the flexbeam as is required to accommodate the automatic pitch change due to flatwise bending.

The coupling influence of collective pitch angle is shown in comparisons of Figure 103 with 104 and/or Figure 105 with 106. This coupling is seen to increase the nonuniform phasing of the resultant modes; in general, the component displacement distributions are increasingly dissimilar from their respective component velocity distributions. A comparison of Figures 104 and 106 shows, for both the subcritical and supercritical designs, a high degree of blade motion in all components for the coupled second edgewise bending (2E) mode. The significantly larger θ and $\overset{*}{\theta}$ content in the coupled mode for the subcritical configuration is due mainly to the closer proximity of the torsional frequency (10.42P) to the subcritical uncoupled (2E) modal frequency: (7.28P) vs. (4.14P) for the supercritical configuration.

(Nonvacuum) Coupled Mode Damping Levels - The results obtained from limited usage of the nonvacuum eigensolution calculation are shown in Figures 107 through 110. Each of these figures shows the variations of the critical damping ratios for the six (6) coupled mode eigenvalues, with concurrent variations in collective pitch angle and (spanwise) variable inflow. The inflow (or, equivalently, induced velocity) assumed is conventional (see Reference 16) and, at each radial station depends upon the local total pitch angle. Figures 107 and 108 present coupled modal damping ratios for the subcritical and supercritical configurations, respectively, wherein linear, unstalled NACA 0012 section aerodynamic coefficients are assumed. That is, c_ℓ is assumed proportional to angle-of-attack using a Mach number dependent lift curve slope, c_d is assumed equal to c_{d_o} (again with Mach number dependence) and $c_{m_{c/4}}$ is assumed zero. With these simplifications the analysis is aerodynamically compatible with other similar existing analyses (References 17 through 19, for example) and provides a basis for evaluating the effects of stall. It is thus not unexpected that the results of the present analysis should predict, as do References 17 and 18, flap-lag instabilities and/or general reductions in damping at large values of collective pitch angle for both subcritical and supercritical rotor configurations. The major

instabilities are seen to involve motions predominately comprised of first flatwise bending and first edgewise bending. Comparison of these two figures shows that for the subcritical configuration, it is the first edgewise (1E) eigenvalue "branch" which goes unstable whereas for the supercritical configuration, it is the first flatwise (1F) branch. A further comparison shows that, for the subcritical configuration, as the instability is approached all flat and edge modes lose damping and the branch which goes unstable is already lightly damped. In contrast, for the supercritical configuration, the (stable) first edgewise branch increases in damping, but the initially heavily damped first flatwise branch precipitously loses substantial damping to go unstable. The present findings are qualitatively consistent with the findings of Reference 17 which, for subcritical configurations, predict the lead-lag (i.e., first edgewise) eigenvalue branch to be the one to go unstable. Direct quantitative comparison of the present results with those of the above cited works is difficult at best. Significant structural details (highly nonlinear twist, several intercoupling modes, generally nonuniform section properties, etc.) of the realistic blade configuration considered herein are either not treated with sufficient rigor or are neglected entirely in these references.

A more realistic set of nonvacuum eigensolution results is presented in Figures 109 and 110 again for the subcritical and supercritical configurations, respectively. For these results the complete (nonlinear) conventional NACA 0012 airfoil data, including both stall and compressibility effects, were utilized. The perturbational airloads were obtained utilizing perturbations of the three sectional aerodynamic coefficients with respect to both angle-of-attack and Mach number, as is outlined in a section of Reference 1. Comparisons of Figure 107 with 109, and 108 with 110 show that the basic aeroelastic behavior identified by the eigensolutions with linear airloads is carried over and is but modified with the inclusion of perturbational airloads with stall. Generally, the effect of stalled airloads is to aggravate the stability bounds so identified; the same general trends with collective angle are qualitatively duplicated, but occur at lower collective angles. Again, these results are in good qualitative agreement with previous findings (Reference 20), i.e., that for either subcritical or supercritical configurations the flap or lag eigenvalue branch with the higher frequency is the one to go unstable.

The following observations can be made of the above discussed nonvacuum eigensolutions:

1. In light of (1) the consistency of the present findings with those obtained by other investigators for considerably simpler but basically hingeless rotor systems, and (2) the fact that the eigensolution results generated herein by the analysis (Reference 1) do

not consider the higher order effects of the redundant analysis (which are inherent to the composite bearingless rotor, CBR, concept), it is most likely that the present findings are typical of all hingeless rotors and not limited to the CBR concept.

2. The built-in twist distribution for this rotor together with the assumed variable inflow, tends to produce a relatively uniform angle of attack distribution, and since for a NACA 0012 airfoil the static stall angle tends to decrease with Mach number, the spanwise extent of stall should tend to propagate inward from the blade tip. Since Figures 109 and 110 show the instabilities occurring at collective angles above that wherein the 75 percent span station stalls, these instabilities represent conditions of deep stall which are not easily reached operationally.

3. These results retain qualitative usefulness in the context of providing limited understanding of the aeroelastic behavior of rotor blades in forward flight. Momentarily high pitch angles and conditions near to and above stall can and do occur on the retreating portions of the disk in forward flight.

Summary of Eigensolution Results - The principal findings gleaned from the above described eigensolution analyses are:

1. The subcritical blade as originally configured is free of any n/rev resonance problems.

2. The supercritical blade, when configured with a softened torque tube (25 percent nominal bending stiffnesses), is free of any n/rev resonance problems.

3. The effects of torque tube bending stiffness and blade pitch angle are to produce highly complex coupled mode shapes with nonuniform phasing.

4. The existence of hingeless rotor flap-lag instability at high pitch angle and in deeply stalled hovering conditions, as reported in the literature, was confirmed. This hovering instability, in itself, is neither a result of the innovative features of the CBR nor poses any problem for the rotor within any realistic operational envelope.

Trimmed Forward Flight Cases

The remainder of the aeroelastic analysis is confined to investigations of various of the rotor characteristics in forward flight. For these investigations the eigensolution analysis is inadequate and the time-history solution capability of the aeroelastic analysis program must be used. For such investigations, especially with the attendant required parameter variations, the rotor must first be simulated in (stable) trim configurations to have practicality. This subsection describes the results of the use of the time-history solution to obtain these trim configurations. In particular, the selection of the particular trim conditions is first discussed. Then the resulting blade bending moments, stresses and torsion moments experienced by the two basic blade configurations in trimmed straight and level forward flight are discussed in turn.

Selection of Trimmed Flight Conditions - For present purposes a high speed condition ($\mu = 0.44$) with moderate blade loading ($C_L/\sigma = 0.057$) was selected. More specifically, the rotor was trimmed to a lift and propulsive force of 59610 N (13,400 lb) and 7430 N (1670 lb), respectively, with hub moments less than 5420 Nm (4000 lb-ft) in magnitude; a high forward flight speed of 86.9 m/sec (169 kts) at standard sea level conditions was selected. Uniform inflow was assumed and the aeroelastic analysis was used in the automatic trim mode to adjust the three control angles and the inflow ratio iteratively to achieve the above defined flight condition. Three basic trim conditions were calculated: one each for the subcritical and supercritical configurations discussed in an above subsection (case Nos. 1 and 2, respectively) and an additional case (No. 3) for the subcritical configuration. For this latter subcritical configuration, the push-rod attachment point was repositioned further outboard to investigate the effects of increased pitch-flat coupling. These three basic flight conditions are summarized in Table X.

Blade Moment and Stress Distributions - Figures 111 through 113 present the calculated distributions of blade one-half peak-to-peak (½ PTP) and median bending and torsion moments over the (total) blade span for each of the two basic blade configurations. In these figures the moment values presented for the structurally redundant, flexbeam-torque tube spanwise stations (those inboard of the juncture station, $\bar{r} \leq 0.29$) are those appropriate only to the respective primary elastic structures. Thus, in Figures 111 and 112 the bending moments presented for stations inboard of the juncture are those experienced by the flexbeam; conversely, in Figure 113 the torsion moments presented for these inboard stations are those experienced by the torque tube. Explicit calculations of the complementary bending and torsion moment distributions (in the torque tube and flexbeam, respectively) were not available. However, their presence and the relative significance of structural redundancy is indicated by the jump magnitudes in the various moment distributions at the juncture station. The effect of structural redundancy for these configurations

is thus seen to be small for flatwise bending, but moderate for edgewise bending and for torsion. Not unexpectedly, the maximum blade bending moments are seen to occur at the blade root. The negative median flatwise bending moments near the blade tip shown in Figure 111 are due mostly to the inclusion of an 11.3 kilogram tip weight and a greater than optimal built-in preconing angle.

Significant differences are shown in the respective bending and torsion moments for the subcritical and supercritical configurations. Figures 111 and 112 show the supercritical configuration to exhibit both flatwise and edgewise bending moments which are generally lower than those for the subcritical configurations. Of particular significance are the marked reductions in edgewise bending moments for the supercritical configuration, both with $\frac{1}{2}$PTP values over the entire span and with median values over the outer portions of the blade. These bending moment reductions are well recognized to be inherent in supercritical blade designs and result from the favorable "vibration absorber" and equivalent hinge characteristics of this type of design. Figure 113 compares the torsion moment distributions obtained for the two designs. It shows that the torsional moment carried by the flexbeam for the supercritical configuration is less than that for the subcritical as indicated by the reduced jump values at the juncture. This result is consistent with the reduction in nonlinear ΔEI torsion coupling obtained when approaching a matched stiffness design. Figure 113 also shows a generally outward shift of the spanwise peak of the torsion moment (disregarding the jumps at the juncture) with the supercritical design; the torsion moment distribution for this design is thus more uniform over the span.

The flatwise and edgewise stress distributions over the flexbeam span for the two blade configurations are shown in Figures 114 and 115. The curves shown in these figures are obtained from the bending moment distributions of Figures 111 and 112 divided by appropriate I/c values. The most remarkable result shown in these figures is that in contrast to the moment distributions the stress distributions for the two blade configurations are quite similar. Indeed, the vibratory ($\frac{1}{2}$PTP) edgewise stresses for the supercritical design are even somewhat larger than those for the subcritical, while the median edgewise stresses for the supercritical are significantly larger than the median stresses for the subcritical. From the results of the above Composite Materials Investigation and Full Scale Design sections, maximum allowable bending and torsion stresses of 379 MN/m^2 (55,000 psi) and 24 MN/m^2 (3500 psi), respectively, were established. Figures 114 and 115 thus show that the blade designs are satisfactory from a root bending stress standpoint.

Azimuthal Time Histories of Critical Stresses and Loads - From Figures 114 and 115 it can be seen that the critical bending stress point is near the blade root and is herein taken to be the center of the first blade segment: r = 0.054. Figure 116 compares the azimuthal variations of the flatwise and edgewise

stresses at the blade root for both the subcritical and supercritical configurations. It can be noted that the flatwise stresses for the two configurations are quite similar and, commensurate with zero trimmed hub moments, show predominately 2P and 3P content. Comparison of the edgewise stresses for the two configurations shows predominantly 1P content for each configuration but with opposite phasing. Since the edgewise bending dynamic system is lightly damped, a change of phase angle of nearly 180° is to be expected for responses whose natural frequencies are either greater than or less than predominant 1P forcing frequency.

An additional stress item of interest is the critical flexbeam torsion (shear) stress; this stress is typically located at the blade station where the twist rate is maximum which occurs where the sectional dimensions are minimum. Since the flexbeam is tapered over its entire length, this station is herein taken to be the outer boundary of the outermost segment of the flexbeam: $\bar{r} = 0.288$. Although explicit torsional stress distributions over the flexbeam span were not available from the analysis, the torsion moment in the flexbeam immediately inboard of the juncture was available as part of the calculation of the redundant analysis. This torsion moment was converted to a maximum torsion stress within the section using the sectional dimensions and standard stress analysis formulae (Reference 21). Figure 117 compares the flexbeam torsion stresses at the juncture for the two blade configurations. These stresses are seen to be almost entirely 1P and reflect the predominantly B_{1_s} cyclic control input. The relative lack of bias in these flexbeam torsion stresses is due to the assumed flexbeam pretwist of 13.5 deg (corresponding to a built-in collective angle of 11.66 deg). The half peak-to-peak values of flexbeam torsion stress for the subcritical and supercritical are 22.8 MN/m^2 and 22.6 MN/m^2, respectively. Although below the allowable torsion stress of 24 MN/m^2, these values do not leave the margin initially predicted in the Full Scale Design section. The reason for this discrepancy is that the preliminary design stress calculation was based on the assumption of a constant section flexbeam. The actual design, however, does have substantial taper giving rise to a significant increase in torsion stress at the outboard end: In this case that increase is approximately 23 percent.

In addition to the critical stresses described above, an important dynamic response variable is the push-rod load. Besides reacting those loads required to twist the flexbeam cyclically, the push-rod must equilibrate the blade in torsion and, hence, react the inertial and aerodynamic pitching moment distributions on the blade. The azimuthal variations in push-rod load, shown in Figure 118 for the two blade configurations, reflect these load characteristics. Comparison of Figure 118 with Figure 117 shows the steady and 1P content of the push-rod load to be closely phased with the steady and 1P torsion moment required to twist the flexbeam to achieve the trimmed control angles. Note that, due to the trailing edge push-rod attachment location selected for these

designs, a positive (up) push-rod load produces a negative (leading edge down) flexbeam torsion stress. In addition, however, significant higher harmonic content is evident in these push-rod load time-histories which result from the outer blade inertial and aerodynamic moment loadings. Of particular interest is the intermittent (approximately) 1OP excitation of the torsion mode in the retreating blade quadrants.

Effects of Simplified Modeling of the Structural Redundancy - As was stated above, the nominal calculation of the various time-history solutions comprising the forward flight portions of the aeroelastic analysis assumes the complete modeling of the structural redundancy (see Reference 1). Briefly the structural redundancy arises from the presence of dual load paths, over the flexbeam-torque tube span, for both bending and torsion loads. The redundant analysis formulated for the solution of this structural problem involves a full interaction of all bending and torsion loads at the juncture point as well as a statement of consistent torsion deformation at that point. An alternate simplified formulation of the structural dynamics of this portion of the rotor blade is afforded by making the following approximations:

1. The torque tube consists of an infinitely rigid massless link, hinge connected to the span at the juncture by equivalent rotary springs in the flatwise and edgewise senses.

2. The flexbeam is torsionally equivalent to a simple linear rotary spring.

3. The nonlinear torsion excitation (due to ΔEI bending-deflection effects) over the flexbeam span is approximated by weighting the usual nonlinear elastic torsion load distribution by the pseudo-torsion mode shape (see Reference 1). Since the pseudo-torsion mode is a monotonically increasing function less than unity over the flexbeam span, this weighting results in an attenuation of this term.

It is to be noted that the incorporation of this alternate simplified formulation reduces the analysis in large measure to that for a "conventional" hingeless rotor. Remaining differences are the time variation in structural twist and the attenuation of the nonlinear torsion excitation for the composite bearingless rotor.

Using these nonredundant analysis simplifications together with the control angles defined in Table X for trim cases 1 and 2, two additional time-history cases were generated. These cases are herein denoted 1A and 2A for the subcritical and supercritical configurations, respectively. It was found that substantially the same performance was achieved for cases 1A and 2A as

for cases 1 and 2; the nonredundant analysis cases were equally found to satisfy the trim criteria enunciated above. The azimuthal variations of the critical stresses for the nonredundant analysis are compared with those calculated using the complete redundant analysis in Figure 119a. This figure shows negligible differences in the flatwise and edgewise bending stresses and in the flexbeam torsion stresses for the two calculation methods. Substantial differences are noted, however, in the azimuthal variations of the push-rod load shown in Figure 119b. It is significant to note that the respective azimuthal variations, with and without the full redundant analysis, show similar higher harmonic signatures and differ mainly in their lower harmonic contents.

Aerodynamic Stability Derivatives

Two basic requirements exist for obtaining partial derivatives of the hub loads with respect to the control angles and components of hub velocity: First, such derivatives are needed for determining the static stability characteristics of the entire aircraft, as well as the control power characteristics of the rotor. Second, the derivatives can be used to generate trim derivative matrices for obtaining the required control angles and inflow for perturbations in the flight conditions. The following subsections discuss the aerodynamic stability derivative matrices defined by these requirements; results are obtained for the three basic trim cases discussed in the previous section and summarized in Table X.

Basic Static Stability Derivative Matrices - For each of the three basic trim cases a matrix of partial derivatives is obtained; the partial derivatives are numerically obtained by perturbing (both positive and negative perturbations) the control parameter inputs of each trim case using the time-history solution of the analysis. The partial derivatives of each of the six (6) hub loads (3 forces and 3 moments) with respect to the three (3) control angles, A_{1_s}, B_{1_s}, and $\theta_{.75R}$, inflow ratio and advance ratio form a 6 x 5 matrix of fundamental derivatives. These derivatives are then modified to reflect the substitution of shaft angle and (nondimensional) forward flight speed as the fourth and fifth independent control parameters. The results of performing the numerical differentiation and modification are presented in Table XI where the various static stability derivative matrices are defined as:

$$[S] = \left[\frac{\partial Z_i}{\partial P_j}\right], \text{ where:}$$

$$Z_i = \left(\frac{C_L}{\sigma}, \frac{C_{PF}}{\sigma}, \frac{C_{PM}}{\sigma}, \frac{C_{RM}}{\sigma}, \frac{C_Q}{\sigma}, \frac{C_Y}{\sigma}\right)$$

$$P_j = (A_{1_s}, B_{1_s}, \theta_{.75R}, \alpha_s, \bar{V}) \quad \text{(angles in degrees)}$$

Comparison of the static stability derivative matrices of trim cases 1 and 3 shows that the net effect of increasing the push-rod attachment point radius (to achieve increased pitch-flat coupling for the first flatwise mode) was actually to reduce the control power of the rotor. This can be seen by comparing elements S_{12}, S_{13}, S_{32}, S_{33} and S_{41} for these two cases. This control power reduction is contrary to what one would typically expect considering only the increased (positive) pitch-flat coupling of the first flatwise mode. This behavior can be explained by noting in Table X for case 3, the significantly increased (negative) pitch-flat coupling of the second flatwise mode associated with the outwardly repositioned push-rod attachment point. Since for trim conditions 1 and 3 the first harmonic responses of the first and second flatwise modal responses were, in fact, calculated to be in phase, the pitch-flat coupling of the second flatwise mode is thus seen to be preempting that of the first mode.

Trim Derivative Matrices - For purposes of calculating additional trim cases a portion of the above defined fundamental derivative matrices for the three trim cases were inverted to form the trim derivative matrices presented in Table XII. These trim derivative matrices are defined as:

$$[T] = \left[\frac{\delta Q_i}{\delta X_j}\right], \text{ where}$$

$$Q_i = (A_{1_s},\ B_{1_s},\ \theta_{.75R},\ \lambda) \qquad \text{(angles in degrees)}$$

$$X_j = \left(\frac{C_L}{\sigma},\ \frac{C_{PF}}{\sigma},\ \frac{C_{PM}}{\sigma},\ \frac{C_{RM}}{\sigma}\right)$$

Transient Responses Due to Control Inputs

Trim cases 1 and 2, whose parameters are given in Table X and whose stress characteristics are discussed in an above subsection, form the bases for investigating the transient blade responses due to control angle inputs. The effects of the control angle inputs were studied by combining the respective trim control angles with separate time variable increments in each of the three control angles, $\theta_{.75}$, A_{1_s} and B_{1_s}. Those initial conditions on the response variables, appropriate to the unperturbed trim cases, were selected so that the deviations of the transient (stress) responses from the trimmed responses would provide direct measures of the effects of the incremental control inputs. For each control angle two increments were made of the types shown in Fig. 120. Both the ramp-step and pulse incremental inputs shown in this figure have a maximum amplitude of 0.5 deg with finite rise times to that amplitude. The responses due to the ramp-step input would be expected to be more severe as they represent off-trim conditions and would not generally converge to the original azimuthal stress response signatures.

The transient stress and control load responses due to these incremental control angles are presented in Figures 121 thru 126 . For each of these figures, duplicate reference (trim) response time-histories are given for two periods (rotor revolutions comprising 360 deg of azimuth). The initial transient stress responses are given for these two revolutions and then the continuing responses at subsequent revolutions are overlayed on these two revolutions, as indicated. Within any one plot the transient responses are plotted only up to and including the maximum (and minimum) amplitudes. For those transients wherein several revolutions are required for convergence, only selected portions of the time-histories which include local maxima are included. Within each of the following subsections describing the effects of each of the incremental control inputs, results are presented, in turn, for the subcritical and supercritical configurations (trim cases 1 and 2, respectively).

Incremental Collective Angle, $\Delta\theta_{.75R}$ - The results of the incremental ramp-step and pulse collective angle inputs are shown in Figures 121a through 122b. Observations to be made of these results are as follows:

1. The responses all tend to show higher harmonic content than their respective trim responses during the initial transient revolutions. Thus, the incremental half peak-to-peak responses will not, in general, be linearly dependent functions of incremental input amplitude.

2. With regard to the flatwise and edgewise bending stresses for both rotor configurations (Figures 121a and 122a), the converged maximum and minimum peaks are not attained until some elasped time (3 or 4 rotor revolutions) after the incremental collective input has been completed. The convergence tends to occur somewhat sooner with the subcritical configuration, however.

3. Comparison of the flatwise bending responses for the two rotor configurations shows the transient maximum and minimum peaks for the subcritical configuration to be significantly more negative than those for the supercritical configuration although the peak-to-peak amplitudes are comparable.

4. Comparison of the edgewise bending responses shows the supercritical rotor to be significantly more sensitive in edgewise bending to the incremental collective control angle input than is the subcritical.

5. As shown in Figures 121b and 122b, both rotor configurations show negligible incremental flexbeam torsion stresses due to incremental collective angles other than that due to the additional 0.5 deg of flexbeam twisting.

6. Comparison of the transient push-rod loads for the two rotor configurations shows the subcritical rotor to be significantly more sensitive in torque tube torsion (of which push-rod load is a measure) to the incremental collective control angle than is the supercritical. In particular, the increased sensitivity is confined to the retreating blade quadrants wherein the local incipient (9P - 10P) torsion excitation, already present in the trimmed responses, is substantially amplified. While a complete investigation of this phenomenon is beyond the scope of this study, it appears, from an examination of the available moment load distributions, that this increased higher harmonic excitation arises from the ΔEI nonlinear bending-deflection torsion excitation. As would be expected, the supercritical configuration which is more nearly "stiffness-matched" is less prone to this type of excitation and it concurrently shows less sensitivity.

Incremental Longitudinal Cyclic Angle, ΔA_{1_S} - The similar results of incremental ramp-step and pulse longitudinal cyclic angle inputs are shown in Figures 123a through 124b. As with the transient responses described above, those due to incremental A_{1_S} cyclic angle also show higher harmonic content during the initial transient revolutions, than do their respective trim responses. Contrary to the incremental collective angle responses, those due to incremental A_{1_S} cyclic angle are relatively benign and show little variation from the trimmed values. Two main reasons exist for this subdued behavior. First, incremental longitudinal cyclic for rotors with low flatwise stiffness (first flatwise modal frequency < 1.1P) will produce mainly incremental first sine harmonic flapping. This flapping does not increase the effective ram inflow as does first cosine harmonic flapping which would result from both collective and B_{1_S} cyclic angle increments. Secondly, because the A_{1_S} (and B_{1_S}) control angles are impressed cyclically, the average incremental blade pitch angle around the azimuth due to incremental A_{1_S} would inherently be no more than half that due to incremental collective. Consistent with previous results the effect of incremental A_{1_S} control angle on transient push-rod loads are greater for the subcritical than for the supercritical.

Incremental Lateral Cyclic Angle, ΔB_{1_S} - Figures 125a through 126b present the results of incremental ramp-step and pulse lateral cyclic angle inputs. Comparison of Figures 125a and 126a shows that the transient flatwise stresses due to the B_{1_S} inputs for the two rotor configurations are quite similar and are generally well converged within three rotor revolutions. Comparison of the transient edgewise stresses shows again that the higher harmonic content is increased with the application of the incremental control input; this characteristic is seen to be more prevalent with the subcritical rotor configuration. Comparison of Figures 125b and 126b shows that the flexbeam torsion stresses are little affected by the incremental B_{1_S} cyclic angle. Consistent with previous results, the transient push-rod loads for the subcritical rotor configuration are seen to be significantly more affected by the

incremental control angle than is the supercritical configuration. It is to be noted that, for the subcritical configuration, the increased higher harmonic edgewise stress responses occur over the same portion of the azimuth (retreating blade quadrants) as do the push-rod load responses.

Transient Characteristics Due to Partial Material Failure

As is discussed in the above Composite Material Investigation section, composite materials typically fail by developing noncatastrophic cracks which reduce their elastic moduli. Thus, flexbeam failure becomes more of a structural dynamics problem. That is, assuming a material failure (which will generally be of the form of partial reductions in stiffness), can the structure withstand the dynamic loads without destructive stress magnifications and/or aeroelastic instabilities? An assessment of the material failure problem was made by investigating the stress responses of the two blade configurations due to instantaneous reductions in the flexbeam bending stiffnesses.

More specifically, the two blade configurations were first analyzed for their frequencies and mode shapes with separate 15 percent reductions in flatwise and edgewise bending stiffnesses. The results of these reductions on the blade uncoupled natural frequencies are shown in Table XIII. Using these uncoupled natural frequencies and their associated mode shapes, together with the control angles and modal initial conditions for trim cases 1 and 2, transient time-history solutions were obtained in a manner similar to the transients due to control inputs. In this case, however, the sources of input disturbance were the modal initial conditions. For lack of a more comprehensive stress analysis of failed composite materials the "failed" stresses were computed using the force-integrated bending moments together with the "unfailed" I/c values.

Figures 127 and 128 present the transient flatwise and edgewise bending stresses for the subcritical and supercritical configurations, respectively. In each figure are shown the reference (trim) stress time-histories, previously discussed, together with the transient stresses accruing from instantaneous partial reductions in flexbeam flatwise or edgewise bending stiffness. As these figures show, the effects of these instantaneous stiffness reductions are practically negligible. Indeed, the flexbeam torsion stress and push-rod load time-histories were not included since the off nominal results could not be distinguishably plotted together with the reference time-histories. That so little incremental dynamic stress is generated by the instantaneous partial failures is consistent with the results of Table XIII. Therein it is seen that the stiffness reduction caused only small excursions in modal natural frequencies which were still reasonably well separated from integral harmonics. The small deviations of the stresses from the reference (nominal stiffness) responses can generally be explained on the basis of the changes in resultant dynamic magnification factors caused by frequency change. Most notable are the changes in edgewise stress for the two configurations upon reduction of the flexbeam edgewise stiffness. Since the edgewise stiffness reductions brought the first edgewise natural frequencies closer to and further from 1P,

respectively, for the subcritical and supercritical configurations, it is reasonable that the 1P edgewise stresses should increase and decrease, respectively, for these two configurations.

Effects of Unsteady Airloads

An important aspect of the aeroelastic analysis of any helicopter rotor blade is the effect that unsteady airloads have on the structural responses. The formulation of unsteady airloads used in the present aeroelastic analysis is the variant of the (α, A, B) method described in Reference 22. Briefly, this formulation states that the unsteady aerodynamic section coefficients are, for any fixed Mach number, generally nonlinear functions not only of angle-of-attack, α, but of nondimensional angle-of-attack rate, $A(= c\dot{\alpha}/2U)$, and angle-of-attack acceleration, $B(= c^2\ddot{\alpha}/4U^2)$. While it has been noted in Reference 23 that a proper simulation of stall-flutter requires the inclusion of variable inflow, it was decided that the effect of unsteady airloads should be determined using only constant inflow for a more meaningful comparison with the herein nominal quasi-static results.

The application of unsteady airloads in the aeroelastic analysis was confined to an examination of its effects, with variations in blade loading, on the response characteristics of the subcritical configuration. The variations in blade loading were achieved by straight-forward variations in the (constant) inflow, λ, or equivalently, the rotor shaft angle-of-attack, α_s. A meaningful comparison of the results obtained with and without unsteady airfoil is complicated by the fact that the various pertinent structural response quantities ($\frac{1}{2}$PTP stresses, etc.) are strongly dependent upon the state of rotor trim. The approach selected for constructing a meaningful comparison was, therefore, to make inflow variations on cases which were initially trimmed to the same hub loads. Accordingly, an additional trim case was calculated wherein the analysis included the unsteady airloads formulation; the control parameters found to trim the analysis with this inclusion are as follows: ($A_{1s} = -1.22$ deg, $B_{1s} = 9.39$ deg, $\theta_{.75R} = 12.09$ deg, $\lambda = -.0733$).

In Figure 129 are presented the results of the variations of rotor performance with shaft angle, α_s, using the aeroelastic analysis with and without the unsteady airloads formulation. In this figure are shown the two trim points about which the inflow variations were made. Note that, for comparison, an isolated point on each curve is presented wherein the control parameters appropriate to the norminal quasi-static airloads (case 1) were used in the analysis with the inclusion of the unsteady airloads. A comparison of the C_T/σ curves with and without the unsteady airloads shows that, at the higher blade loading conditions, the performance calculated with unsteady airloads is rising at a greater rate and would appear to be "stalling out" at a higher

overall level. The rotor drag levels with unsteady airloads are, furthermore, seen to be less than those with the quasi-static formulation. These results reflect the generally acknowledged effect of unsteady airloads on rotors: that dynamically stalled airloads create stall delays and hence lift overshoots. These stall delays cause the airfoil sections to generally operate more efficiently than quasi-static theory would indicate in creating more average lift per (effective) rotor angle-of-attack. Further observations from Figure 129 are that the two trim points occur at different shaft angles and that the quasi-static trim point lies on a portion of the C_L/σ - α_s curve which has discernable curvature. From these observations it would appear that, as calculated, basic trim case No. 1 is a partially stalled rotor operation condition. It should be noted that the higher power absorbed by the rotor with unsteady airloads is commensurate with its ability to pull more lift.

Comparisons of the concurrent vibrational stresses and push-rod loads for the analysis with and without the unsteady airloads are shown in Figure 130. Of particular interest is the substantially higher vibratory flatwise stresses for the quasi-static formulation at the higher blade loadings. Although much of this difference is attributable to the quasi-static results being further out of moment trim than those for the unsteady airloads, it was nevertheless found that all harmonics of this stress through the tenth were substantially greater for the quasi-static than for the unsteady airloads formulation results. The comparison of $\frac{1}{2}$PTP push rod loads in this figure shows a similar result for the two formulations. Here too, the results using the quasi-static formulation have substantially higher harmonic content through the tenth harmonic than do those using the unsteady airloads formulation.

It is significant to note that these vibratory stress and push-rod load results are contrary to what one would expect based on established stall flutter theory. Stall-flutter is generally attributed to the energy extraction mechanism provided by the hysteretic moment coefficient characteristic inherent in the unsteady airloads formulation. As such, stall flutter is generally a single degree-of-freedom torsional response phenomenon. The present findings indicate, however, that the onset of the excessive torsion responses and amplified flatwise bending responses found using quasi-static airloads is delayed with the incorporation of unsteady airloads. As was shown in an above subsection describing the effects of structural redundancy, at high frequencies, the CBR tends to behave much like a "conventional" hingeless rotor. It would thus appear that the excessive torsion and flatwise bending responses found at the high blade loadings, and previously found to a limited degree for incremental blade collective angle, constitute a potentially new phenomenon associated with the analysis of hingeless rotors using quasi-static airloads. As was shown in Reference 23, a satisfactory calculation of stall flutter generally requires the inclusion of variable inflow which was lacking

in the present calculations. Thus, that stall-flutter per se was not encountered using the unsteady airloads is not prima facie evidence that stall-flutter would not occur on the composite bearingless rotor at these elevated blade loadings. An adequate exploration of this phenomenon is, however, beyond the scope of this study.

Forward Flight Stability Analysis

The aeroelastic stability of rotor blades operating in forward flight conditions is, as best, difficult to analyze for the basic reason that the governing differential equations of motion are significantly more complicated than those for which the usual mathematical tools for stability analysis were developed. In contrast to the familiar linear, homogeneous equations of motion with constant coefficients, those for the rotor blade in forward flight are highly nonlinear, contain periodic coefficients in various dominant linear, as well as nonlinear, terms and are substantially excited in all lower harmonics. Consequently, for any time-history response of finite duration the transient responses often defy categorization as to exponential growth and/or transient convergence to periodicity.

Mathematically, the stability of such nonlinear systems can be defined in terms of the linear stability of small perturbations away from some nominal periodic solution. This solution is but a converged time-history of the original harmonically excited nonlinear equations. The differential equations for the perturbations, however, are generally linear with periodic coefficients, and as such, constitute a problem in Floquet analysis for which several solution methods are available. However, two major difficulties in applying this general technique to the differential equations of the rotor blade are as follows:

1. A converged time-history solution of the original nonlinear equations may not be available. Indeed, for cases of most interest, wherein the degree of stability is marginal, the (numerical) time-history solutions will not generally converge to periodicity within a practical period of time.

2. The linear perturbational equations, to which Floquet theory must be applied, are not generally available in explicit form owing to the complexity of the original differential equations and to the aforemention lack of converged solution.

Because of these two difficulties the stability of the rotor was analyzed herein using a combination of three basic ideas and/or mathematical tools: First, and most elementary, is to observe the time histories for responses

which clearly increase monotonically in amplitude until unreasonably large amplitudes are reached. Time-histories of such responses could clearly be defined as unstable in the global sense, but quantification of the level of instability often becomes meaningless or undefinable. The second mathematical tool is to use the "frozen azimuth" eigensolution available in the aeroelastic analysis program to ascertain general coupled frequencies and trends in damping due to parameter variation. This second tool is used primarily as a guide for interpreting the results of the third mathematical tool available. This last and potentially most powerful mathematical tool for analyzing the rotor stability is the transient spectral stability analysis (TSSA) described in detail in Reference 24 and briefly in Reference 1. The results obtained from the TSSA are the values of the predominant frequencies inherent in the given time-histories as well as the equivalent characteristic exponents associated with each of these identified predominant frequencies. These equivalent characteristic exponents are interpreted in the same way as are the real parts of the familiar eigenvalues defined for linear systems with constant coefficients.

Two separate bodies of stability analysis results were calculated and are presented in this section. The first is an exploratory study of possible blade instabilities of one of the test models whose characteristics are described in previous sections. The second is an investigation of the transient stability characteristics of the full-scale design to complete the aeroelastic analysis section of this study. The model results are included in this subsection rather than in the model correlations section because they are entirely of an analytic nature with a lack of quantitative data with which to correlate. These results furthermore serve as an introduction to and complement the similar results obtained for the full-scale design.

Exploratory Study of Model Rotor with Cantilevered Torque Tube - Of the two basic model rotor configurations tested, that with the cantilevered torque tube was selected as the one most likely to show adverse stability characteristics. This selection was made based on this configuration's inherently softer torsion system arising from flexbeam bending effects (wobble mode), and on its pronounced pitch-flat coupling effects. Furthermore, it was found experimentally that the cantilevered torque tube configuration manifested more unusual aeroelastic response characteristics than did the pinned-pinned torque tube configuration, and would thus be more susceptible to potential instabilities. The remainder of this subsection describes stability results obtained for the cantilevered torque tube configuration. The pinned-pinned configuration was considered to be stable and, consequently wasn't analyzed.

In accordance with the above described approach for stability analysis, the aeroelastic analysis program was run in all three calculation modes: eigensolution, time-history solution, and transient spectral stability analysis. Parametric variations were made on advance ratio and rotor speed for

two push-rod attachment positions giving relatively large (+) and (-) values of first mode pitch-flat coupling, respectively. Advance ratio, μ, was varied up to a value of 0.47 at the nominal fixed value of rotor speed, ΩR, of 99.1 m/sec. Rotor speed was varied up to the nominal value holding advance ratio fixed at 0.47; forward flight speed was thus varied in proportion to rotor speed to maintain fixed advance ratio. Leading and trailing edge push-rod attachment points were used which gave respective first mode pitch-flat couplings of 0.883 and -0.654, respectively.

The eigensolution was calculated at zero azimuth to more nearly obtain azimuthally average eigensolutions. All time-histories were calculated with zero control angles, an inflow ratio of -0.005, and (nominal) initial conditions of .02 on the first flatwise and edgewise bending mode deflections only with all other modal initial conditions zero. The time-histories were calculated for time periods sufficiently long to obtain data string channels of 512 points for use in the transient spectral stability analysis. The time-history quantities selected for these data string channels were out-of-plane and in-plane deflections (z_5 and y_5, respectively) and torsional deflection (θ_e), all as calculated at the blade tip.

The eigenvalue results for selected nominal tip speed cases are shown in Table XIV. Presented are the real and imaginary parts of the eigenvalues together with indications of the predominant modal components comprising the coupled mode shapes. Note that the 2T modal component in these results denotes the rigid body torsion mode resulting from flexbeam bending effects and is herein referred to as the "wobble mode". Of most significance in these results is the sensitivity of the eigenvalues to the initial conditions and to advance ratio. These results are useful primarily in identifying modal response frequencies, ω, and in revealing destabilizing trends. Most noteworthy of these results is the ability of blade deflections to destabilize one of the coupled second flatwise bending modes and the ability of advance ratio to coalesce the first flatwise and edgewise bending modes. Since these eigensolutions are "frozen azimuth" results they are not generally indicative of the effective stability over the whole rotor azimuth. For this, the time-history solution together with the transient spectral stability analysis must be employed.

The effects of advance ratio variation on modal frequency and blade stability are shown in Figures 131 and 132 for the trailing and leading edge push-rod configurations, respectively. Based on the eigensolution results the frequency range of interest was deemed to be from 0.8P to 3.5P; resonant frequency identification and equivalent characteristic exponent calculation were therefore restricted to this frequency range. For both configurations the results indicate little variation in modal frequency and generally stable characteristics, as indicated by the uniformly negative values of equivalent characteristic exponent, σ. In the reduction and interpretation of the

transient spectral stability results various of the identified frequencies were omitted from the presented results. Those frequencies which were either: integral harmonics with negligible damping (responses due to harmonic excitation) or of nonintegral harmonic frequencies but with the same noninteger part and same characteristic exponent as other identified frequencies (image or nonfundamental resonances), were so omitted in the interests of clarity.

Detailed comparison of Figures 131 and 132 shows first that although both configurations are stable, the leading-edge attachment configuration (with positive pitch-flat coupling) has significantly less margin than does the trailing edge configuration. Also shown are the generally lower modal frequencies identified for the leading-edge attachment configuration. This result is consistent with known effects of positive pitch-flat coupling. Finally, it should be noted that although a single frequency of approximately 1.36P was identified for each of the three channels, consistently different damping levels are indicated for the flapping (z_5) channels as shown with dashed lines in the figures. It can furthermore be noted that these 1.36P characteristic exponents (for the flapping channel) are more and less stable, respectively, for the trailing and leading edge push rod attachment configurations, than their corresponding inplane and torsion 1.36P characteristic exponents.

The effects of rotor speed variation on the stability characteristics of the trailing edge push-rod configuration are shown in Figures 133 and 134. Figure 133 shows the variations in the "frozen azimuth" eigensolutions with rotor speed variation. Of most significance in this figure is the coalescense of the wobble mode (2T) with the second flatwise mode (2F) at 3.2P for the nominal rotor speed of 99.1 m/sec and the associated indicated instability. As demonstrated in Table XIV this unstable eigenvalue is deflection dependent and is not applicable to conditions around the entire rotor azimuth. Figure 134, on the other hand, presents the transient spectral stability results, but in the same format as Figure 133 for direct comparison. It is to be noted that several features of the frequency variations are well duplicated including the frequency coalescence near 3P, and the first flatwise and edgewise mode frequencies. Comparison of the damping levels shows remarkable similarities despite the effects of the nonlinearities and periodic coefficients. Significantly, the destabilizing trend of the low frequency inplane (edgewise) mode is well duplicated in the two figures. In Figure 134, the dashed line denoting damping results for the low frequency flapping mode indicates a quantitatively undetermined connection, established qualitatively on the basis of the frequency results. The lack of damping determinancy at 85.34 m/sec for this mode resulted from the erratic nonmonotonic behavior of the amplitude of this frequency content within the flapping channel time-history. These figures also show remarkable similarity in predicting a general loss of damping with the coalesence of the flatwise and torsion modes. It should be noted that

well damped modes leave little vibratory content to be identified by the transient spectral stability analysis. Hence the well-damped modes found by the eigensolution will generally be missing from the TSSA results.

The effects of rotor speed variation on the frequency and stability characteristics of the leading edge push-rod configuration are presented in Figure 135. The eigenvalue results for this case were found not to differ significantly from those for the trailing edge configuration shown in Figure 133 and hence, were omitted herein. Drawing upon those results, however, the identified frequency plot was constructed. The dashed curve was constructed by subtracting a nondimensional frequency value of 2 from the second curve (ω_2) recognizing that the ω_2 curve could possibly be an image resonance, and that the so constructed ω_2-2 curve connects with the identified frequency at the nominal rotor speed to create a smooth curve exactly where one should exist. Examination of the characteristic exponent curves and comparison with Figure 134 shows a general relative lack of stability margin for the leading-edge push-rod attachment configuration. Indeed, at a tip speed of 30.5 m/sec, the time-history solution calculated could be unquivocally termed unstable. Not only were the characteristic exponents for all identified modal frequencies found to be positive, but the responses achieved unreasonably large magnitudes and were terminated in the fourth rotor revolution.

The principal findings of the model rotor exploratory study are first that the trailing-edge push-rod configuration with negative (first mode) pitch-flat coupling is significantly more stable than the leading-edge push rod configuration. Second, whereas unstable responses were calculated for the latter configuration, none were calculated for the former. Third, no instabilities were calculated for either configuration at the nominal rotor speed at any advance ratio up to the maximum tested value of 0.47. These findings are thus consistent with the generally stable experimental results found within the test envelope. These calculations serve the additional purpose of introducing the stability analysis techniques also used in the following subsection.

Transient Stability of Full Scale Designs - In contrast to the above discussed cantilevered torque-tube configured model rotor, the full-scale design configurations with inboard snubber demonstrated generally more stable response characteristics. Once again, the evaluation of these stability characteristics required the consideration of results produced by the three basic mathematical tools available. For this portion of the study parametric variations were made about each of the two basic configuration trim conditions. Those parameters so varied were equivalent blade mass ratio (air density), blade loading (rotor shaft angle with fixed controls), advance ratio, push-rod attachment station (pitch-flat coupling), and torque tube flatwise bending stiffness. For each parameter variation, the blade response initial conditions were selected to be the appropriate trim values but with increments of

0.02 added each to the first flatwise and first edgewise bending modal degrees-of-freedom. Additionally, for some of the increased air density cases, the trim parameters were proportionately reduced to preclude unrealistic rotor stall conditions from obscuring the transient stability characteristics at issue.

Results of the stability analysis for the full-scale designs are shown in Table XV and in Figures 136 thru 138. Table XV shows both rotor design trim conditions to be stable from a "frozen azimuth" eigensolution standpoint. Furthermore, all calculated time-histories required to form the above enumerated parametric variations were found to be stable; that is, in every case the response amplitudes were well bounded and devoid of any divergent characteristics.

The results of using the transient spectral stability analysis (TSSA) on the calculated time-histories are presented in Figures 136 thru 138. These figures show the various identified resonant frequencies together with the equivalent (linear) characteristic exponent associated with each such frequency. Figure 136 shows the results for variations in equivalent blade mass ratio, $\gamma_{equ.}$, and in rotor shaft angle, α_s. Figure 137 presents the effects of varying advance ratio at the nominal value of mass ratio of 10.45 as well as at the augmented value of 12.54 (1.2 x nominal). Lastly, the results of varying push-rod attachment station (to achieve indirect variation in pitch-flat coupling) are shown in Figure 138.

Interpretation of the results of Figures 136 thru 138 must be made not only in light of the generally stable indications afforded by the eigensolutions and by the stable boundedness of the time-histories, but also by considering the selected operation of the transient spectral stability analysis. Typical TSSA operation involved utilizing all of approximately $14\frac{1}{4}$ azimuthal revolutions of time-history for frequency identification. However, the selection of only 100 time shifts in the calculations for the characteristic exponents appears to have been too few because it effectively limited this calculation to a relatively short window within the time histories from the start of the revolution 6 thru to 75 percent of revolution 8. Another factor to be considered in the interpretation of these results is that the TSSA identified significant Floquet-like behavior. By far the most consistently identified mode was the lightly damped first edgewise mode. However, as is shown in these figures, other modes were identified which had frequencies separated from the edgewise mode by integral harmonics and which were generally found to have approximately the same characteristic exponents. A general feature of these figures, however, is that most of these multiple or image roots demonstrate stable (negative) characteristic exponents. A significant point to be made is that although the basic supercritical trim case was calculated to

exhibit positive (unstable) characteristic exponents, it is, nonetheless, stable since it did in fact converge to periodicity.

The principal findings of the full-scale design transient stability analysis are first that, for all parametric variations, both designs were found to be stable. This evaluation is based principally on the fact that all time-history responses were found to be bounded for time periods corresponding to sixteen (16) rotor revolutions. Second, as a quantitative analysis tool, use of the transient spectral stability analysis to predict stability levels was generally unsuccessful. Due to an improper selection of operational parameters the TSSA did not use sufficient data for resolution of the calculated characteristic exponents.

An addendum to these findings is that in the course of making these parametric variations it was found that some of the increased air density cases, which used the nominal trim parameters, were found to produce unbounded responses. It is conjectured that these responses are stall related and similar to others obtained under high blade loading conditions and discussed in the "Transient Responses due to Control Inputs" and "Effects of Unsteady Airloads" subsections. The mechanism of this phenomenon is not fully understood and was not explored herein since it was beyond the scope of this study.

CONCLUSIONS AND RECOMMENDATIONS

1. Based on model rotor wind tunnel experiments, the Composite Bearingless Rotor with pinned-pinned control torque tube, is stable over a tested range of flight conditions and exhibits performance and blade response characteristics similar to conventional hingeless rotors.

2. Based on static and fatigue tests, graphite/epoxy is ideally suited to satisfy the strength and modulus requirements of the Composite Bearingless Rotor (CBR).

3. A relatively low stiffness rigid body torsion mode is inherent in the cantilever torque tube design causing significant pitch washout and potentially destabilizing pitch-flap coupling.

4. Based on a preliminary design study, a reduction in rotor system weight of 23 percent can be achieved with the CBR as compared to a conventional articulated rotor of the same size.

5. The unique structural characteristics of the CBR flexbeam, with its azimuthally varying twist distribution, can be analytically modelled.

6. As predicted by theory, and confirmed by experiment the effect of flexbeam twist on flat to edge coupling for the pinned-pinned configurations is minimal. The edgewise responses appear to be dominated by the 1 P and 2 P drag airloads.

7. Use of uncoupled modes together with appropriate twist related displacment correction functions provides a viable method for obtaining coupled mode response characteristics of rotor blades with arbitrary nonlinear (continuous or discontinuous) and time-variable twist as is typical of the composite bearingless rotor.

8. The significance of the rigourous modeling of the structural redundancy features of the CBR concept appears to be limited to the lower harmonics of the torque tube torsion stresses and, consequently, the push-rod loads.

9. Of the two torque tube configurated rotor models tested, the pinned-pinned and cantilevered, the former is the more practical for immediate further development. In contrast to the latter, it generally demonstrated typical hingless rotor characteristics consistently devoid of aeroelastic anomalies.

10. Although the cantilevered torque tube configurations of the model rotor were generally stable within the test envelope, the leading edge attachment configurations would appear to have less stability margin than the trailing edge configurations and could lose aeroelastic stability entirely at conditions of concurrent reduced rotor speed and moderate advance ratio.

11. Based on the results of the model rotor tests and preliminary attempts to achieve trimmed stable flight conditions for a full-scale cantilevered torque tube design, the alternate full-scale design incorporating a snubber torque tube can more readily and practically be developed. (from this basic conclusion it was further concluded that only the snubber design would be included within the scope of the full-scale study.)

The following additional conclusions relate to the evaluation of the full-scale (snubber torque tube) designs on the basis of limited aeroelastic considerations:

12. The use of the CBR concept in a full-scale helicopter main rotor application is practical.

13. Neither of the two configurations considered, one subcritical and one supercritical, are susceptible to any instabilities by virtue of the unique CBR features. While various instabilities were demonstrated for extreme combinations of blade loadings and advance ratio, they appear to be phenomena generally characteristic of all hingeless rotor systems.

14. Both full-scale designs can be configured to be free of any significant n/rev coupled frequency resonances. The bending stiffening of the torque tube needs to be considered and carefully controlled for the supercritical (soft edgewise) design to avoid 1/rev dynamic magnifications.

15. The selected trimmed flight conditions at high speed ($\mu = 0.44$) and moderate blade loading ($C_L/\sigma = 0.057$) represent partially stalled conditions and, hence, ones near to an operational stall boundary.

16. The designs are practical from the standpoint of flexbeam vibratory bending and torsional shear stresses. The flexbeam torsional stresses are marginally satisfactory at the high speed design condition, and an additional design iteration would be justified if greater margin were desired.

17. Transient blade bending stresses induced by perturbational control angles and partial material failures (15% reductions) are not critical .

18. At those combinations of blade loading and high forward speed defining the stall boundary blade torsion moments and, consequently, push-rod loads could become critical due to interactions of nonlinear ΔEI torsion excitation (accruing from hingeless rotor flatwise x edgewise bending) together with unsteady aerodynamics (dynamic stall and variable inflow). Because of the more nearly "stiffness-matched" characteristics inherent in the supercritical design, this design should be less critical.

19. Although manifesting lower vibratory edgewise bending moments, the supercritical design can exhibit vibratory edgewise stresses greater than or equal to those for the subcritical design. The supercritical design can, furthermore, demonstrate greater sensitivity to perturbational control angles.

20. Nominal bending stiffnesses of the torque tube can be sufficiently high as to result in significant portions of the bending moments at the juncture being carried by the torque tube, and in significant modifications of the coupled natural frequencies.

21. The examination of time-history solutions for boundedness was the most reliable indicator of aeroelastic stability employed. The transient spectral stability analysis, which utilizes Fourier Analysis techniques together with the time-history solutions, produced inconsistent results. This lack of consistency is most probably due to an inefficient implementation and subsequent utilization of this basic and potentially powerful concept.

The following recommendations are suggested which would extend the research in bearingless rotor systems.

1. Exploration into the feasibility of a "matched stiffness" bearingless rotor should be conducted. The rewards of further weight reductions and control loads may be achievable with such a design. Such a design is necessarily a highly supercritical design and the attendant potential for air and ground resonance difficulties must be solved. The application of supplementary integral material damping may provide an important solution to this concept.

2. The analysis should be extended to include (a) the calculation of torque tube bending stresses, and (b) explicit loadings on the torque tube. In direct support of a "matched stiffness" design the analysis should furthermore be extended to include (c) the hub degrees-of-freedom with

multi-blade capability, (d) a modelling of hysteretic structural damping to simulate the application of discrete elastromeric dampers or supplementary integral material damping, and (e) control system dynamics. Such an analysis would thus go beyond the capabilities of the eigensolution and Floquet approaches to include the full influences of nonlinearities, unsteady stalled aerodynamics, and realistic material damping.

3. Detailed studies of the destabilizing pitch-flap coupling mechanisms should be conducted to determine if an exceptable solution to the cantilevered torque tube design exists for main rotor applications.

4. Indications of a potentially critical phenomenon of hingeless rotors have been observed in the calculations. This phenomenon is stall-flutter like in that it involves the higher frequency torsion mode and occurs at high speed near the stall boundary. In contrast, however, it was calculated to occur principally when using only quasi-static airloads, involves appreciable blade bending and, hence, significant torsion excitation through the nonlinear ΔEI term. Whether this phenomenon is an analytic anomaly or a real problem area of hingeless rotors should be resolved.

5. Further development of the transient spectral stability analysis should be made to assess its full potential and to increase its reliability in routine usage.

REFERENCES

1. Bielawa, R. L.: Aeroelastic Analysis for Helicopter Rotor Blades with Time-Variable, Nonlinear Structural Twist and Multiple Structural Redundancy - Mathematical Derivation and Program User's Manual. NASA CR-2638, 1976.

2. Statler, W. H.; Heppe, R. R.; and Cruz, E. S.: Results of the XH-51A Rigid Rotor Research Helicopter Program. American Helicopter Society, 19th Annual National Forum Proceedings, May 1963.

3. Weiland, E. F.: Development and Test of the BO-105 Rigid Rotor Helicopter. Journal of the American Helicopter Society, Vol. 14, No. 1, January 1969.

4. Johnston, J. F.; and Cook, J. R.: AH-56A Vehicle Development. American Helicopter Society, 27th Annual National Forum Proceedings, No. 574, May 1971.

5. Cheney, M. C.: Results of Preliminary Studies of a Bearingless Helicopter Rotor Concept. American Helicopter Society, 28th Annual National Forum Proceedings, No. 600, May 1972.

6. Novak, R. C.: "Investigation of Graphite Filament Reinforced Epoxies," NASC Contract N00019-67-0354, Final Report, 1968.

7. Owen, M. J.; and Morris, S.: "An Assessment of the Potential of Carbon Fibre Reinforced Plastics as Fatigue Resistant Materials, " 24th Annual Conference, SPI, 1970.

8. Holmes, R. D.; and Wright, D. W.: "Creep and Fatigue Characteristics of Graphite/Epoxy Composites," ASME Paper 70-DE-32, 1970.

9. Hoel, P. G.: Introduction to Mathematical Statistics, Second Edition. New York, John Wiley & Sons, Inc., 1958.

10. Bellinger, E. D.; Patrick, W. P.; Greenwald, L. E.; and Landgrebe, A. J.: Experimental Investigation of the Effects of Helicopter Rotor Design Parameters on Forward Flight Stall Characteristics. USAAMRDL Technical Report 74-1, Eustis Directorate, Fort Eustis, April, 1974.

11. Voitsch, W.; and Weiss, H.: Dynamic Behavior of a Hingeless Fiberglass Rotor. AIAA/AHS VTOL Research, Design, and Operations Meeting Proceedings, No. 69-204, February 1969.

12. Donham, R. E.; Cardinale, S. V.; and Sacks, I. B.: Ground and Air Resonance Characteristics of a Soft In-Plane Rigid-Rotor System. AIAA/AHS VTOL Research, Design, and Operations Meeting Proceedings, No. 69-205, February 1969.

13. Crimi, P.: A Method for Analyzing the Aeroelastic Stability of a Helicopter Rotor in Forward Flight. NASA CR-1332, 1969.

14. Hall, W. E.: Application of Floquet Theory to the Analysis of Rotary Wing VTOL Stability. SUDDAR No. 400, Stanford University Center for Systems Research. (NASA Contract NAS-25143), 1970.

15. Friedmann, P.; and Silverthorn, L. J.: Aeroelastic Stability of Coupled Flap-Lag Motion of Hingeless Helicopter Blades at Arbitrary Advance Ratios. (UCLA-ENG-7406, Engineering and Applied Science, UCLA; NASA Grant NGR-05-007-414) NASA CR-132431, 1974.

16. Gessow, A. and Myers, G. D., Jr.: Aerodynamics of the Helicopter. Frederick Ungar Publishing Company, New York, 1967, pp. 67-72.

17. Ormiston, R. A. and Hodges, D. H.: Linear Flap-Lag Dynamics of Hingeless Helicopter Rotor Blades in Hover. Journal of the American Helicopter Society, Vol. 17, No. 2, April 1972.

18. Friedman, P.: Aeroelastic Instabilities of Hingeless Helicopter Blades. Journal of Aircraft, Vol. 10, No. 10, pp. 623-631, 1973.

19. Friedman, P.: Influence of Structural Damping, Preconing, Offsets and Large Deflections on the Flap-Lag-Torsional Stability of a Cantilevered Rotor Blade. AIAA/ASME/SAE 16th Structures, Structural Dynamics, and Materials Conference Proceedings No. 75-780, May 1975.

20. Ormiston, R. A.; and Bousman, W. G.: A Study of Stall-Induced Flap-Lag Instability of Hingeless Rotors. Journal of the American Helicopter Society, Vol. 20, No. 1, January 1975.

21. Baumeister, T., ed: Mark's Standard Handbook for Mechanical Engineers. Seventh ed., McGraw-Hill Book Co., Inc., 1967, p. 5-52.

22. Bielawa, R. L.: Synthesized Unsteady Airfoil Data with Applications to Stall Flutter Calculations. American Helicopter Society, 31st Annual National Forum Proceedings, No. 935, May 1975.

23. Carta, F. O.; Commerford, G. L.; Carlson, R. G.; and Blackwell, R. A.: Investigation of Airfoil Dynamic Stall and Its Influence on Helicopter Control Loads. USAAMRDL Technical Report 72-51. U. S. Army Air Mobility Research and Development Laboratory, Fort Eustis, VA, 1972.

24. Kuczinsky, W. A.: Inflight Rotor Stability Monitor. NASA Symposium on Flutter Testing Techniques, NASA Flight Research Center, Edwards AFB, October 1975.

TABLE I

METRIC TO ENGLISH CONVERSION FACTORS

Multiply	By	To Find
m	3.281	feet
m	39.370	in.
m/sec	1.944	kts.
kg	2.205	lbm
kg/m	.0560	lbm/in.
N	.2248	lb
Nm	.7376	lb-ft
Nm^2	348.5	$lb\text{-}in.^2$
kgm	.2248	$lb\text{-}sec^2$
MN/m^2	.1450	$(lb/in.^2)x10$

TABLE II

Unidirectional HTS Carbon/Epoxy Static Test Results

Material Lot Number	Shear Strength, MN/m^2, (ksi)	Shear Modulus, GN/m^2, (msi)	Flexural Strength, GN/m^2, (ksi)	Flexural Modulus, GN/m^2, (msi)
1A-11	79.3 (11.5)	6.48 (0.94)	1.5 (222)	156 (22.6)
1C-4	99.3 (14.4)	6.55 (0.95)	1.76 (255)	151 (21.9)
1D-52	112.4 (16.3)	*	1.53 (222)	152 (22.1)
1D-52 1A	115.8 (16.8)	*	1.67 (242)	144 (20.9)
1D-52 1B	113.1 (16.4)	*	0.97 (141)	132 (19.1)

* Not measured

TABLE III

Combined Loading Fatigue Results
HTS Graphite/Epoxy Specimens

No.	σ_{edge}	σ_{flat}	σ_{axial}	σ_{total}	τ	N	G_f/G_i	E_f/E_i
	stress units:		MN/m^2,	(Ksi)				
KC4-4	173.7 (25.2)	496 (72.0)	0	670 (97.2)	30 (4.3)	10^7	.96	.85
KC4-3	122.7 (17.8	436 (63.2)	0	558 (81.0)	26 (3.8)	10^7	1.00	1.00
KC4-2	87.6 (12.7)	369 (53.5	0	456 (66.2)	22 (3.2)	10^7	.84	1.00
KC4-1	81.6 (12.7)	369 (53.5)	0	456 (66.2)	22 (3.2)	10^7	.94	1.00
KC1-6*	173.7 (25.2)	496 (72.0)	69 (10)	739 (107.2)	30 (4.3)	10^7	.51	.98
KC1-5	84.1 (12.2)	341 (49.5)	69 (10)	494 (71.7)	21 (3.0)	10^7	1.00	1.00
964-4	135.8 (19.7)	382 (55.4)	69 (10)	587 (85.1)	23 (3.3)	10^7	1.00	1.00

* Split at clamp due to excessive tightening in trying to prevent slipping

TABLE IV

MODEL SCALE BEARINGLESS ROTOR DESIGN PARAMETERS

Parameter	Model Rotor Values	
Torque Tube Design	Cantilever (Fig. 9)	Pinned (Fig. 8)
Design Tip Speed, R, m/sec	99.1	99.1
No. Of Blades, b	4,2	4,2
Radius, R, m	0.610	0.610
Chord, c, m	0.0391	0.0391
Solidity, σ	0.0817, 0.0408	0.0817, 0.0408
Blade Root Offset	0.05R	0.05R
Preconing, a_o, deg	2	2
Flexbeam Length	0283R	0.283R
Airfoil*	NACA 0012	NACA 0012
Linear Twist, θ_1 deg	0	0
c.g. Location*	0.25c	0.25c
e.a. Location*	0.25c	0.25c
Tip Mach No., M	0.291	0.291
Tip Reynolds No., Re	0.287×10^6	0.287×10^6
Lock No., γ	4.27	4.15
Froude No., $\Omega^2 R/g$	1640.	1640.
1st Flapwise Natural Frequency, $\bar{\omega}_{w_1}$	1.09	1.09
2nd Flapwise Natural Frequency, $\bar{\omega}_{w_2}$	2.90	2.66
3rd Flapwise Natural Frequency, $\bar{\omega}_{w_3}$	5.66	4.70
1st Edgewise Natural Frequency, $\bar{\omega}_{v_1}$	1.35	1.35
2nd Edgewise Natural Frequency, $\bar{\omega}_{v_2}$	8.52	7.72
1st Torsional Natural Frequency, $\bar{\omega}_{\theta_1}$	7.15	7.02

* Outboard of Torque Tube.

TABLE V

SCALE FACTOR SUMMARY

Parameter	Factor	
Weight or Mass per Unit of Length	$(R_{FS}/R_{MS})^2$	$\bar{R}^2$
Total Mass	$(R_{FS}/R_{MS})^3$	$\bar{R}^3$
Moment of Inertia per Unit Length	$(R_{FS}/R_{MS})^4$	$\bar{R}^4$
Total Inertia	$(R_{FS}/R_{MS})^5$	$\bar{R}^5$
Force	$(R_{FS}/R_{MS})^2 \ (\Omega R)_{FS}^2/(\Omega R)_{MS}^2$	$\bar{R}^4\bar{\Omega}^2$
Moment	$(R_{FS}/R_{MS}) \ (\Omega R)_{FS}^2/(\Omega R)_{MS}^2$	$\bar{R}^5\bar{\Omega}^2$
Stress	$[(\Omega R)_{FS}/(\Omega R)_{MS}]^{1/2}$	$\sqrt{\bar{\Omega}\bar{R}}$
Stiffness	$(R_{FS}/R_{MS})^4 \ (\Omega R)_{FS}^2/(\Omega R)_{MS}^2$	$\bar{R}^6\bar{\Omega}^2$
Nondimensional Blade Natural Frequencies	ω/Ω	

TABLE VI

FORWARD FLIGHT TEST CONDITIONS

$\Omega R = 99.1$ m/sec

b	μ	Collective Angle, $\theta_{.75}$, deg	Torque Tube Attachment
2	0.25, 0.35, 0.47	4	Pinned
"		8	" "
4	0.25, 0.35, 0.47	4	" "
"	0.25	8	" "
"	0.35	"	" "
"	0.25	9.3	" "
"	0.35	10.1	" "
"	0.47	"	" "
2	0.25	7.4 - 7.5	Cantilever (t.e.)* @ r=0.060R
"	0.35	" "	" "
"	0.47	" "	" "
"	0.25	13.5 - 13.6	" "
"	0.35	" "	" "
"	0.47	" "	" "
"	0.35	16.6 - 17.5	" "
4	0.25	7.5	" "
2	0.25	6.6	Cantilever (t.e.) @ r=0.080R
"	0.25	12.5	" "
4	0.25	7.4	" "
2	0.25	6.1	Cantilever (l.e.)* @ r=0.091R
"	0.35	6.5	" "
"	0.47	5.5	" "
"	0.25	9.5	" "
"	0.25	11.1	" "
"	0.35	11.1	" "
"	0.47	11.1	" "
"	0.35	13.2	" "
"	0.47	14.4	" "
4	0.25	7.4	" "
2	0.25	6.5	Cantilever (l.e.) @ r=0.070R
2	0.25	9.7	" "

NOTE: At each test condition α_s was generally varied over a range of eight or ten degrees in two degree increments.

* t.e. - trailing edge; l.e. = leading edge

TABLE VII

PARTIAL DERIVATIVES OF PERFORMANCE WITH RESPECT TO CONTROL ANGLES

$$(\alpha_s)_{trim} = -6^\circ$$

(a) Lift Coefficient/Solidity, C_L/σ

Torque Tube Type	μ	$\partial/\partial\alpha_s$	$\partial/\partial\theta_{.75R}$	$\partial/\partial A_{1s}$	$\partial/\partial B_{1s}$
		deg^{-1}			
Pinned-Pinned	.25	.00614	.01710	-.00111	-.00674
	.35	.00928	.02161	-.00167	-.01038
Cantilevered (t.e.) @ r = .060R	.25	.00443	.00934	.00077	-.00288
	.35	.00540	.01029	.00098	-.00484
Cantilvered (l.e.) @ r = .091R	.35	.00874	.01639	-.00272	-.00950

(b) Drag Coefficient/Solidity, C_D/σ

Pinned-Pinned	.25	-.00038	-.00226	.00040	.00056
	.35	-.00193	-.00294	.00056	.00167
Cantilevered (t.e.) @ r = .060R	.25	.00029	-.00091	.00026	.00004
	.35	-.00021	-.00119	.00003	.00057
Cantilevered (l.e.) @ r = .091R	.35	-.00130	-.00225	.00025	.00122

(c) Torque Coefficient/Solidity, C_Q/σ

Pinned-Pinned	.25	0	-.00018	.00048	.00114
	.35	.00036	.00030	.00048	.00037
Cantilevered (t.e.) @ r = .060R	.25	.00029	.00033	.00010	.00032
	.35	.00024	.00026	.00008	.00023
Cantilvered (l.e.) @ r = .091R	.35	-.00048	-.00066	-.00031	.00062

TABLE VIII

MODEL TEST PARAMETERS DEFINING CORRELATION CASES

Group	Case	b	Torque-Tube Configuration	Geometric Pitch-Flat Coupling, θ_{w_i}, i =1, 2 ,3*	Density Ratio	Velocity km/sec	Geom, Shaft angle, deg.	$\theta_{.75}$ deg.	A_{1s} deg.	B_{1s} deg.
I	25.03	2	pinned	0., 0., 0.	.9498	88.96	-6.0	8.2	-2.3	5.3
	87.08	4			.9571	88.96	-5.0	7.9	-2.1	6.1
II	22.03	2			.9656	88.96	-8.0	9.8	-2.3	5.4
	22.04				.9638	124.54	-8.0	9.6	-1.0	6.1
	21.05				.9603	167.35	0.	3.1	-1.9	5.2
	22.05				.9585	167.72	-8.0	9.6	-1.6	6.2
III	11.05				.9380	124.90	-6.0	4.0	-0.4	1.4
	11.06				.9345	125.09	-6.0	4.0	-0.4	2.7
IV	82.10		cantilevered	-.656,-.962,10.93**	.9562	89.14	0.	6.7	-0.4	4.8
	83.08				.9579	89.14	-8.0	11.0	0.	6.5
	72.06			+.422,1.302,-11.0***	.9253	168.46	0.	5.6	-0.2	8.0
	73.08				.9187	168.09	-8.0	14.5	-0.7	10.8

*Geometric pitch-flat coupling is computed from flatwise modal distributions and torque tube geometry; cantilevered torque tube is attached to blade spar 19.05 cm from rotor center.

**Push-rod/torque tube attachment point is 4.90 cm from rotor center and 2.97 cm behind feathering axis.

***Push-rod/torque tube attachment point is 5.54 cm from rotor center and 2.96 cm ahead of feathering axis.

TABLE IX

EXPERIMENTAL AND ANALYTIC ROTOR PERFORMANCE FOR CORRELATION CASES

Case	μ	$\lambda_o(\lambda)$*	λ_{1_c}	λ_{1_s}	C_L/σ		C_D/σ		C_Q/σ	
					exp.	anal.*	exp.	anal.*	exp.	anal.*
25.03	.248	-.00374 (-.0315)	-.02518	.00462	.07832	.07832 (.04837)	-.01079	-.00877 (-.00565)	.00925	.00643 (.00532)
87.08	.249	-.00373 (-.0331)	-.02232	.02366	.07410	.07416 (.00388)	-.00898	-.00735 (-.00481)	.00583	.00606 (.00501)
22.03	.247	-.02754 (-.0366)	-.02658	.00469	.07079	.07069 (.05931)	-.01137	-.00992 (-.00808)	.00793	.00748 (.00675)
22.04	.346	-.03201 (-.0483)	.00087	-.01807	.05027	.04931 (.04166)	-.00609	-.00549 (-.00419)	.00573	.00693 (.00608)
21.05	.469	.03275 (.0064)	-.02248	.01342	.04029	.04029 (.00861)	.00017	.00354 (.00323)	.00405	.00310 (.00350)
22.05	.467	-.06672 (-.0584)	-.01292	.00008	.02162	.02184 (.03083)	-.00254	.00075 (-.00022)	.00458	.00503 (.00547)
11.05	.348	-.04175 (-.0324)	-.00260	-.00535	.00138	.00165 (.01312)	.00200	.00247 (.00158)	.00264	.00302 (.00335)
11.06	.349	-.05015 (-.0324)	.00195	.00178	-.01449	-.01411 (.00446)	.00465	.00438 (.00209)	.00241	.00216 (.00315)
82.10	.250	.01905 (.0146)	-.01584	.00124	.06376	.06401 (.06005)	.00162	.00095 (.00101)	.00283	.00308 (.00310)
83.08	.248	-.00421 (-.0397)	.00597	.00501	.07038	.07043 (.03773)	-.01320	-.00989 (-.00472)	.00510	.00553 (.00484)
72.06	.472	.03014 (.0063)	.01304	.01708	.04121	.04086 (.00911)	-.00107	.00334 (.00314)	.00560	.00346 (.00359)
73.08	.468	-.03533 (-.0594)	.01110	-.00611	.04991	.04815 (.02186)	-.00990	-.00372 (.00002)	.00809	.00698 (.00530)

* Nonparenthesized values pertain to trimmed analytic results; parenthesized values pertain to untrimmed analytic results.

TABLE X

SUMMARY OF FULL-SCALE DESIGN FORWARD FLIGHT TRIM CASES

Case	1	2	3
blade configuration	subcritical	supercritical	subcritical
torque-tube bending stiffness	nominal	25% nominal	nominal
radial pushrod attachment point, m.	.533	.483	.635
$\Delta\theta/\Delta q_{w_i}$ $i = 1$	.118	-.013	.383
$\Delta\theta/\Delta q_{w_i}$ $i = 2$	-.330	.029	-1.053
$\Delta\theta/\Delta q_{w_i}$ $i = 3$	.748	-.024	2.301
$\theta_{.75R}$, deg.	12.07	11.25	11.82
A_{1_s}, deg.	-1.19	-1.89	-1.36
B_{1_s}, deg.	9.69	8.07	9.47
λ	-.0609	-.0642	-.0581

TABLE XI

AERODYNAMIC STATIC STABILITY DERIVATIVE MATRICES, $[S]$

A. trim case 1 (basic subcritical configuration)

$$\begin{bmatrix} -.002090 & -.009384 & .015010 & .009280 & -.224900 \\ -.000060 & .000522 & .000378 & -.000432 & -.051680 \\ -.000177 & -.001431 & .001708 & .000685 & .000306 \\ .000790 & -.000089 & .000166 & .000022 & .002155 \\ -.000067 & -.000245 & .001318 & .000302 & -.009352 \\ .001148 & -.000076 & .000034 & -.000112 & .001190 \end{bmatrix}$$

B. trim case 2 (basic supercritical configuration

$$\begin{bmatrix} -.000800 & -.009808 & .016630 & .009280 & -.196000 \\ -.000079 & .000444 & .000653 & -.000315 & -.046590 \\ -.000066 & -.001364 & .001225 & .000427 & .004698 \\ .000902 & -.000299 & .000857 & .000140 & -.005363 \\ -.000046 & -.000186 & .001176 & .000214 & -.007553 \\ .001137 & .000297 & -.000379 & -.000340 & .002126 \end{bmatrix}$$

C. trim case 3 (subcritical configuration with modified pitch-flat coupling)

$$\begin{bmatrix} -.004567 & -.008454 & .014690 & .009394 & -.257600 \\ .000052 & .000483 & .000515 & -.000423 & -.051220 \\ -.000490 & -.001310 & .001583 & .000723 & -.002830 \\ .000594 & -.000477 & .000602 & .000236 & .000931 \\ -.000165 & -.000281 & .001376 & .000362 & -.015480 \\ .000950 & -.000538 & .000572 & .000147 & .000852 \end{bmatrix}$$

TABLE XII

TRIM DERIVATIVE MATRICES, $[T]$

A. trim case 1 (basic subcritical configuration)

$$\begin{bmatrix} 3.3 & -86.9 & -130.4 & 1238.2 \\ 115.4 & 747.4 & -1188.6 & 96.5 \\ 24.2 & 896.5 & 157.7 & 167.9 \\ 1.3 & -5.4 & -11.3 & 0.8 \end{bmatrix}$$

B. trim case 2 (basic supercritical configuration)

$$\begin{bmatrix} -17.5 & -449.0 & -247.7 & 1036.1 \\ 56.4 & 427.0 & -1002.5 & 13.4 \\ 15.0 & 787.7 & 128.3 & 91.5 \\ 1.0 & -7.6 & -10.0 & -0.5 \end{bmatrix}$$

C. trim case 3 (subcritical configuration with modified pitch-flat coupling)

$$\begin{bmatrix} 6.3 & -52.6 & -532.5 & 1297.5 \\ 123.2 & 570.3 & -1287.7 & -165.3 \\ 18.2 & 789.3 & 113.4 & 164.1 \\ 1.3 & -5.6 & -12.0 & 1.69 \end{bmatrix}$$

TABLE XIII

EFFECTS OF PARTIAL FLEXBEAM BENDING STIFFNESSES ON BLADE NATURAL FREQUENCIES

Mode	Flexbeam Bending Stiffness		
	Nominal	$(EI_F)_{FB}$= 0.85 x Nominal	$(EI_E)_{FB}$= 0.85 x Nominal
Subcritical Design			
ω_{w_1}	1.080P	1.076P	1.080P
ω_{w_2}	2.174P	2.701P	2.714P
ω_{w_3}	4.843P	4.814P	4.834P
ω_{v_1}	1.328P	1.328P	1.270P
ω_{v_2}	7.281P	7.281P	7.111P
Supercritical Design			
ω_{w_1}	1.080P	1.076P	1.080P
ω_{w_2}	2.714P	2.701P	2.714P
ω_{w_3}	4.843P	4.814P	4.834P
ω_{v_1}	0.794P	0.794P	0.763P
ω_{v_2}	4.138P	4.138P	4.063P

TABLE XIV

SELECTED EIGENSOLUTIONS FOR MODEL ROTOR WITH CANTILEVERED TORQUE TUBE

Trailing Edge Push-Rod Attachment at .09R.
ΩR = 99.1 m/sec., ψ = 0
$\theta_{.75R} = A_{1s} = B_{1s} = 0$, λ (inflow) = -.005

Case & Condition	*σ	*ω	Modal Content
I. μ = 0.1	-.244	1.194	1F, 2T
zero initial conditions	-.026	1.356	1E
	-.210	2.947	2T, 2F, 1T
	-.367	3.433	2T, 1T
	-.176	5.794	1T, 2T, 3F
II. μ = 0.1	-.227	1.292	1F, 2T, 1E
nominal initial conditions	-.019	1.382	1E, 2T, 1F
($q_{w_1} = q_{v_1}$ = 0.02)	+.052	3.145	2T, 1T, 1F, 2F
	-.648	3.130	2T, 1T, 1F, 2F
	-.181	5.792	1T, 2T, 3F
III. μ = 0.47	-.200	1.392	1F, 2T, 1E
nominal initial conditions	-.039	1.393	1E, 1F, 2T
	+.054	3.198	2T, 1T, 1F, 1E
	-.666	3.166	2T, 1T, 1F, 1E
	-.187	5.821	2T, 1T, 1F, 1E

*Eigenvalue, $\lambda = \sigma \pm i\omega$

TABLE XV

EIGENSOLUTIONS FOR FULL SCALE DESIGN
CONFIGURATIONS AT TRIM CONDITIONS

ΩR = 198.1 m/sec, ψ = 0

(initial conditions)=(initial conditions)$_{trim}$+(Δq_{w_1}, Δq_{v_1} = .02)

Case	*σ	*ω	Modal Content
I. Subcritical (Configuration No.1)	-.499	1.201	1F, 1E, 1T
	-.067	1.403	1E, 1F, 1T
	-.389	2.836	2F, 1T, 1E, 1F
	-.473	4.789	3F, 1E, 1T, 2F
	-.147	7.575	1T, 2E, 1F
	-2.713	10.059	1T
II. Supercritical (Configuration No.2)	-.058	.847	1E, 1F
	-.563	1.304	1F, 1E
	-.413	2.808	2F, 1E, 1F, 1T
	-.081	4.078	1T, 2E, 1F, 3F
	-.505	4.944	3F, 1E, 1T, 2E
	-2.646	10.081	1T
*Eigenvalue $\lambda = \sigma \pm i\omega$			

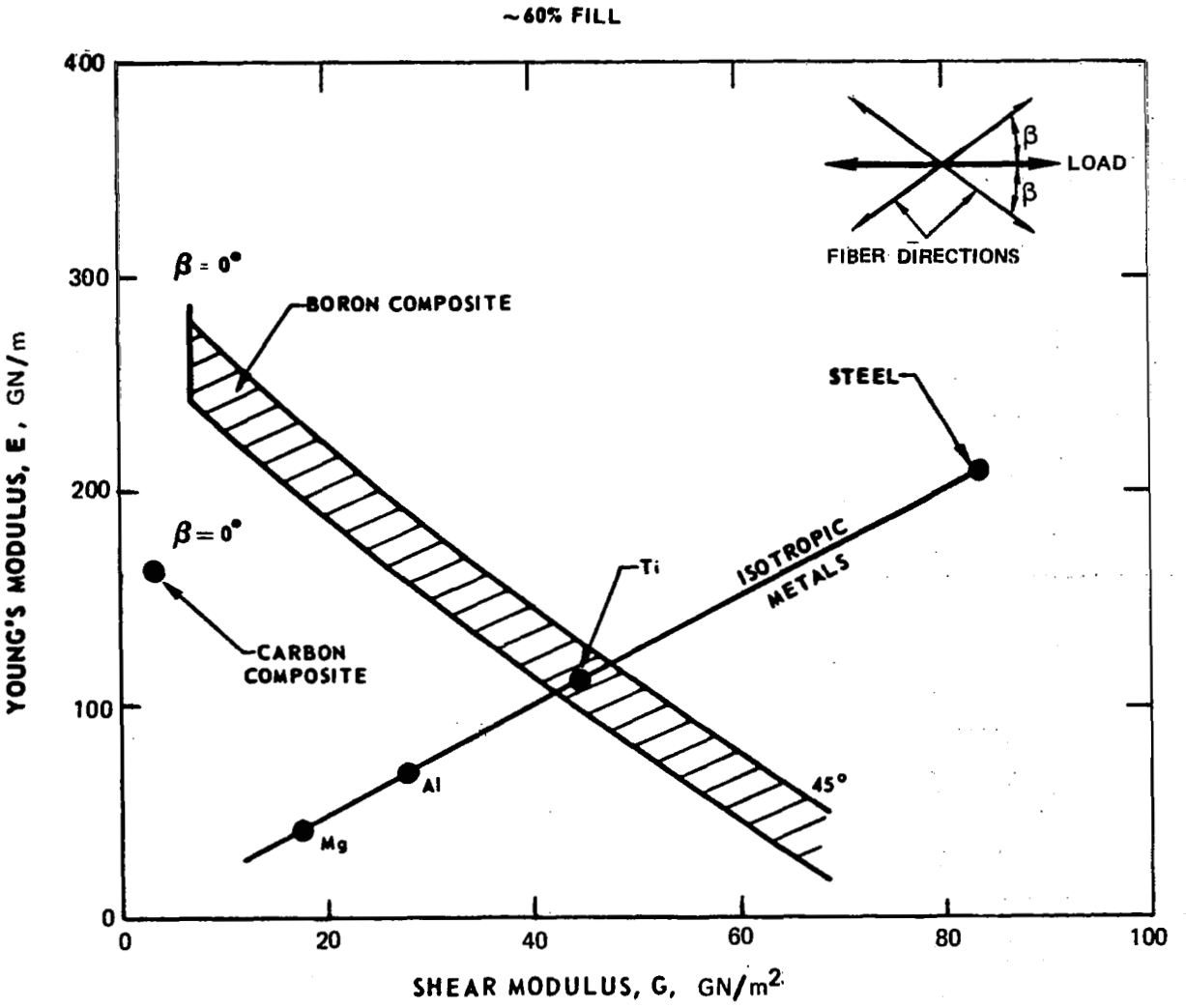

Figure 1. - Typical Combinations of E and G.

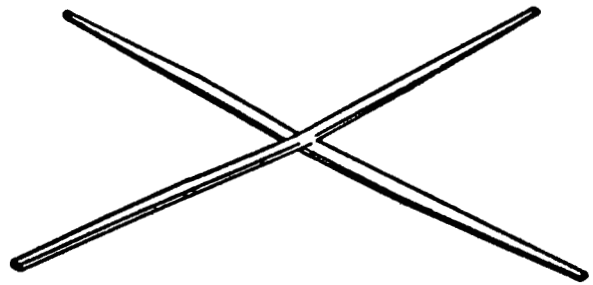

SPAR ASSEMBLY

(a)

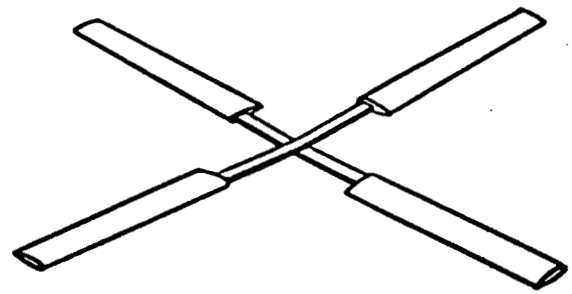

+ AIRFOIL ASSEMBLY

(b)

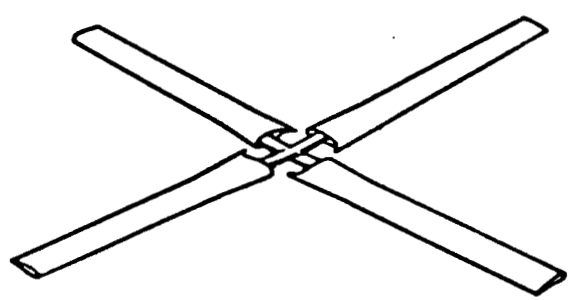

+ TORQUE TUBE ASSEMBLY

(c)

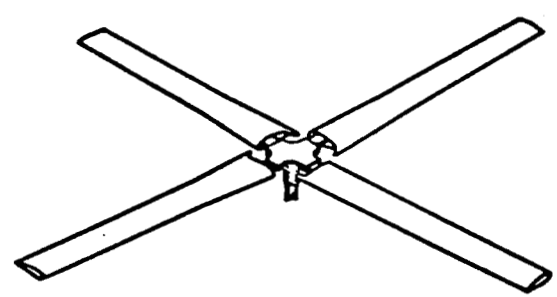

+ HUB ASSEMBLY

(d)

Figure 2. - Composite Bearingless Rotor

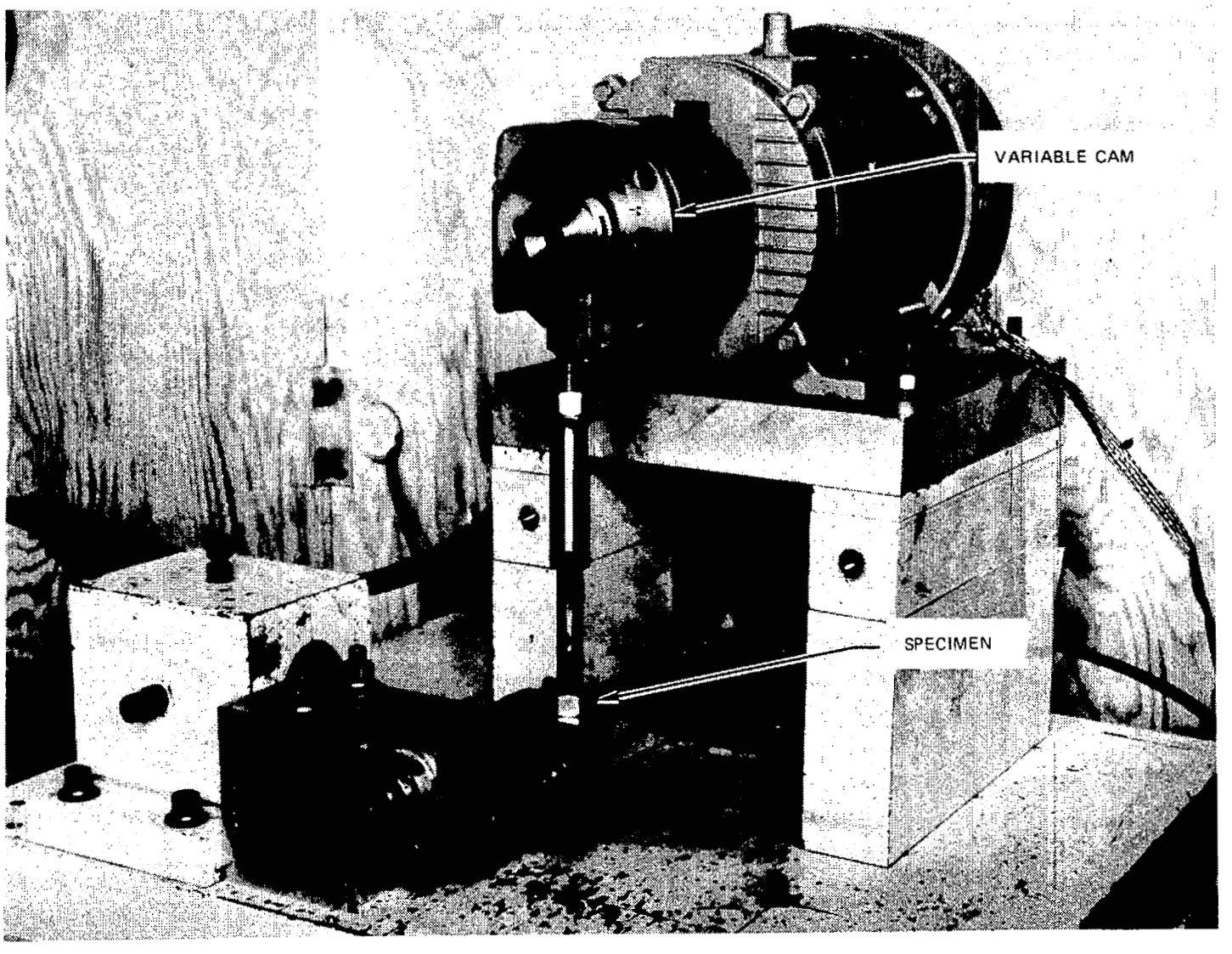

Figure 3. - Fatigue Test Setup

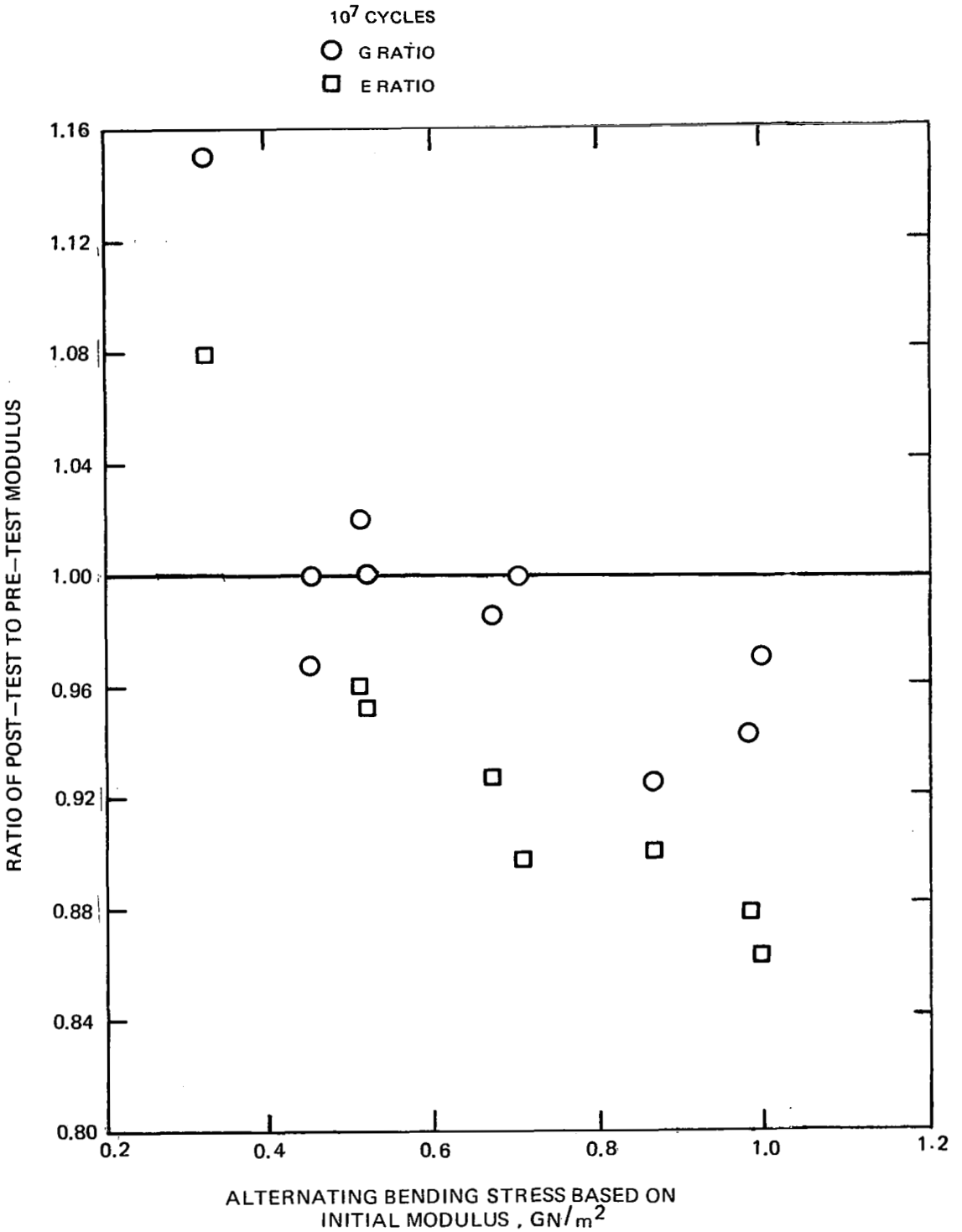

Figure 4. - Bending Fatigue Results.

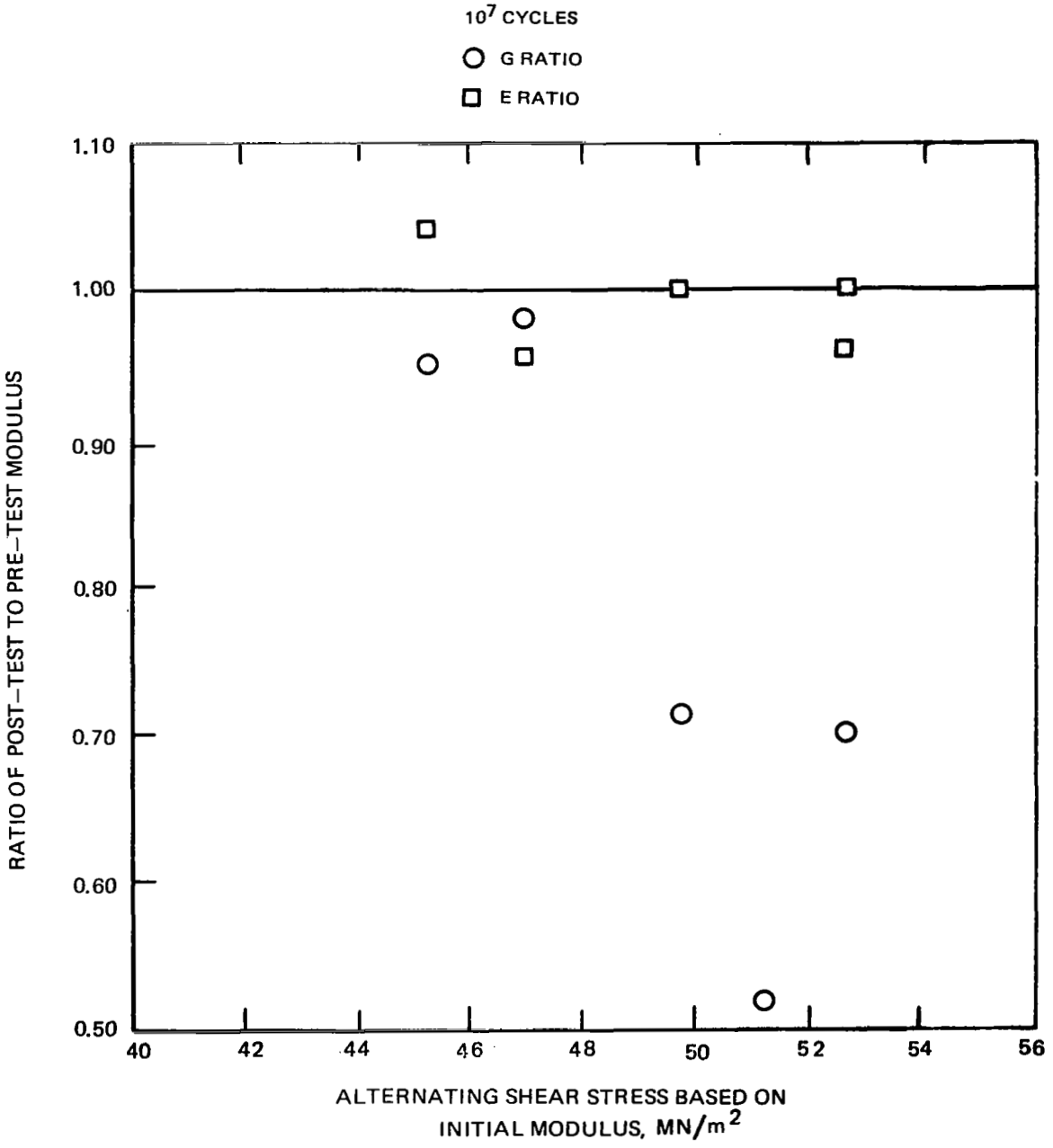

Figure 5. - Torsion Fatigue Results.

± 52.7 MN/m^2 PURE TORSION

5 X 10^6 CYCLES

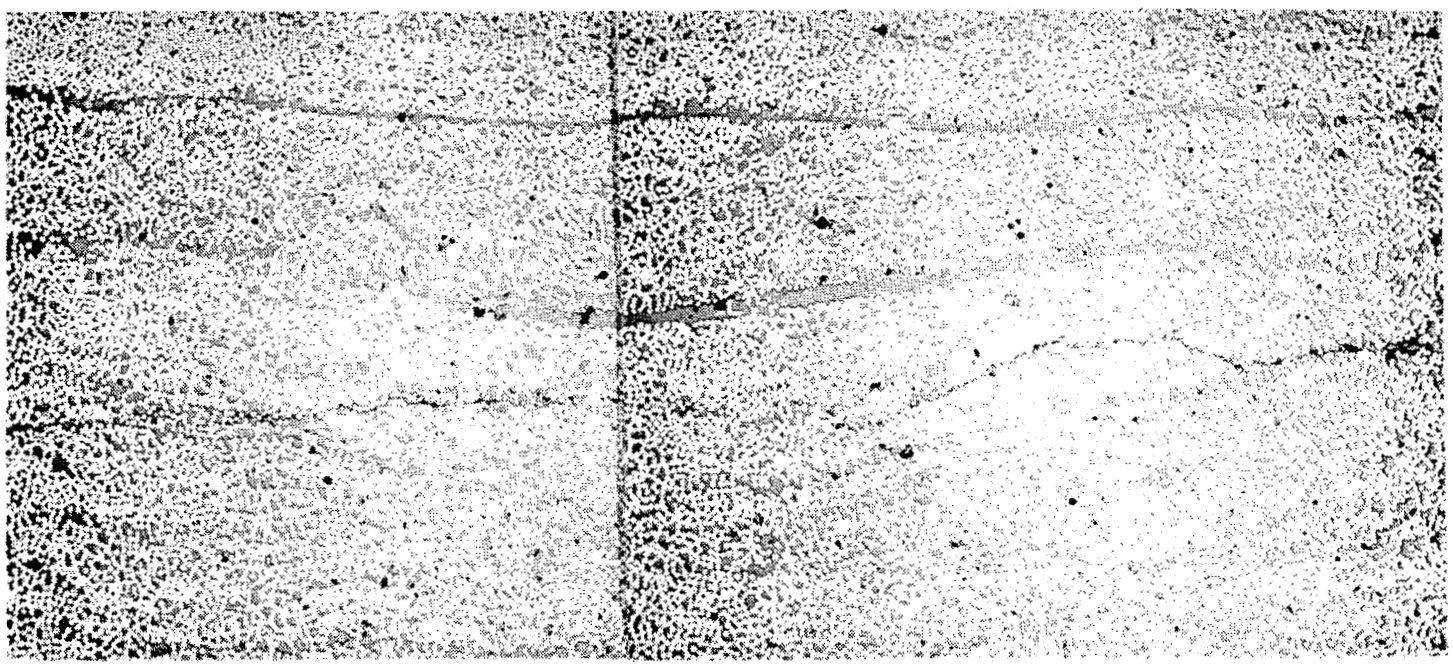

100 μm

Figure 6. - Failed Graphite/Epoxy Fatigue Specimen

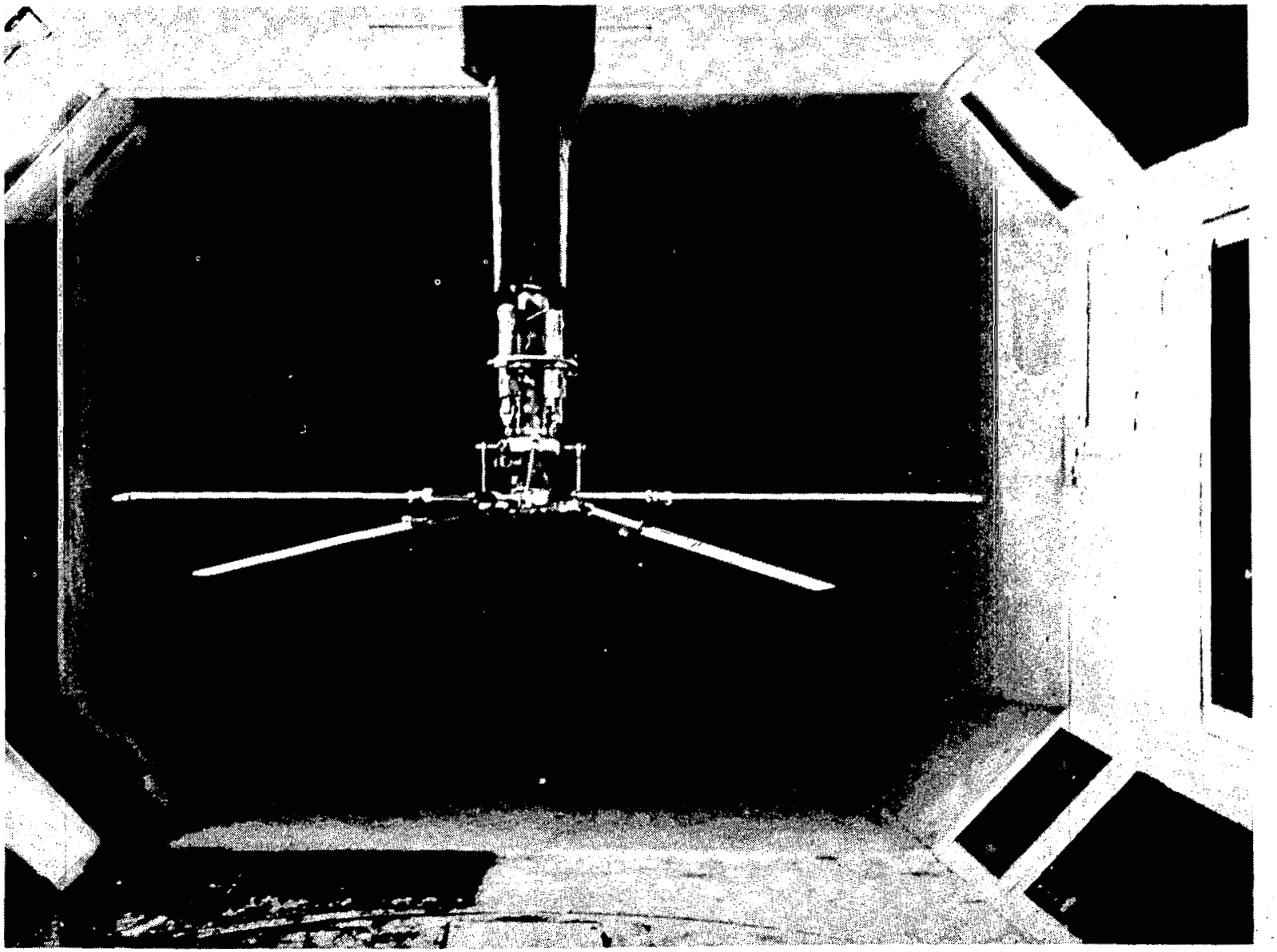

Figure 7. - Model Rotor and Test Rig Installed in Wind Tunnel Test Section

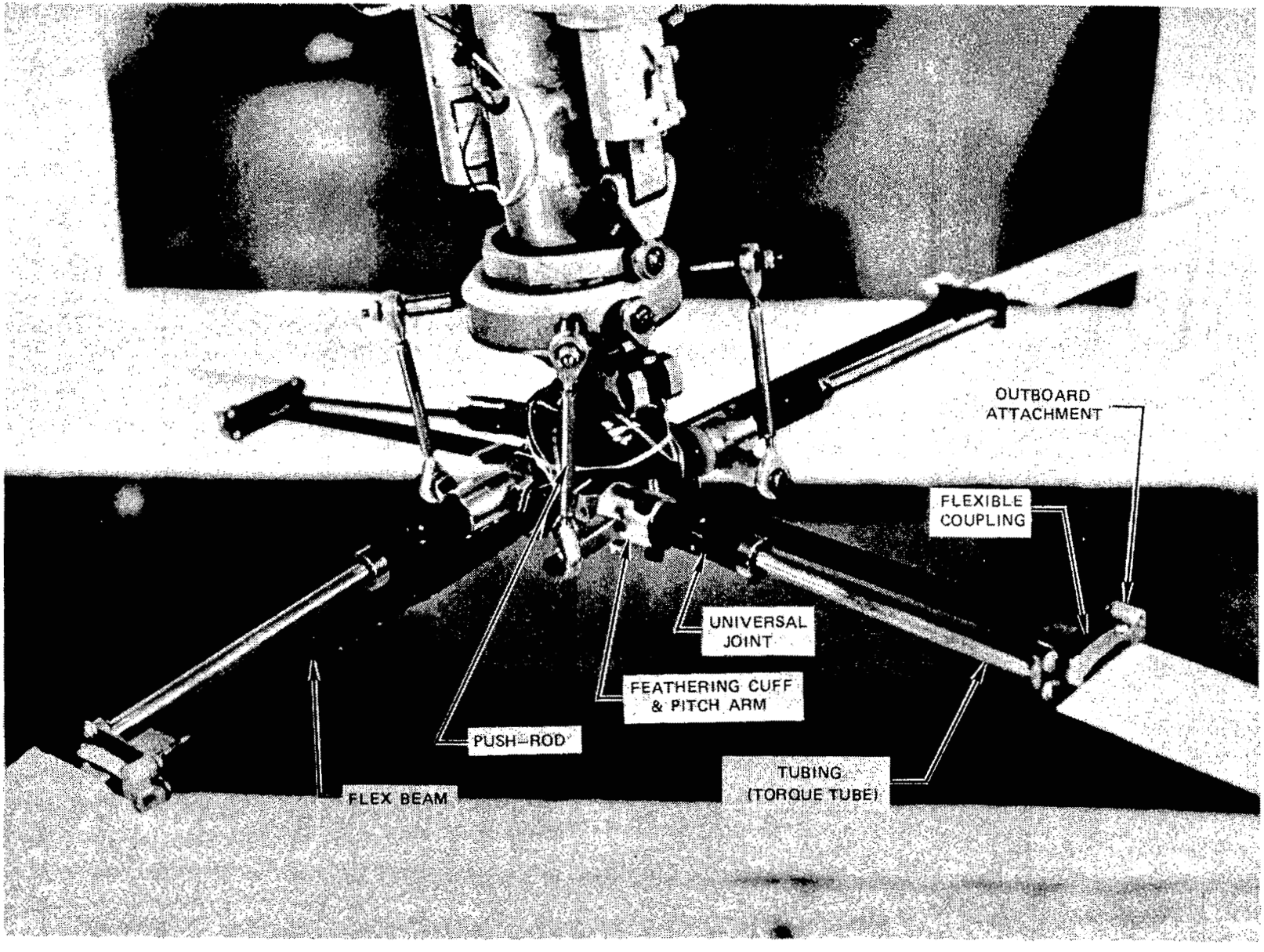

Figure 8. - Details of Pinned-Pinned Torque Tube

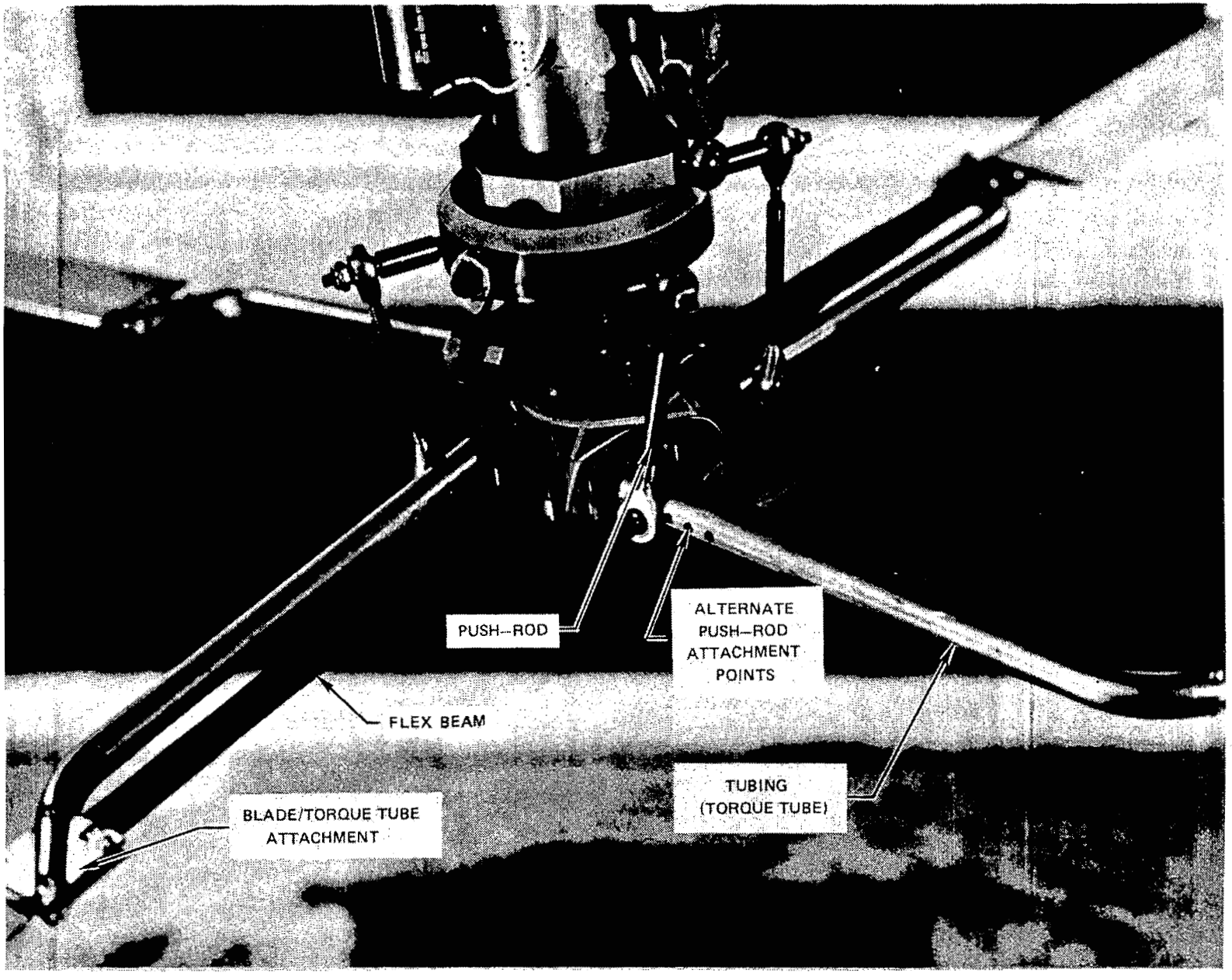

Figure 9. - Details of Cantilevered Torque Tube.

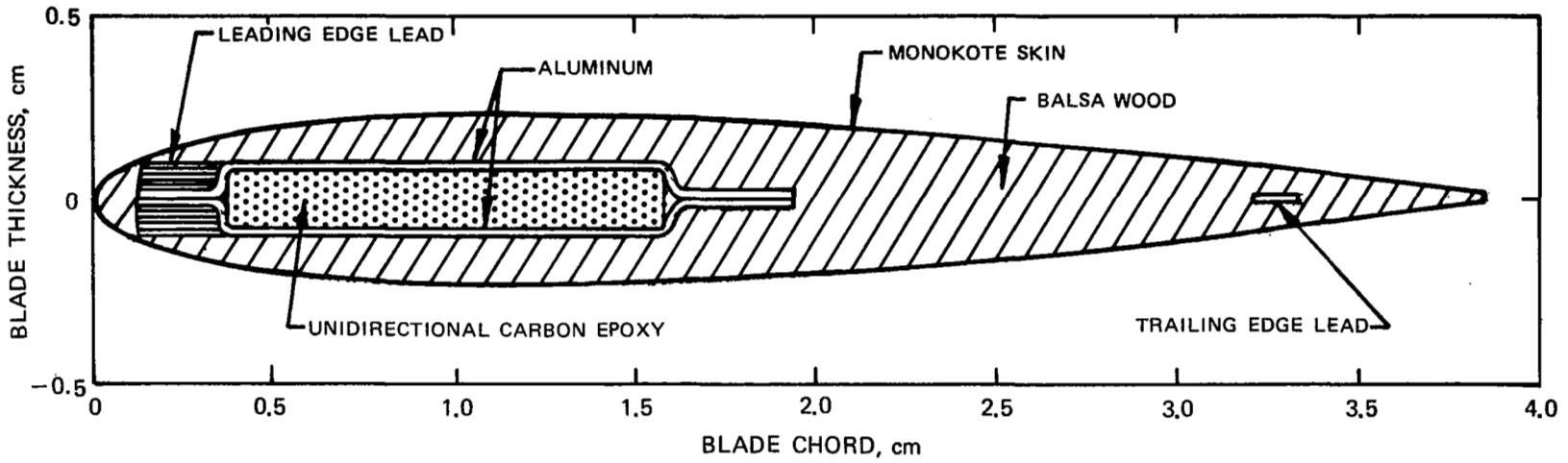

Figure 10. - Typical Cross Section of Model Blade.

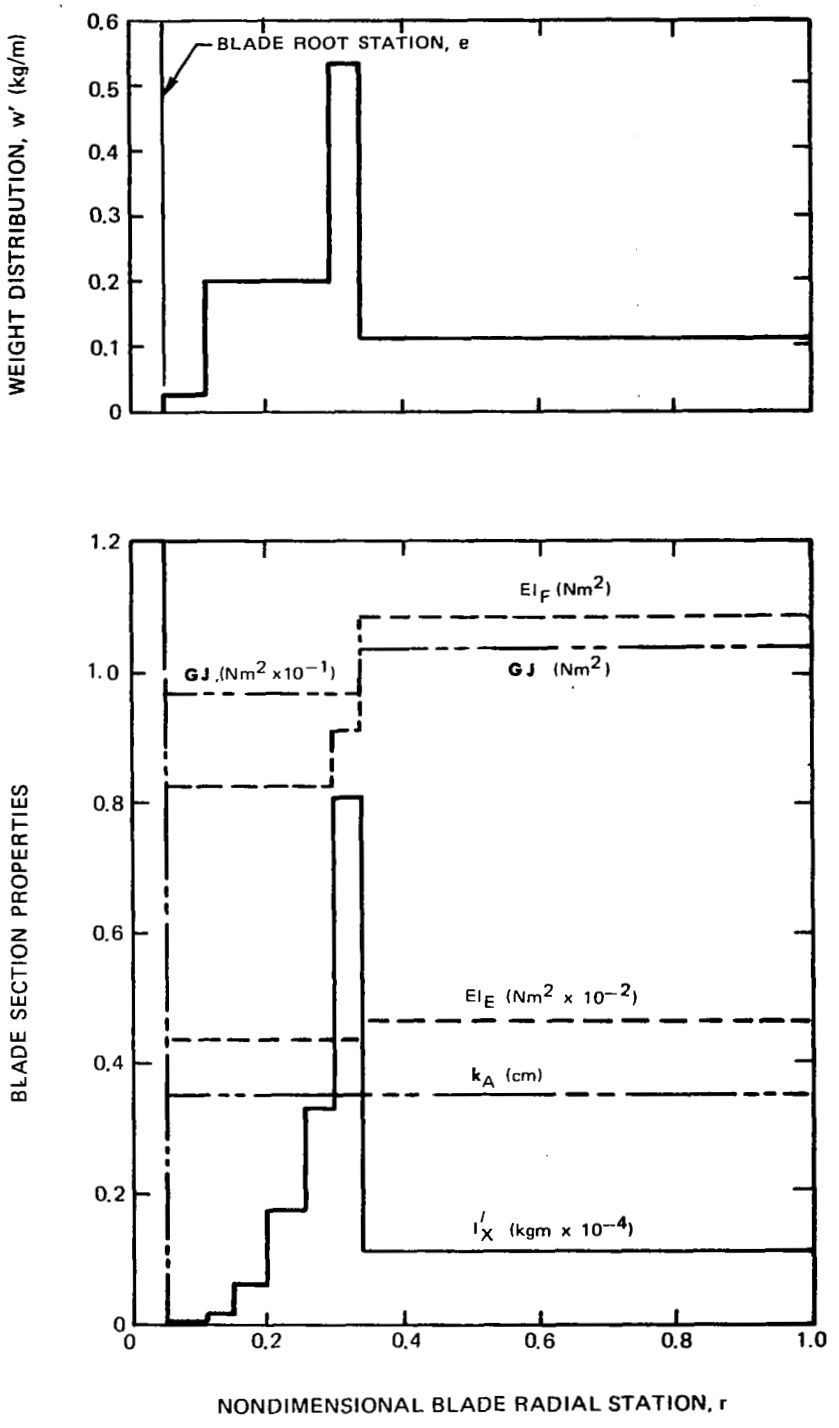

Figure 11. -Idealized Section Property Distributions for Model Blade with Pinned-Pinned Torque Tube.

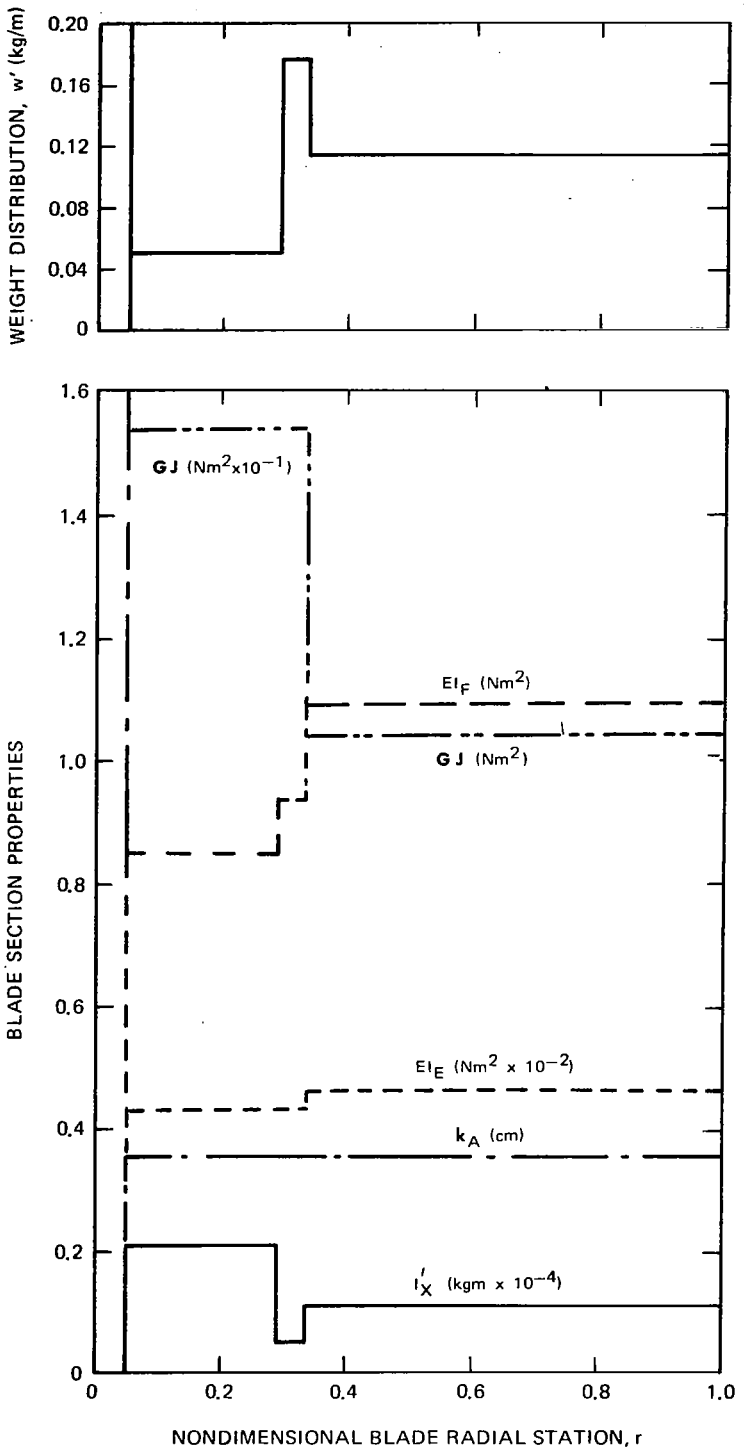

Figure 12. -Idealized Section Property Distributions for Model Blade with Cantilevered Torque Tube.

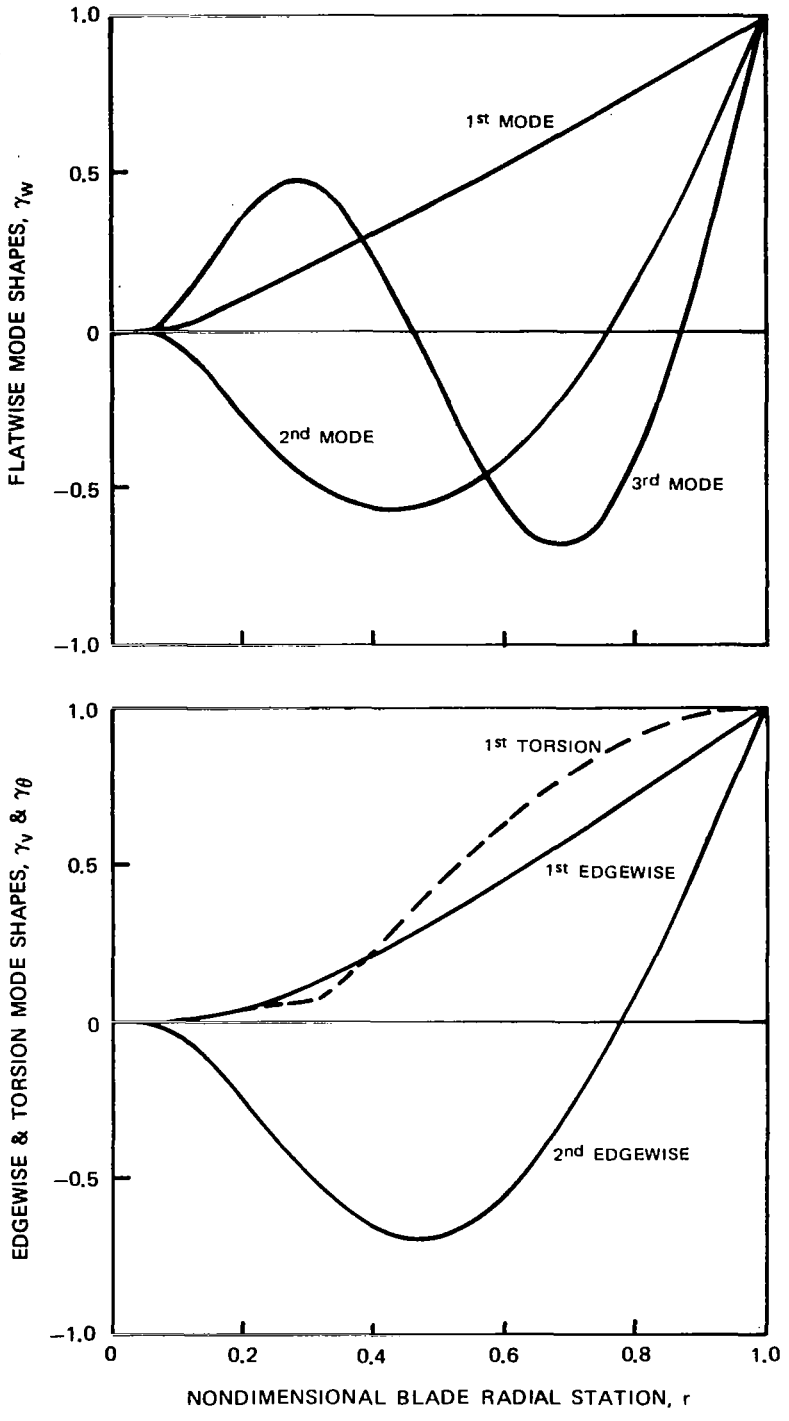

Figure 13. -Calculated Normal Mode Shapes, Pinned-Pinned Torque Tube, $\Omega R = 99$ m/sec.

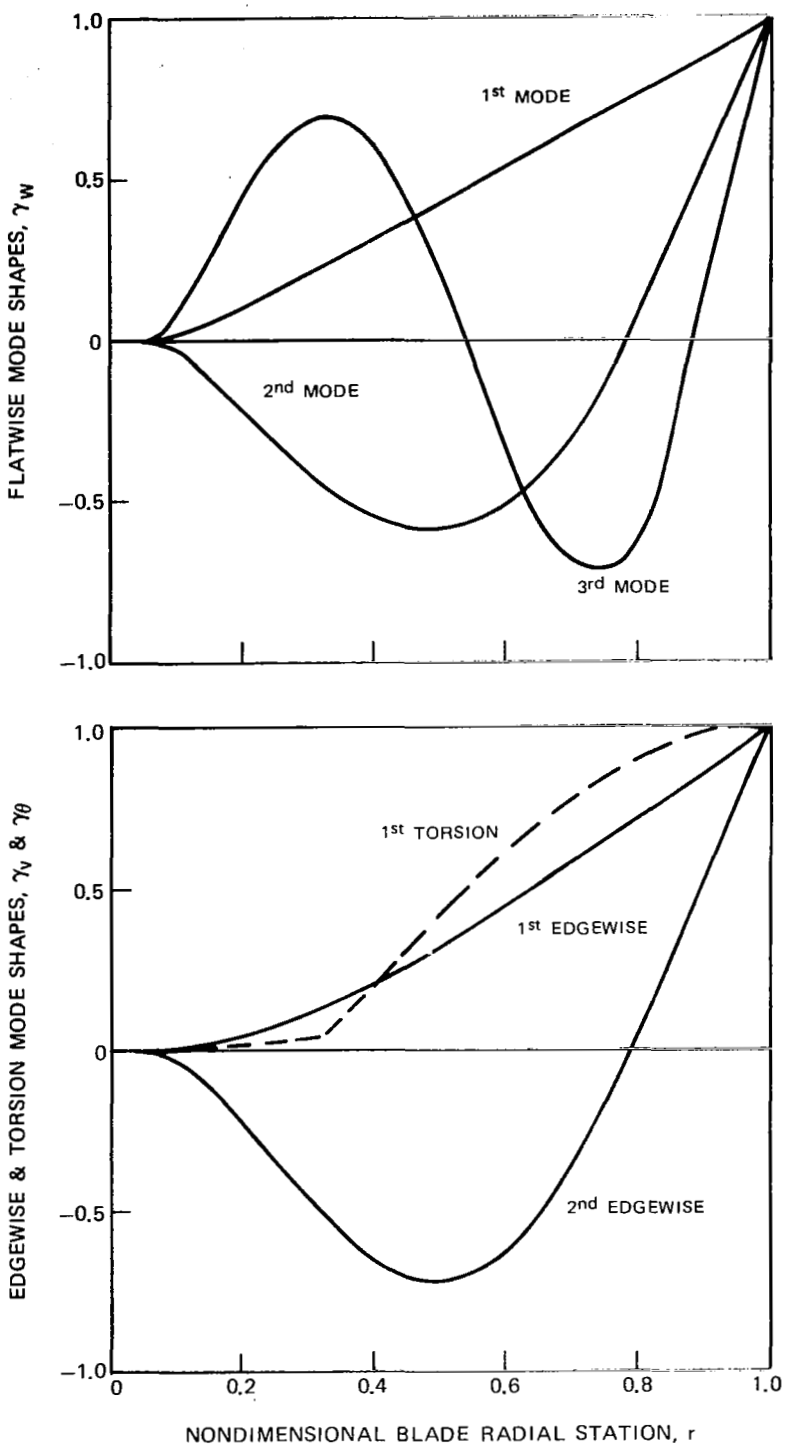

Figure 14. - Calculated Normal Mode Shapes, Cantilevered Torque Tube, $\Omega R = 99$ m/sec.

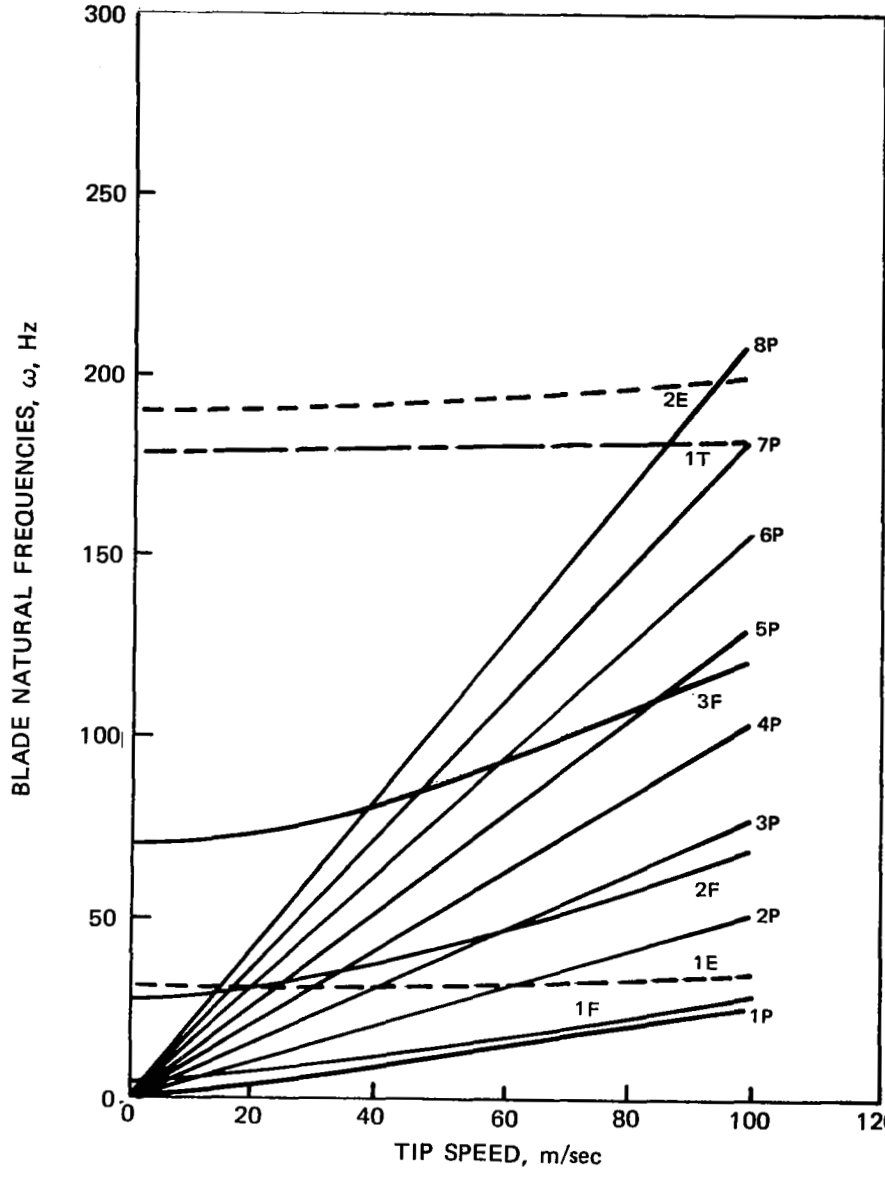

Figure 15. - Variation of Blade Natural Frequencies with Tip Speed, Pinned-Pinned Torque Tube.

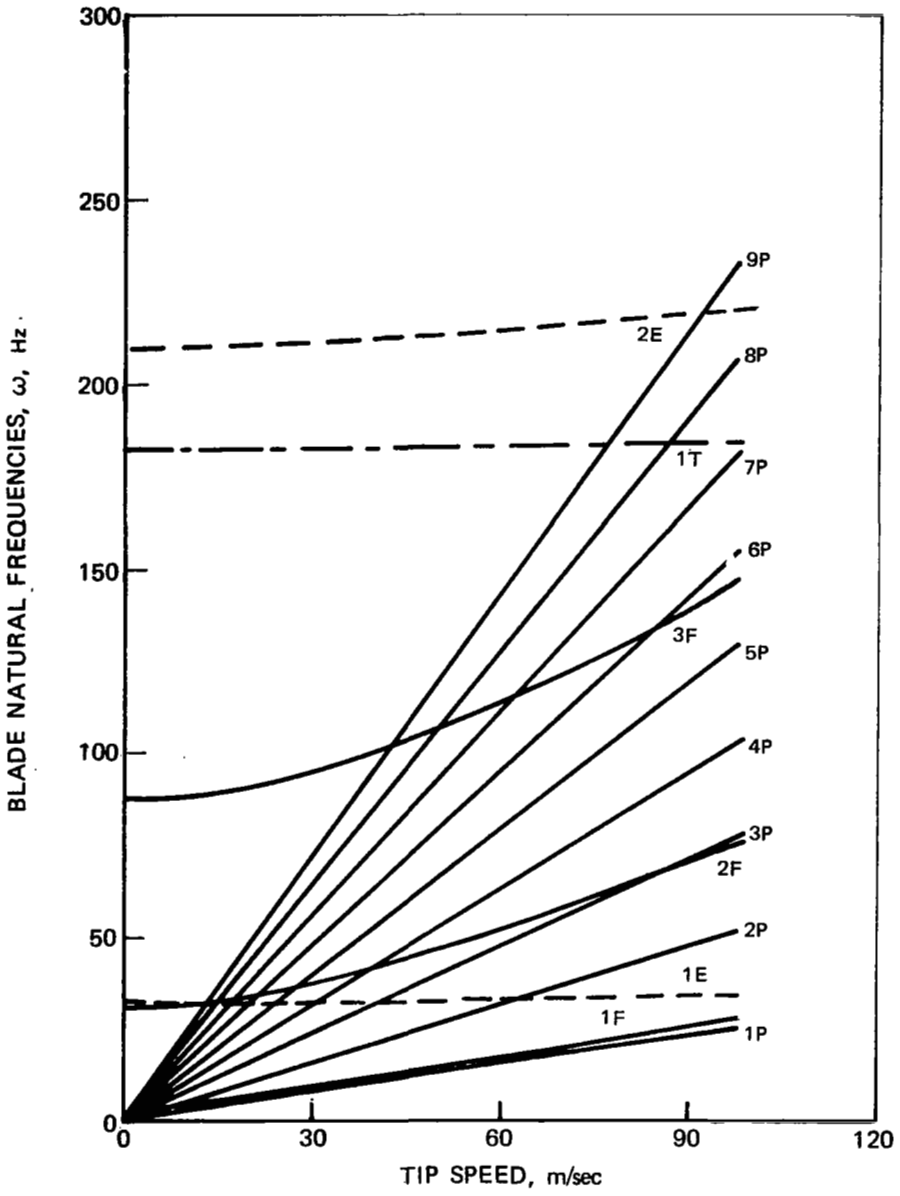

Figure 16. - Variation of Blade Natural Frequencies with Tip Speed, Cantilevered Torque Tube.

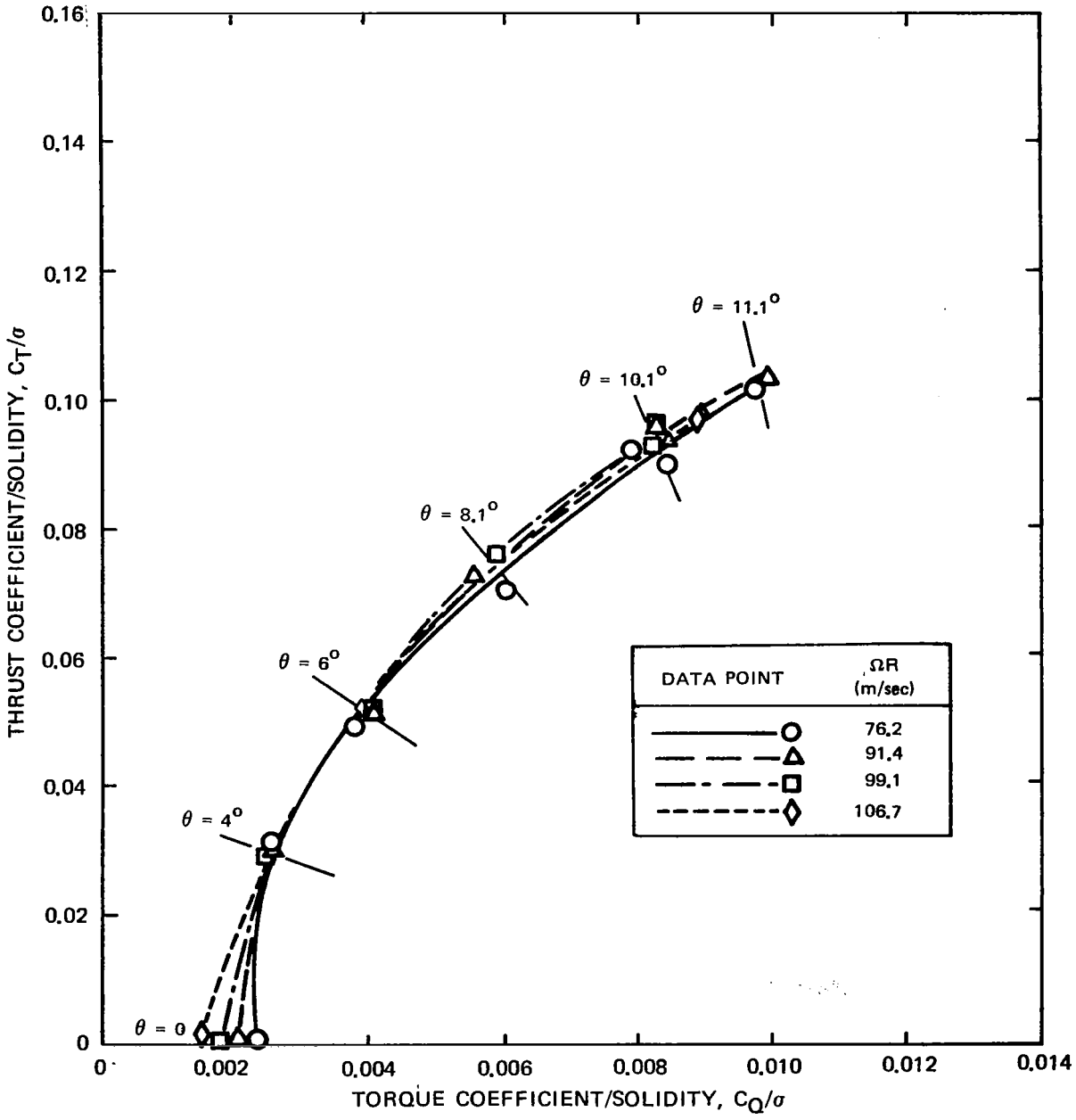

Figure 17. - Model Rotor Hover Performance, Pinned-Pinned Torque Tube, σ = 0.0408.

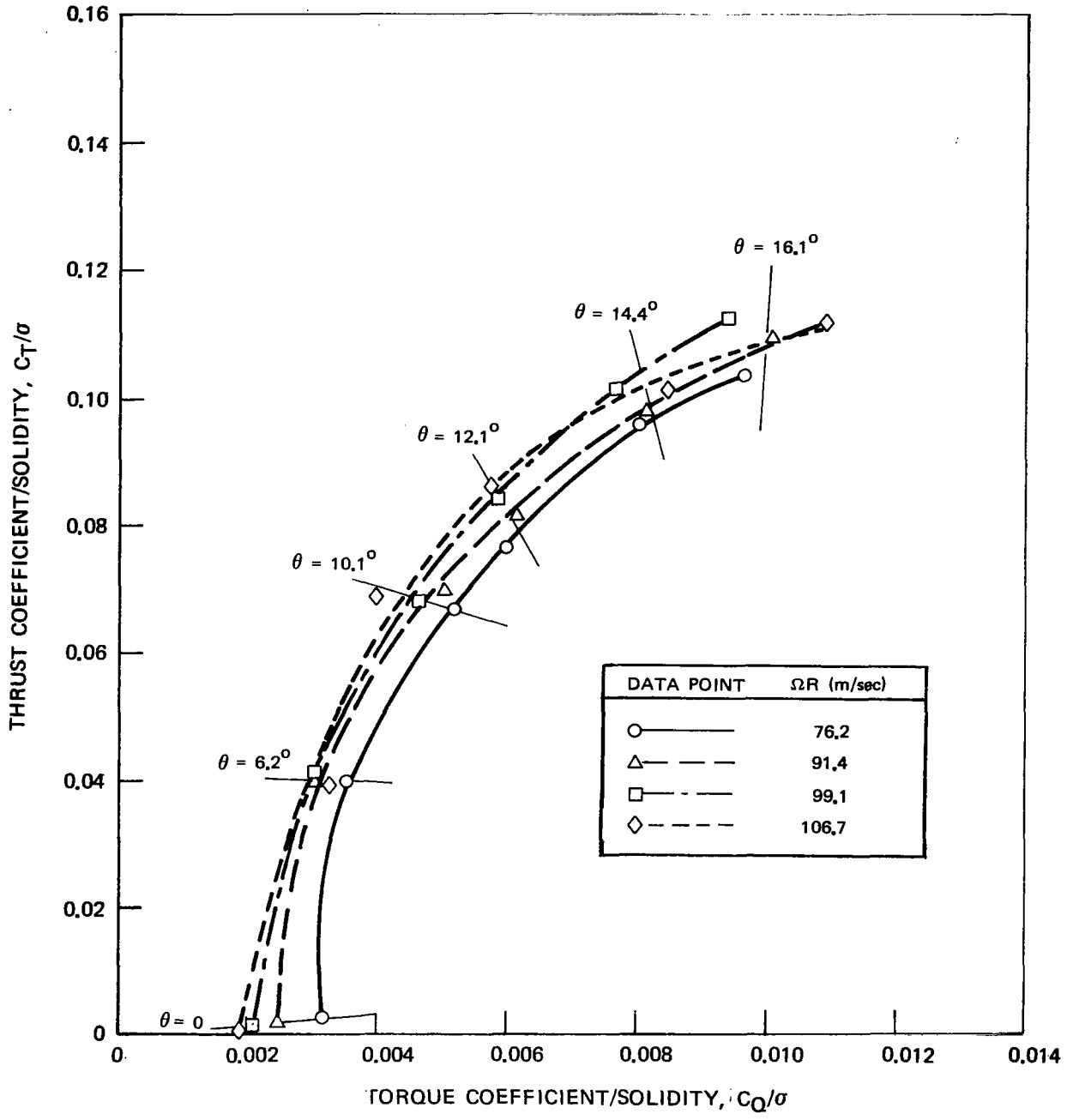

Figure 18. - Model Rotor Hover Performance, Cantilevered Torque Tube, Trailing Edge Push-Rod Attachment at 0.06 R, σ = 0.0408.

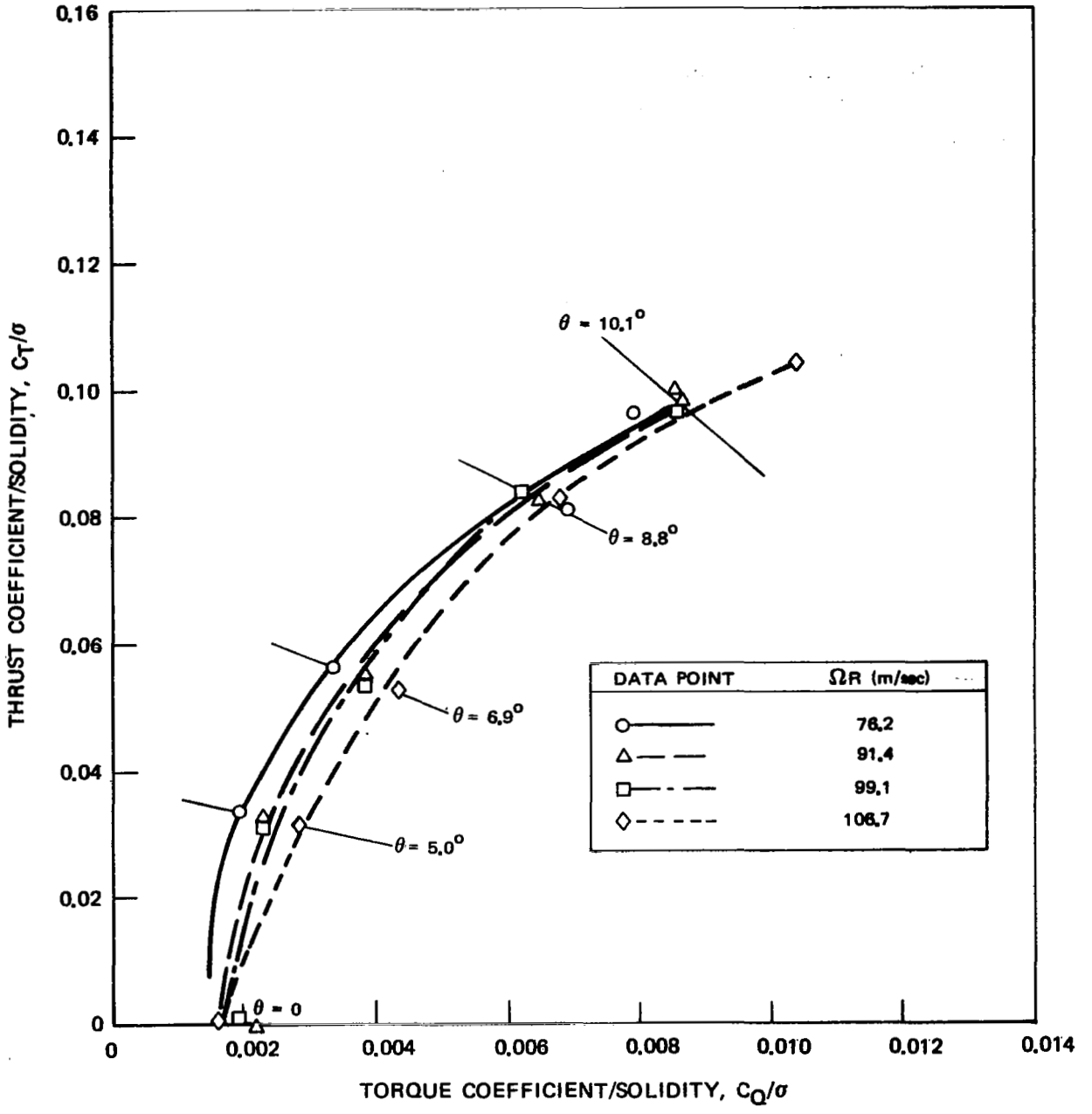

Figure 19. - Model Rotor Hover Performance, Cantilevered Torque Tube, Leading Edge Push-Rod Attachment at 0.07 R, σ = 0.0408.

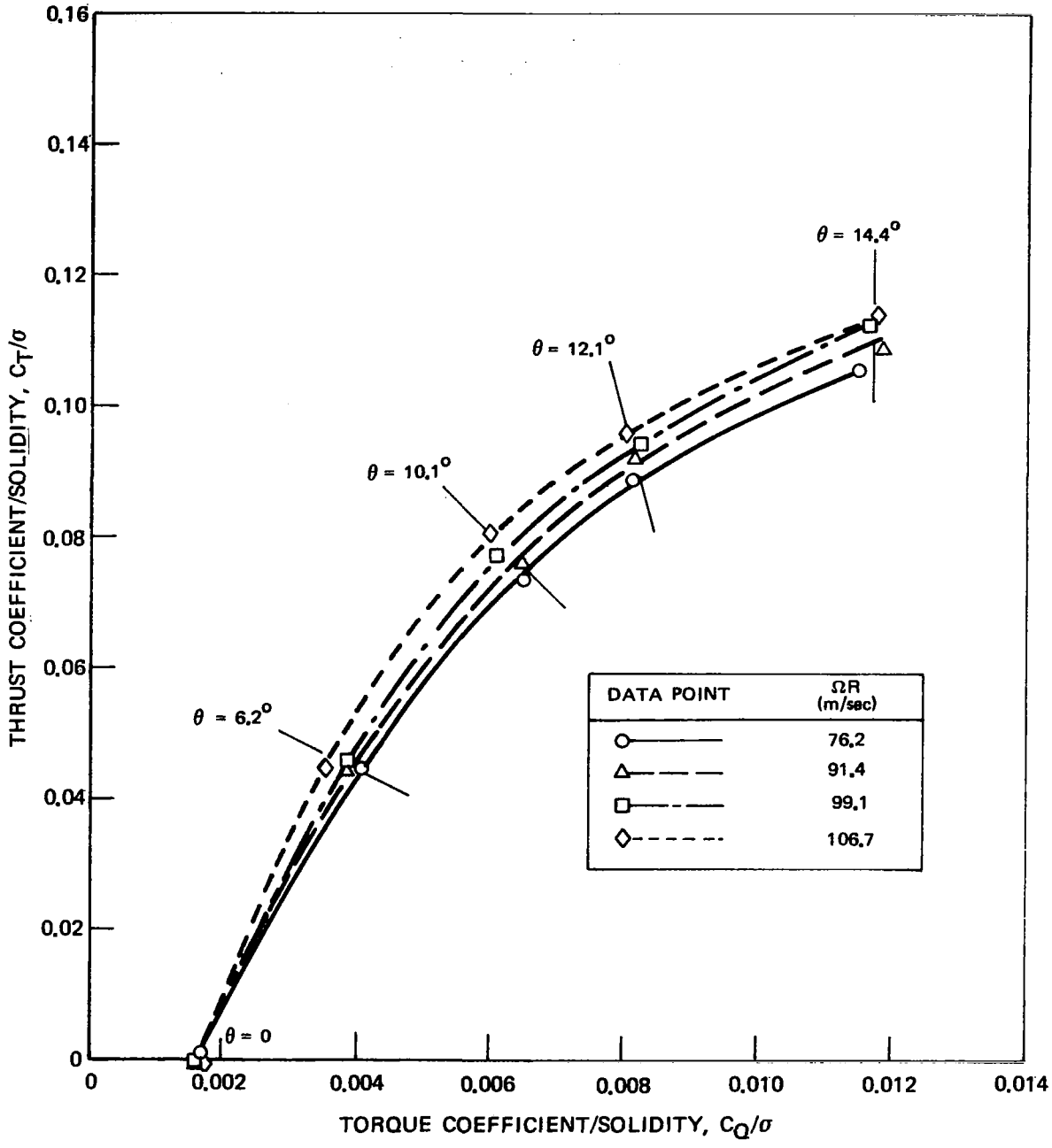

Figure 20. - Model Rotor Hover Performance, Cantilevered Torque Tube, Trailing Edge Push-Rod Attachment at 0.08 R, σ = 0.0408.

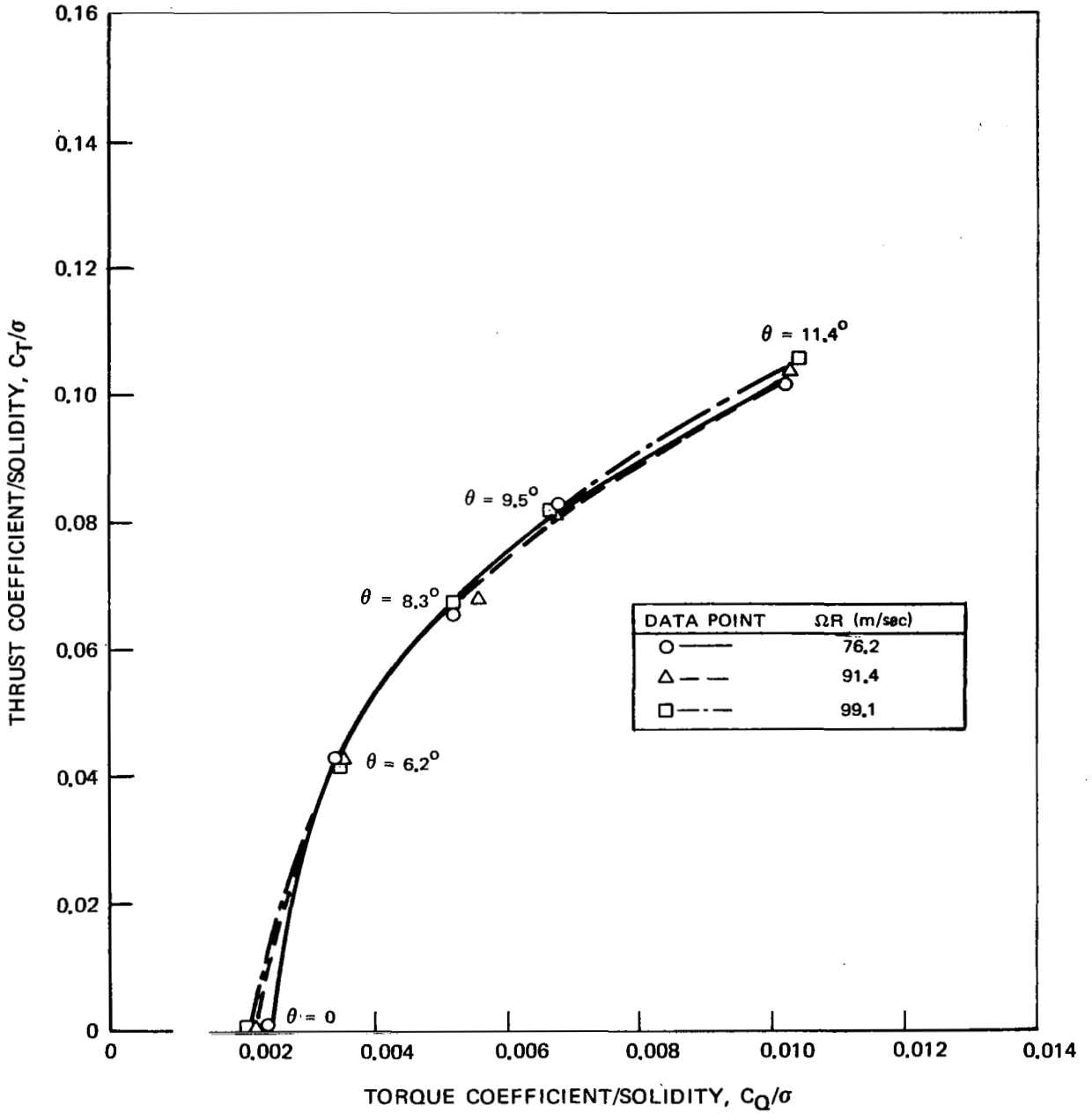

Figure 21. - Model Rotor Hover Performance, Cantilevered Torque Tube, Leading Edge Push-Rod Attachment at 0.09 R, σ = 0.0408.

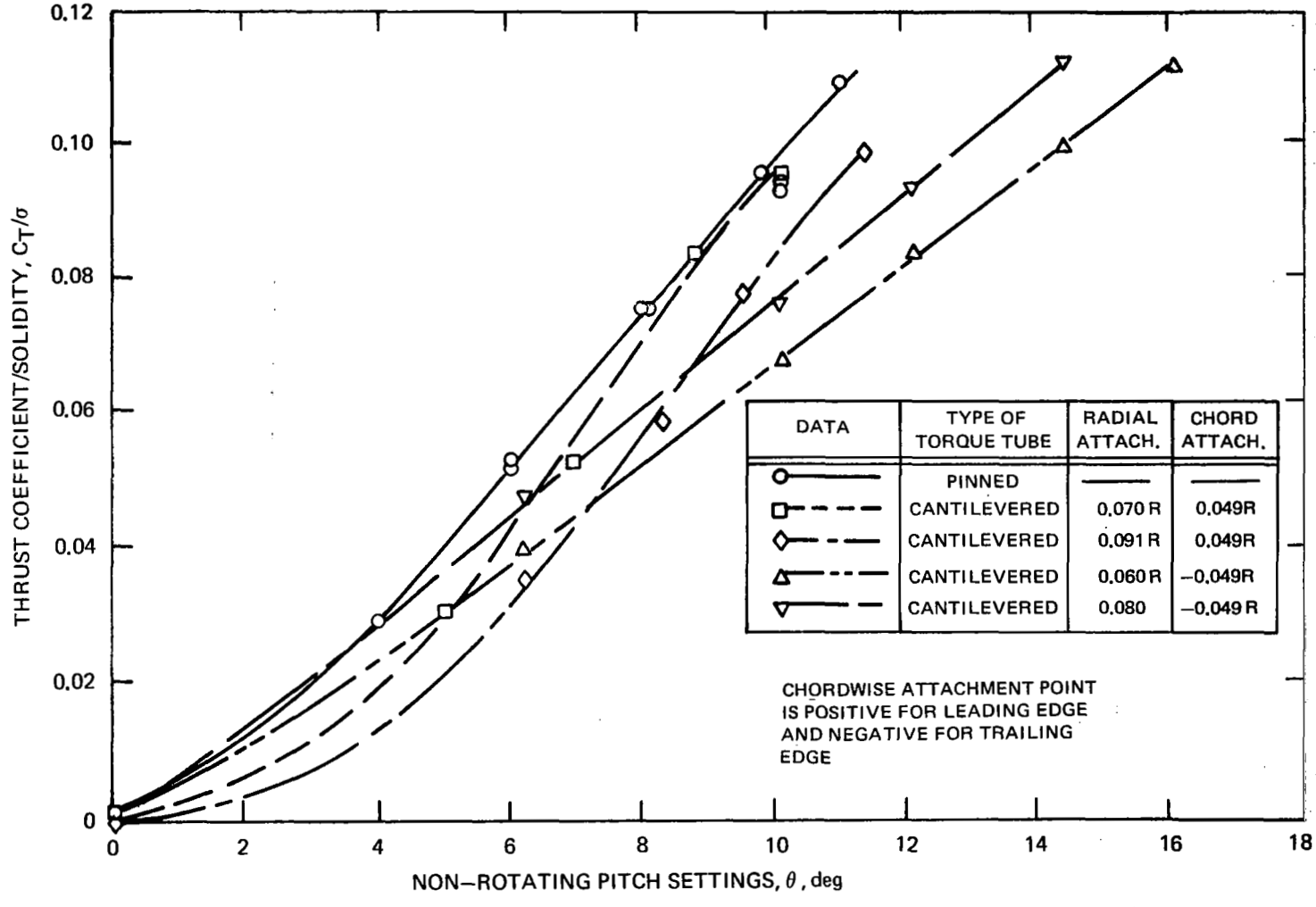

Figure 22. -Effect of Blade Pitch Setting and Push Rod Attachment Point Location on Model Rotor Hovering Thrust, ΩR = 99 m/sec, σ = 0.0408.

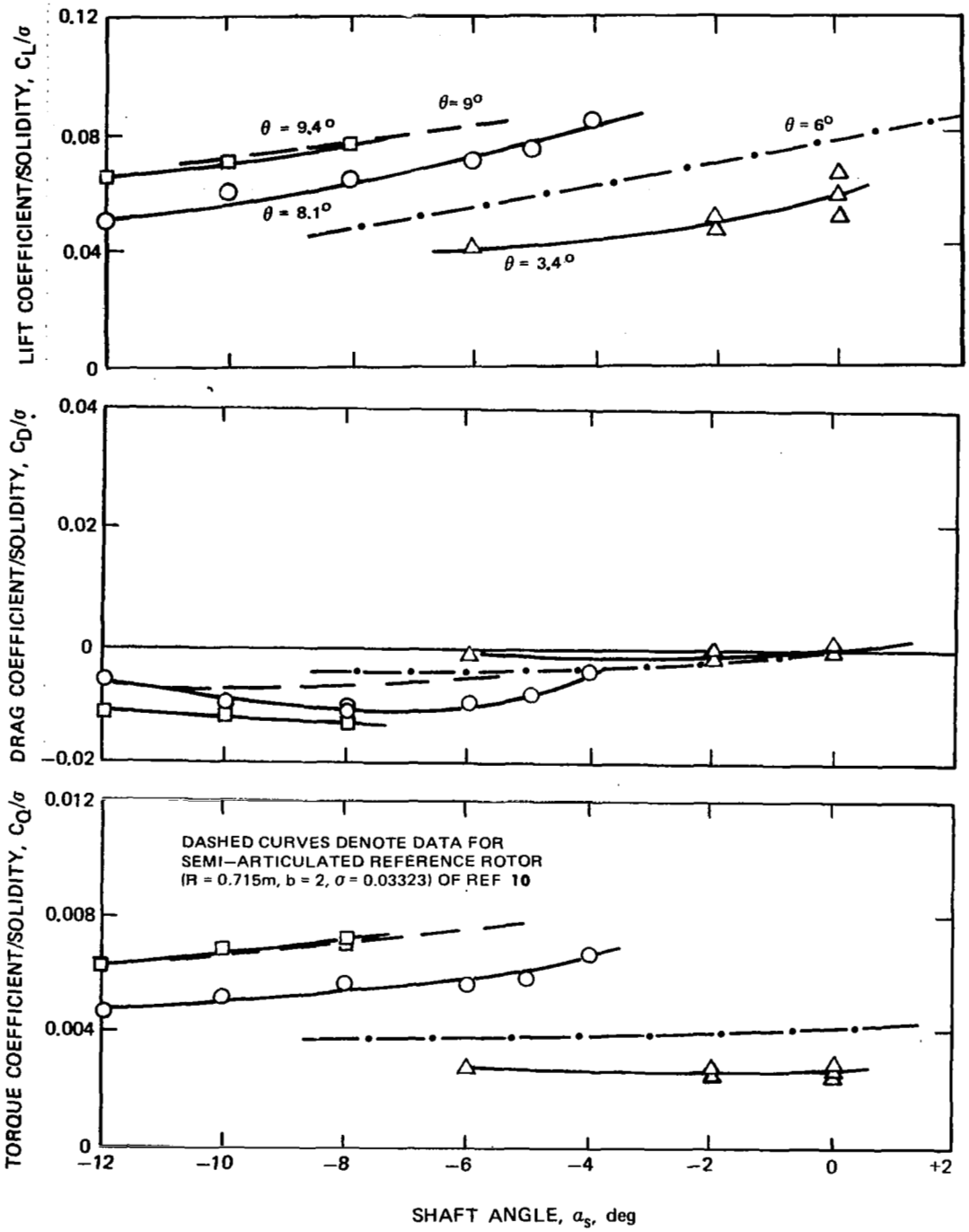

Figure 23. -Effects of Input Collective Angle and Shaft Angle Variations on Forward Flight Performance of Model Rotor with Pinned-Pinned Torque Tube, $\mu = 0.25$, $\sigma = 0.0817$.

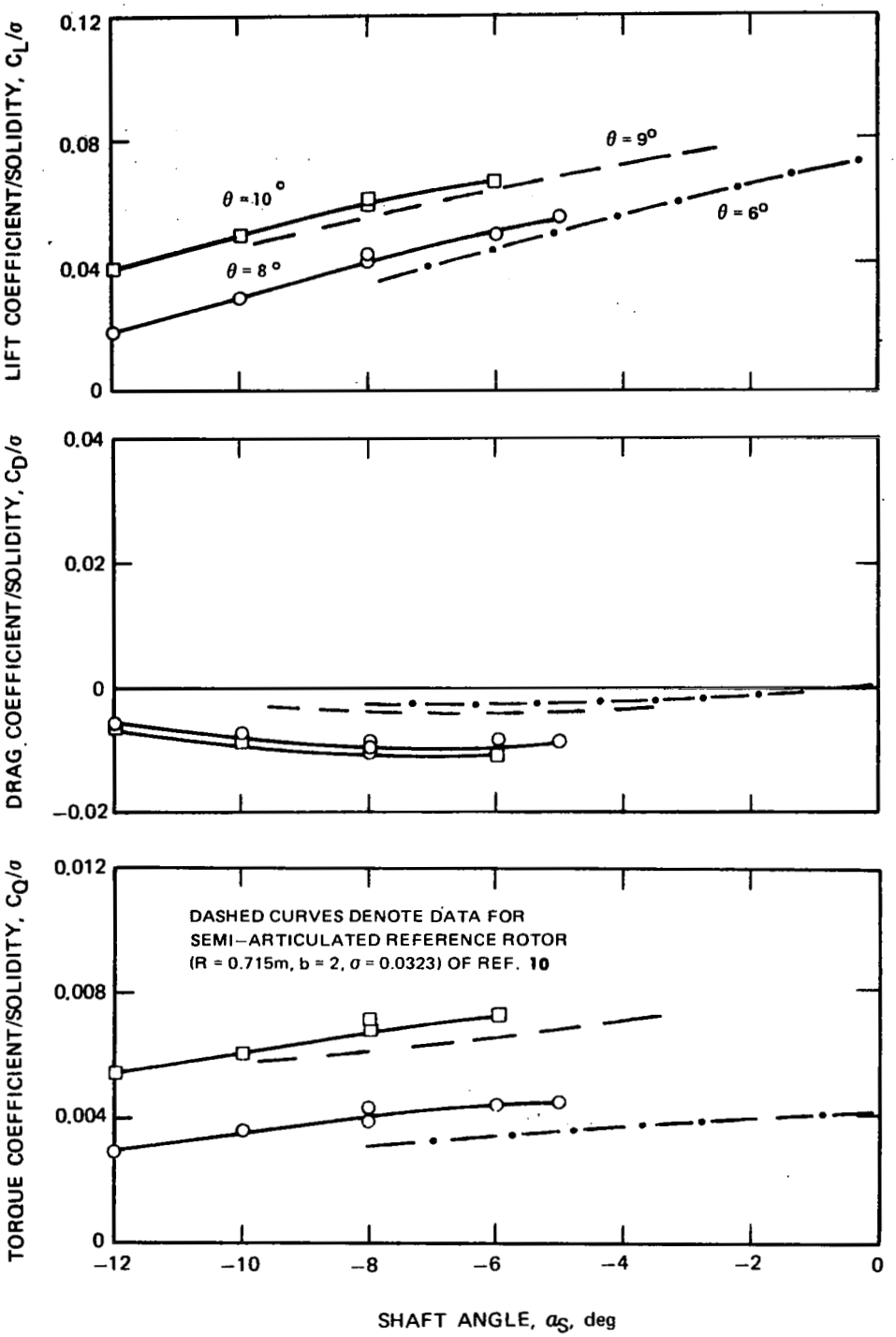

Figure 24. -Effects of Input Collective Angle and Shaft Angle Variations on Forward Flight Performance of Model Rotor with Pinned-Pinned Torque Tube, $\mu = 0.35$, $\sigma = 0.0817$.

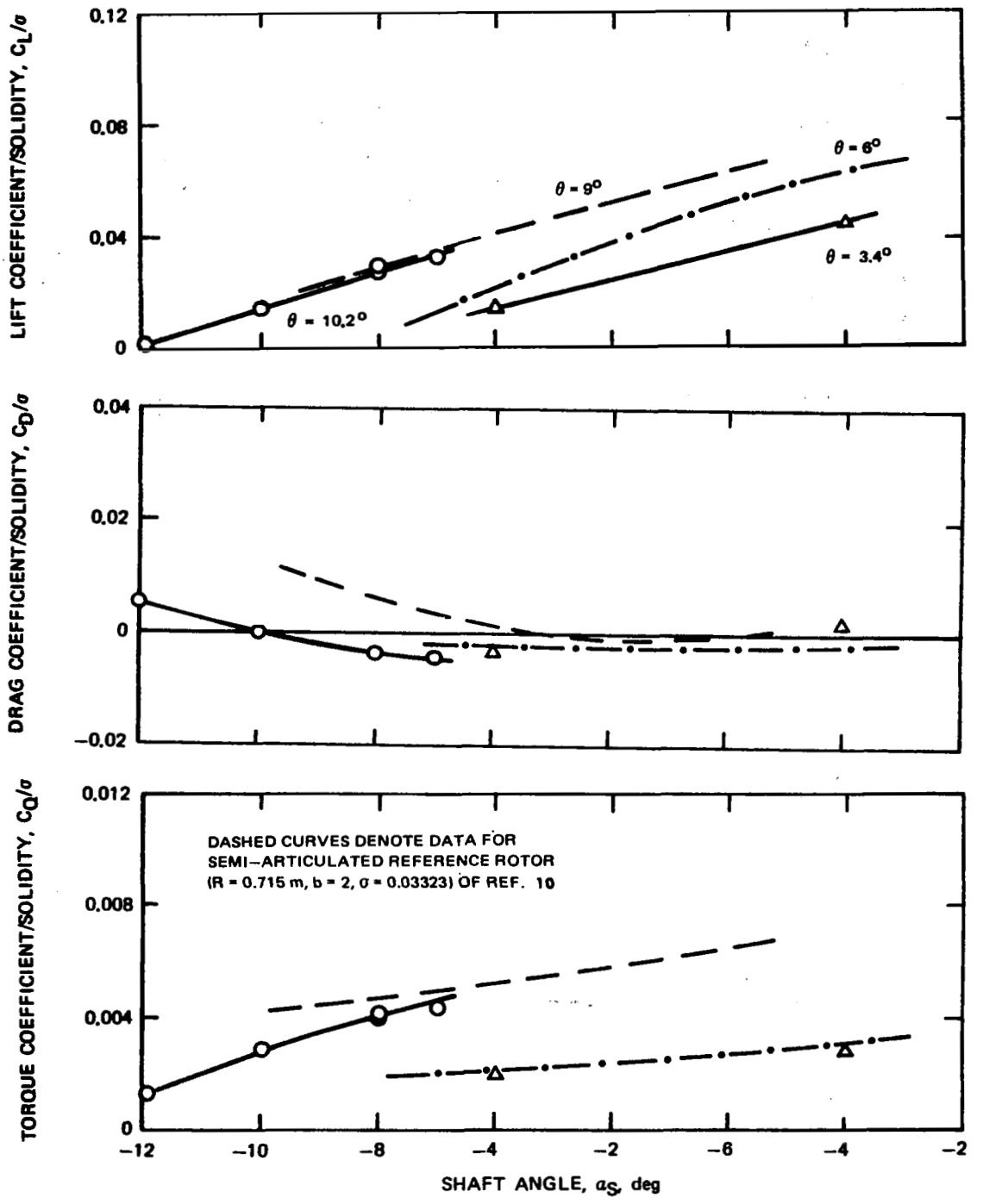

Figure 25. -Effects of Input Collective Angle and Shaft Angle Variations on Forward Flight Performance of Model Rotor with Pinned-Pinned Torque Tube, μ = 0.47, σ = 0.0817.

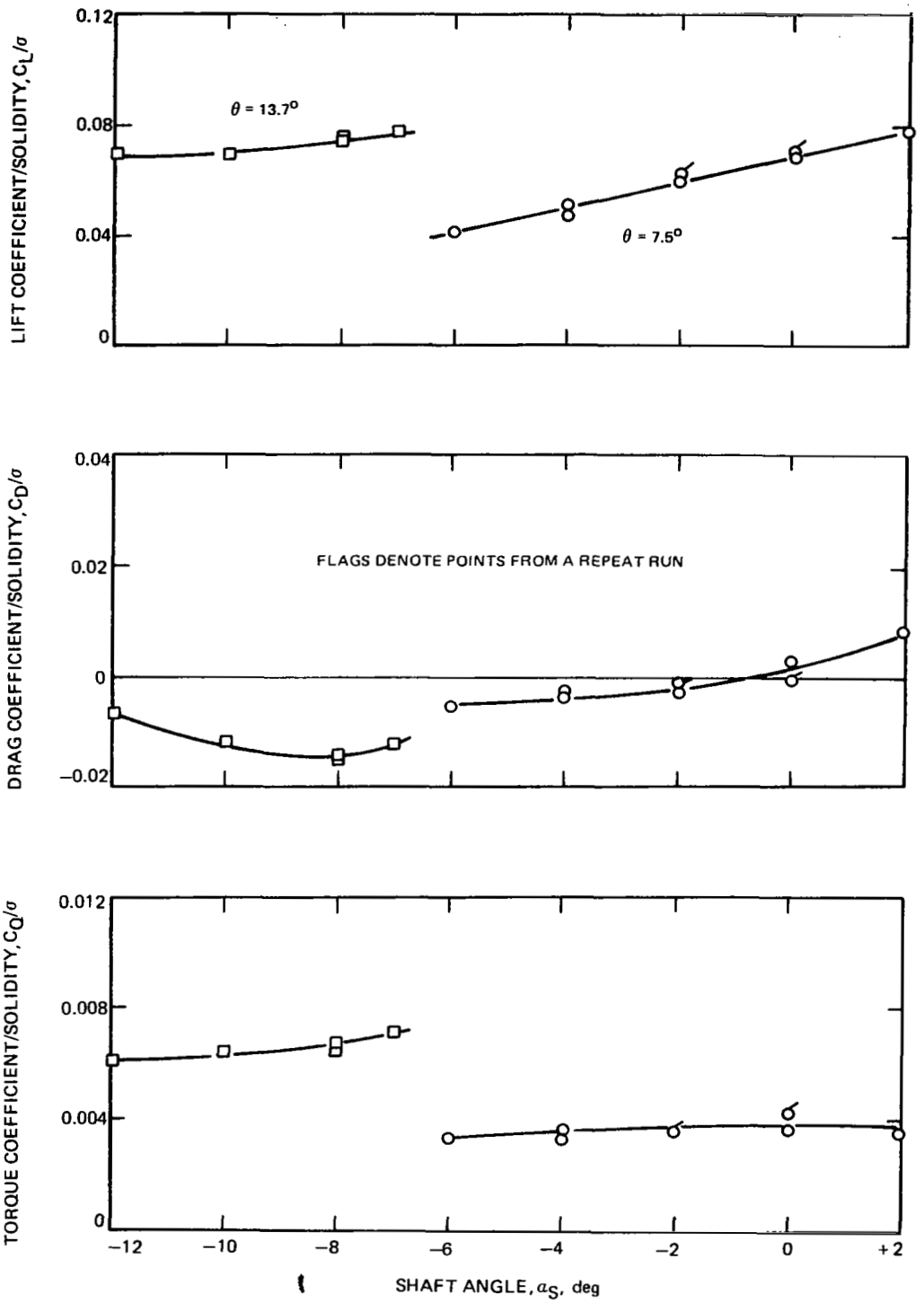

Figure 26. -Effects of Input Collective Angle and Shaft Angle Variations on Forward Flight Performance of Model Rotor with Cantilevered Torque Tube, Trailing Edge Push-Rod Attachment @ 0.06 R, μ = 0.25, σ = 0.0408.

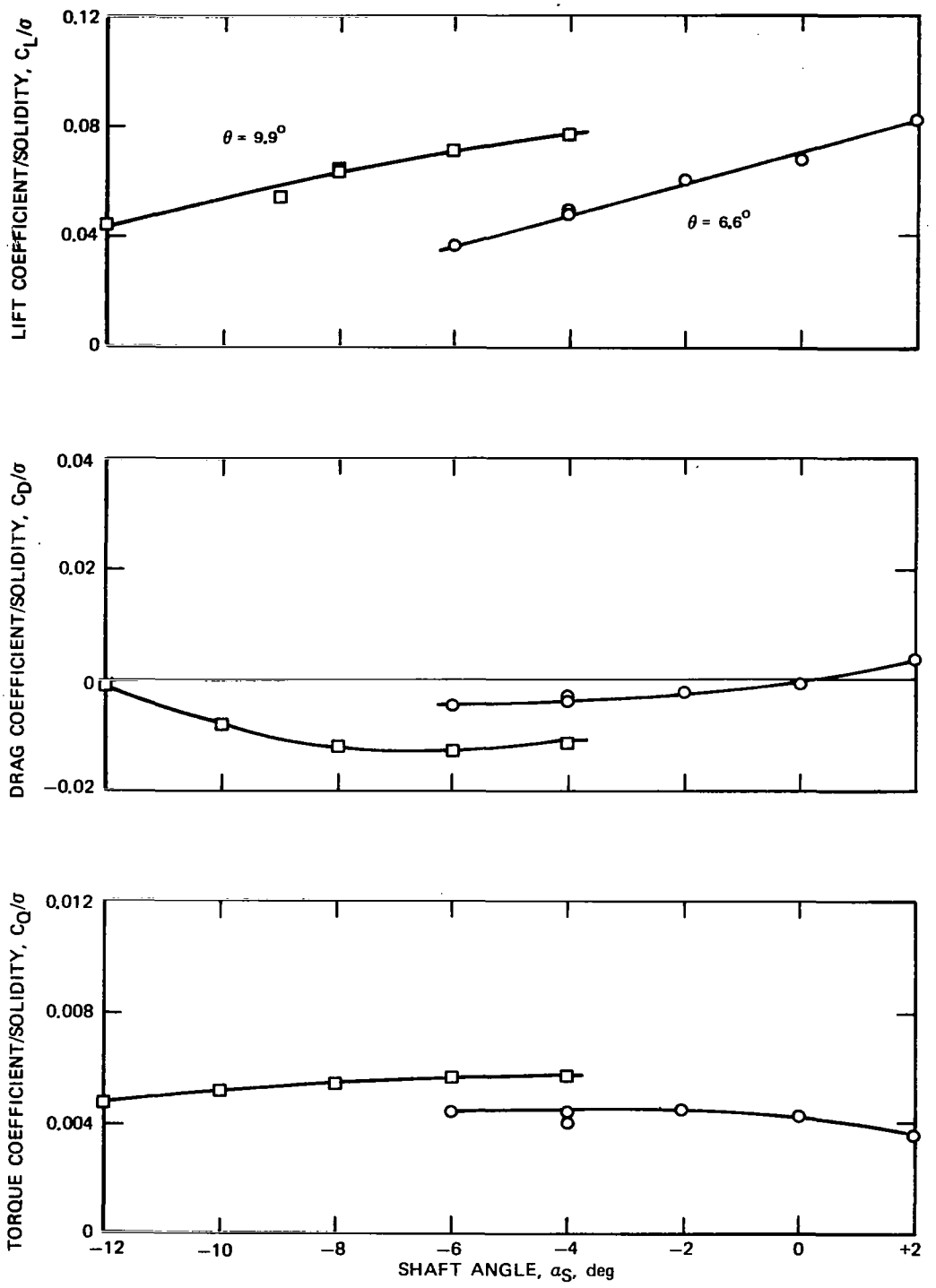

Figure 27.-Effects of Input Collective Angle and Shaft Angle Variations on Forward Flight Performance of Model Rotor with Cantilevered Torque Tube, Leading Edge Push-Rod Attachment @ 0.07 R, $\mu = 0.25$, $\sigma = 0.0408$.

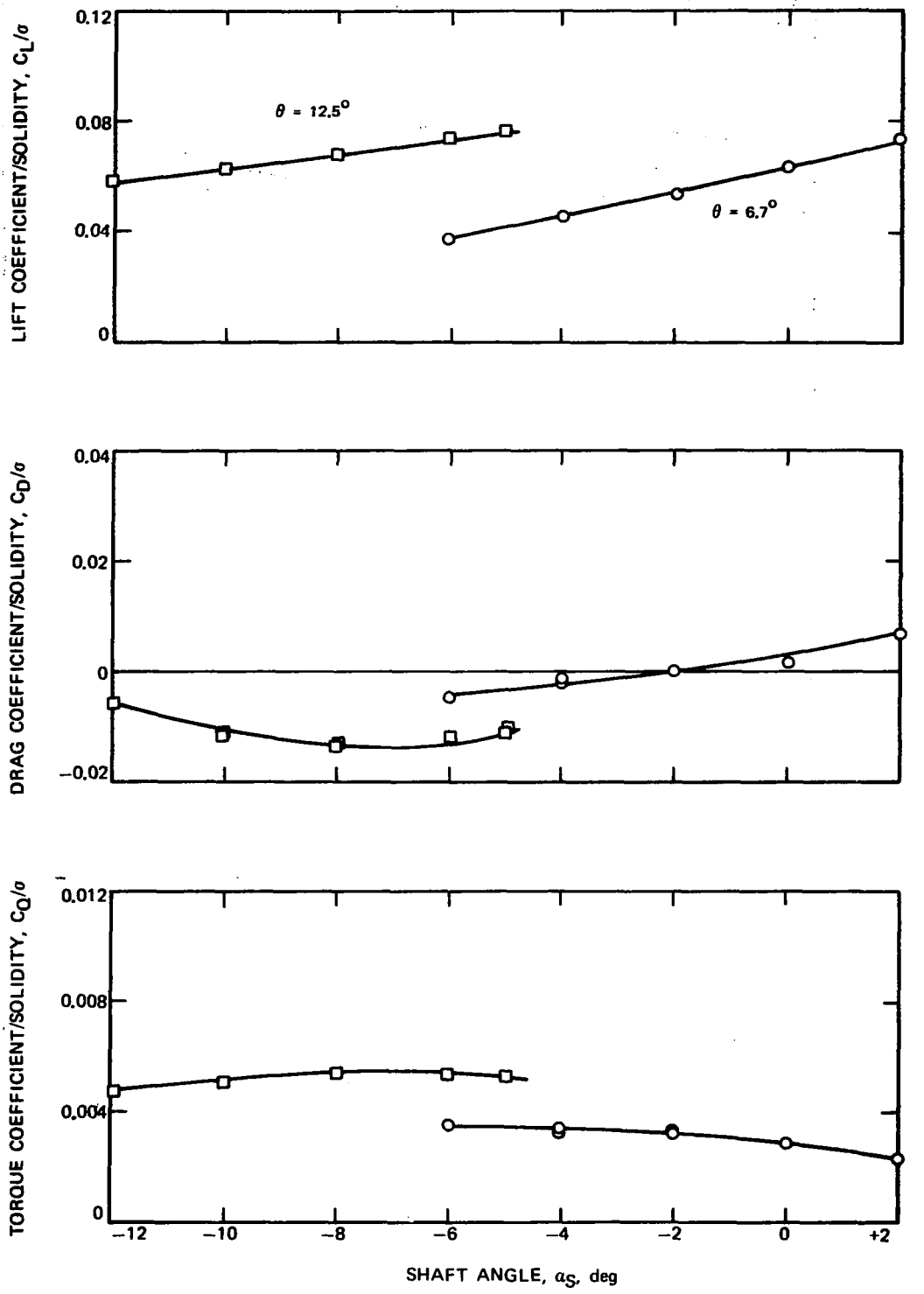

Figure 28.-Effects of Input Collective Angle and Shaft Angle Variations on Forward Flight Performance of Model Rotor with Cantilevered Torque Tube, Trailing Edge Push-Rod Attachment @ 0.08 R, $\mu = 0.25$, $\sigma = 0.0408$.

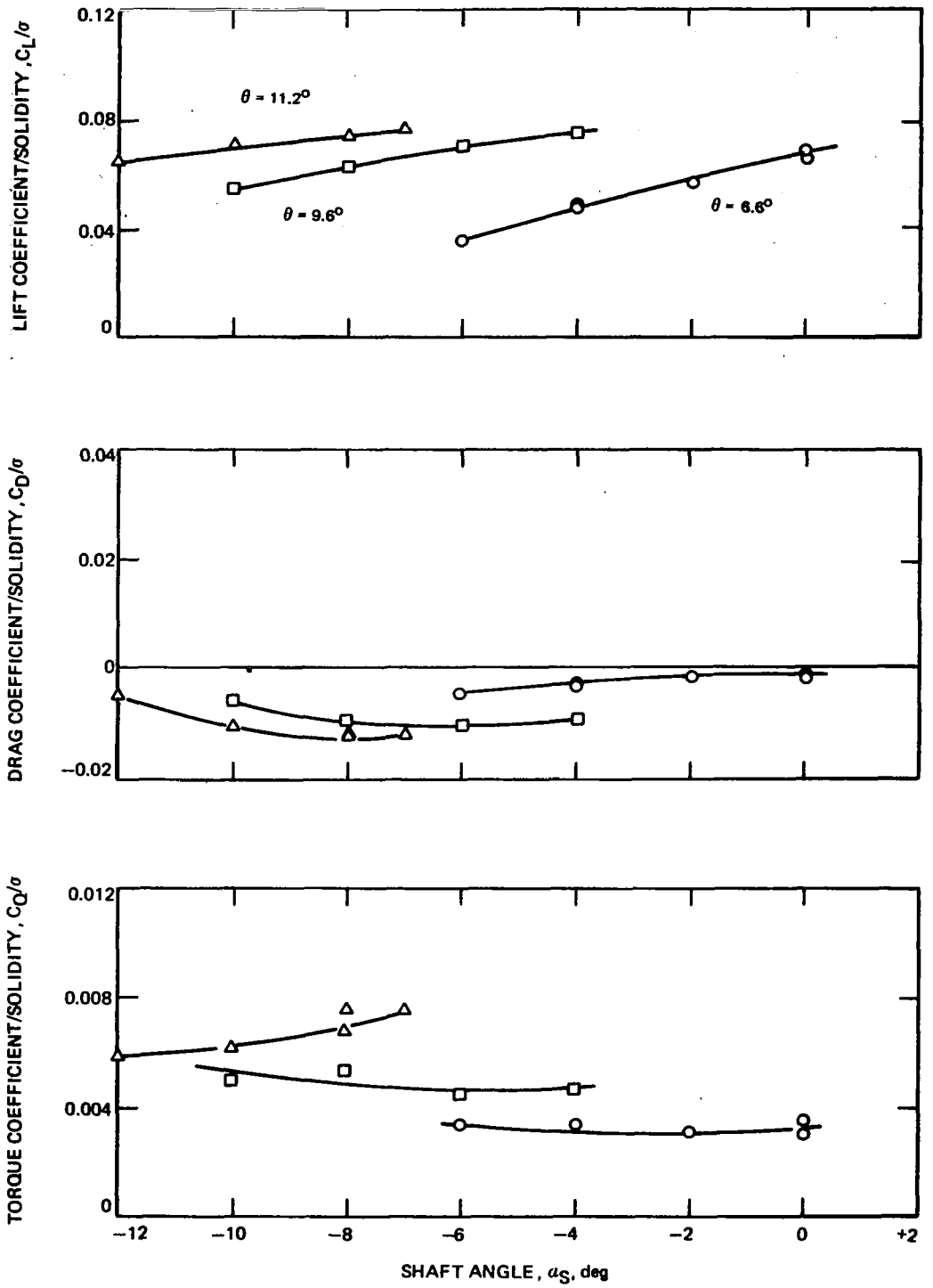

Figure 29. -Effects of Input Collective Angle and Shaft Angle Variations on Forward Flight Performance of Model Rotor with Cantilevered Torque Tube, Leading Edge Push-Rod Attachment @ 0.09 R, μ = 0.25, σ = 0.0408.

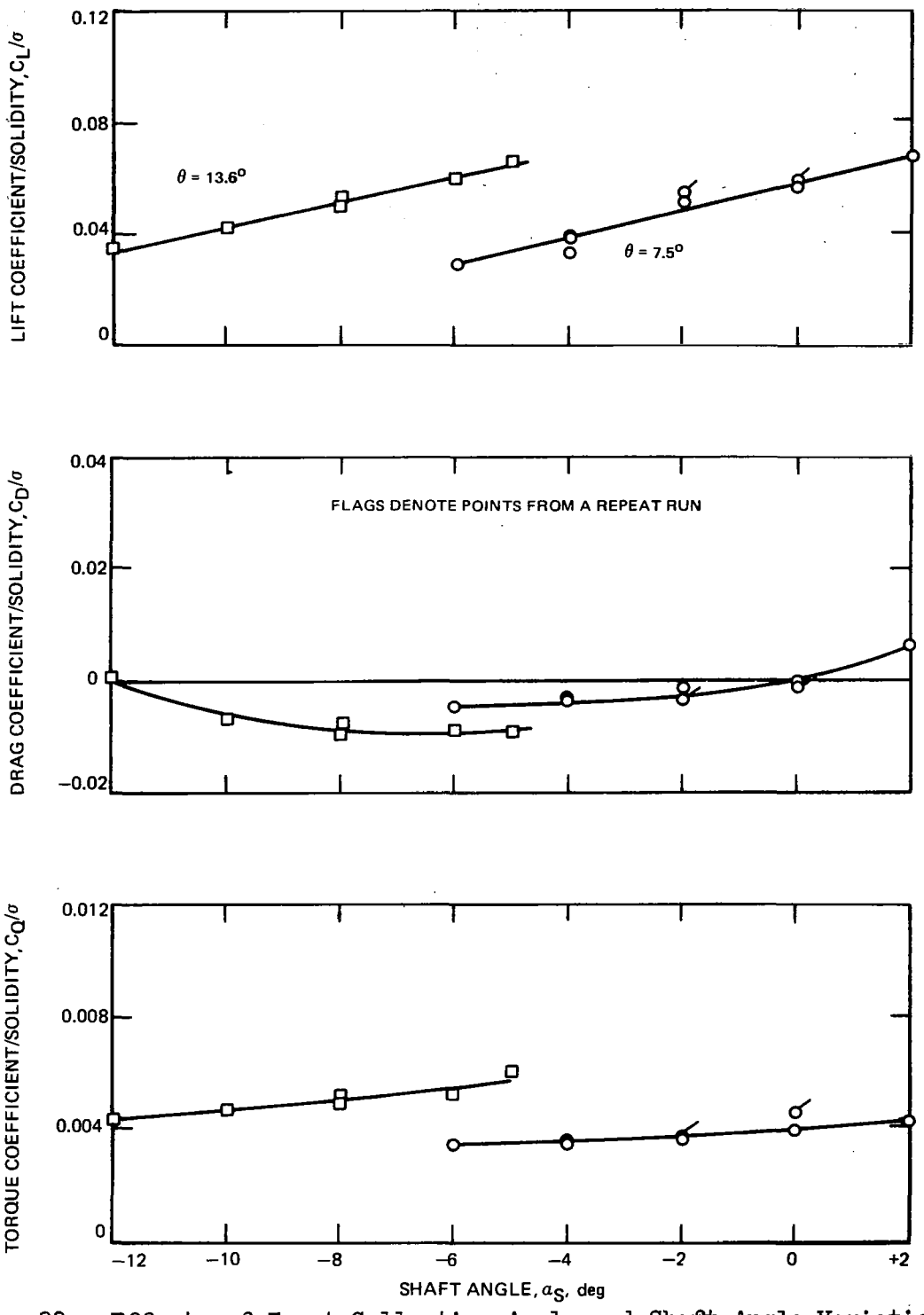

Figure 30. -Effects of Input Collective Angle and Shaft Angle Variations on Forward Flight Performance of Model Rotor with Cantilevered Torque Tube, Trailing Edge Push-Rod Attachment @ 0.06 R, μ = 0.35, σ = 0.0408.

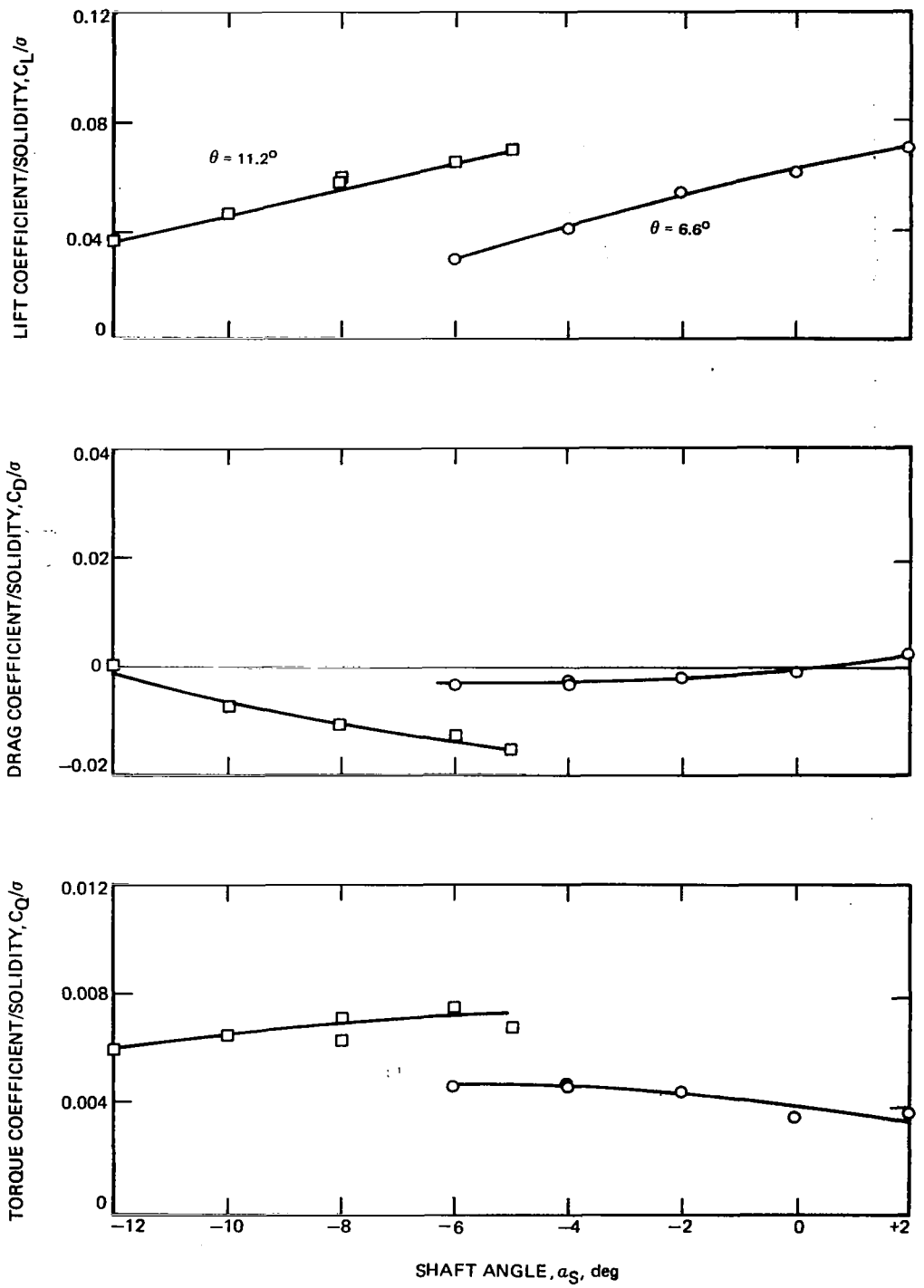

Figure 31. - Effects of Input Collective Angle and Shaft Angle Variations on Forward Flight Performance of Model Rotor with Cantilevered Torque Tube, Leading Edge Push-Rod Attachment @ 0.09 R, μ = 0.35, σ = 0.0408.

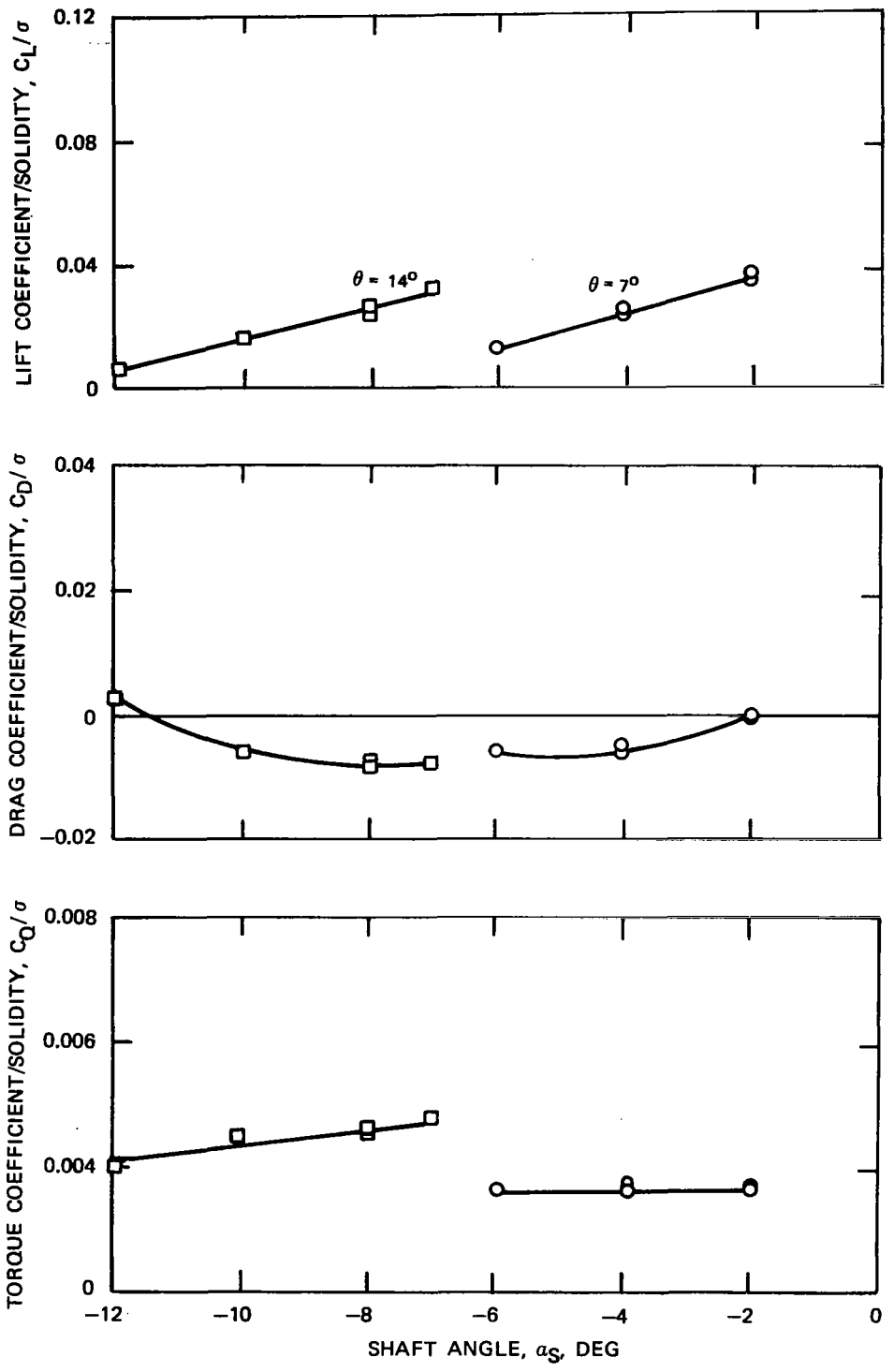

Figure 32. - Effects of Input Collective Angle and Shaft Angle Variations on Forward Flight Performance of Model Rotor with Cantilevered Torque Tube, Trailing Edge Push-Rod Attachment @ 0.06 R, μ = 0.47, σ = 0.0408.

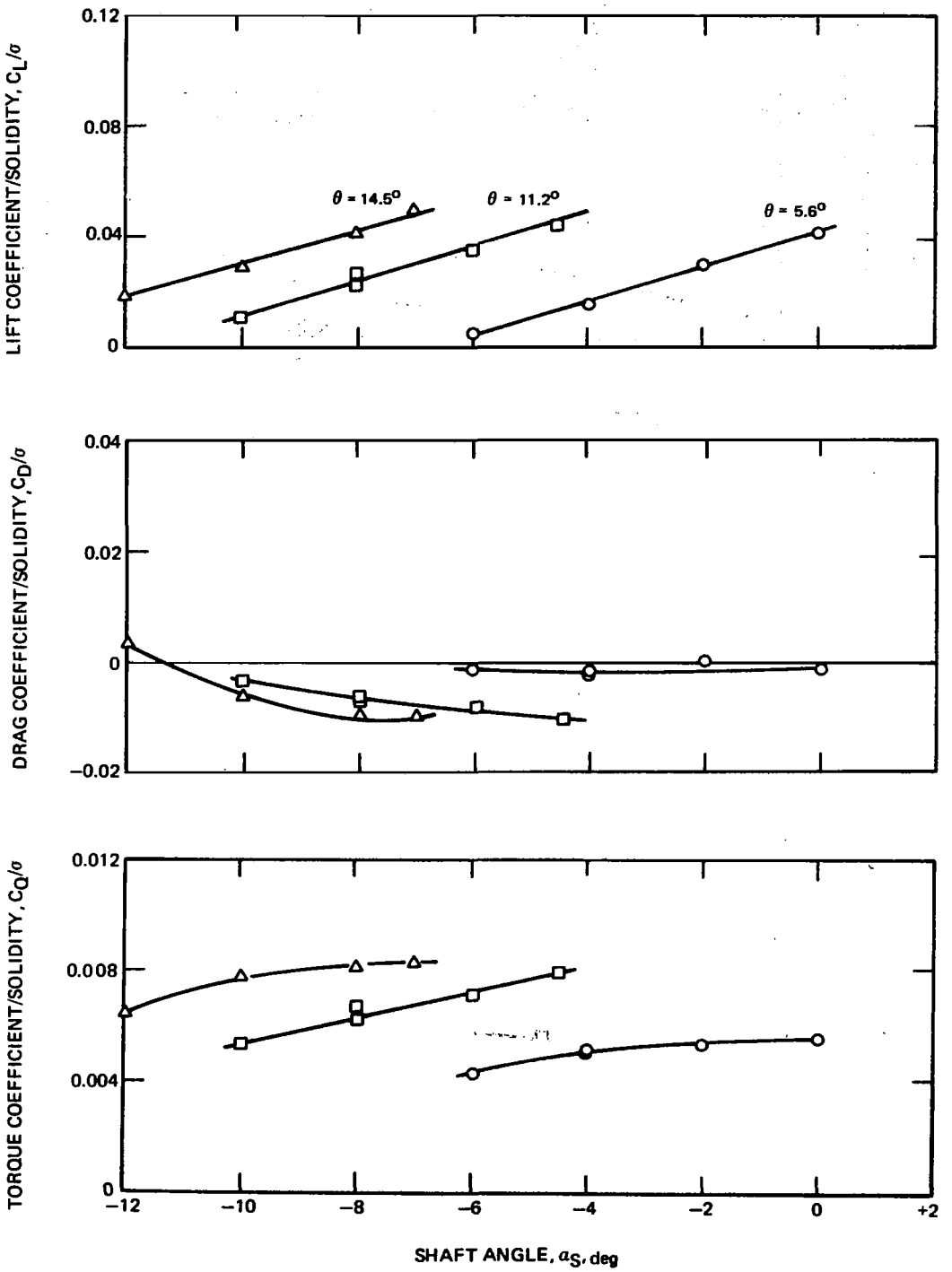

Figure 33.-Effects of Input Collective Angle and Shaft Angle Variations on Forward Flight Performance of Model Rotor with Cantilevered Torque Tube, Leading Edge Push-Rod Attachment @ 0.09 R, μ = 0.47, σ = 0.0408.

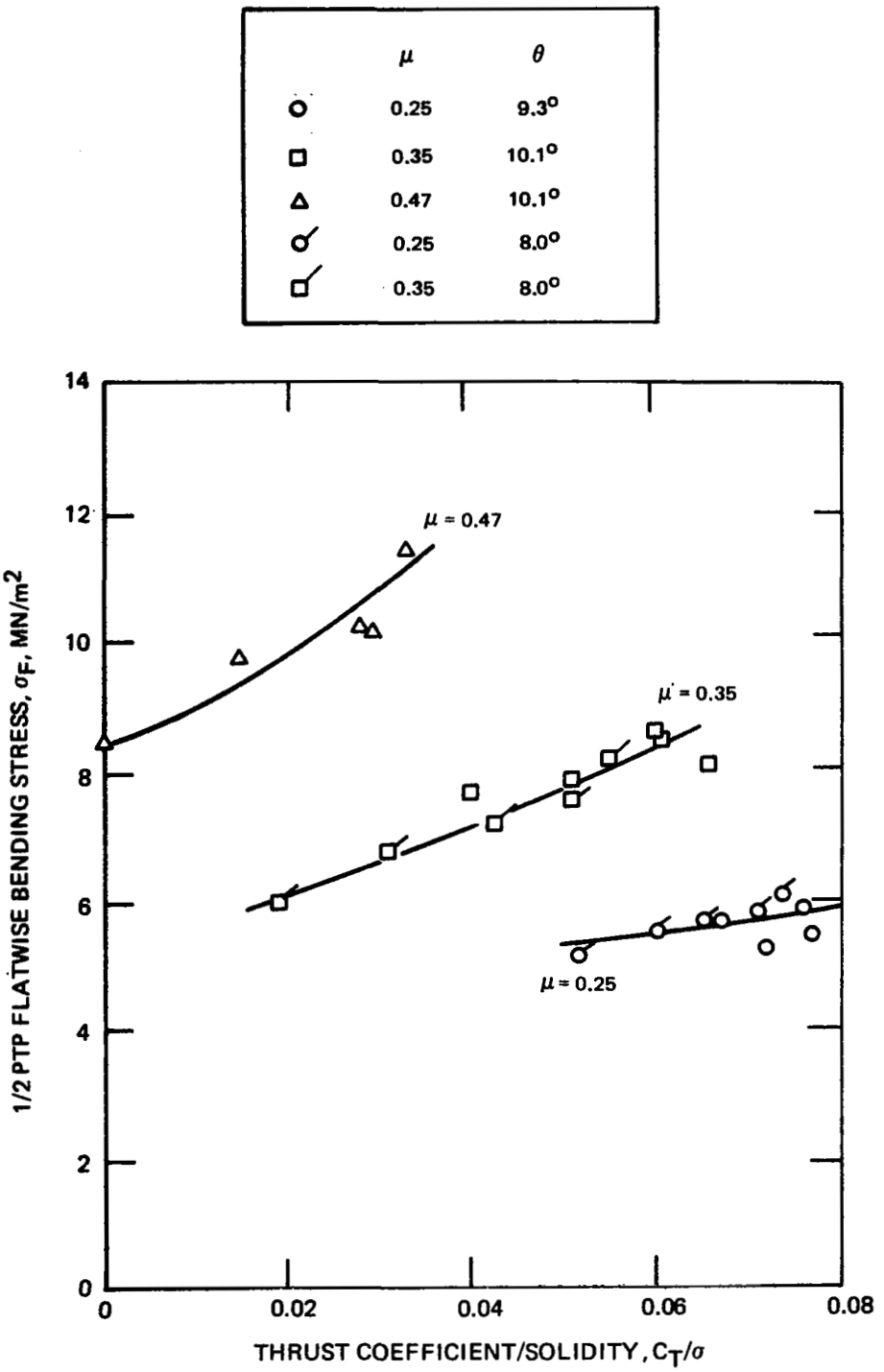

Figure 34. -Effects of Advance Ratio and Blade Loading on Vibratory Inboard Flatwise Stresses of Model Rotor with Pinned-Pinned Torque Tube, r = 0.06 R, σ = 0.0817.

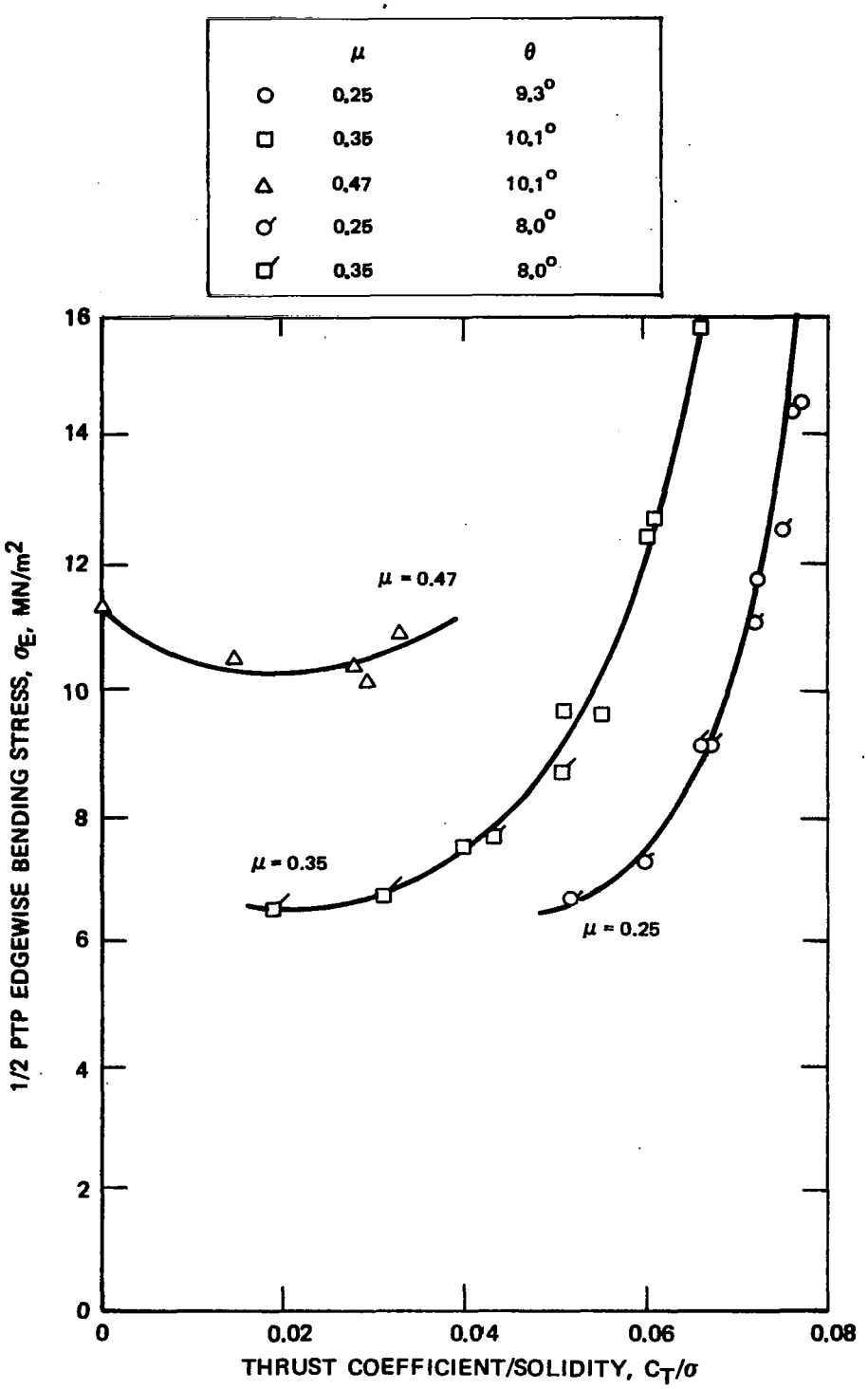

Figure 35. -Effects of Advance Ratio and Blade Loading on Vibratory Inboard Edgewise Stresses of Model Rotor with Pinned-Pinned Torque Tube, r = 0.06 R, σ = 0.0817.

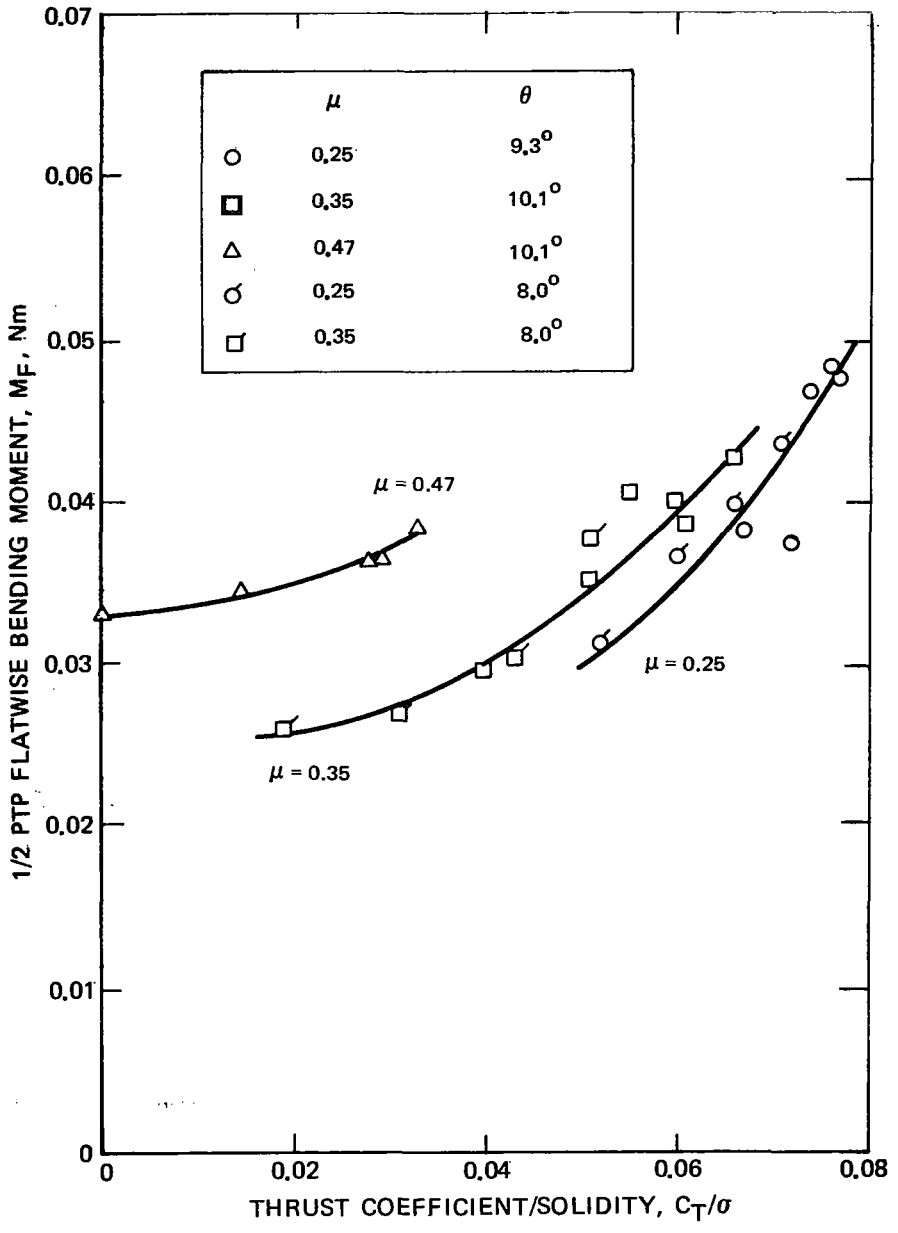

Figure 36. - Effects of Advance Ratio and Blade Loading on Vibratory Outboard Flatwise Bending Moment of Model Rotor with Pinned-Pinned Torque Tube , r = .42 R, σ = 0.0817.

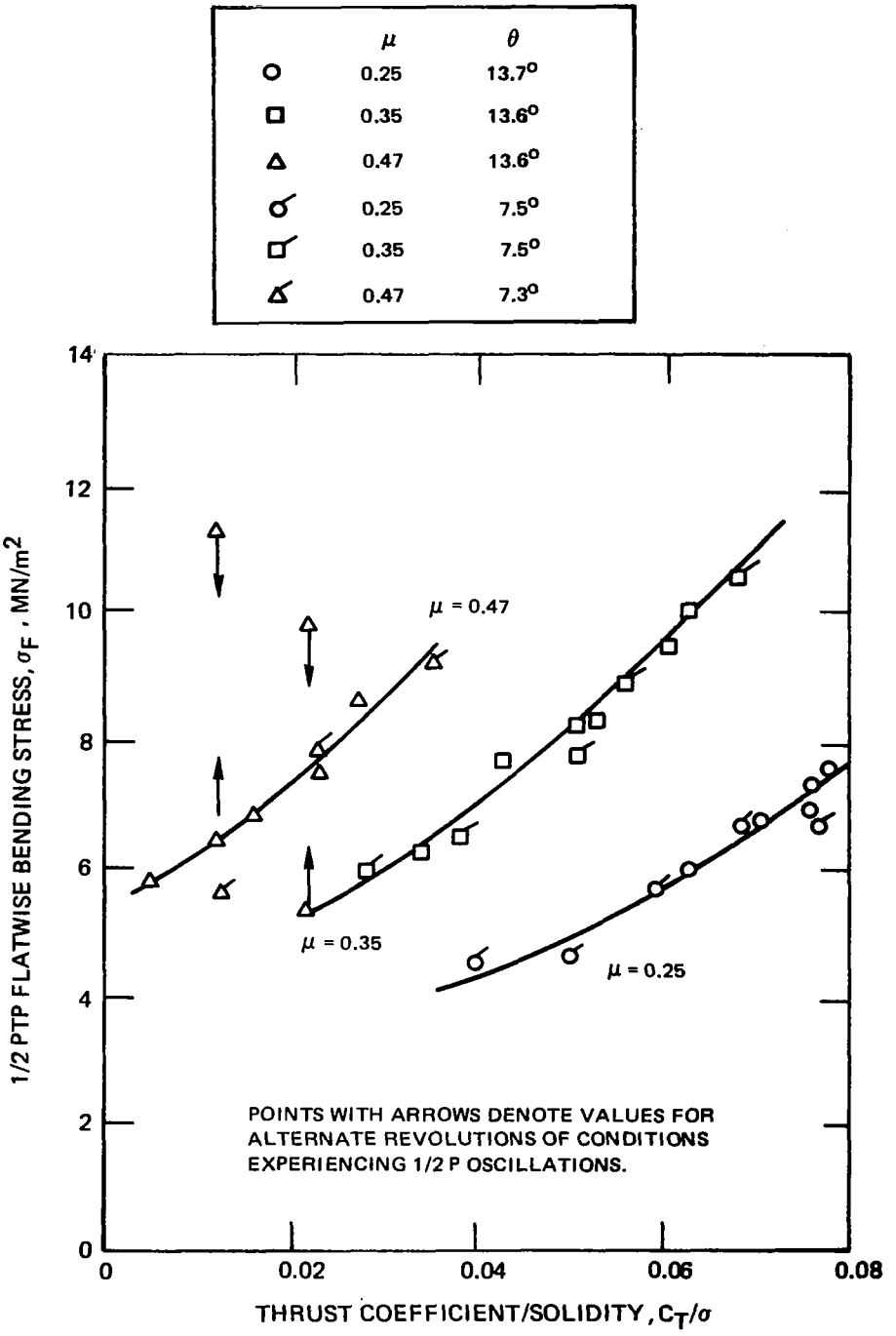

Figure 37. -Effects of Advance Ratio and Blade Loading on Vibratory Inboard Flatwise Stresses of Model Rotor with Cantilevered Torque Tube, Trailing Edge Push-Rod Attachment @ 0.06 R, r = 0.06 R, σ = 0.0408.

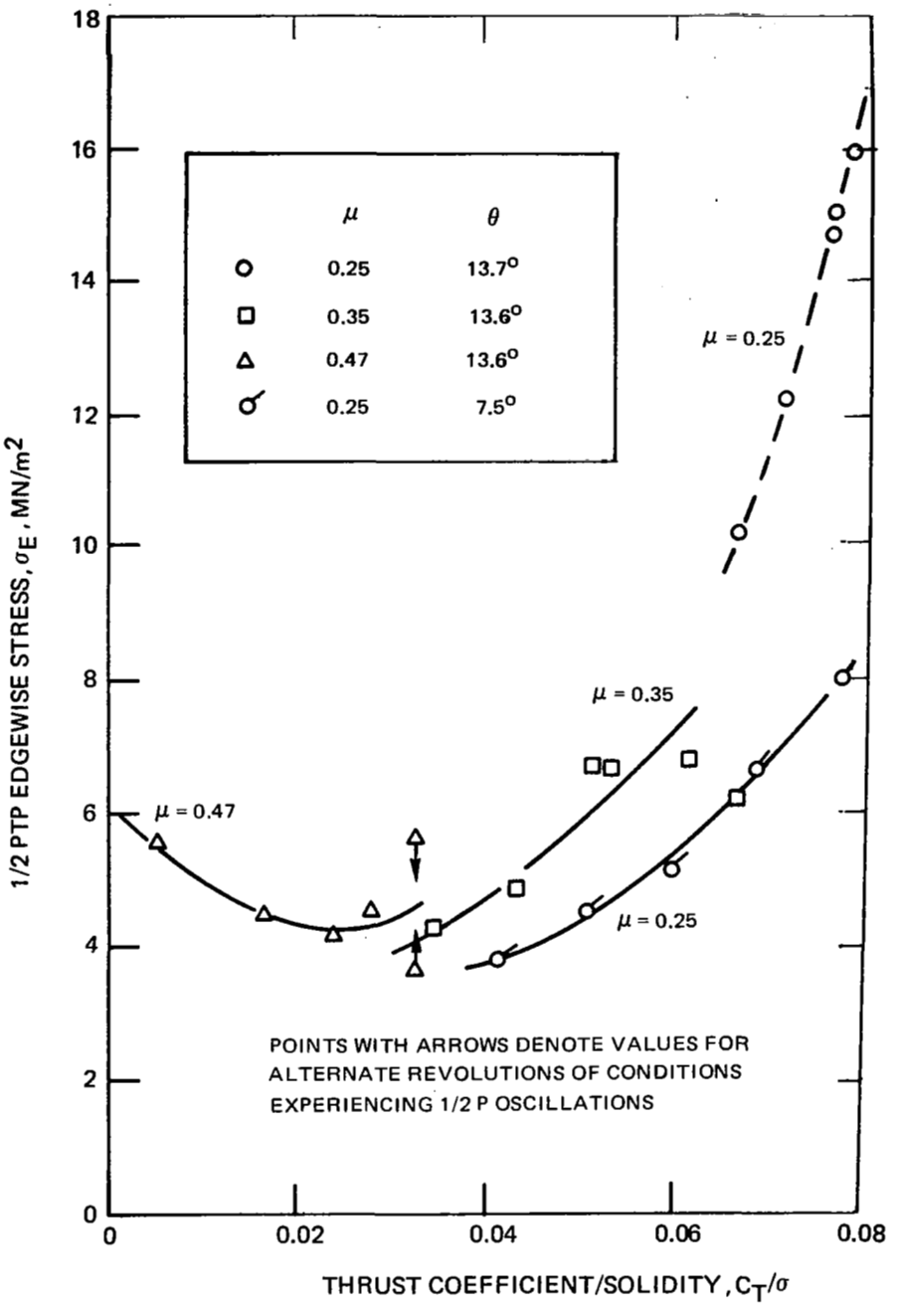

Figure 38.-Effects of Advance Ratio and Blade Loading on Vibratory Inboard Edgewise Stresses of Model Rotor with Cantilevered Torque Tube, Trailing Edge Push-Rod Attachment @ 0.06 R, r = 0.06 R, σ = 0.0408.

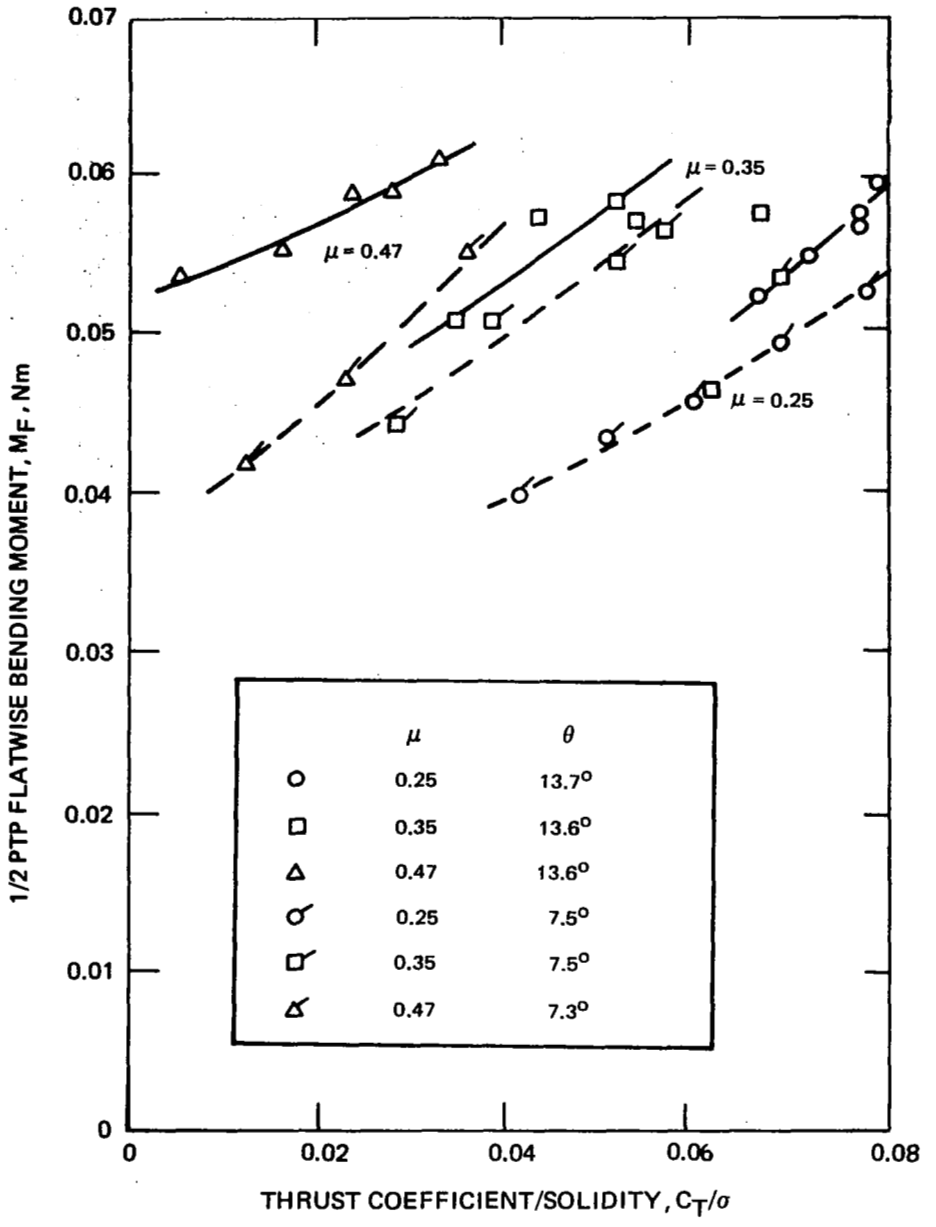

Figure 39. -Effects of Advance Ratio and Blade Loading on Vibratory Outboard Flatwise Bending Moment of Model Rotor with Cantilevered Torque Tube Trailing Edge Push-Rod Attachment @ 0.06 R, r = 0.42 R, σ = 0.0408.

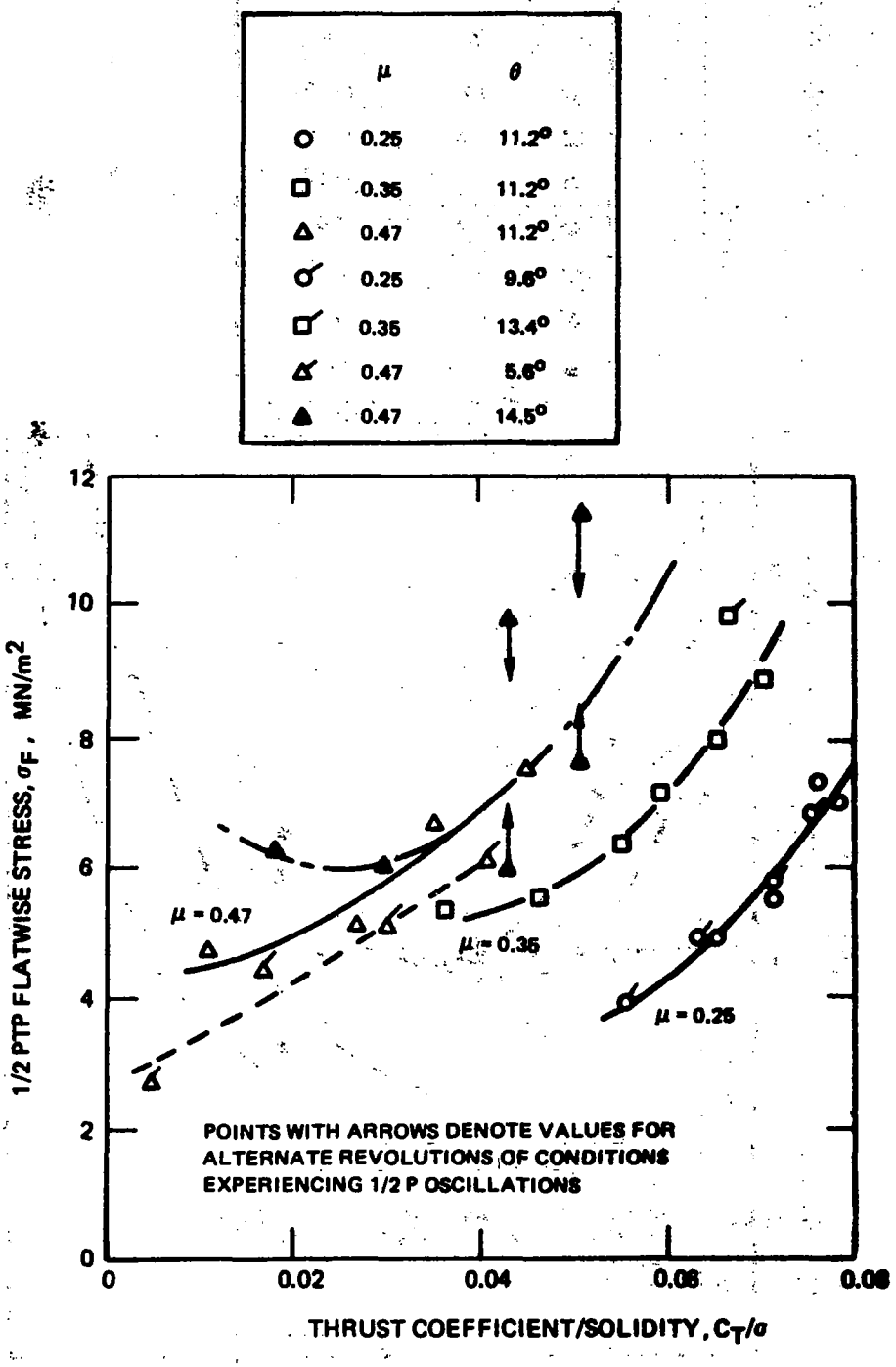

Figure 40. -Effects of Advance Ratio and Blade Loading on Vibratory Inboard Flatwise Stresses of Model Rotor with Cantilevered Torque Tube, Leading Edge Push-Rod Attachment @ 0.09 R, r = 0.06 R, σ = 0.0408.

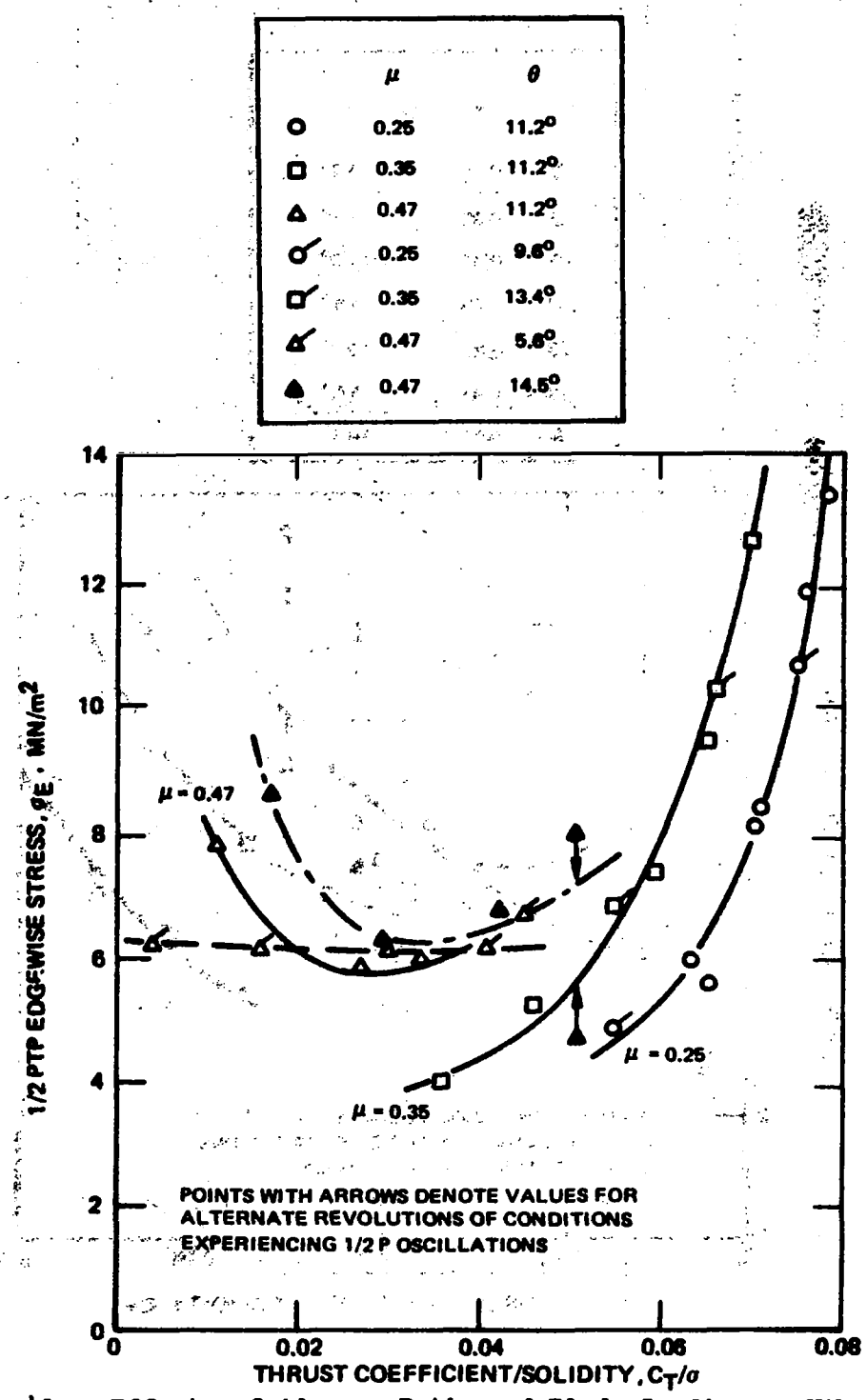

Figure 41. - Effects of Advance Ratio and Blade Loading on Vibratory Inboard Edgewise Stresses of Model Rotor with Cantilevered Torque Tube, Trailing Edge Push-Rod Attachment @ 0.06 R, r = 0.06 R, σ = 0.0408.

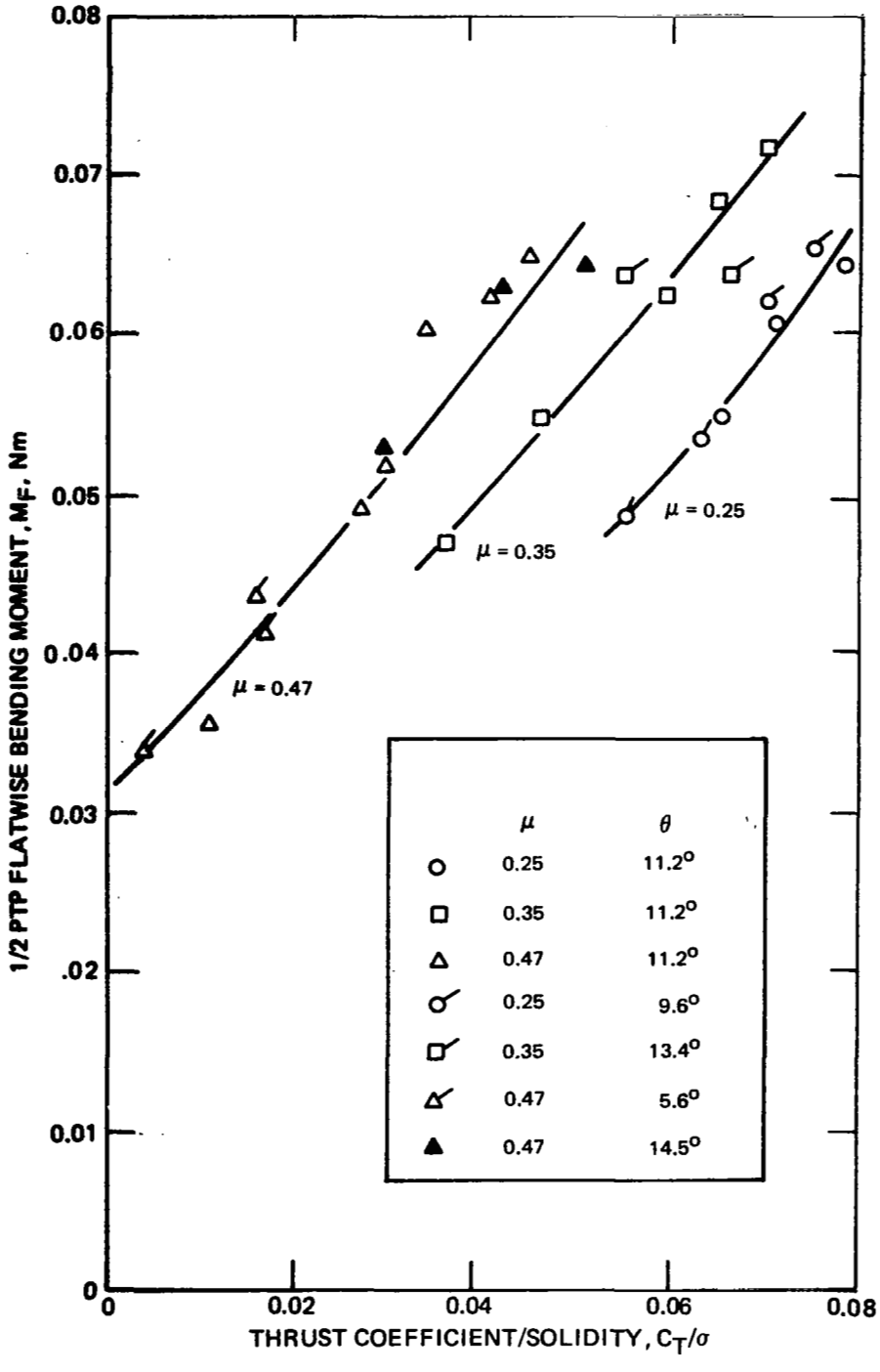

Figure 42. - Effects of Advance Ratio and Blade Loading on Vibratory Outboard Flatwise Bending Moment of Model Rotor with Cantilevered Torque Tube Trailing Edge Push-Rod Attachment @ 0.06 R, r = 0.42 R, σ = 0.0408.

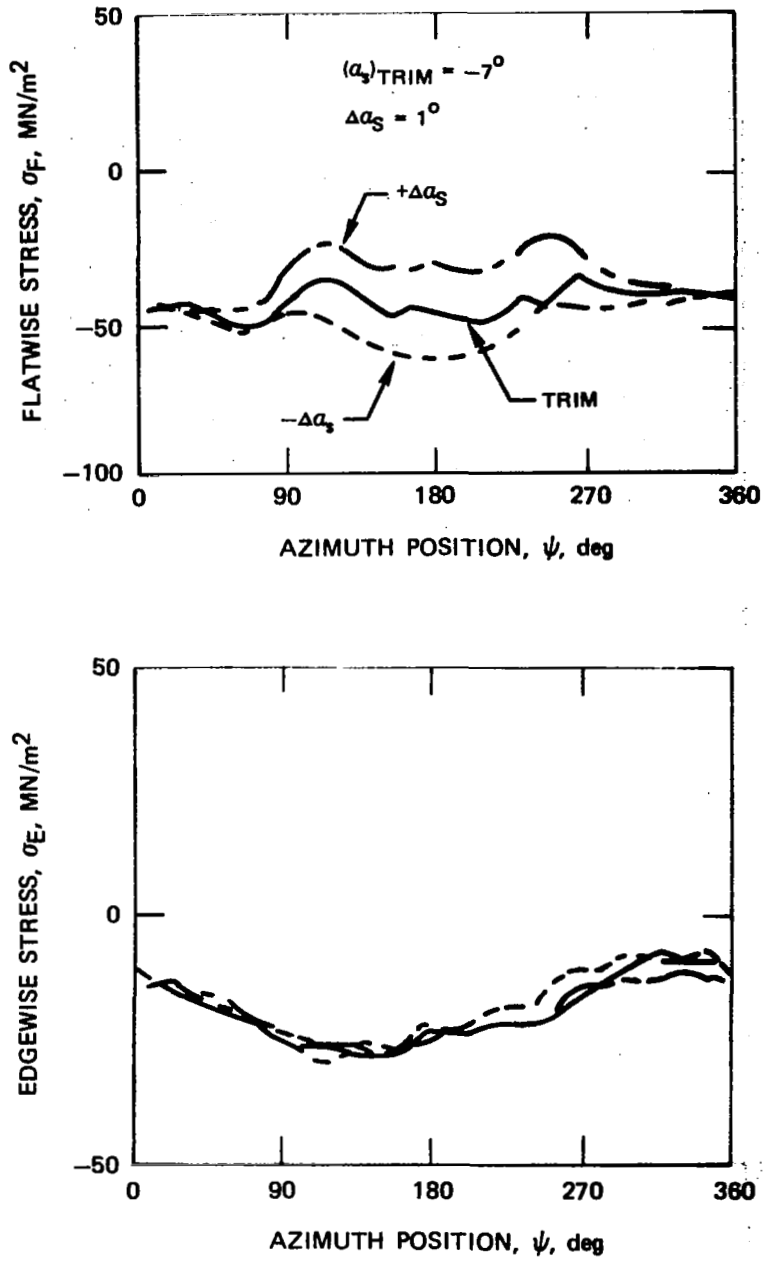

(a) SHAFT ANGLE PERTURBATIONS

Figure 43. -Perturbations of Azimuthal Variations of Inboard Flatwise and Edgewise Stresses for Model Rotor with Pinned-Pinned Torque Tube, $\mu = 0.25$, $\sigma = 0.0408$.

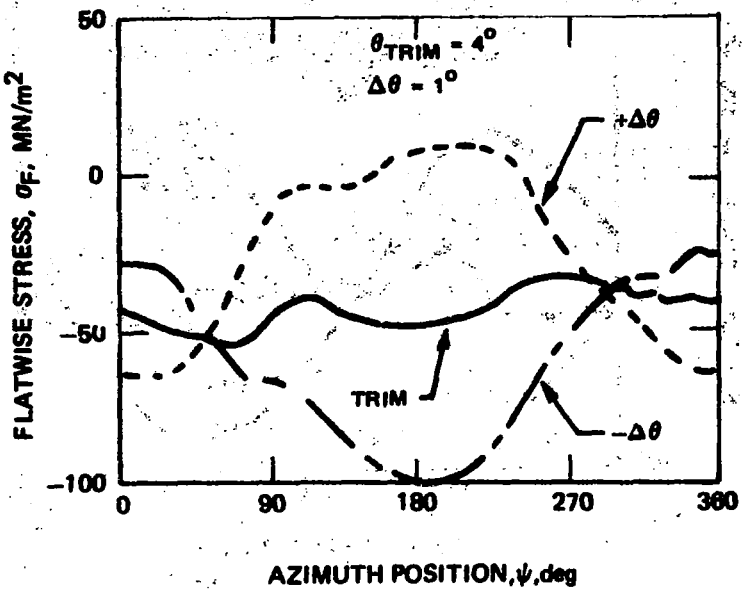

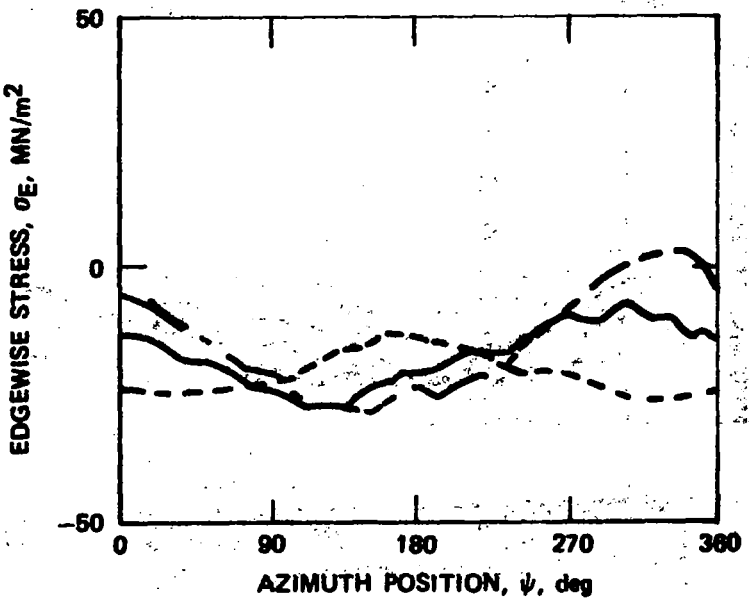

(b) COLLECTIVE PITCH PERTURBATIONS

Figure 43. - (Continued)

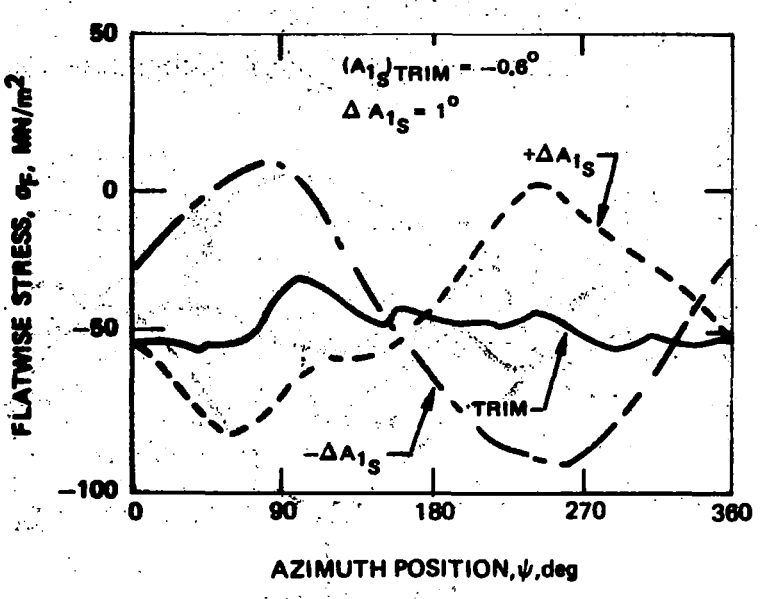

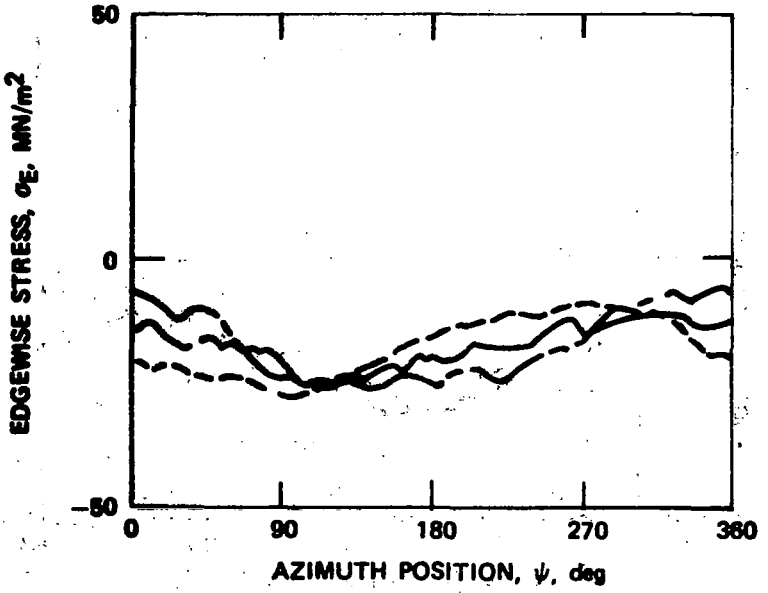

(c) LONGITUDINAL CYCLIC PERTURBATIONS

Figure 43. - (Continued)

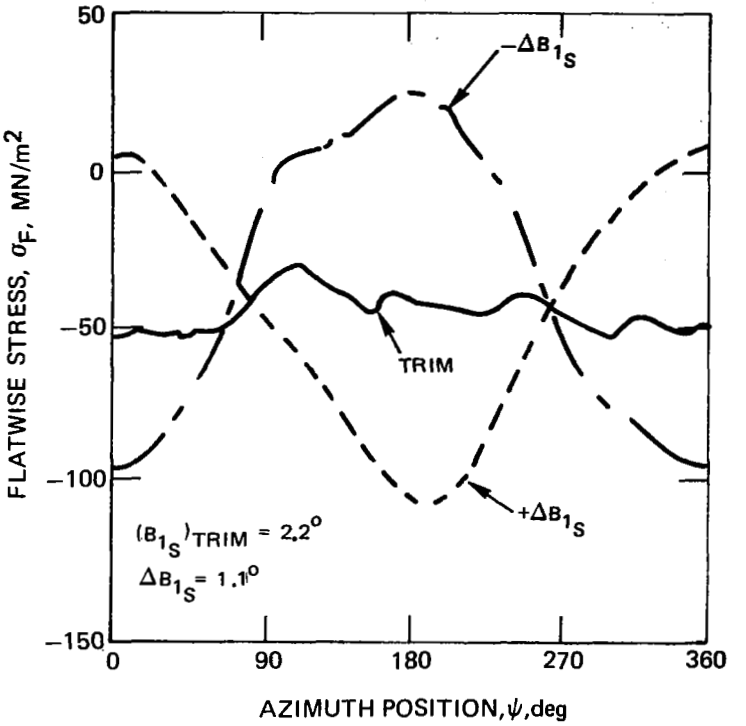

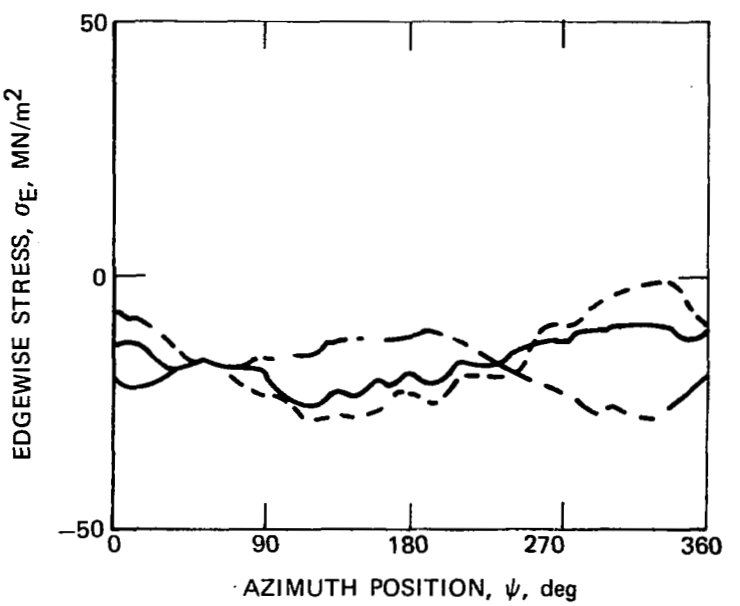

(d) LATERAL CYCLIC PERTURBATIONS

Figure 43. - (Concluded)

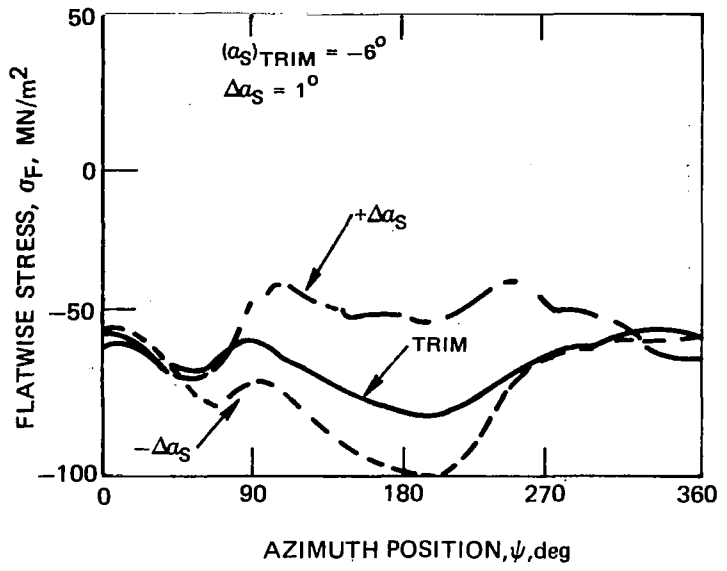

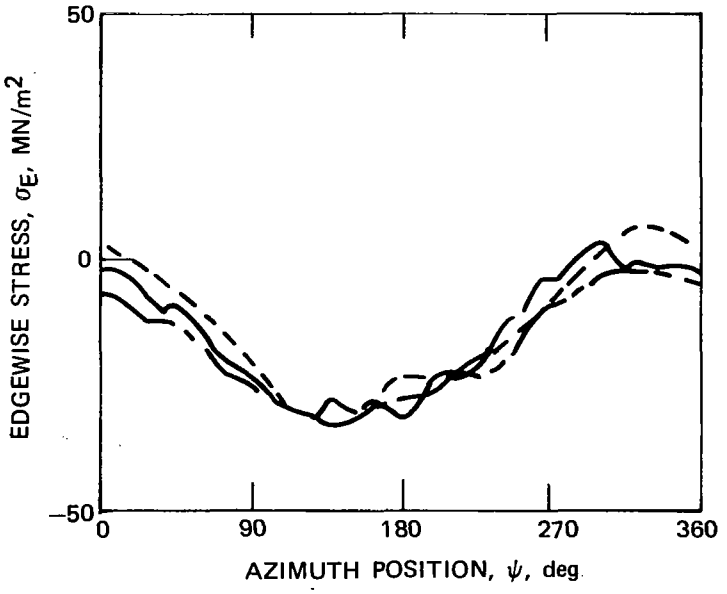

(a) SHAFT ANGLE PERTURBATIONS

Figure 44. -Perturbations of Azimuthal Variations of Inboard Flatwise and Edgewise Stresses for Model Rotor with Pinned-Pinned Torque Tube, $\mu = 0.35$, $\sigma = 0.0408$.

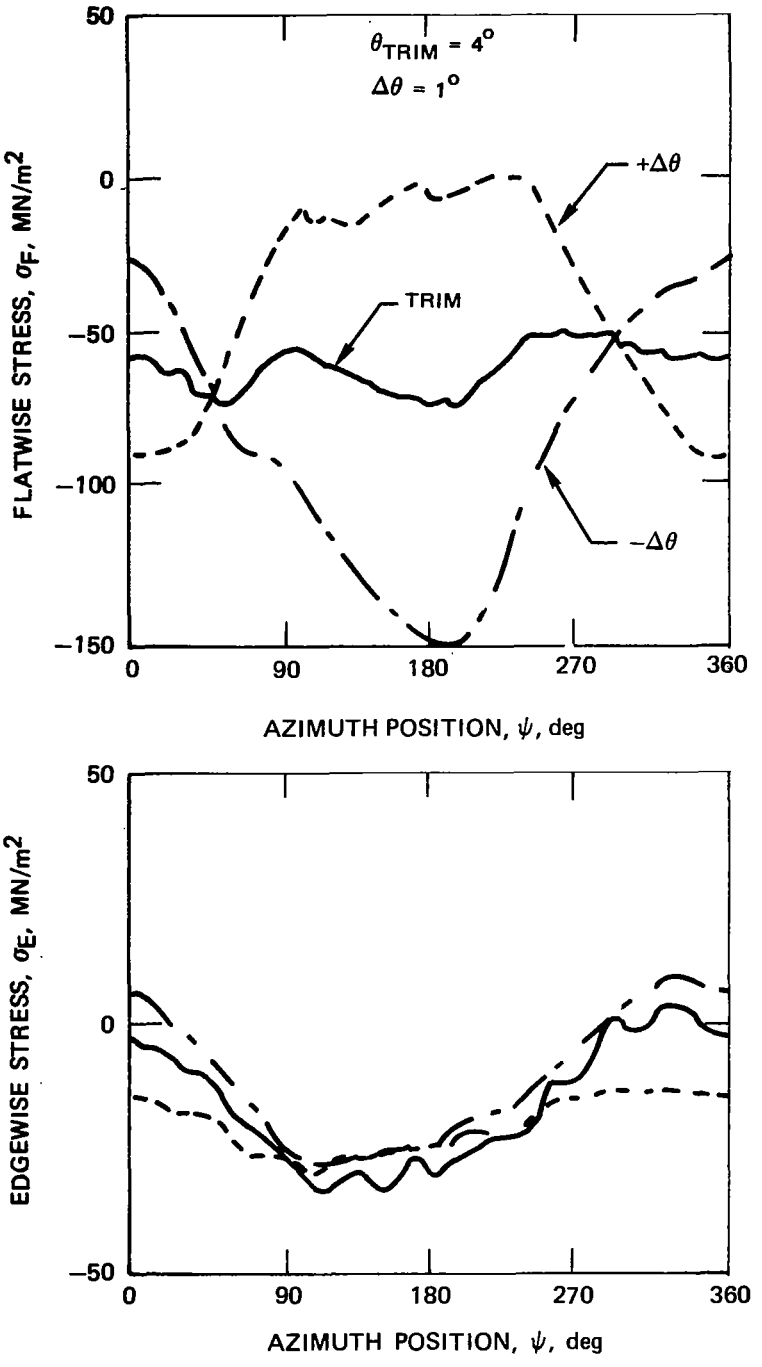

(b) COLLECTIVE PITCH PERTURBATIONS

Figure 44. - (Continued)

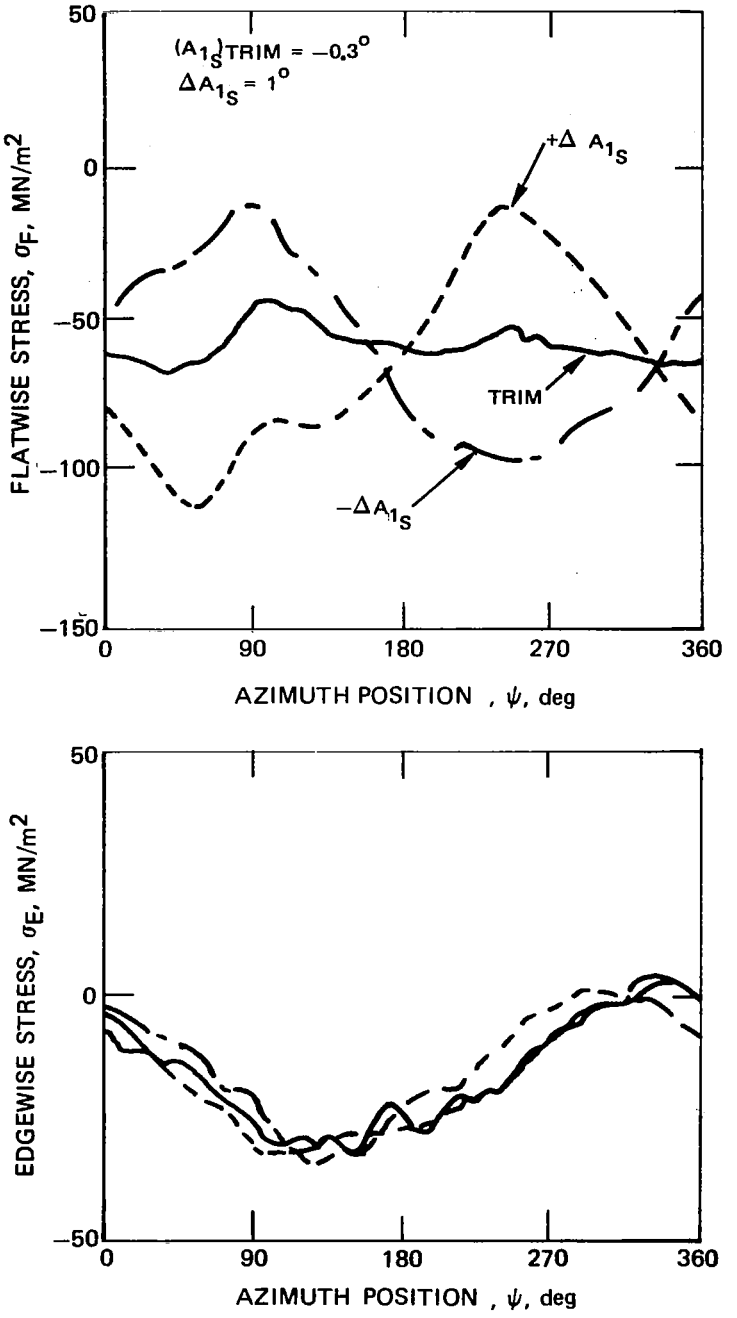

(c) LONGITUDINAL CYCLIC PERTURBATIONS

Figure 44. - (Continued)

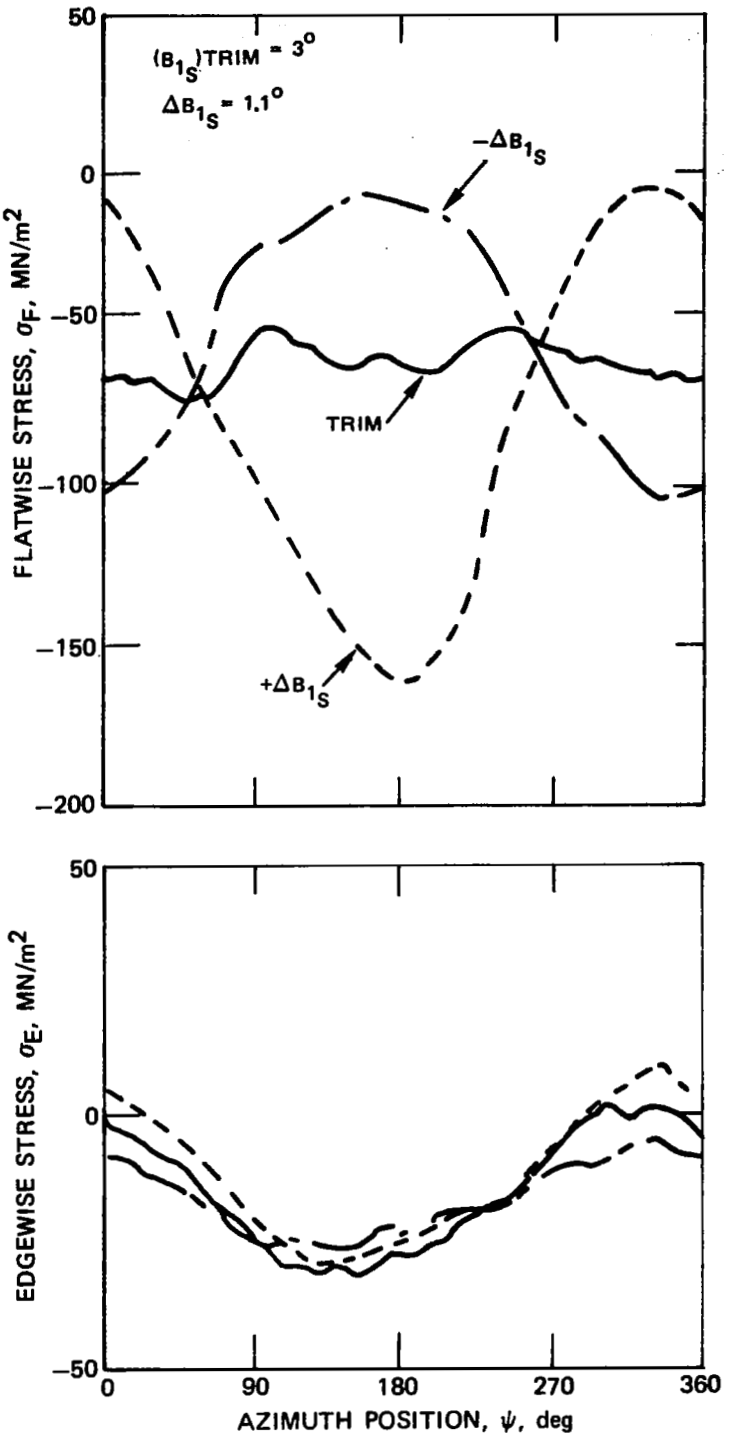

(d) LATERAL CYCLIC PERTURBATIONS

Figure 44. - (Concluded)

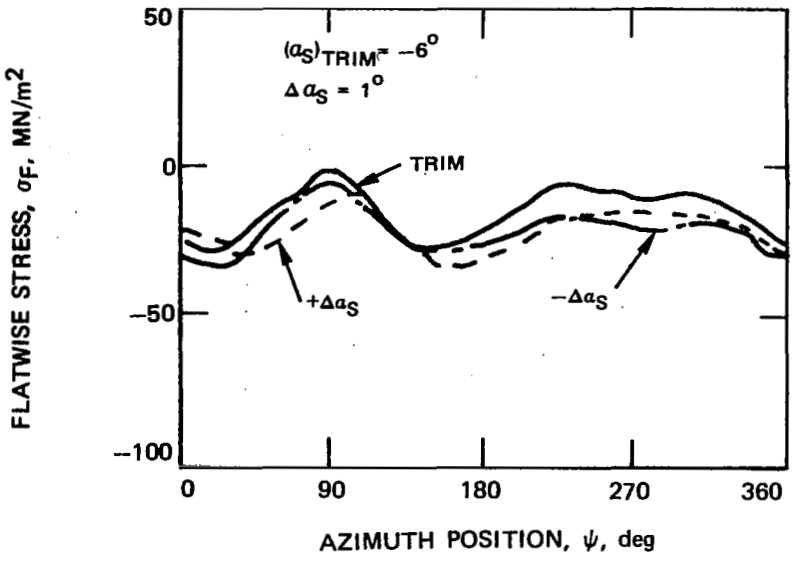

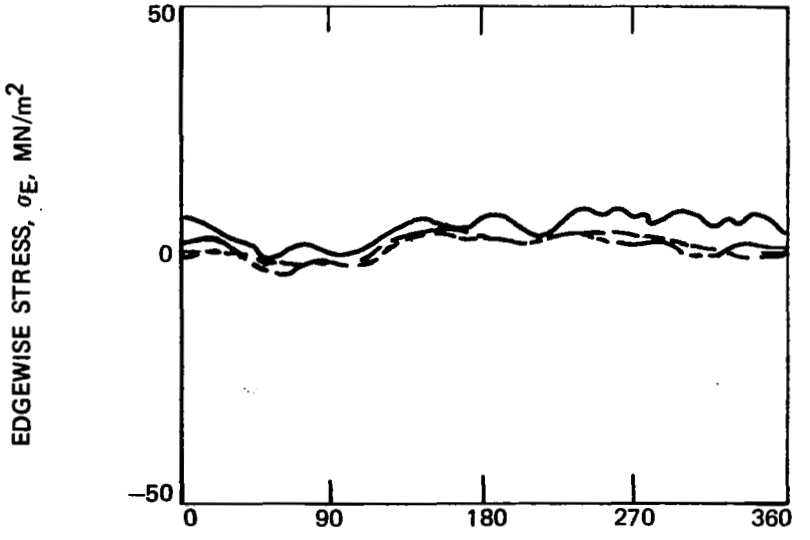

(a) SHAFT ANGLE PERTURBATIONS

Figure 45. - Perturbations of Azimuthal Variations of Inboard Flatwise and Edgewise Stresses for Model Rotor with Cantilevered Torque Tube, Trailing Edge Push-Rod Attachment @ 0.06 R, $\mu = 0.25$, $\sigma = 0.0408$.

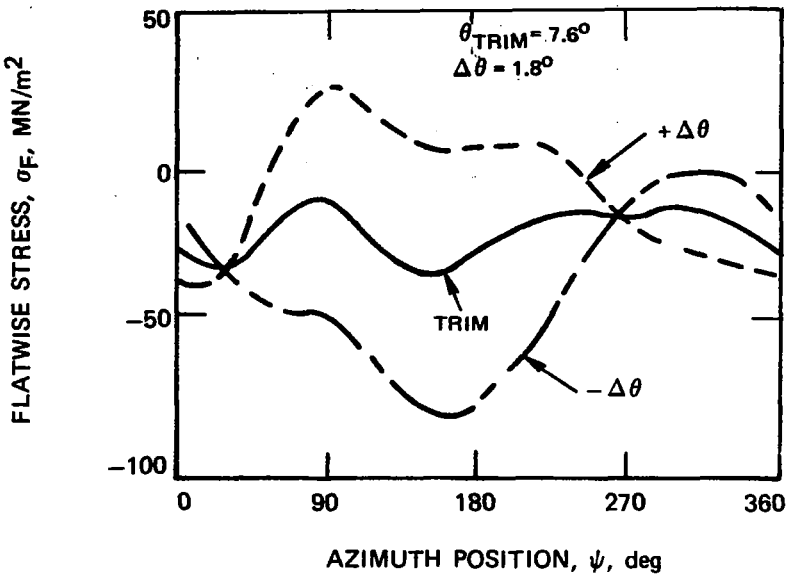

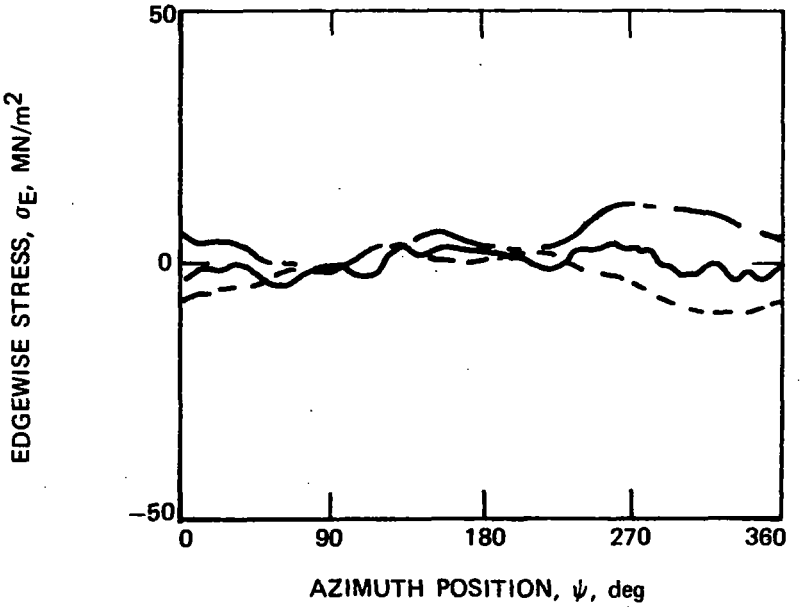

(b) COLLECTIVE PITCH PERTURBATIONS

Figure 45. - (Continued)

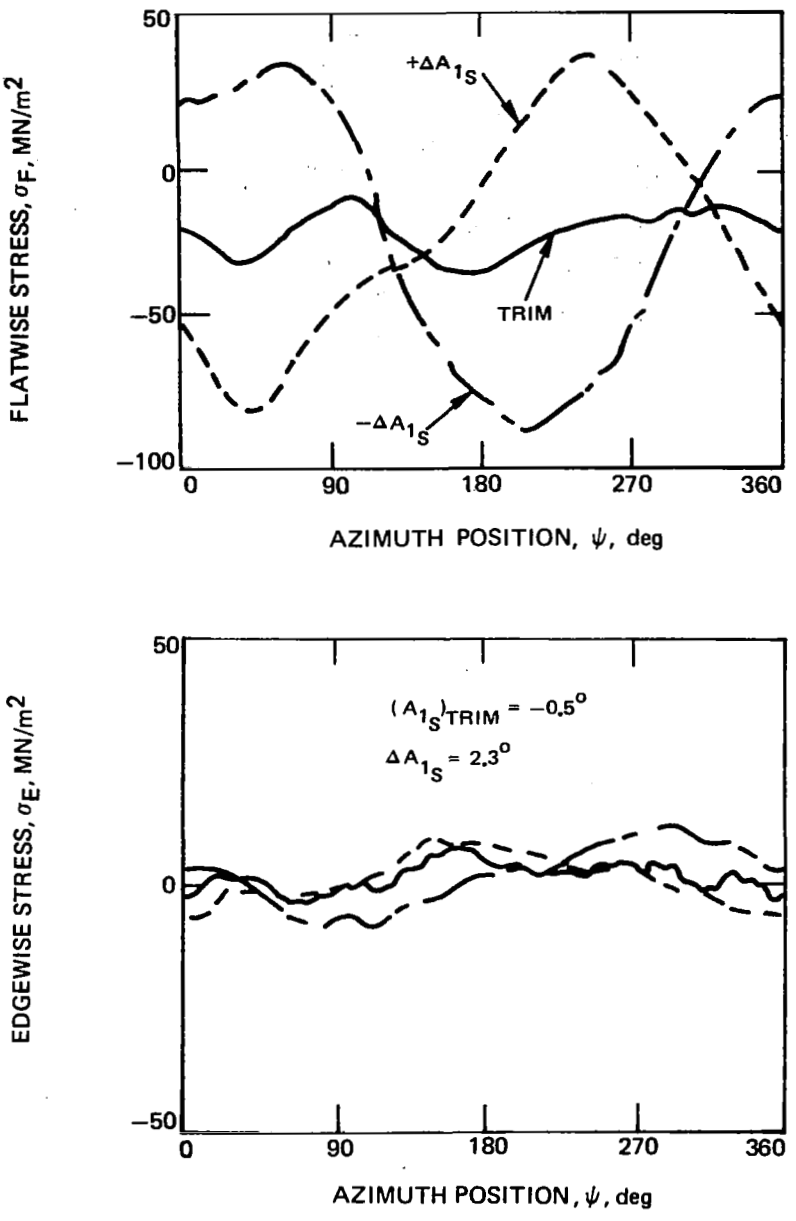

(c) LONGITUDINAL CYCLIC PERTURBATIONS

Figure 45. - (Continued)

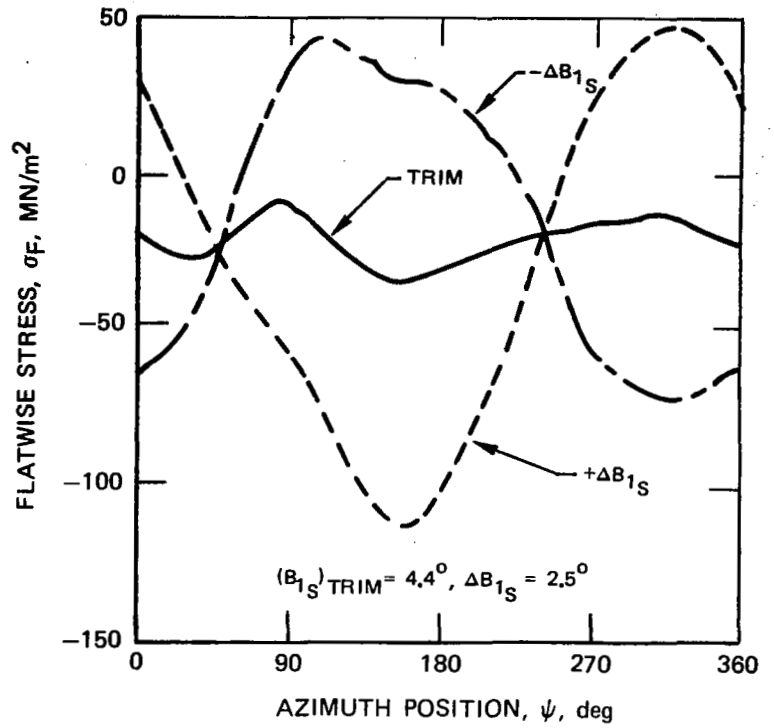

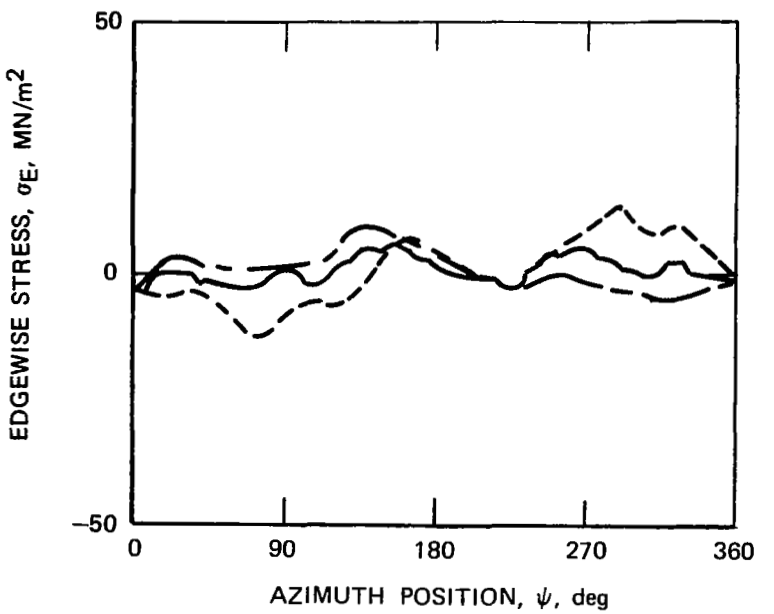

(d) LATERAL CYCLIC PERTURBATIONS

Figure 45. - (Concluded)

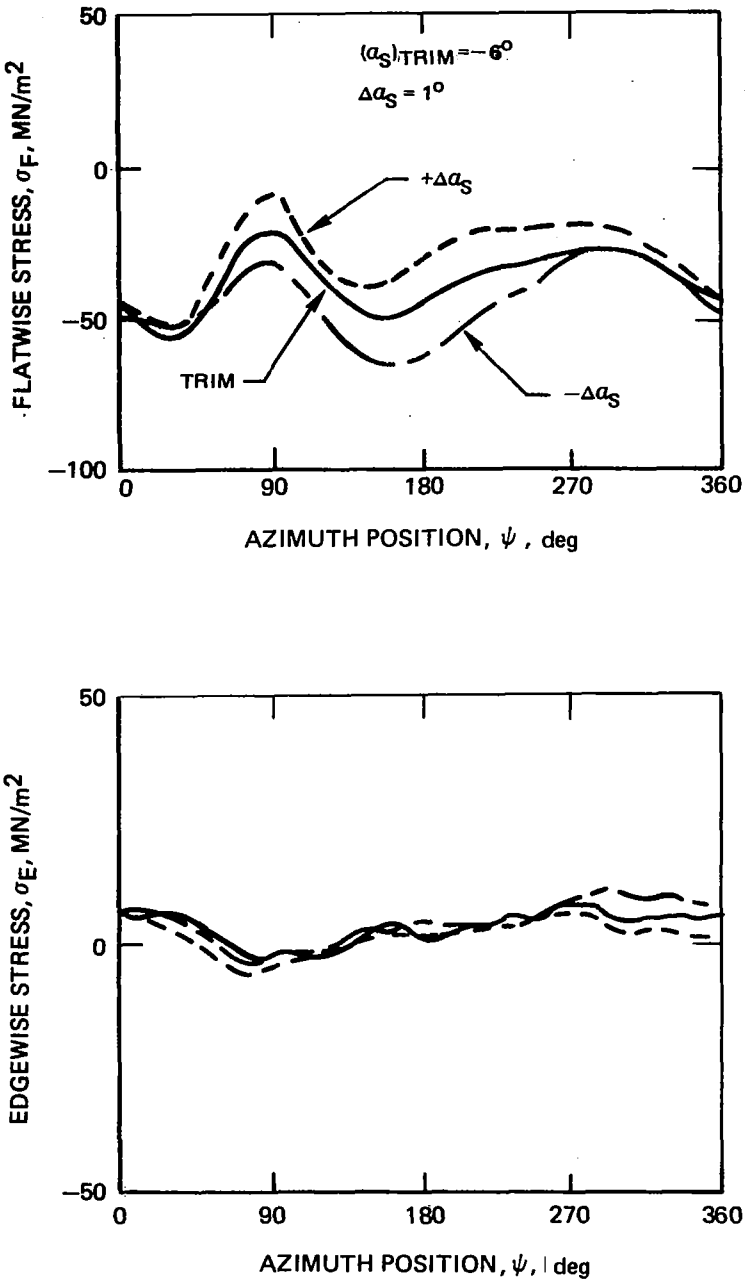

(a) SHAFT ANGLE PERTURBATIONS

Figure 46. -Perturbations of Azimuthal Variations of Inboard Flatwise and Edgewise Stresses for Model Rotor with Cantilevered Torque Tube, Trailing Edge Push-Rod Attachment @ 0.06 R, μ = 0.35, σ = 0.0408.

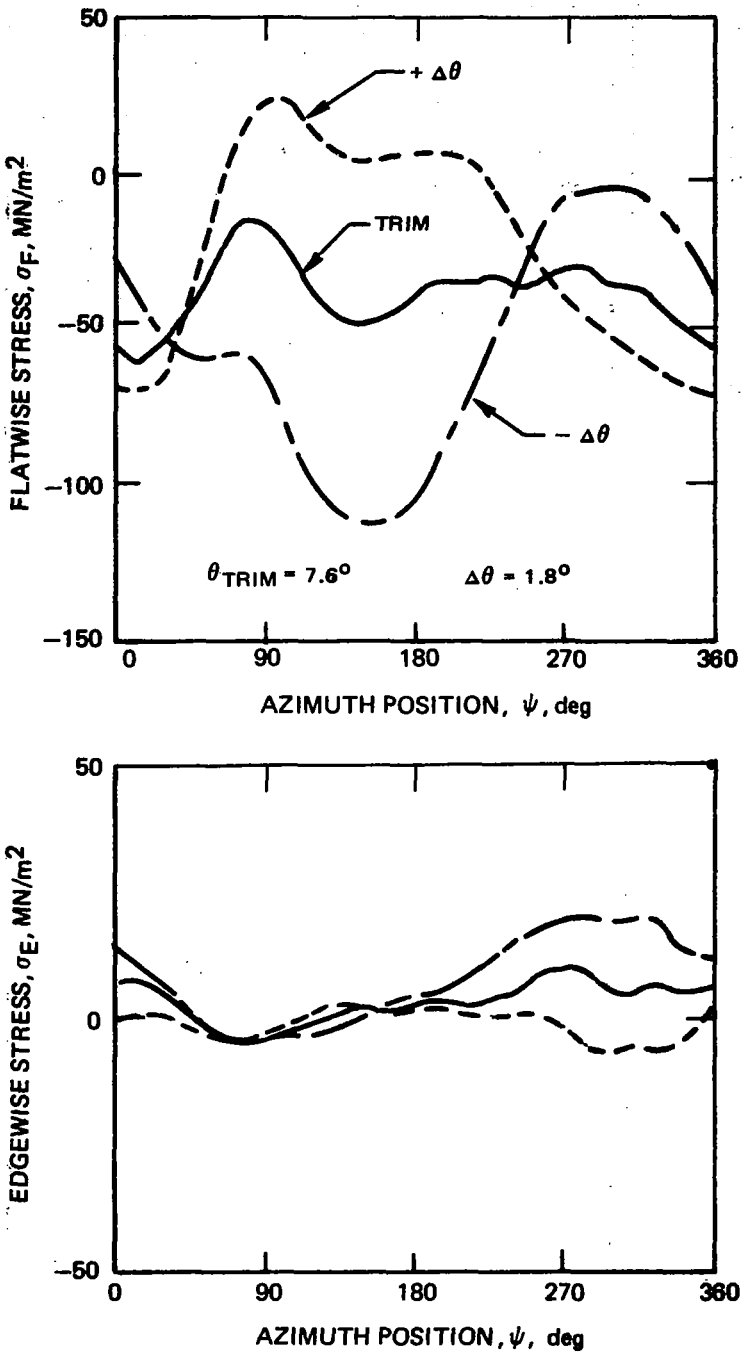

(b) COLLECTIVE PITCH PERTURBATIONS

Figure 46. - (Continued)

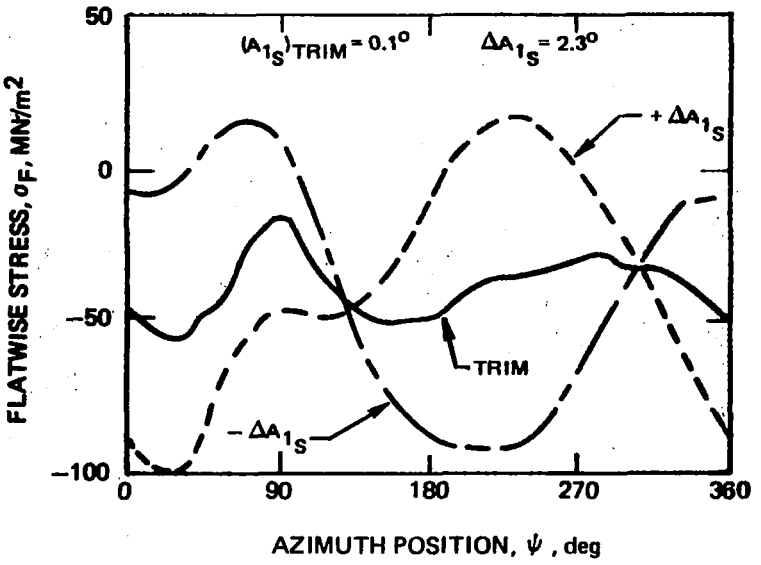

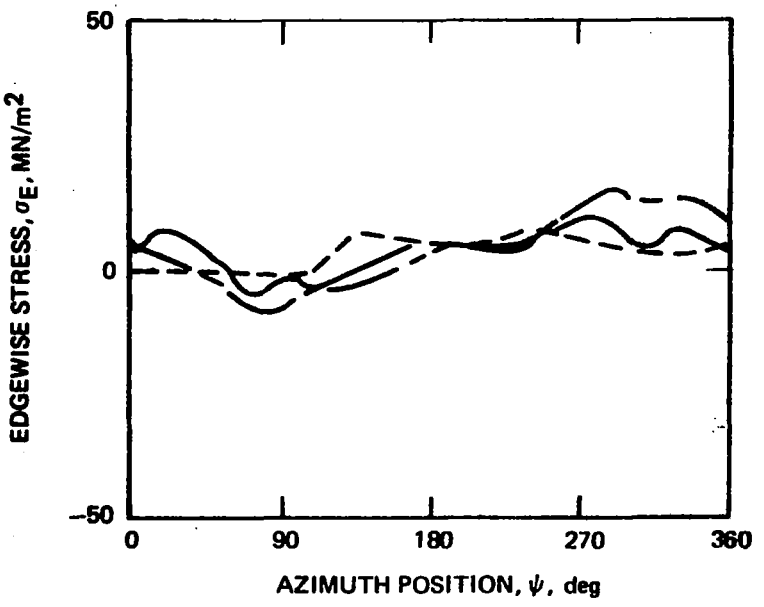

(c) LONGITUDINAL CYCLIC PERTURBATIONS

Figure 46. - (Continued)

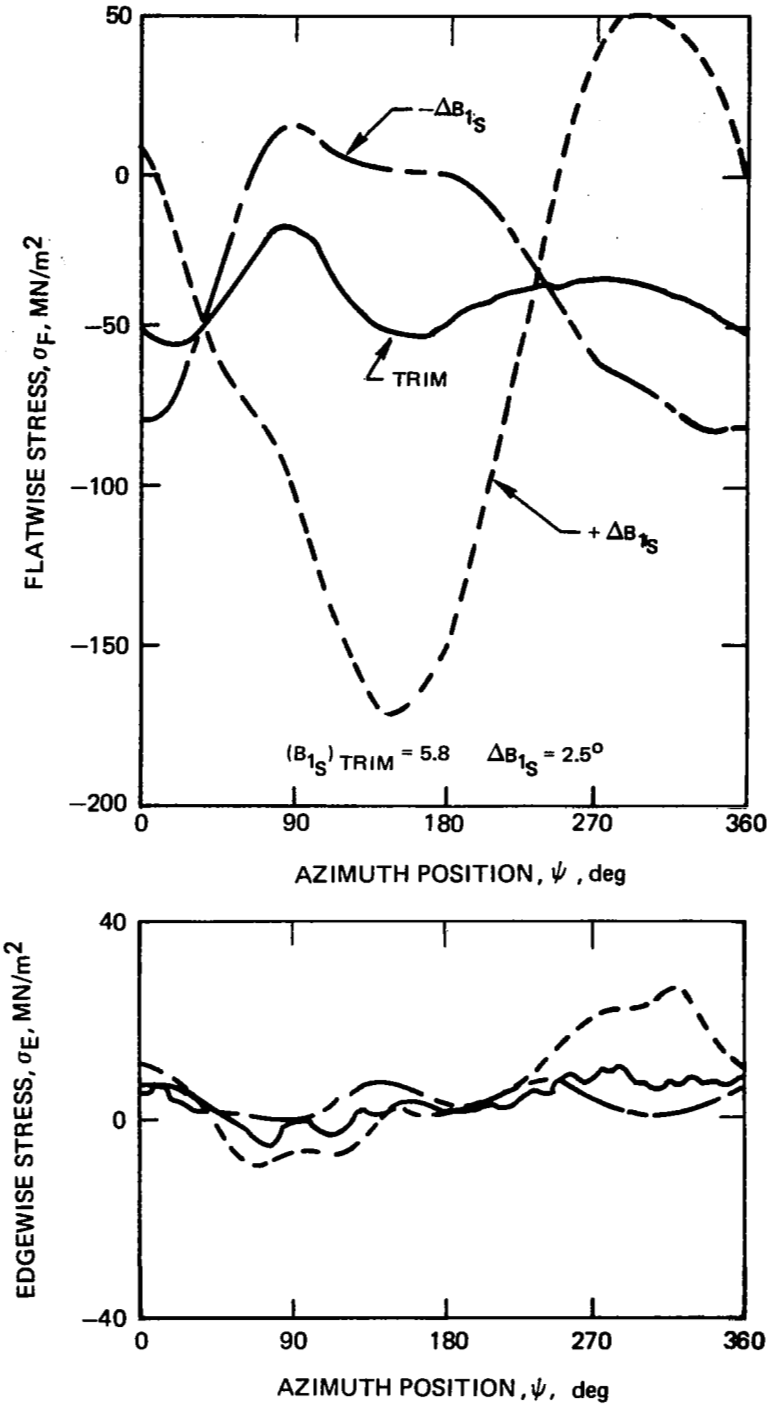

(d) LATERAL CYCLIC PERTURBATIONS

Figure 46. - (Concluded)

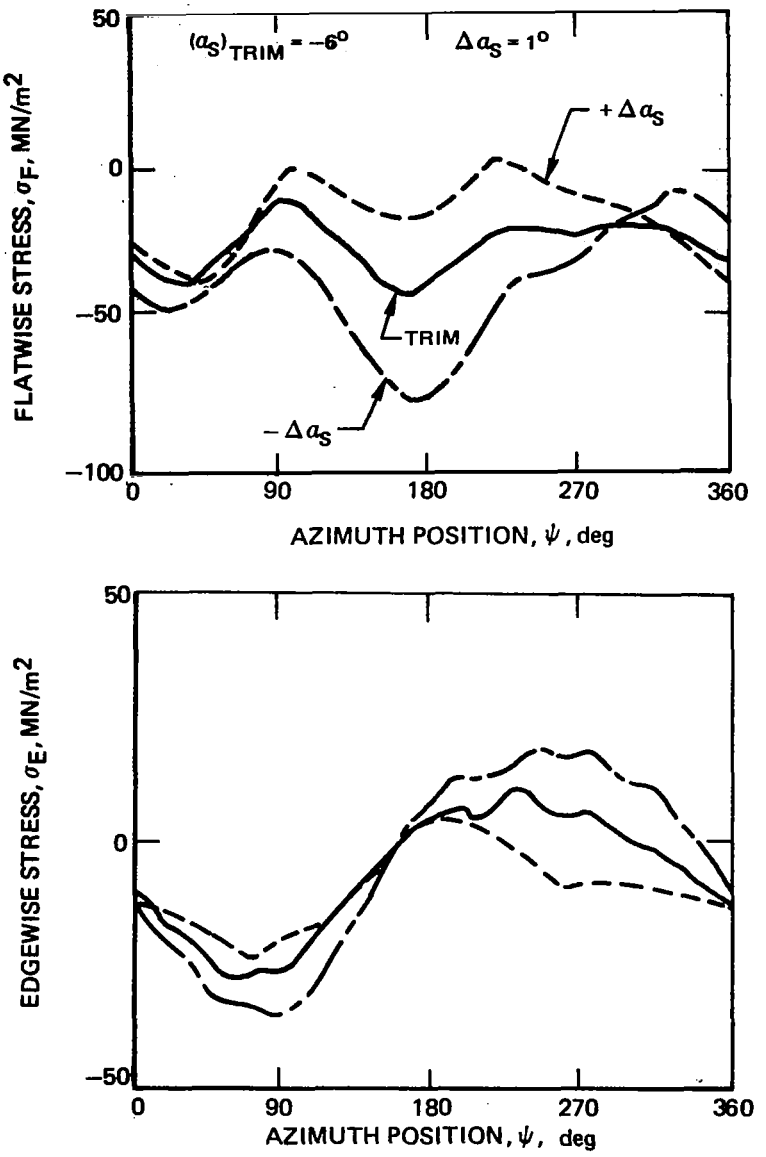

(a) SHAFT ANGLE PERTURBATIONS

Figure 47. -Perturbations of Azimuthal Variations of Inboard Flatwise and Edgewise Stresses for Model Rotor with Cantilevered Torque-Tube, Leading Edge Push-Rod Attachment at 0.09 R, $\mu = 0.35$, $\sigma = 0.0408$.

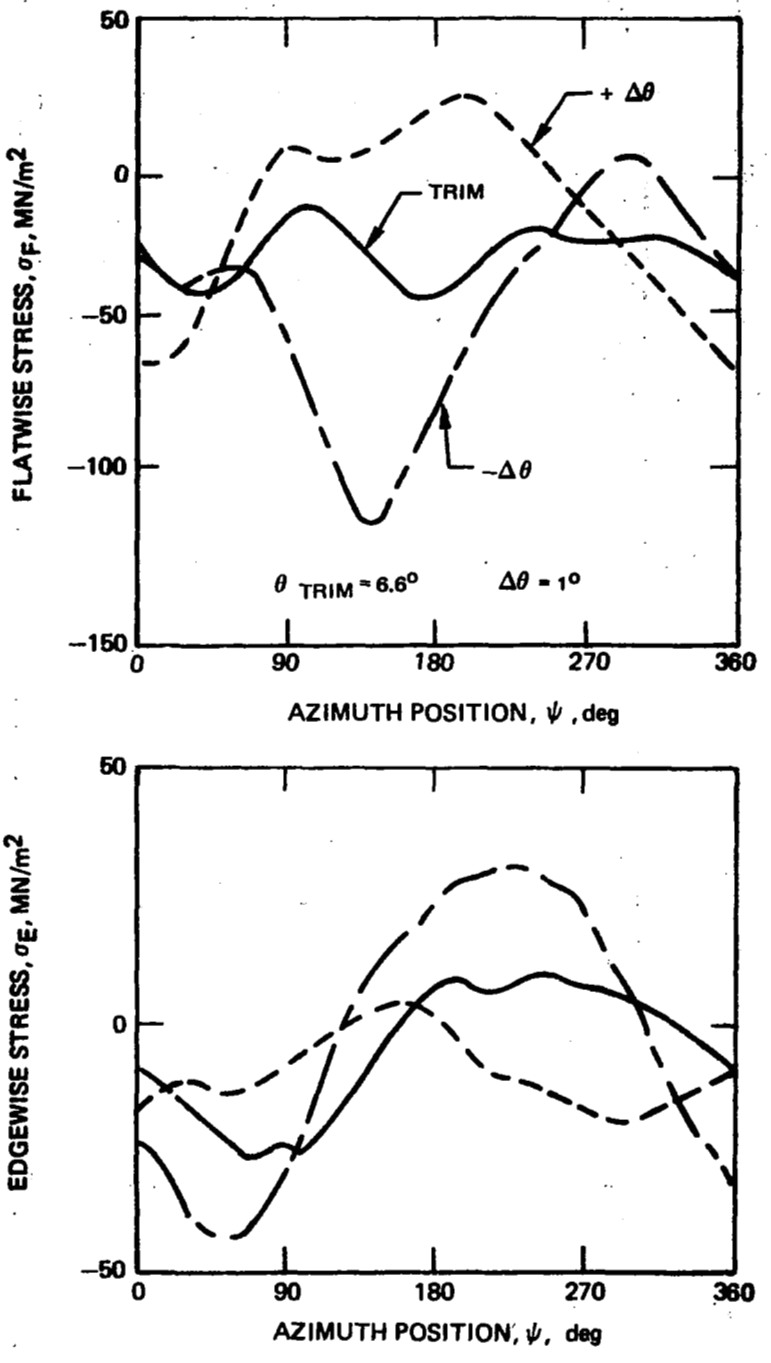

(b) COLLECTIVE PITCH PERTURBATIONS

Figure 47. - (Continued)

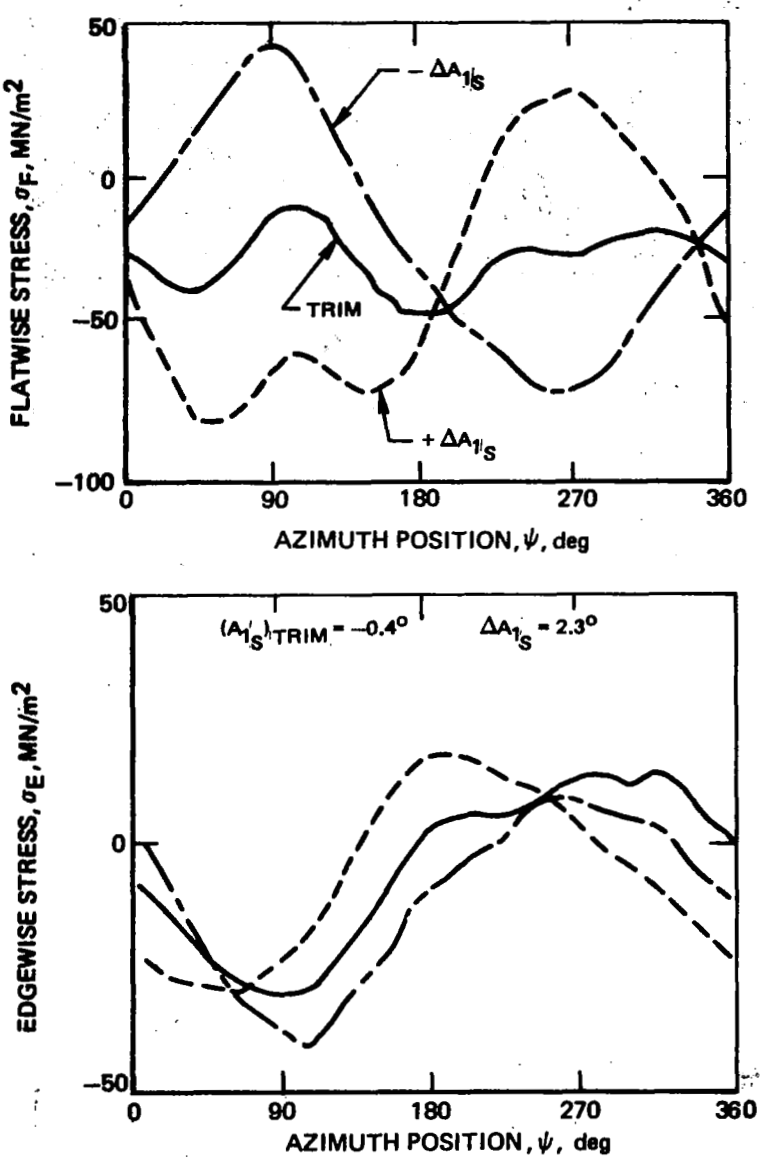

(c) LONGITUDINAL CYCLIC PERTURBATIONS

Figure 47. - (Continued)

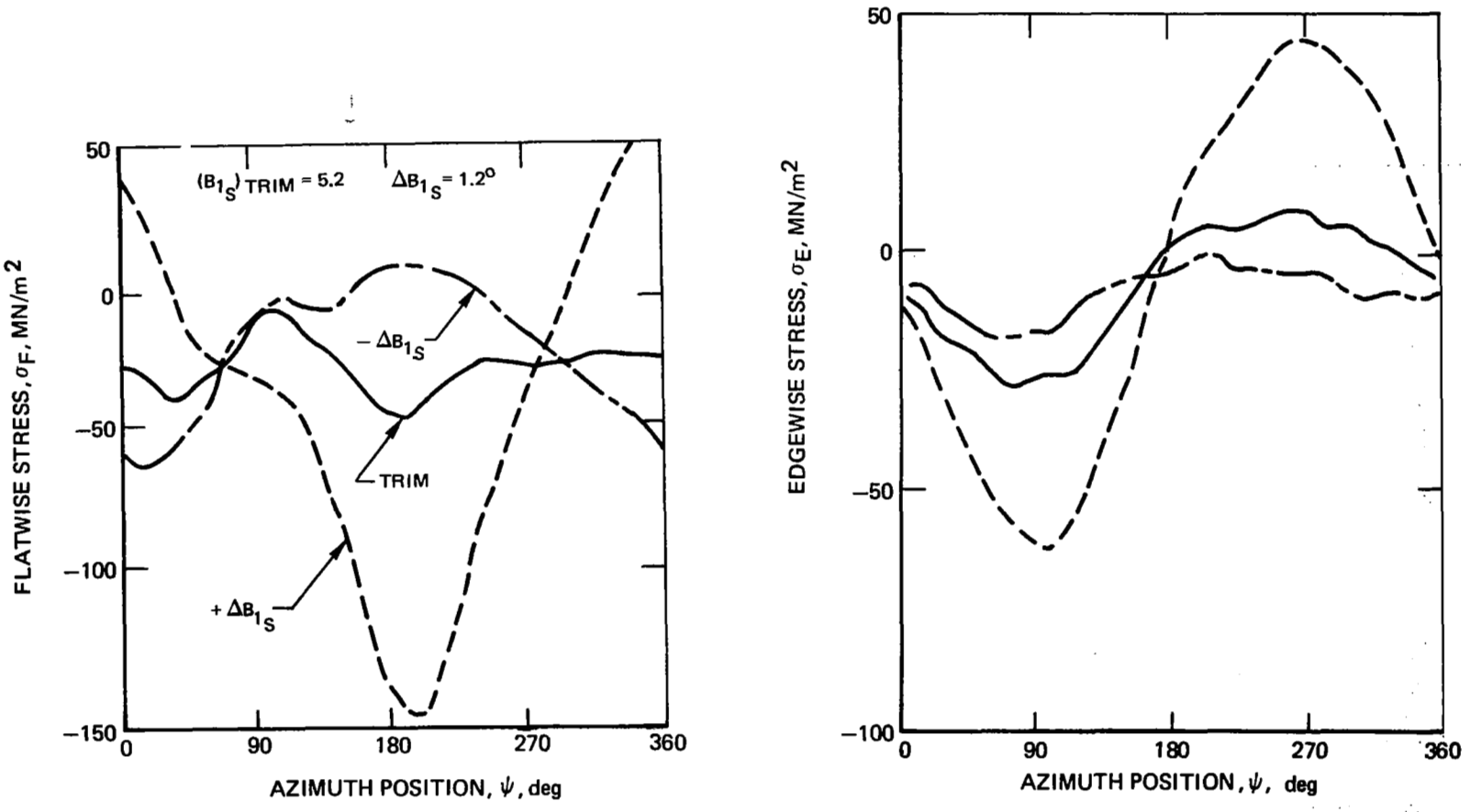

(d) LATERAL CYCLIC PERTURBATIONS

Figure 47. - (Concluded)

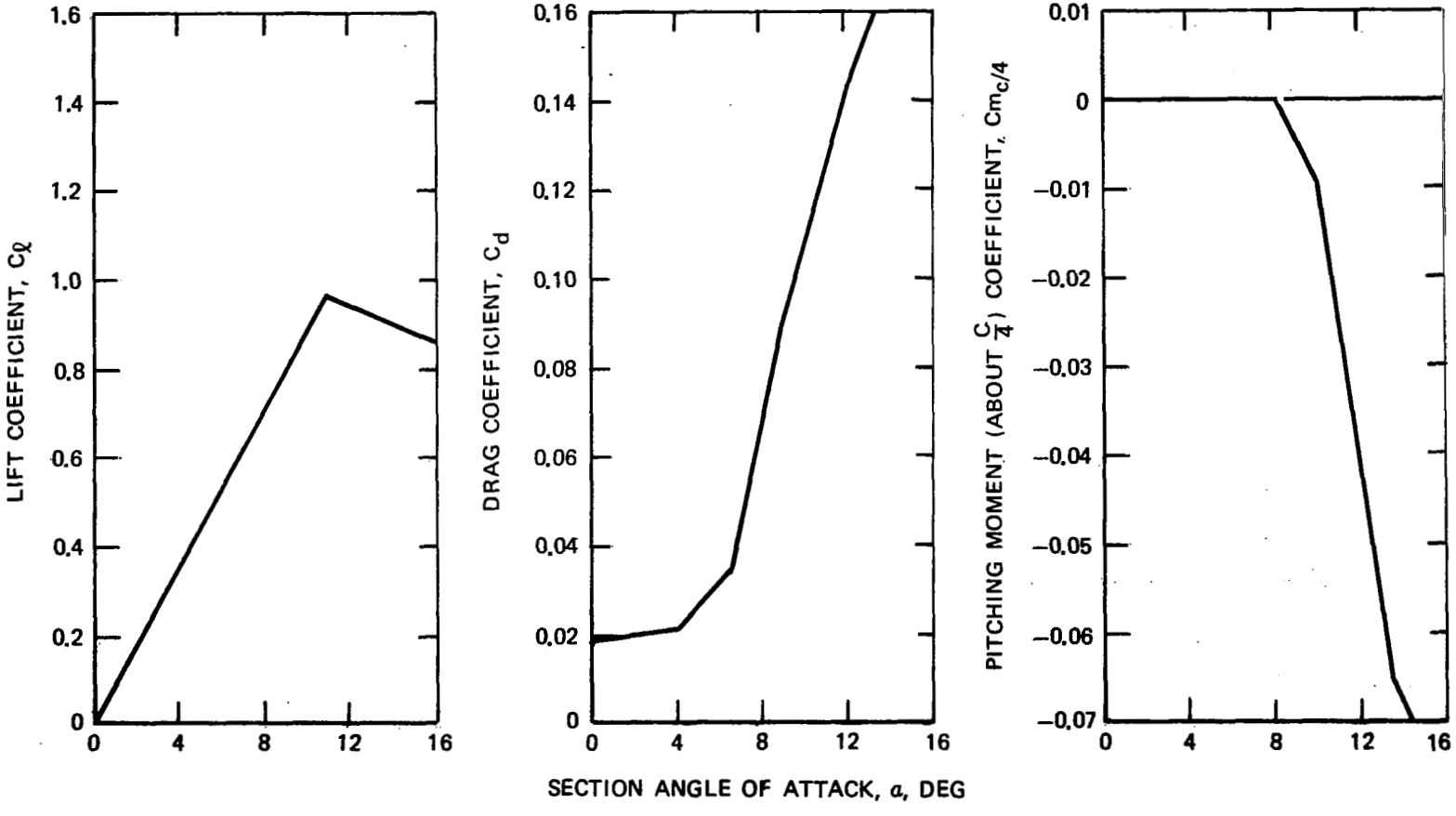

Figure 48. - Airfoil Characteristics Assumed for Model Blade Sections and Used in Correlation Study.

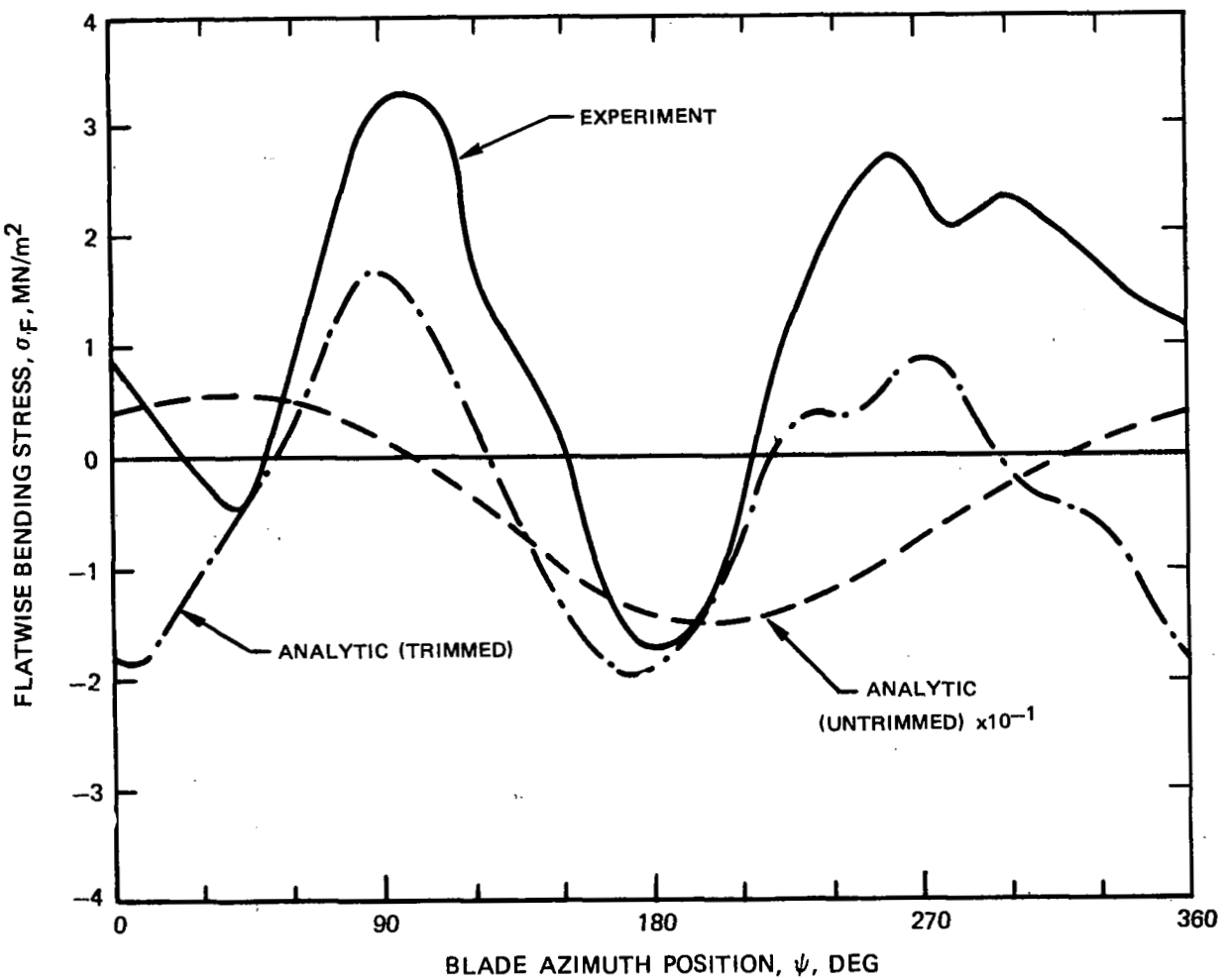

Figure 49. -Experimental and Analytic Time-Histories of Inboard Flatwise Bending Stresses, r = 0.06 R, Case 25.03, C_L/σ = 0.0783, μ = 0.25, b = 2.

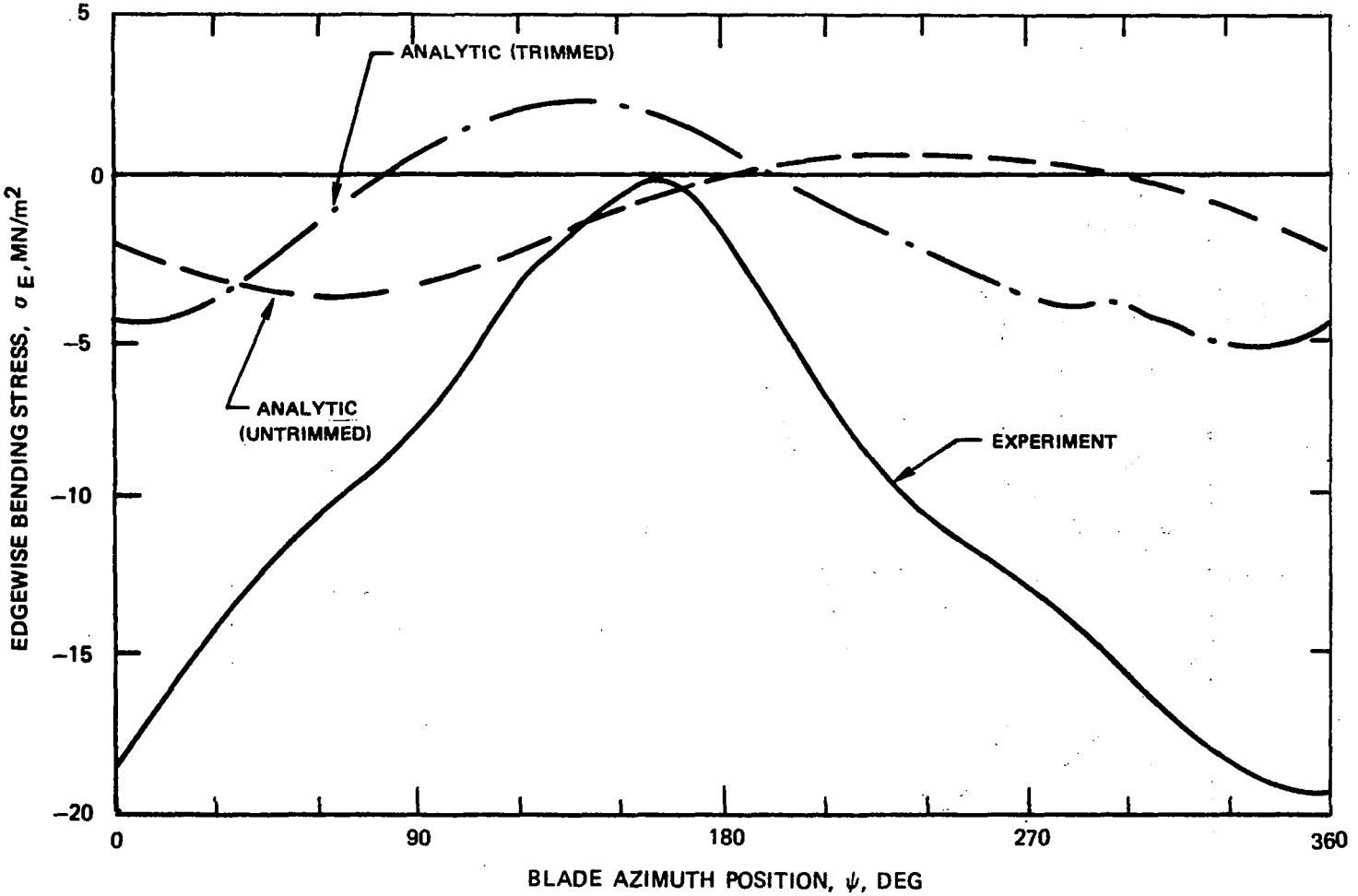

Figure 50. -Experimental and Analytic Time-Histories of Inboard Edgewise Bending Stresses, r = 0.06 R, Case 25.03, C_L/σ = 0.0783, μ = 0.25, b = 2.

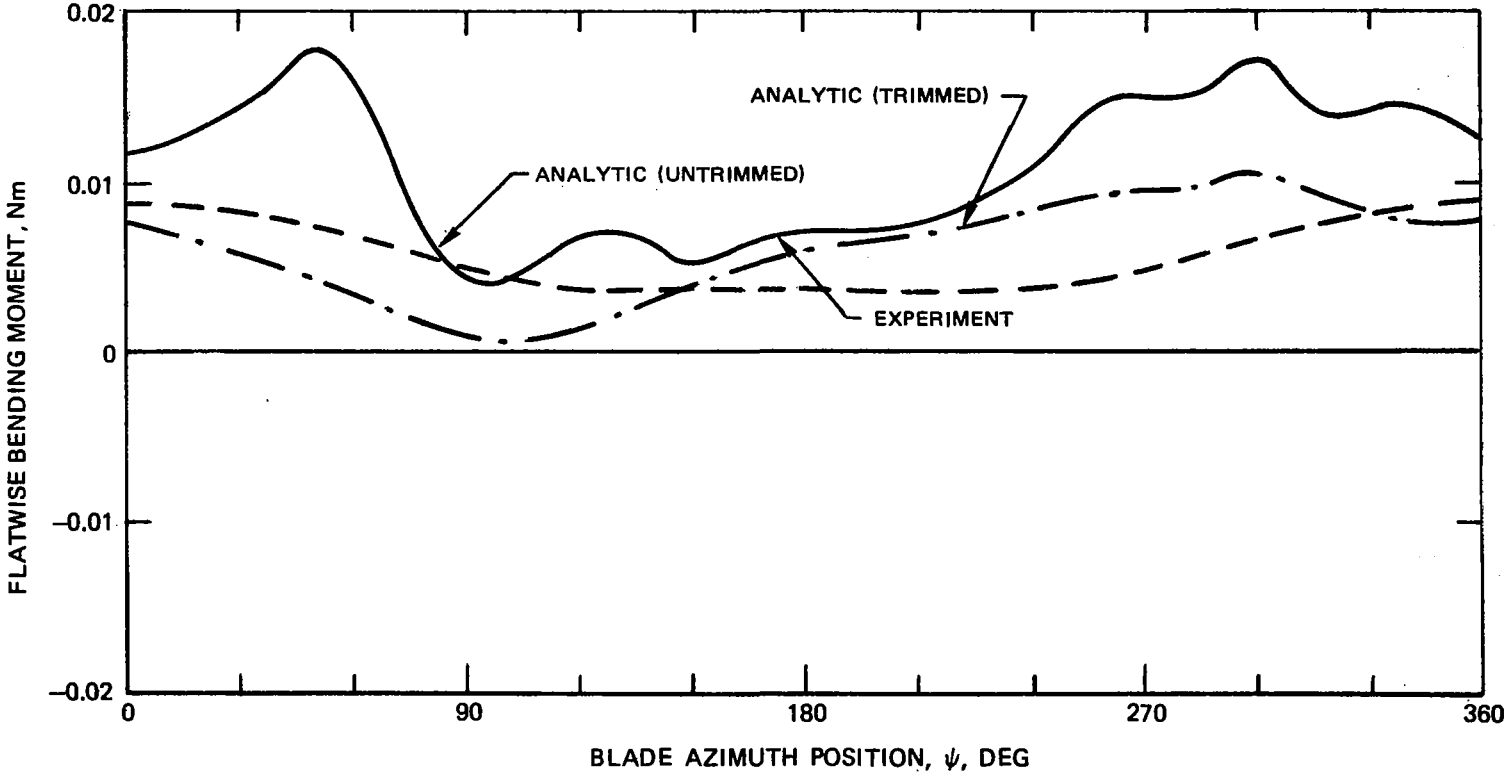

Figure 51. -Experimental and Analytic Time-Histories of Outboard Flatwise Bending Moments, r = 0.42 R, Case 25.03, C_L/σ = 0.0783, μ = 0.25, b = 2.

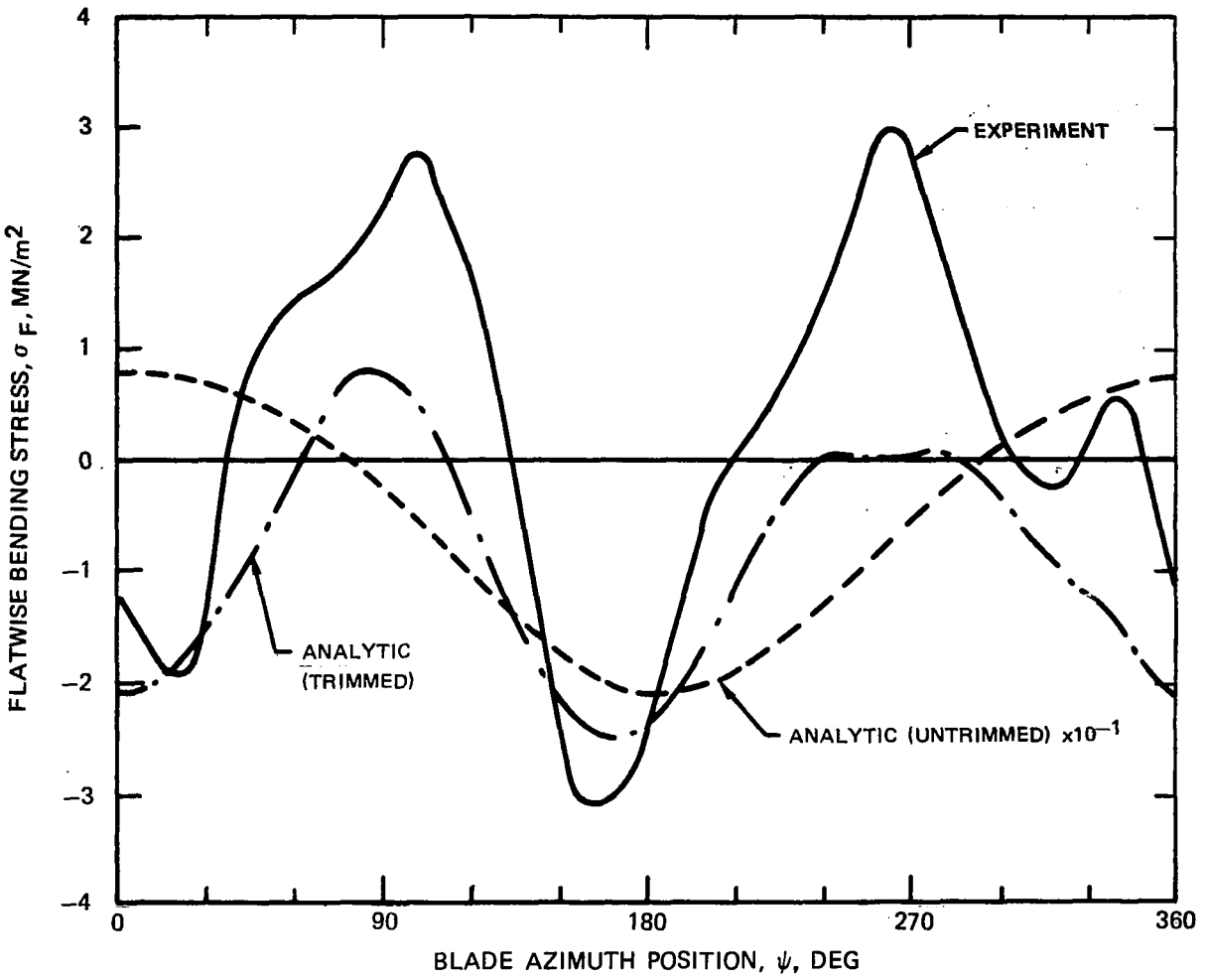

Figure 52. -Experimental and Analytic Time-Histories of Inboard Flatwise Bending Stresses, r = 0.06 R, Case 87.08, C_L/σ = 0.0741, μ = 0.25, b = 4.

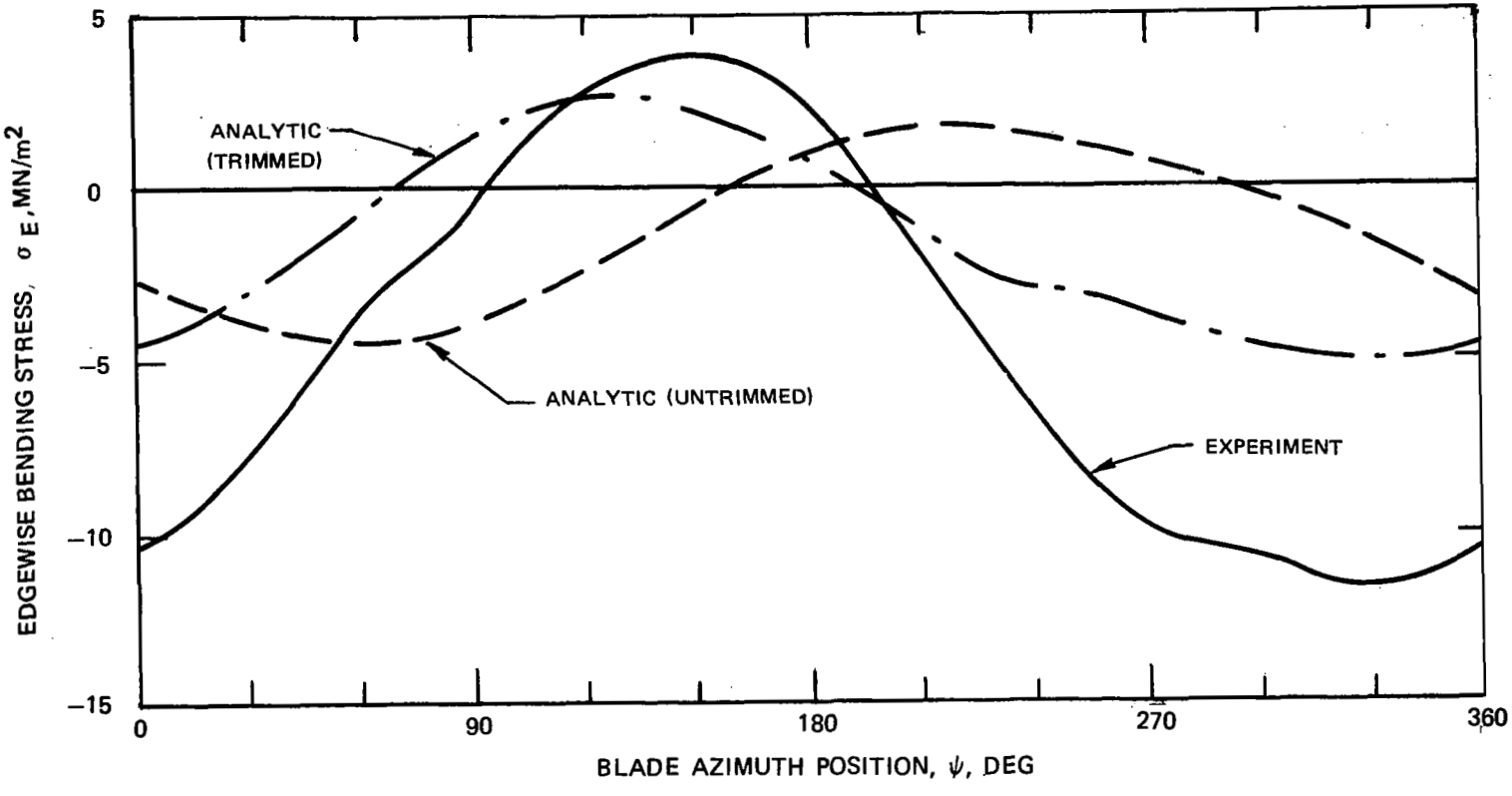

Figure 53. -Experimental and Analytic Time-Histories of Inboard Edgewise Bending Stresses, r = 0.06 R, Case 87.08, C_L/σ = 0.0741, μ = 0.25, b = 4.

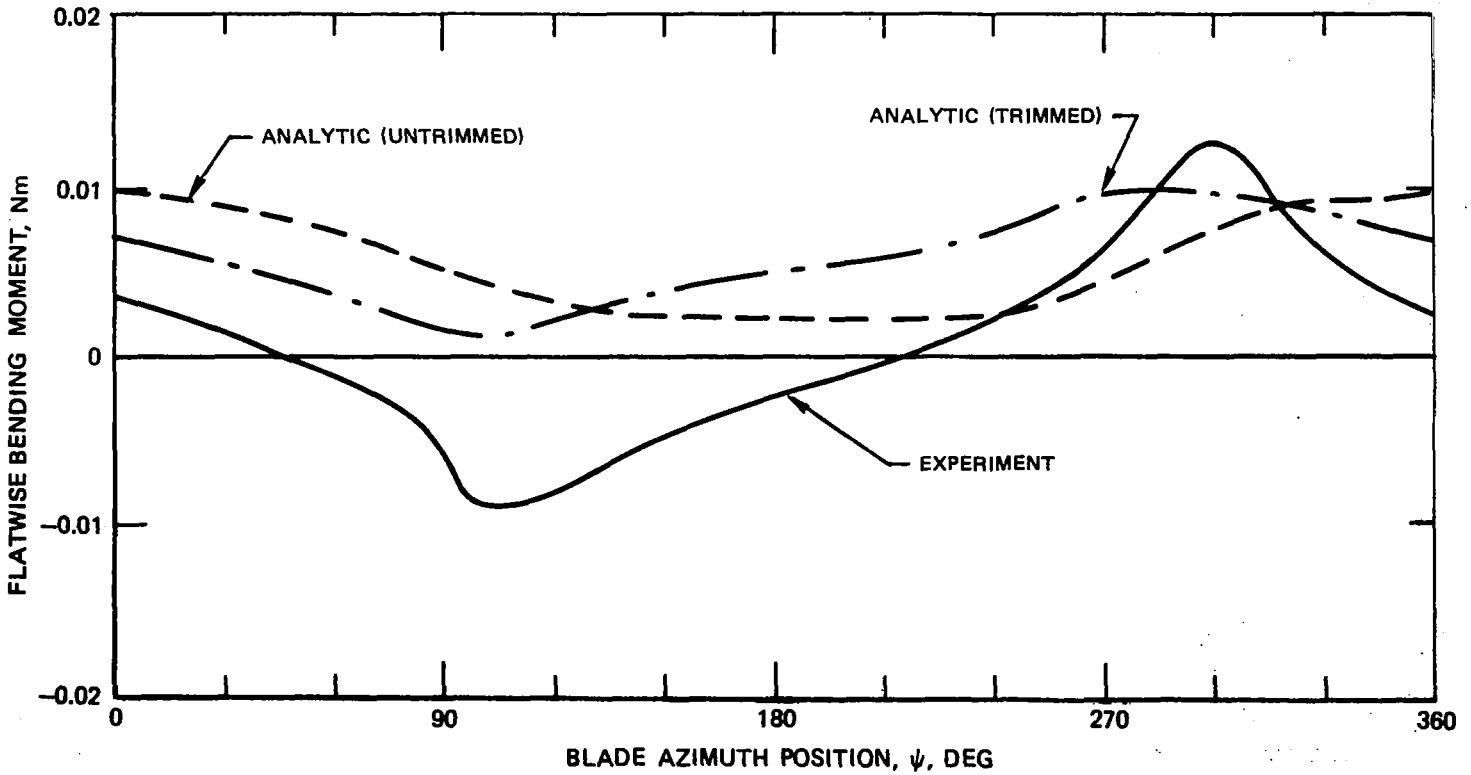

Figure 54. -Experimental and Analytic Time-Histories of Outboard Flatwise Bending Moments, r = 0.42 R, Case 87.08, C_L/σ = 0.0741, μ = 0.25, b = 4.

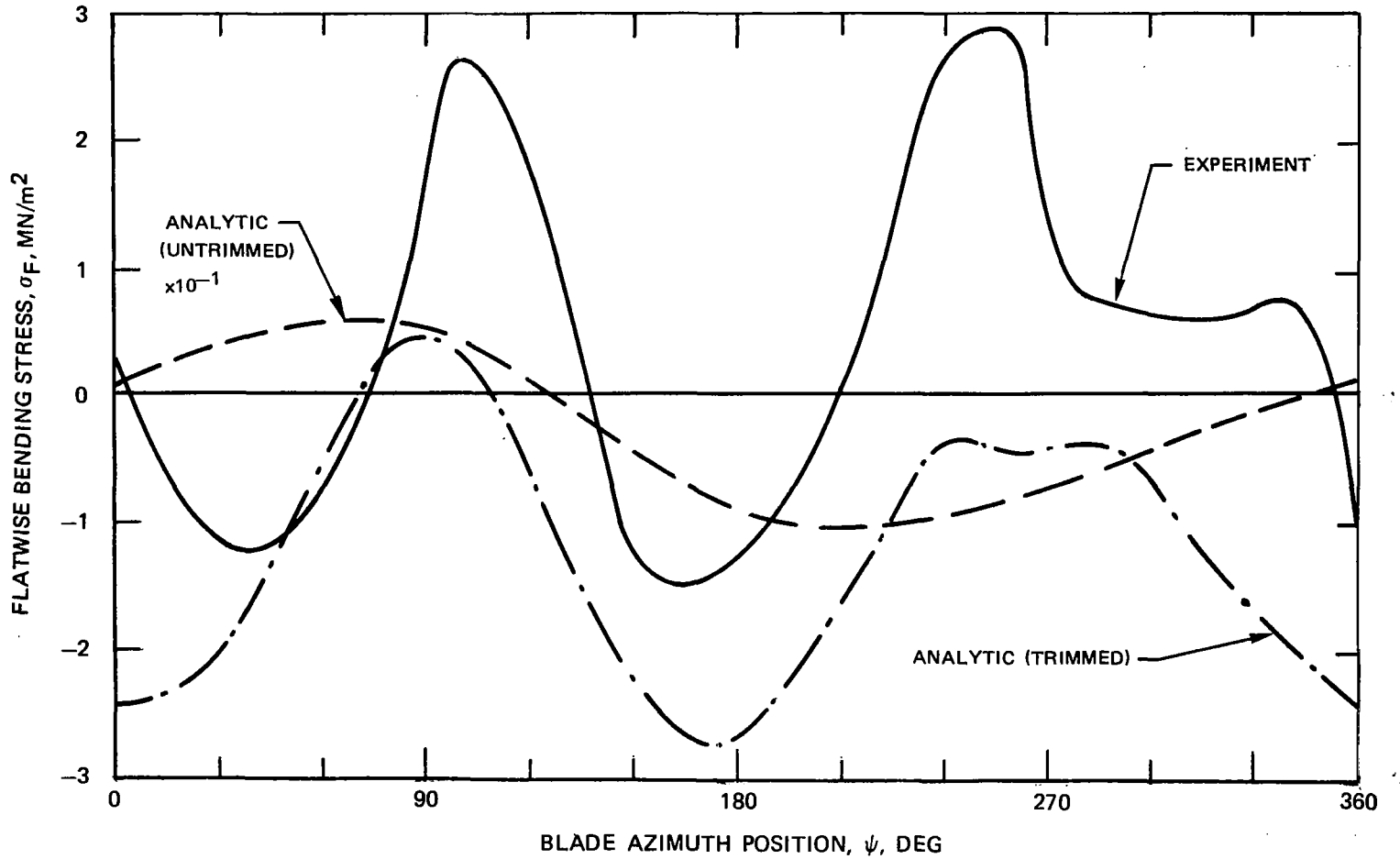

Figure 55. -Experimental and Analytic Time-Histories of Inboard Flatwise Bending Stresses, r = 0.06 R, Case 22.03, C_L/σ = 0.0708, μ = 0.25.

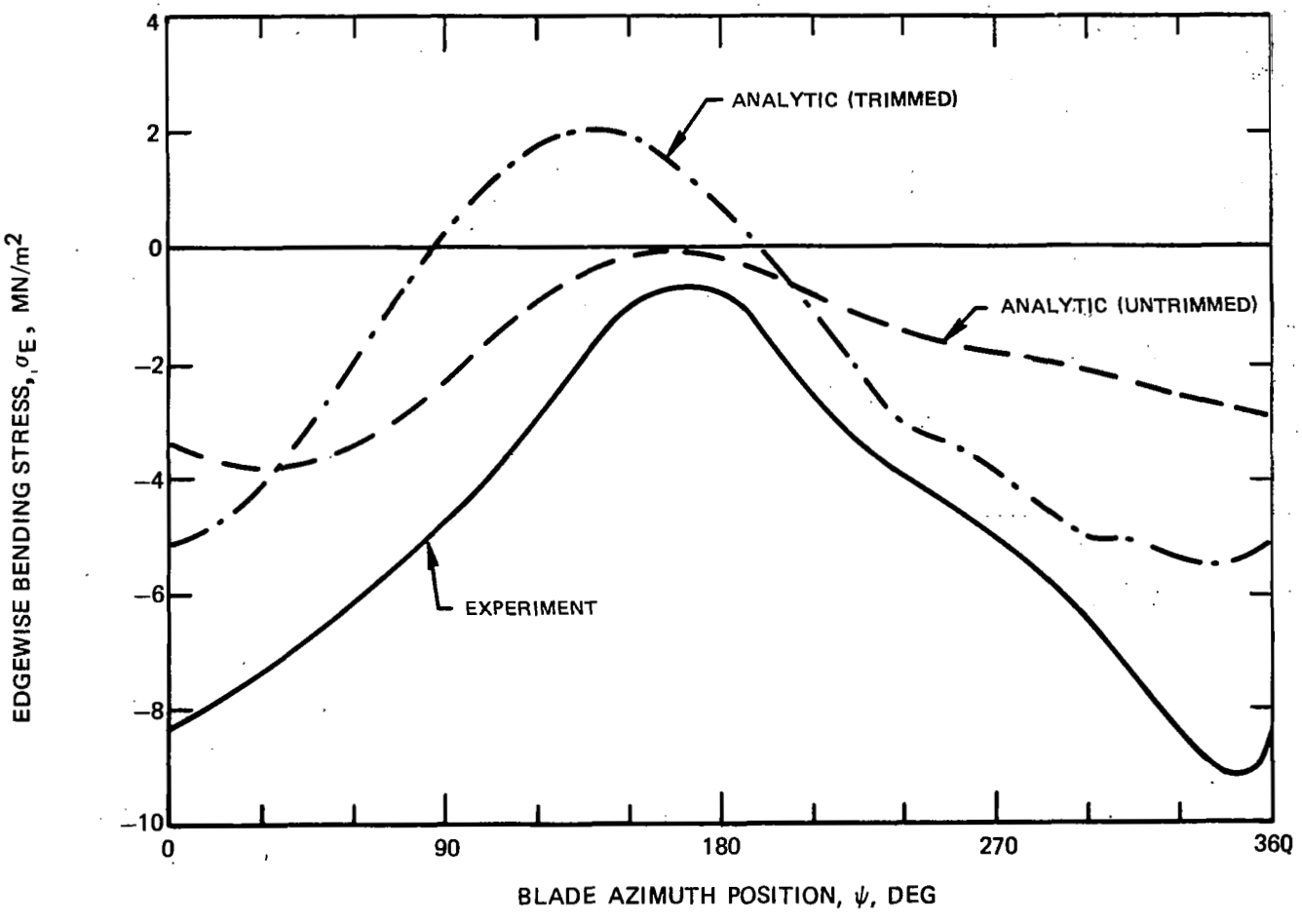

Figure 56. -Experimental and Analytic Time-Histories of Inboard Edgewise Bending Stresses, r = 0.06 R, Case 22.03, C_L/σ = 0.0708, μ = 0.25.

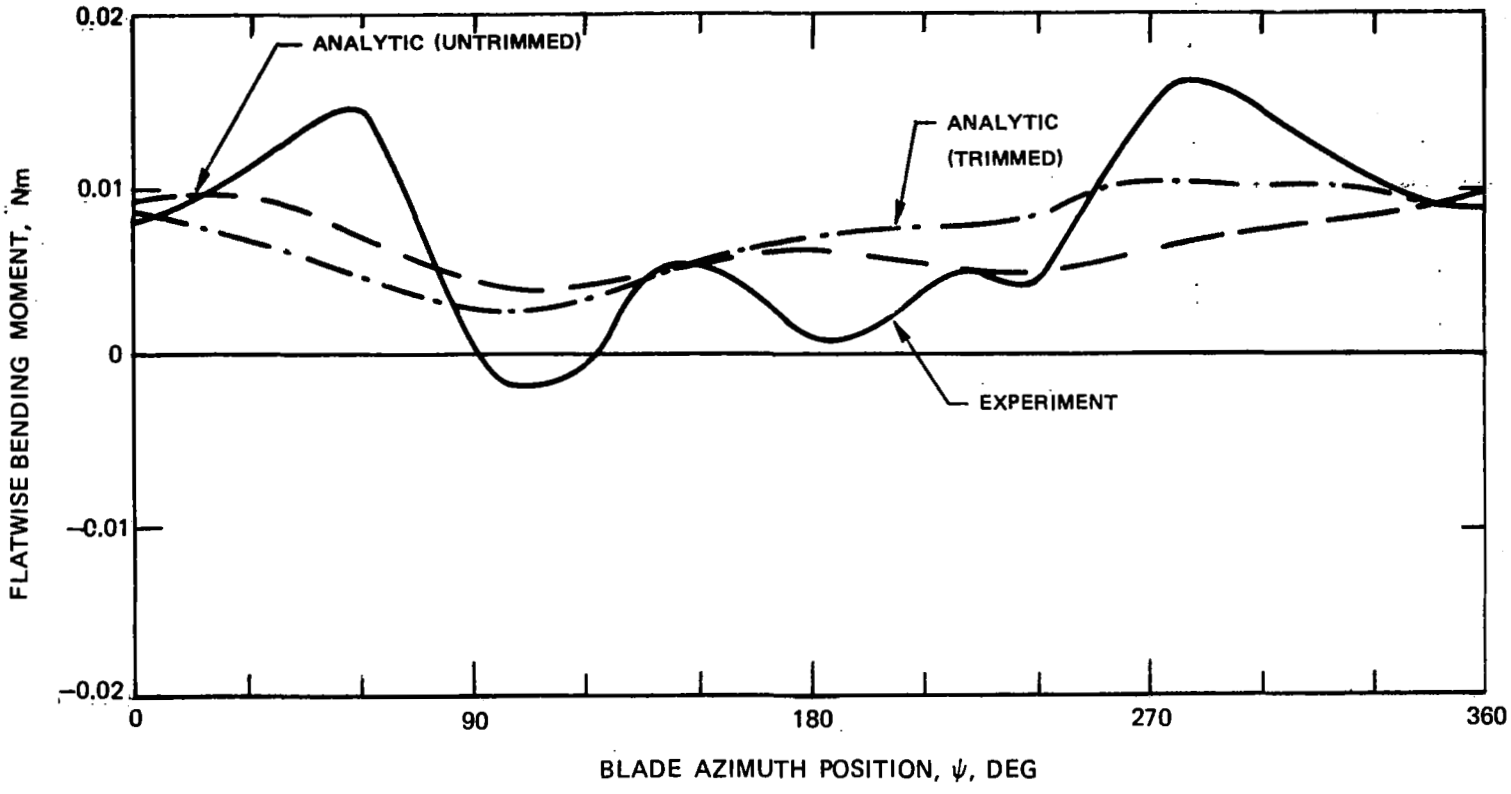

Figure 57. -Experimental and Analytic Time-Histories of Outboard Flatwise Moments, r = 0.42 R, Case 22.03, C_L/σ = 0.0708, μ = 0.25.

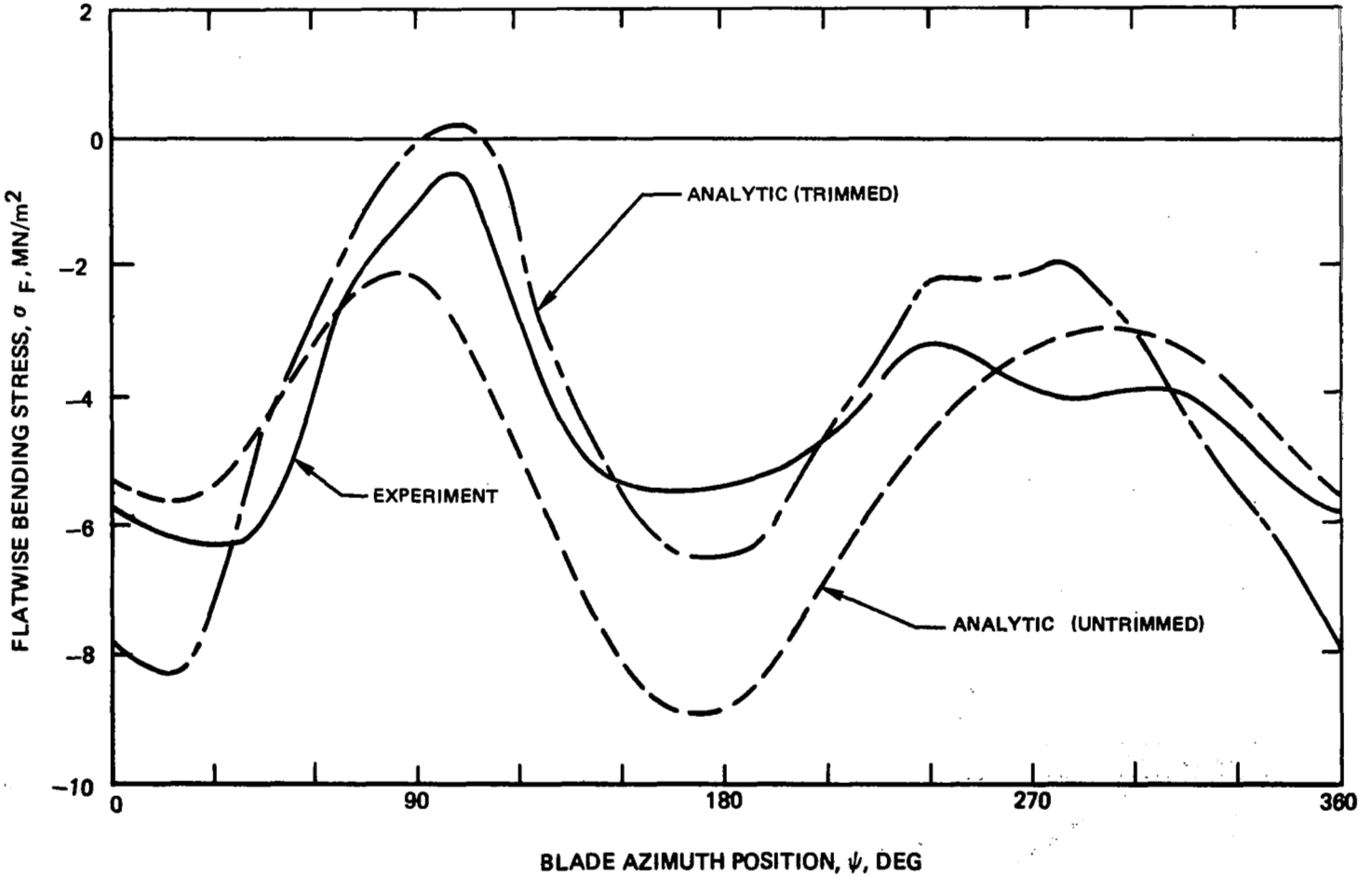

Figure 58. -Experimental and Analytic Time-Histories of Inboard Flatwise Bending Stresses, r = 0.06 R, Case 22.04, C_L/σ = 0.0503, μ = 0.35.

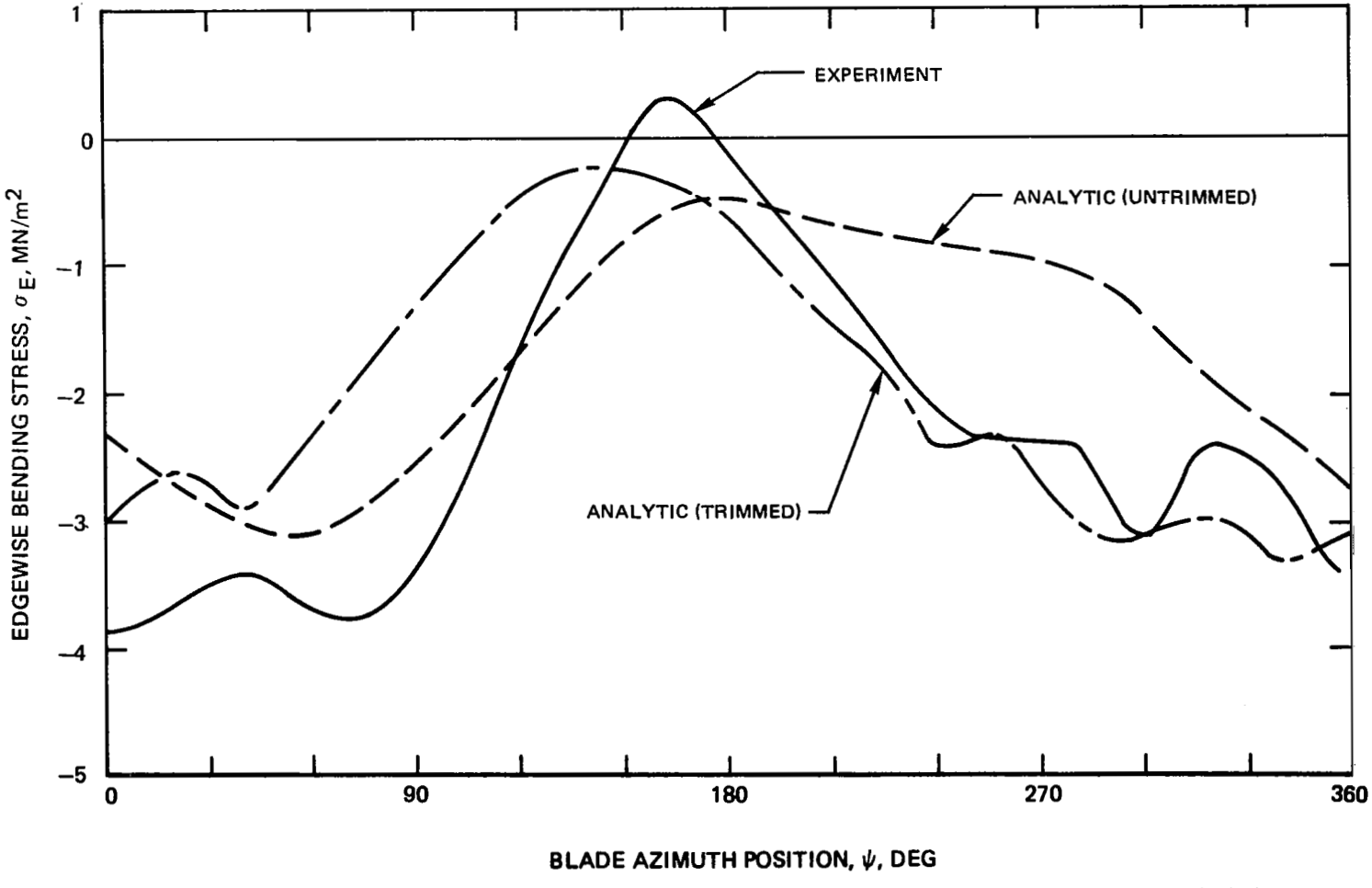

Figure 59. -Experimental and Analytic Time-Histories of Inboard Edgewise Bending Stresses, r = 0.06 R, Case 22.04, C_L/σ = 0.0503, μ = 0.35.

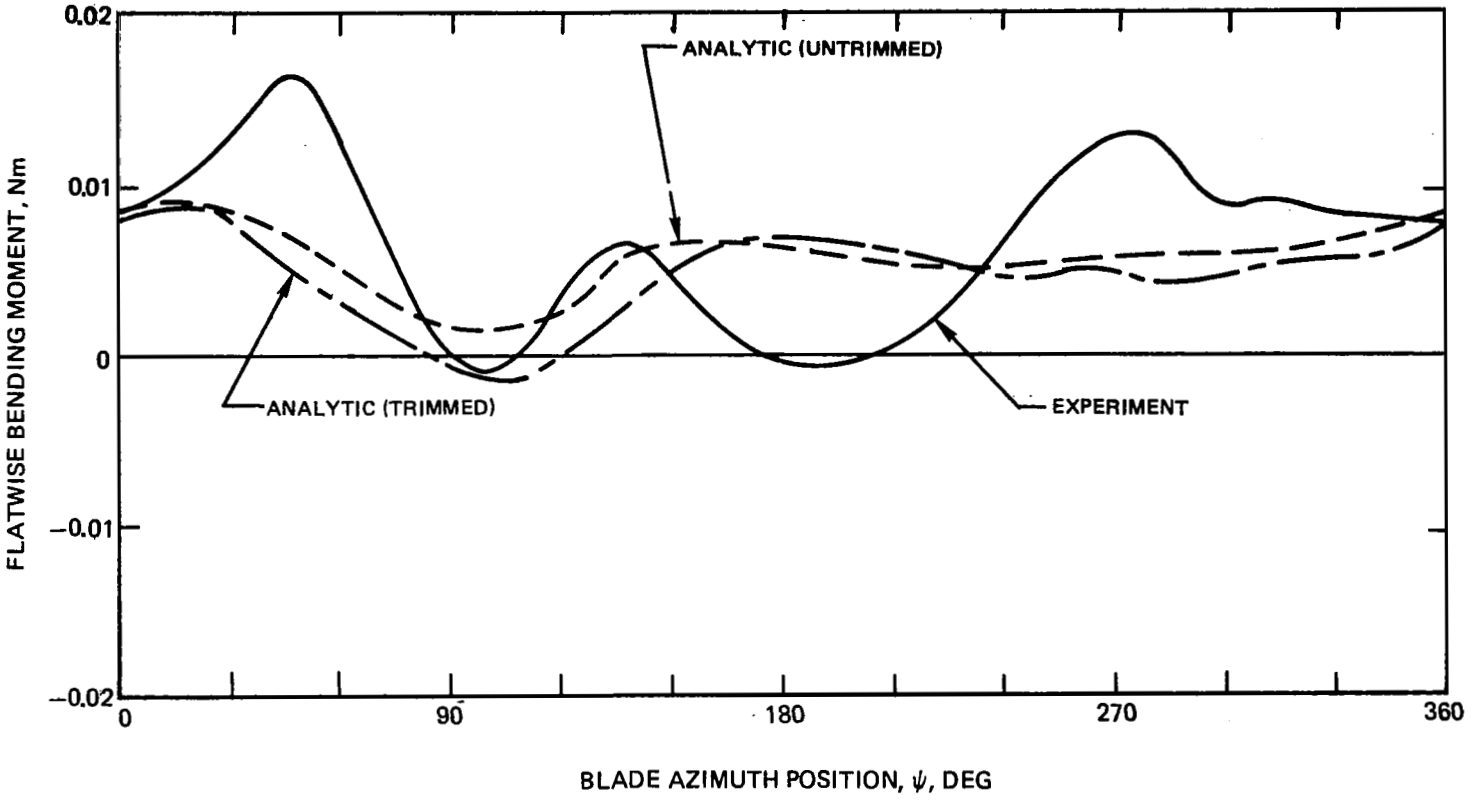

Figure 60. -Experimental and Analytic Time-Histories of Outboard Flatwise Bending Moments, r = 0.42 R, Case 22.04, C_L/σ = 0.0503, μ = 0.35.

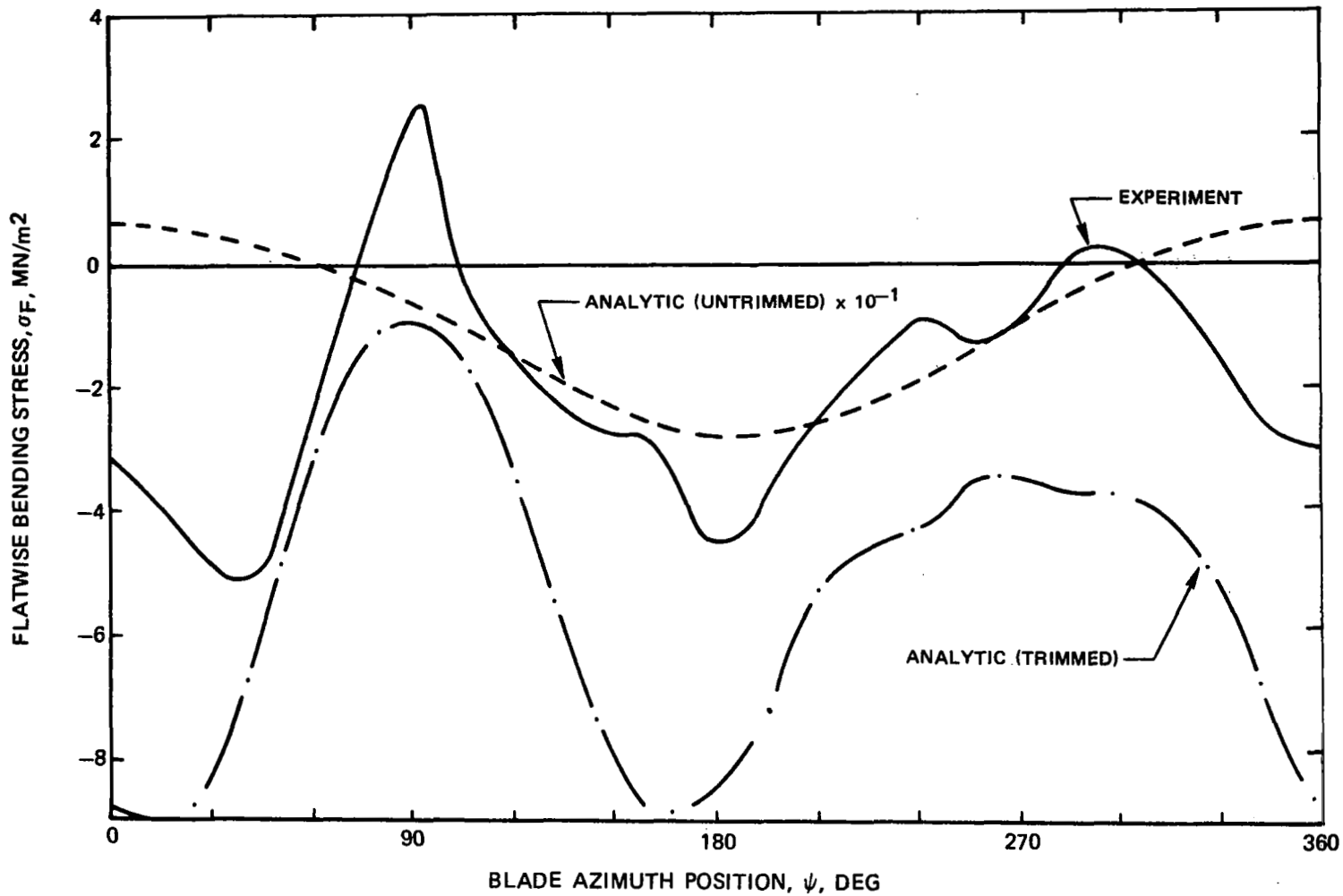

Figure 61. -Experimental and Analytic Time-Histories of Inboard Flatwise Bending Stresses, r = 0.06 R, Case 21.05, C_L/σ = 0.0403, μ = 0.47.

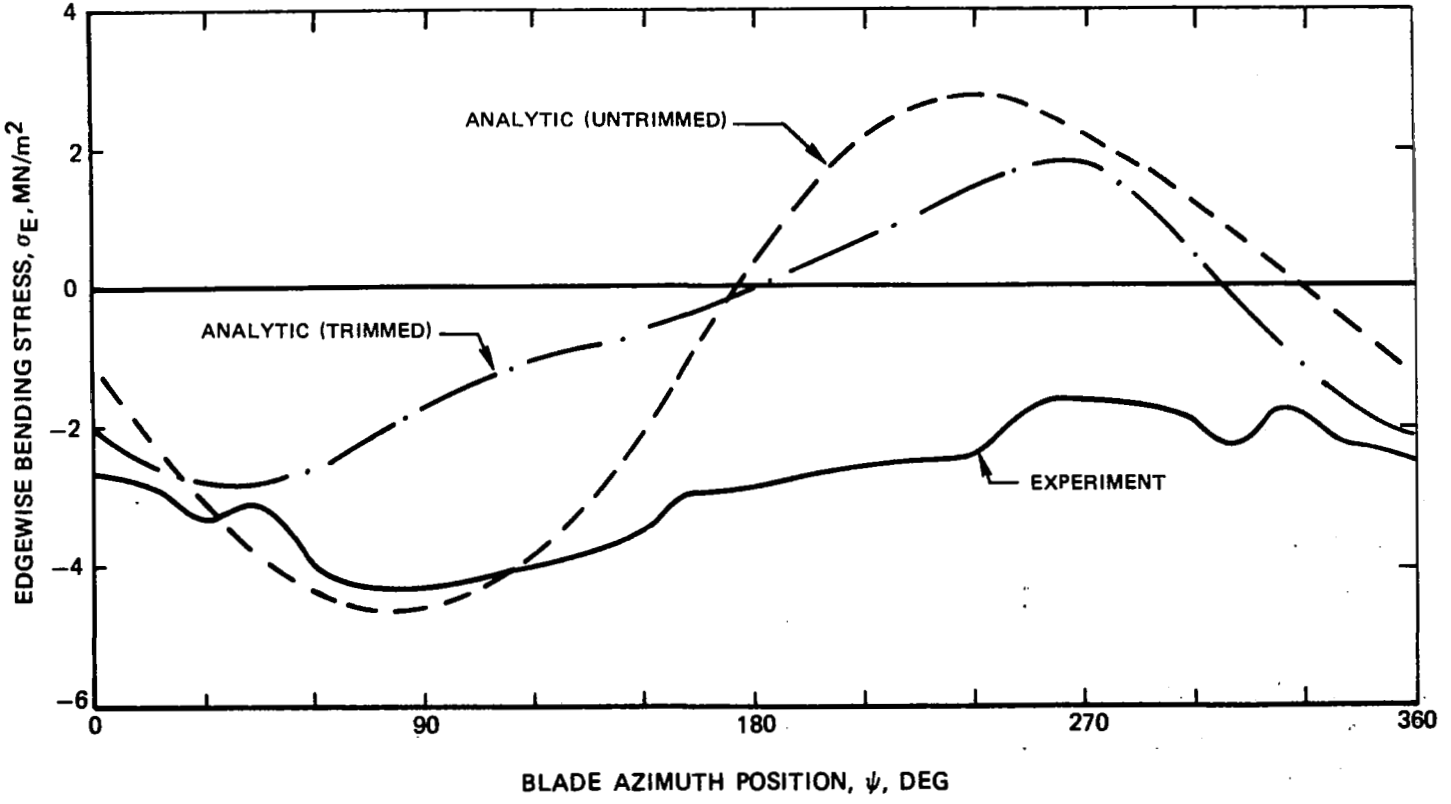

Figure 62. - Experimental and Analytic Time-Histories of Inboard Edgewise Bending Stresses, r = 0.06 R, Case 21.05, C_L/σ = 0.0403, μ = 0.47.

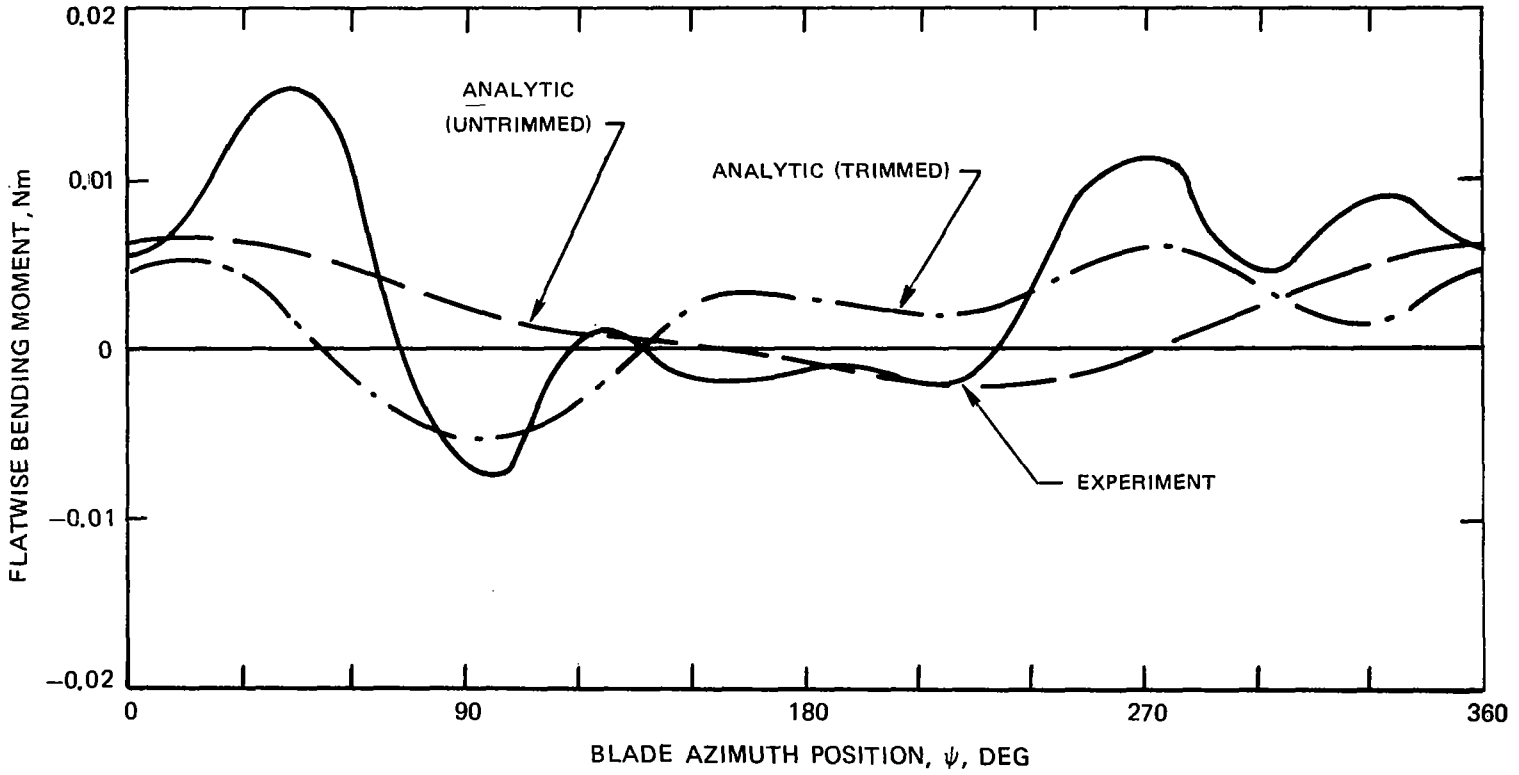

Figure 63. -Experimental and Analytic Time-Histories of Outboard Flatwise Bending Moments, r = 0.42 R, Case 21.05, C_L/σ = 0.0403, μ = 0.47.

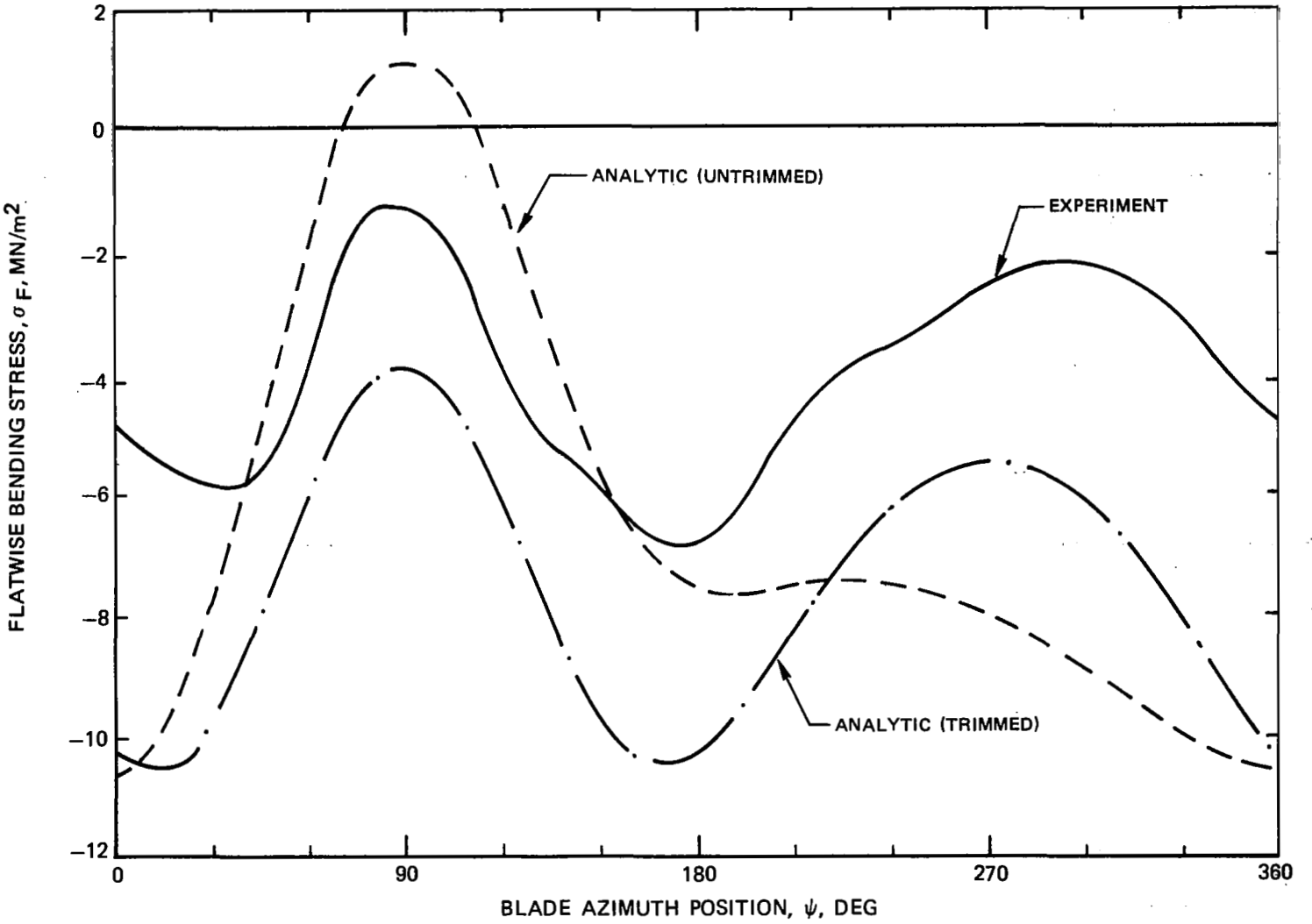

Figure 64. - Experimental and Analytic Time-Histories of Inboard Flatwise Bending Stresses, r = 0.06 R, Case 22.05, C_L/σ = 0.0216, μ = 0.47.

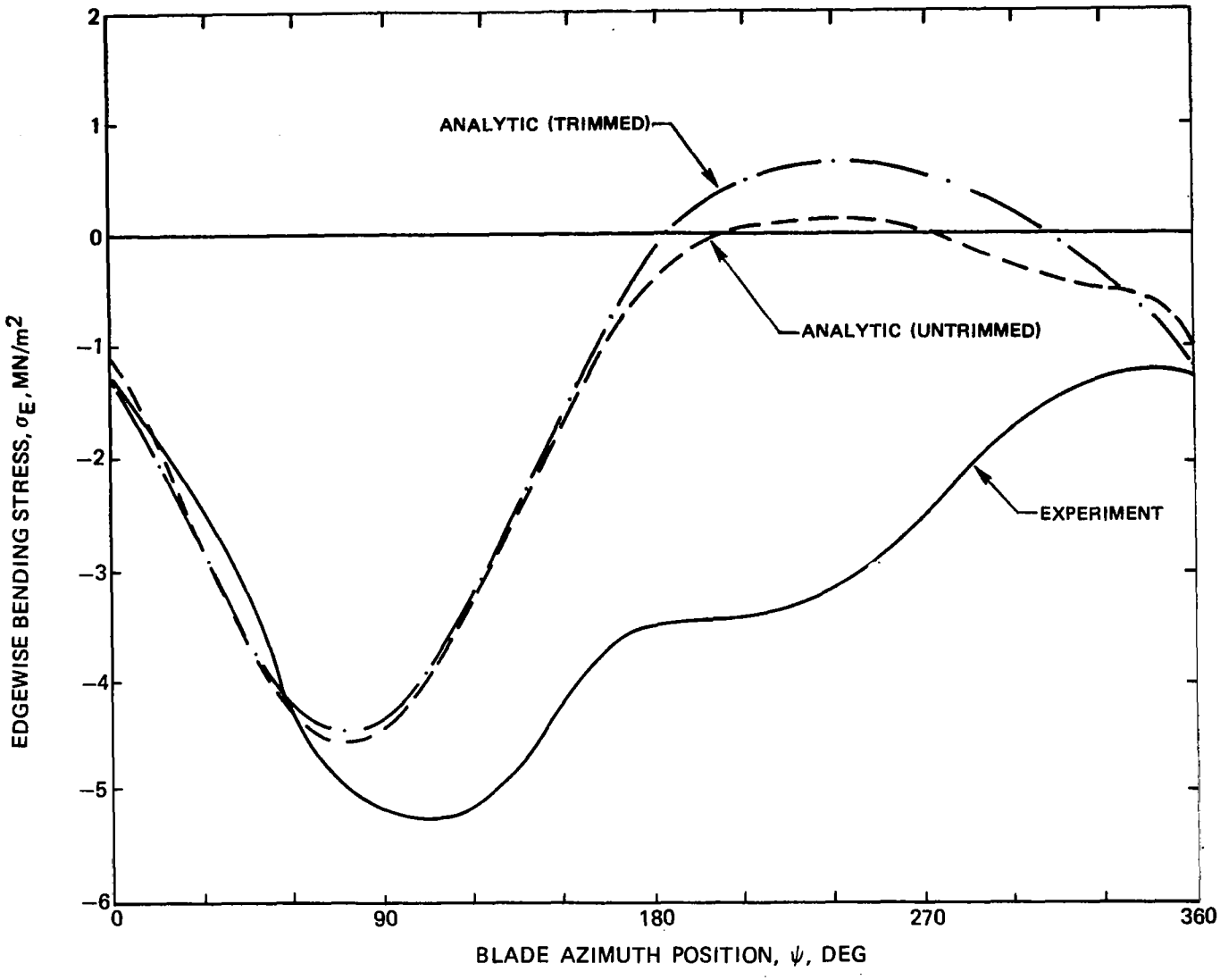

Figure 65. -Experimental and Analytic Time-Histories of Inboard Edgewise Bending Stresses, r = 0.06 R, Case 22.05, C_L/σ = 0.0216, μ = 0.47.

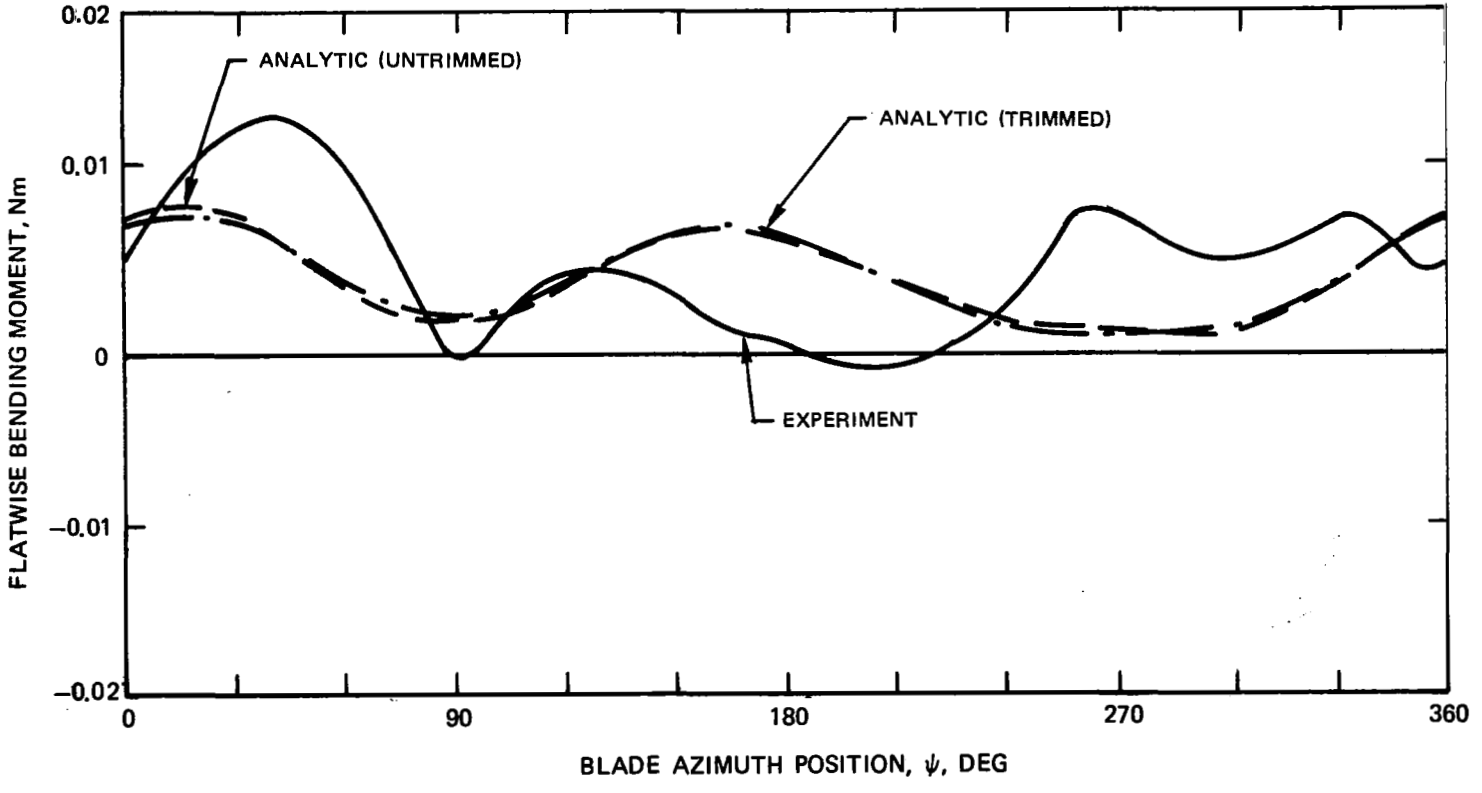

Figure 66. -Experimental and Analytic Time-Histories of Outboard Flatwise Bending Moments, r = 0.42 R, Case 22.05, C_L/σ = 0.0216, μ = 0.47.

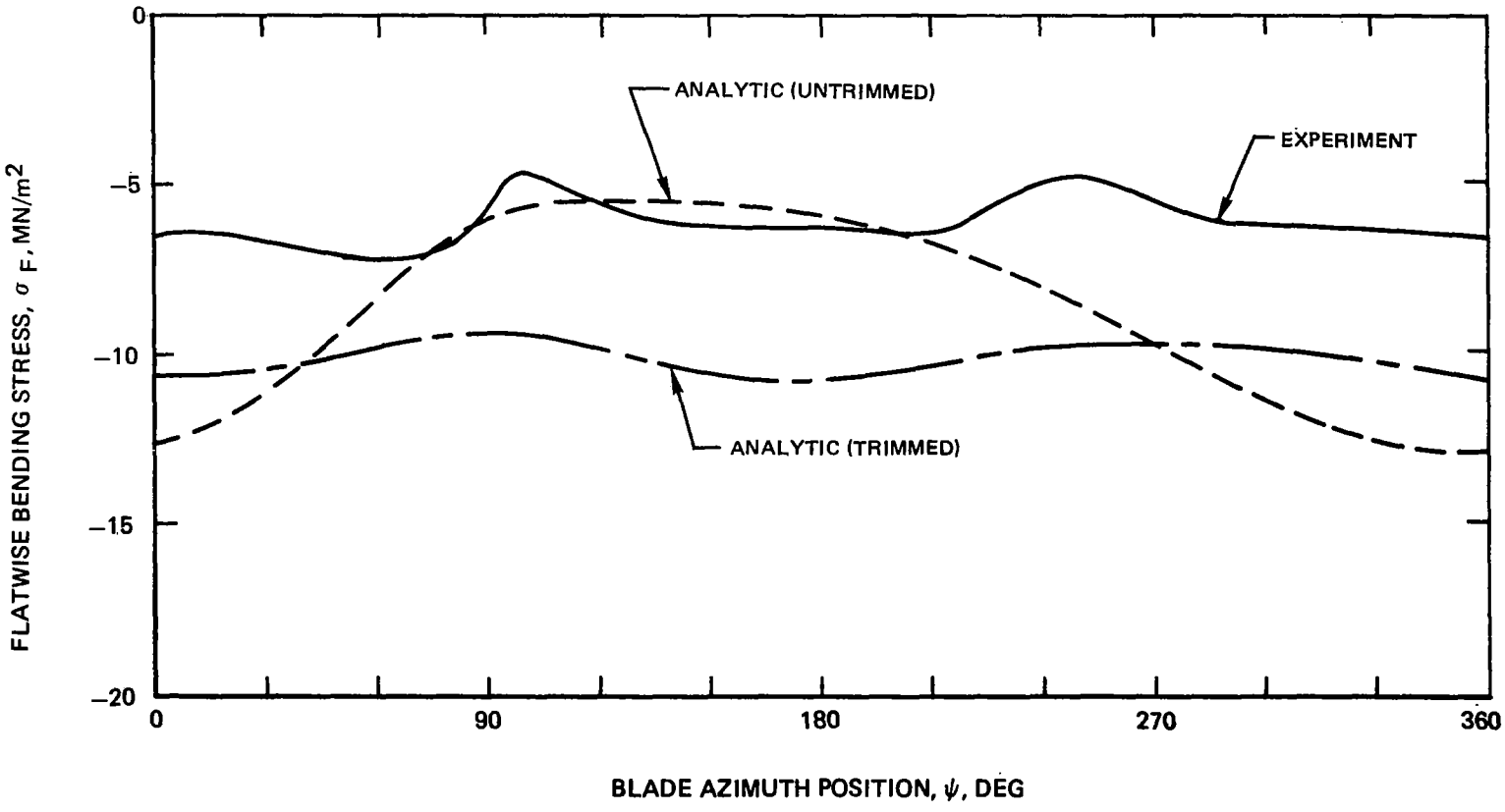

Figure 67. -Experimental and Analytic Time-Histories of Inboard Flatwise Bending Stresses, r = 0.06 R, Case 11.05, C_L/σ = 0.0014, μ = 0.35.

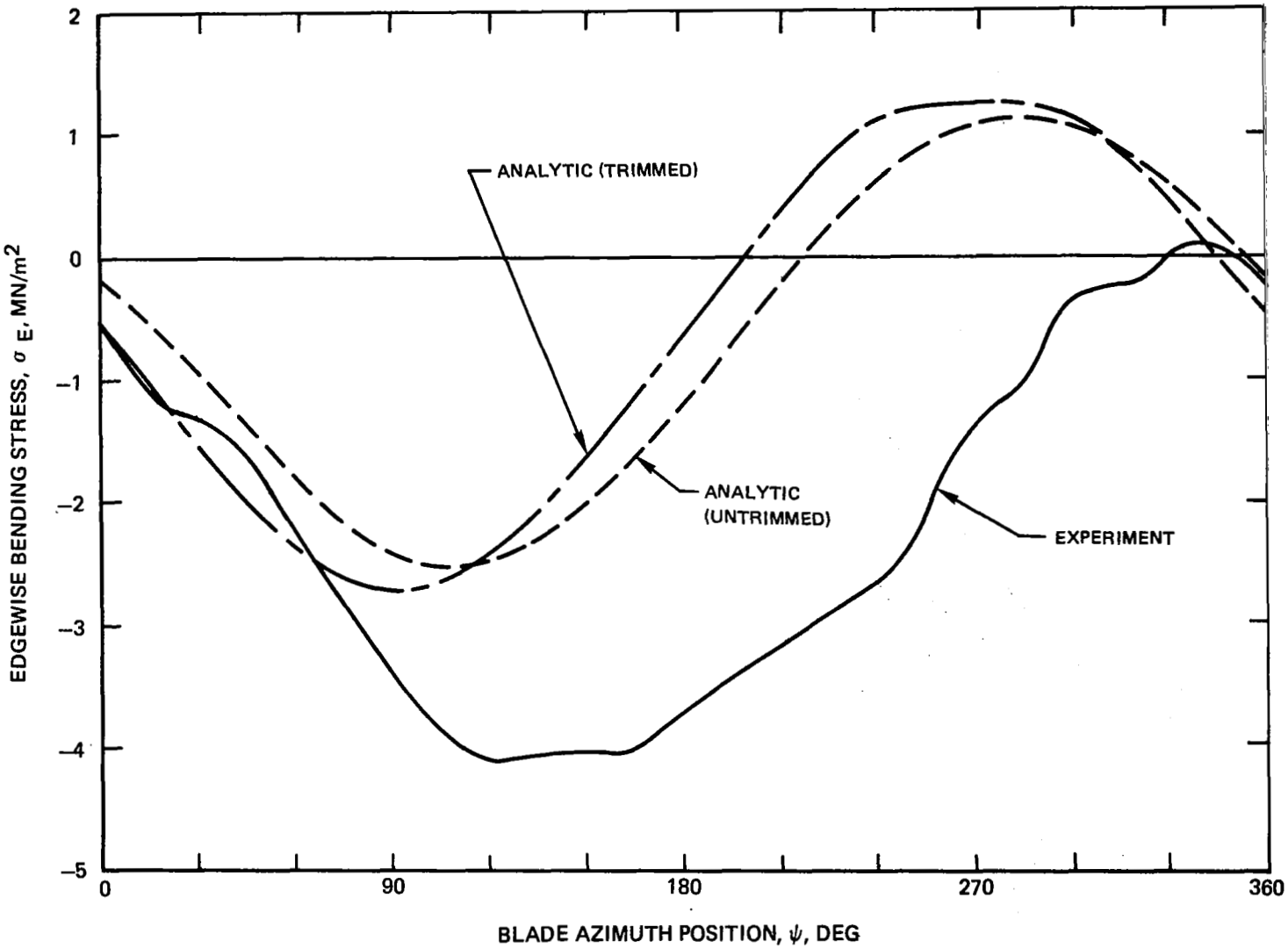

Figure 68. -Experimental and Analytic Time-Histories of Inboard Edgewise Bending Stresses, r = 0.06 R, Case 11.05, C_L/σ = 0.0014, μ = 0.35.

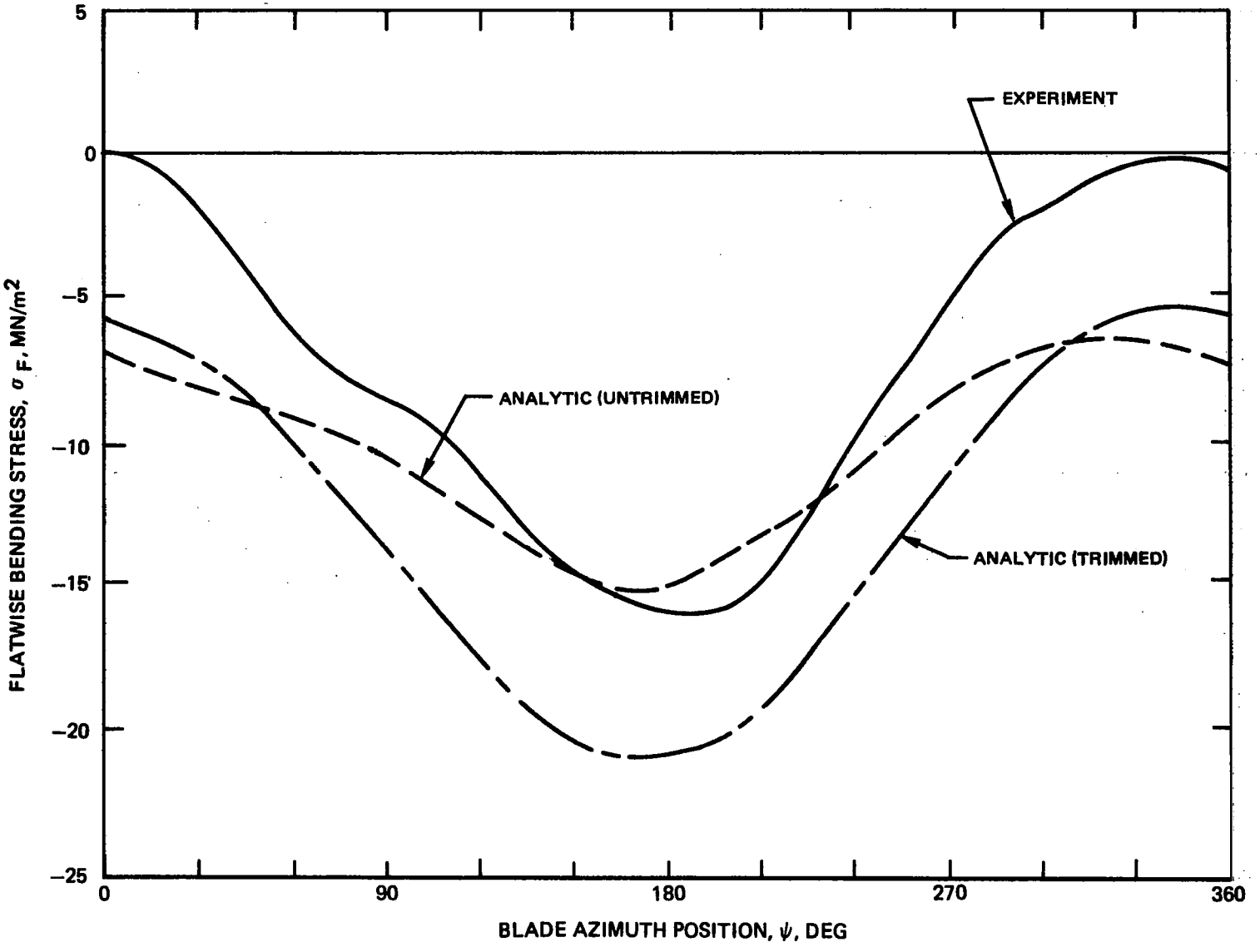

Figure 69. -Experimental and Analytic Time-Histories of Inboard Flatwise Bending Stresses, r = 0.06 R, Case 11.06, $C_L/\sigma = -0.0145$, $\mu = 0.35$.

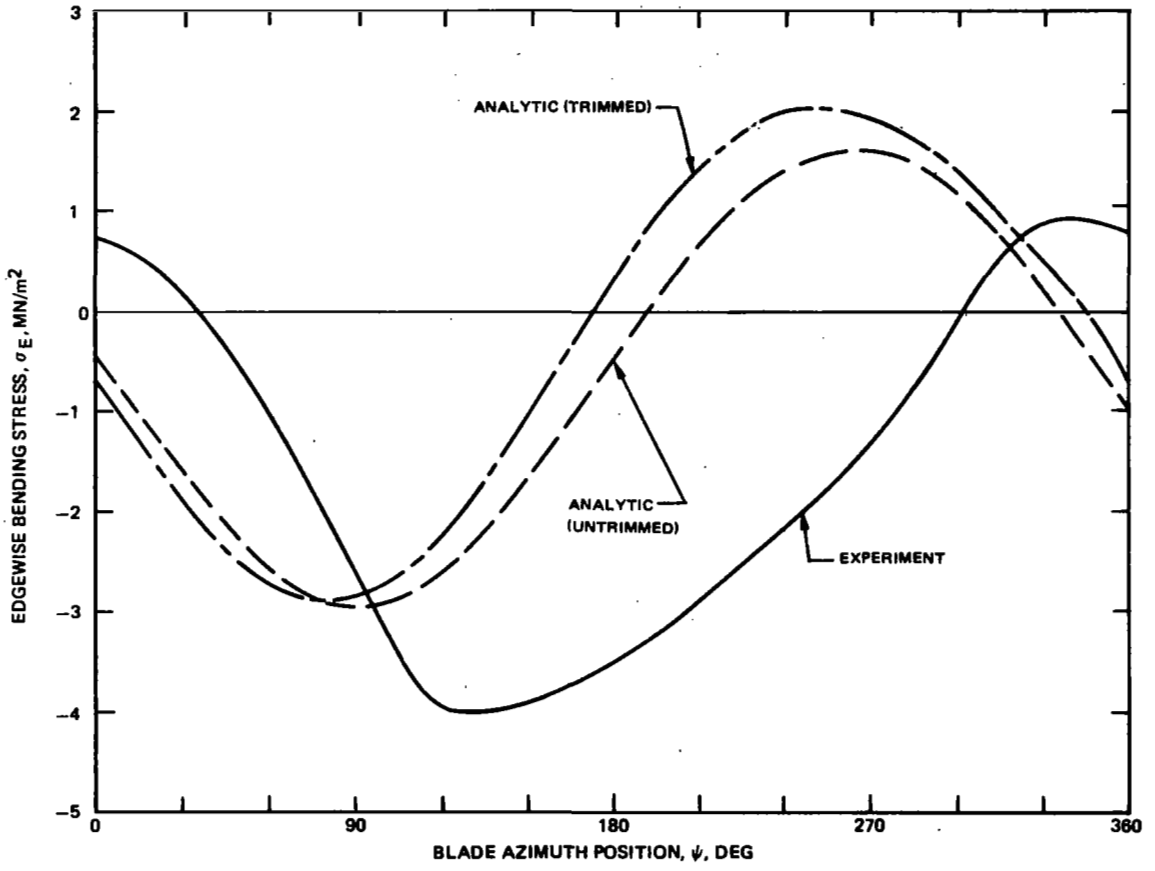

Figure 70. -Experimental and Analytic Time-Histories of Inboard Edgewise Bending Stresses, r = 0.06 R, Case 11.06, $C_L/\sigma = -0.0145$, $\mu = 0.35$.

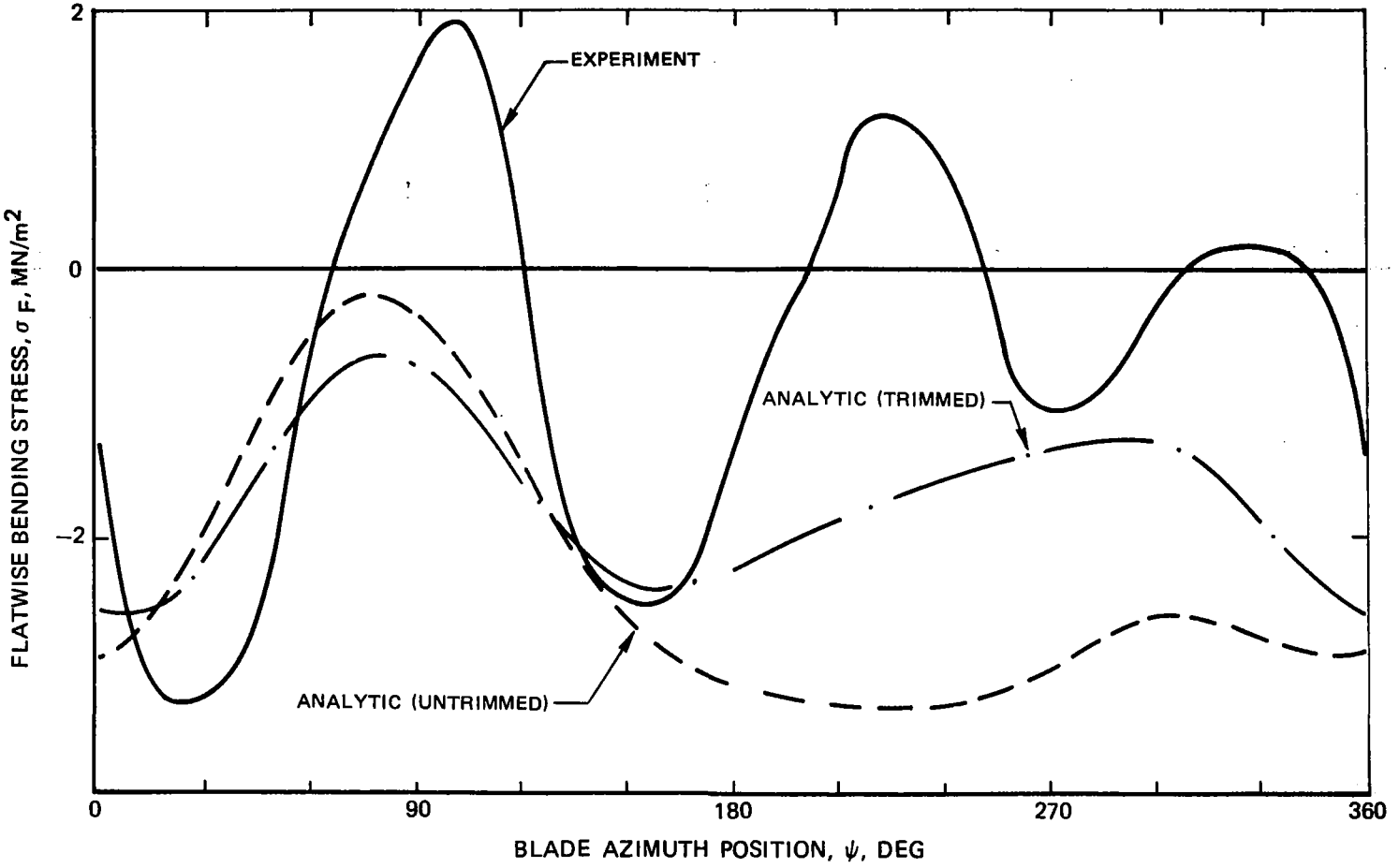

Figure 71. -Experimental and Analytic Time-Histories of Inboard Flatwise Bending Stresses, r = 0.06 R, Case 82.10, C_L/σ = 0.0638, μ = 0.25.

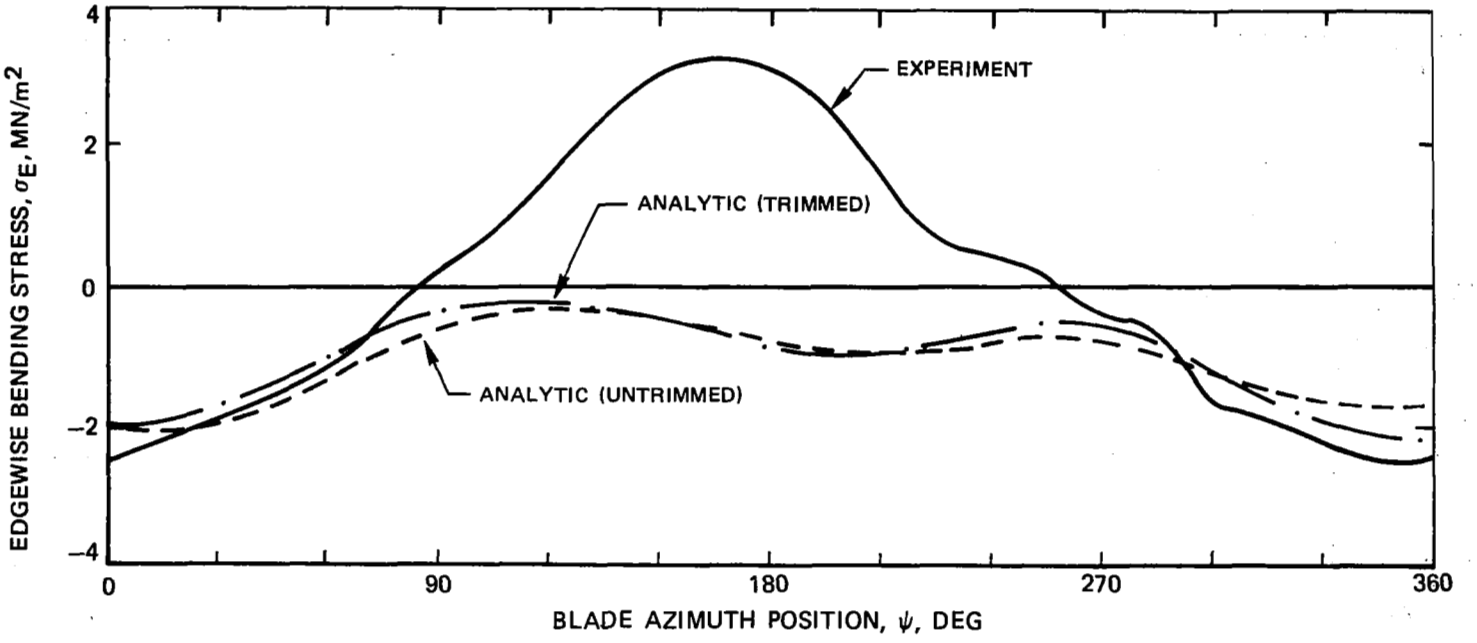

Figure 72. -Experimental and Analytic Time-Histories of Inboard Edgewise Bending Stresses, r = 0.06 R, Case 82.10, C_L/σ = 0.0638, μ = 0.25.

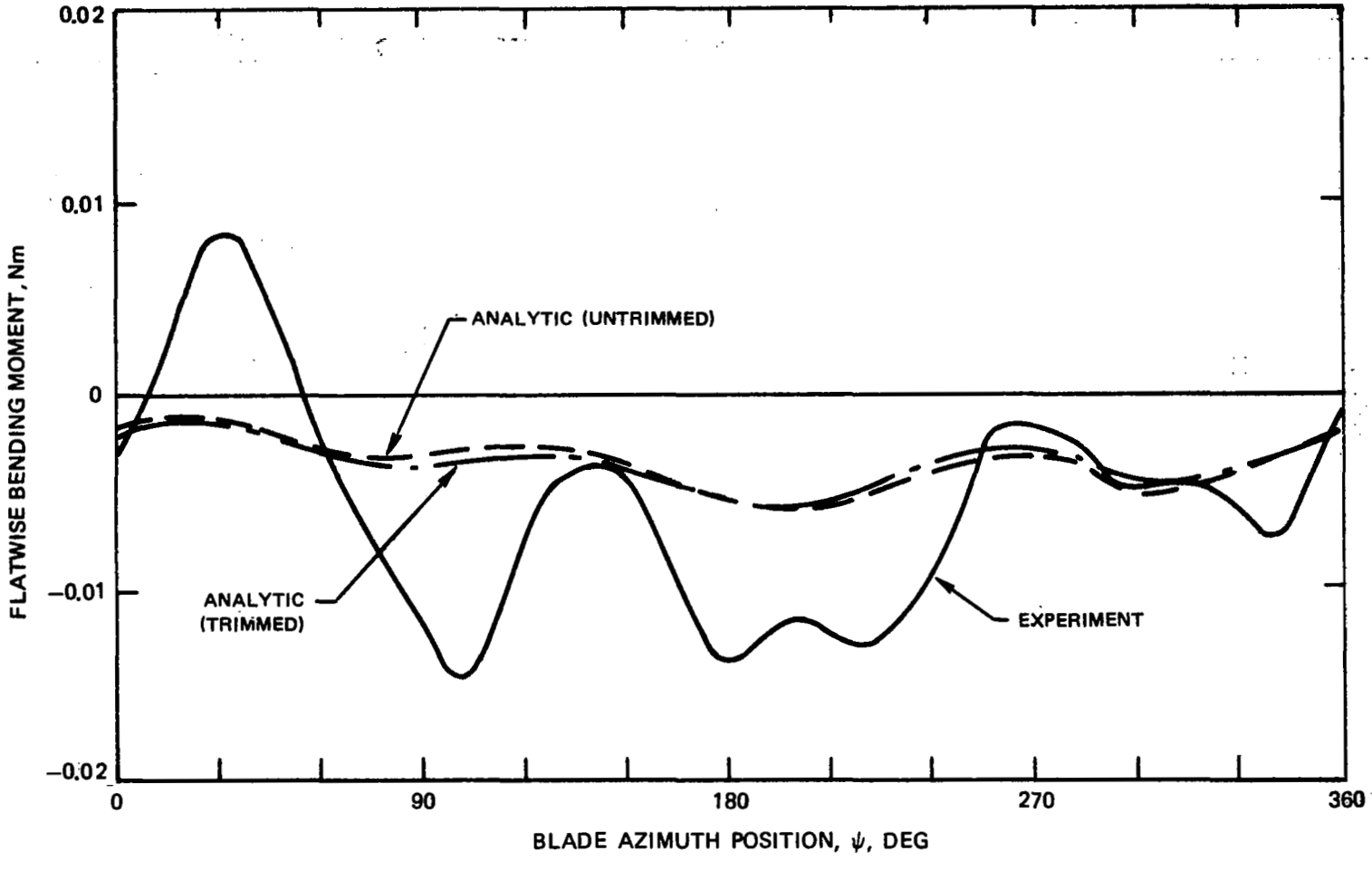

Figure 73. -Experimental and Analytic Time-Histories of Outboard Flatwise Bending Moments, r = 0.42 R, Case 82.10, C_L/σ = 0.0638, μ = 0.25.

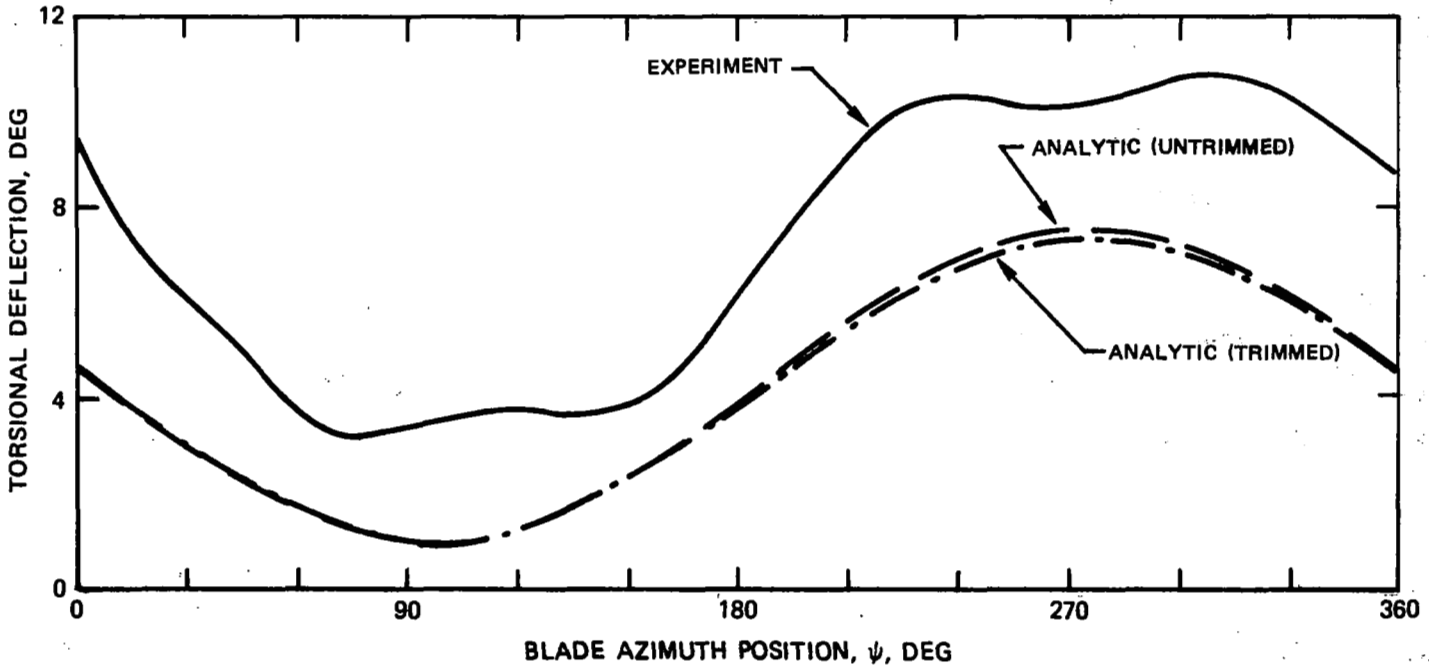

Figure 74. -Experimental and Analytic Time-Histories of Flexbeam Torsional Deflections, Case 82.10, C_L/σ = 0.0638, μ = 0.25.

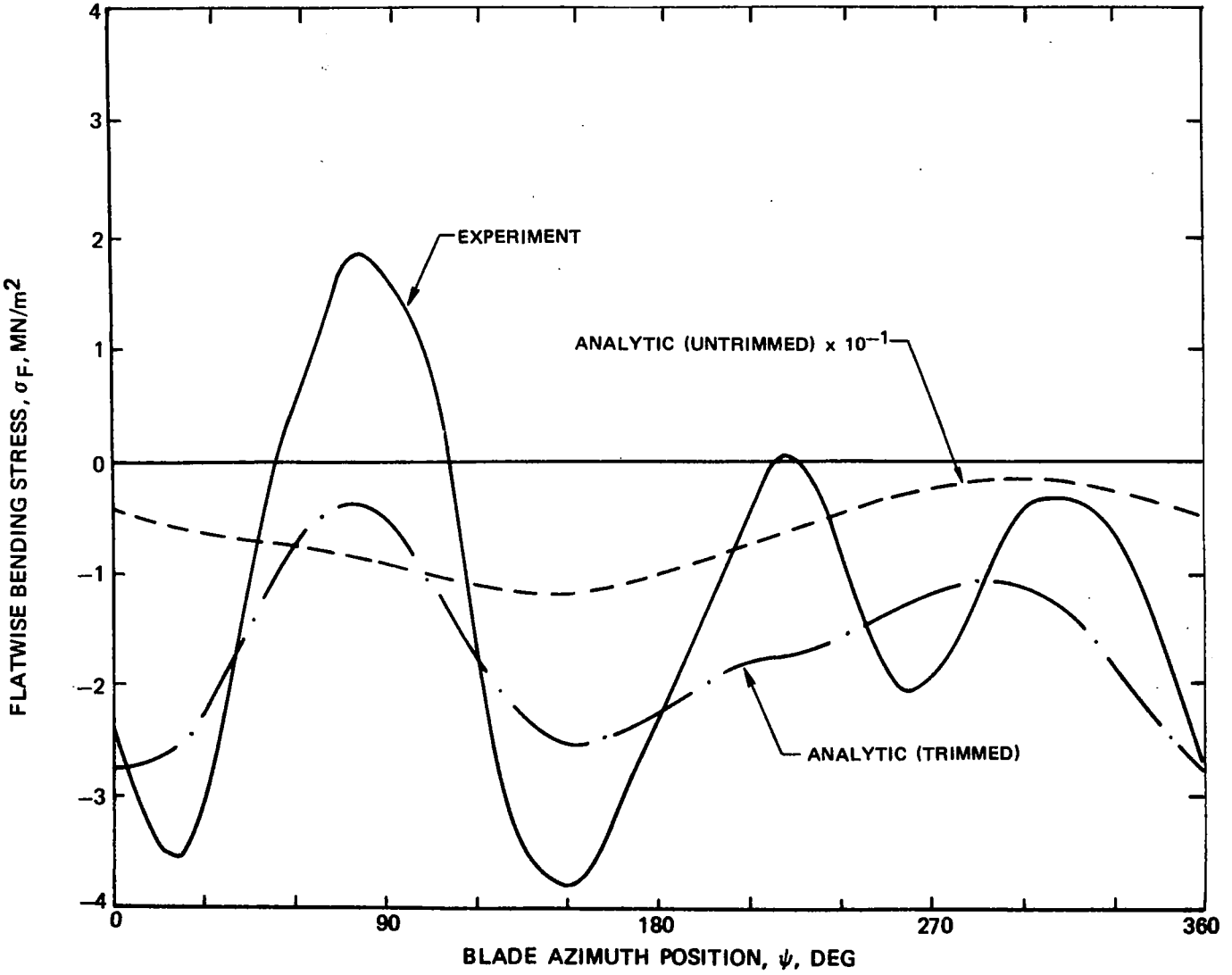

Figure 75. -Experimental and Analytic Time-Histories of Inboard Flatwise Bending Stresses, r = 0.06 R, Case 83.08, C_L/σ = 0.0704, μ = 0.25.

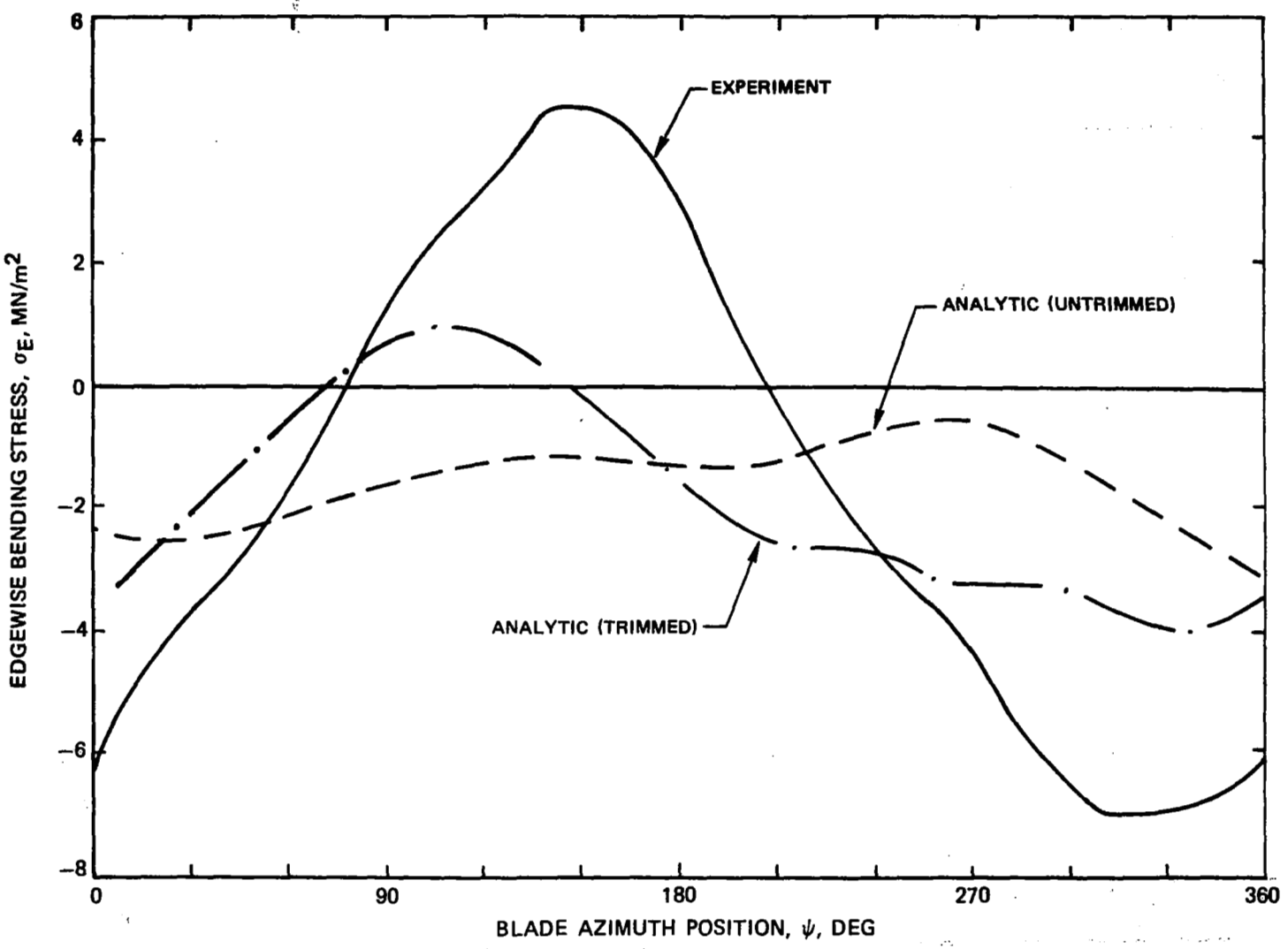

Figure 76. -Experimental and Analytic Time-Histories of Inboard Edgewise Bending Stresses, r = 0.06 R, Case 83.08, C_L/σ = 0.0704, μ = 0.25.

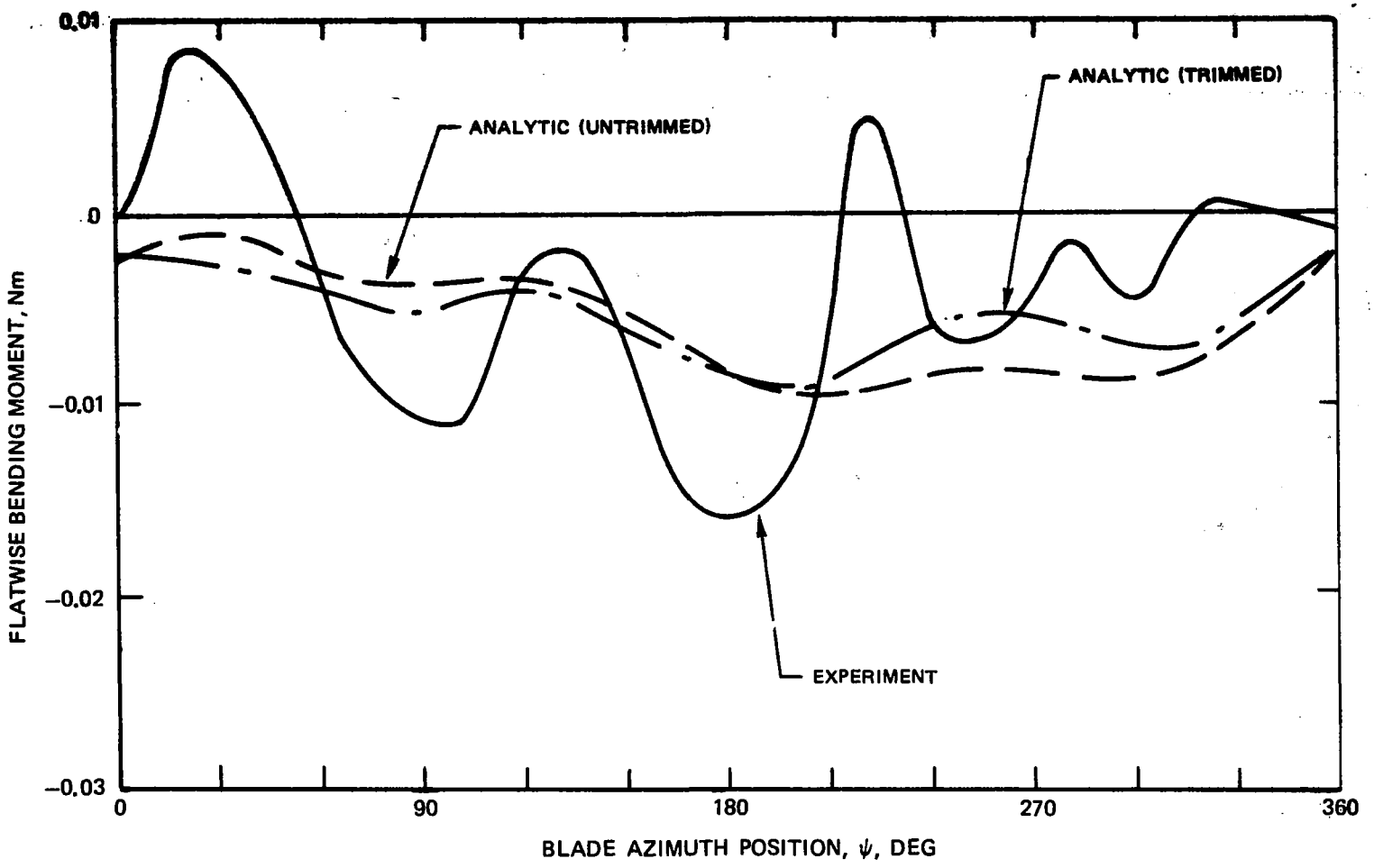

Figure 77. -Experimental and Analytic Time-Histories of Outboard Flatwise Bending Moments, r = 0.42 R, Case 83.08, C_L/σ = 0.0704, μ = 0.25.

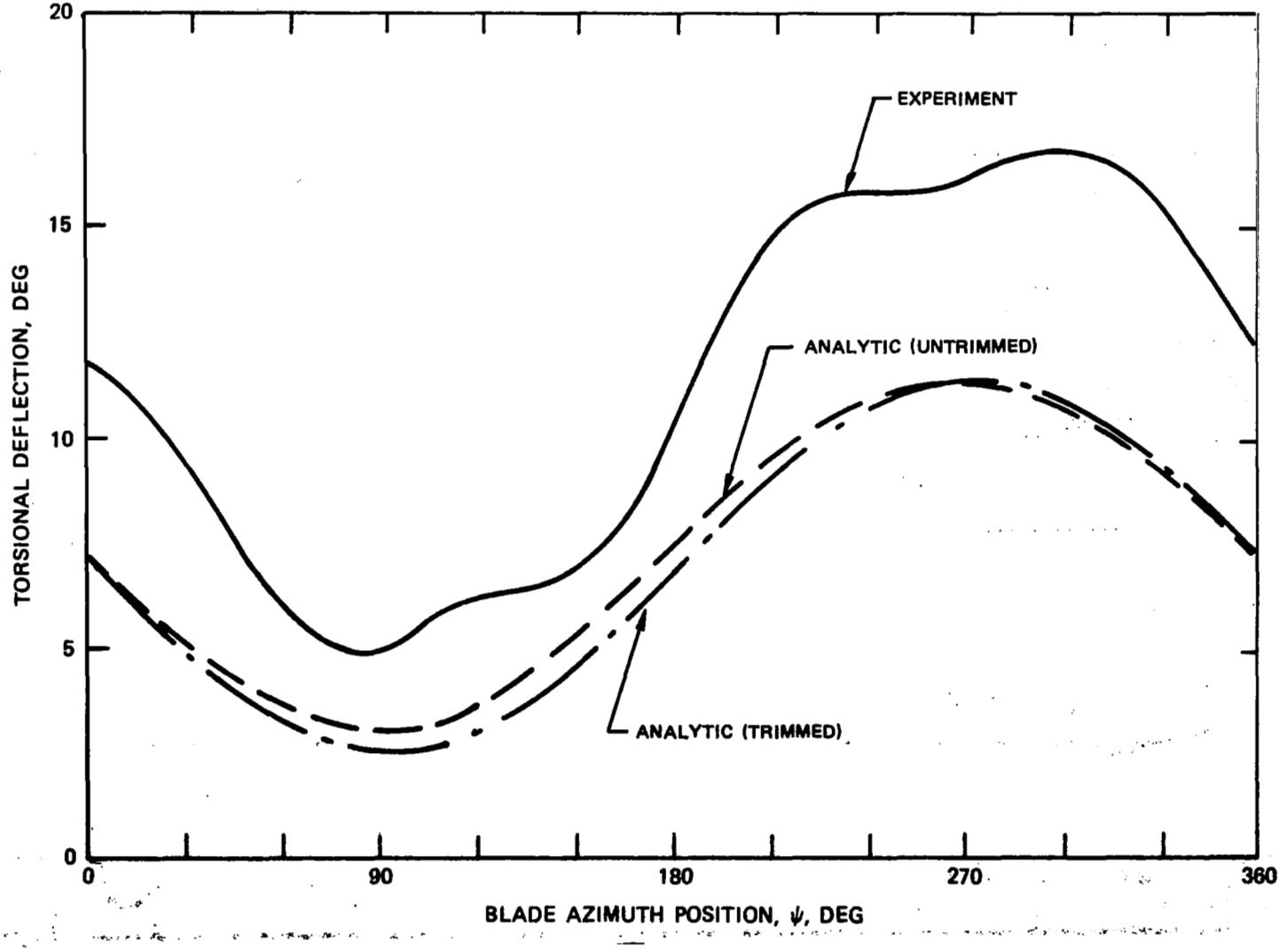

Figure 78. -Experimental and Analytic Time-Histories of Flexbeam Torsional Deflections, Case 83.08, $C_L/\sigma = 0.0704$, $\mu = 0.25$.

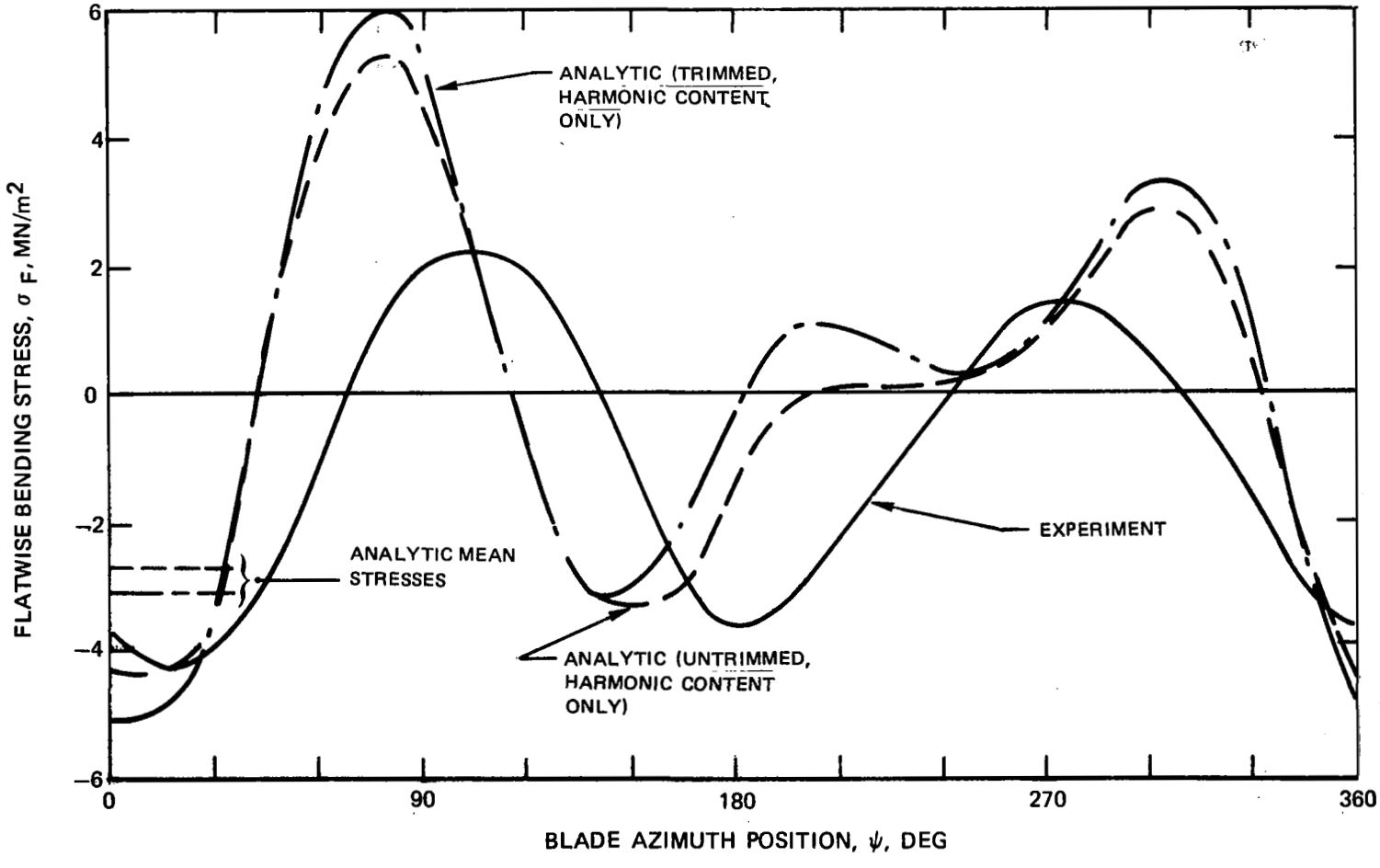

Figure 79. -Experimental and Analytic Time-Histories of Inboard Flatwise Bending Stresses, r = 0.06 R, Case 72.06, C_L/σ = 0.0412, μ = 0.47.

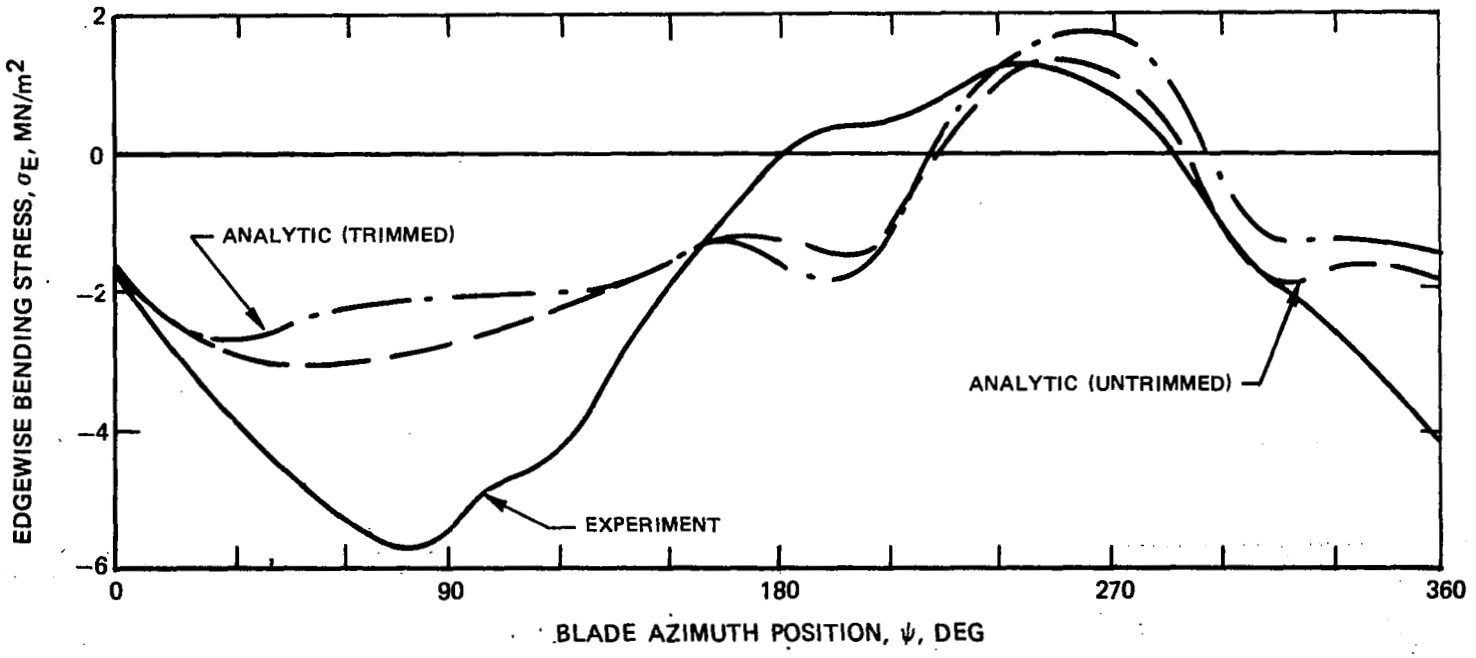

Figure 80. -Experimental and Analytic Time-Histories of Inboard Edgewise Bending Stresses, r = 0.06 R, Case 72.06, C_L/σ = 0.0412, μ = 0.47.

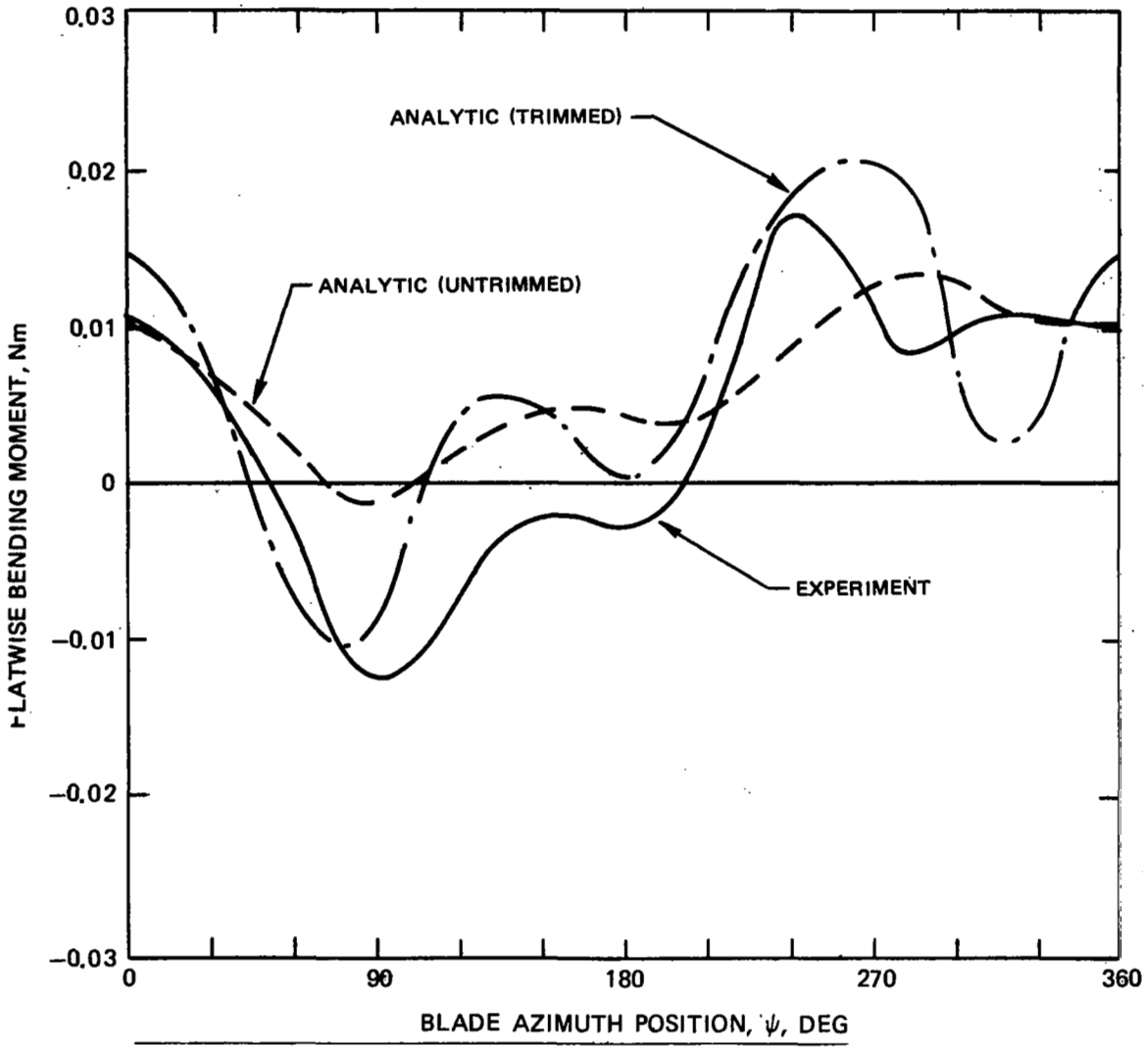

Figure 81. - Experimental and Analytic Time-Histories of Outboard Flatwise Bending Moments, r = 0.42 R, Case 72.06, C_L/σ = 0.0412, μ = 0.47.

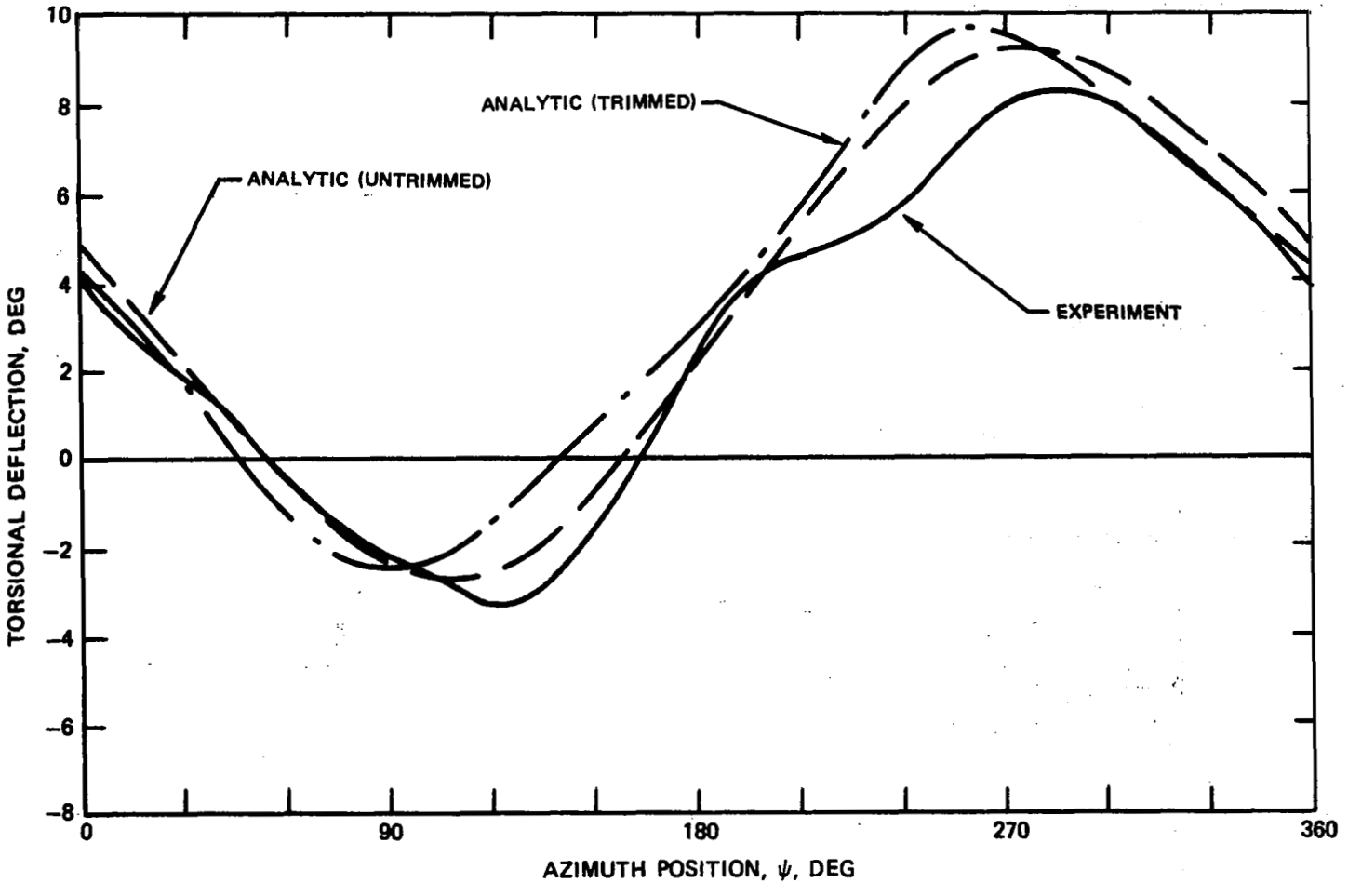

Figure 82. - Experimental and Analytic Time-Histories of Flexbeam Torsional Deflections, Case 72.06, $C_L/\sigma = 0.0412$, $\mu = 0.47$.

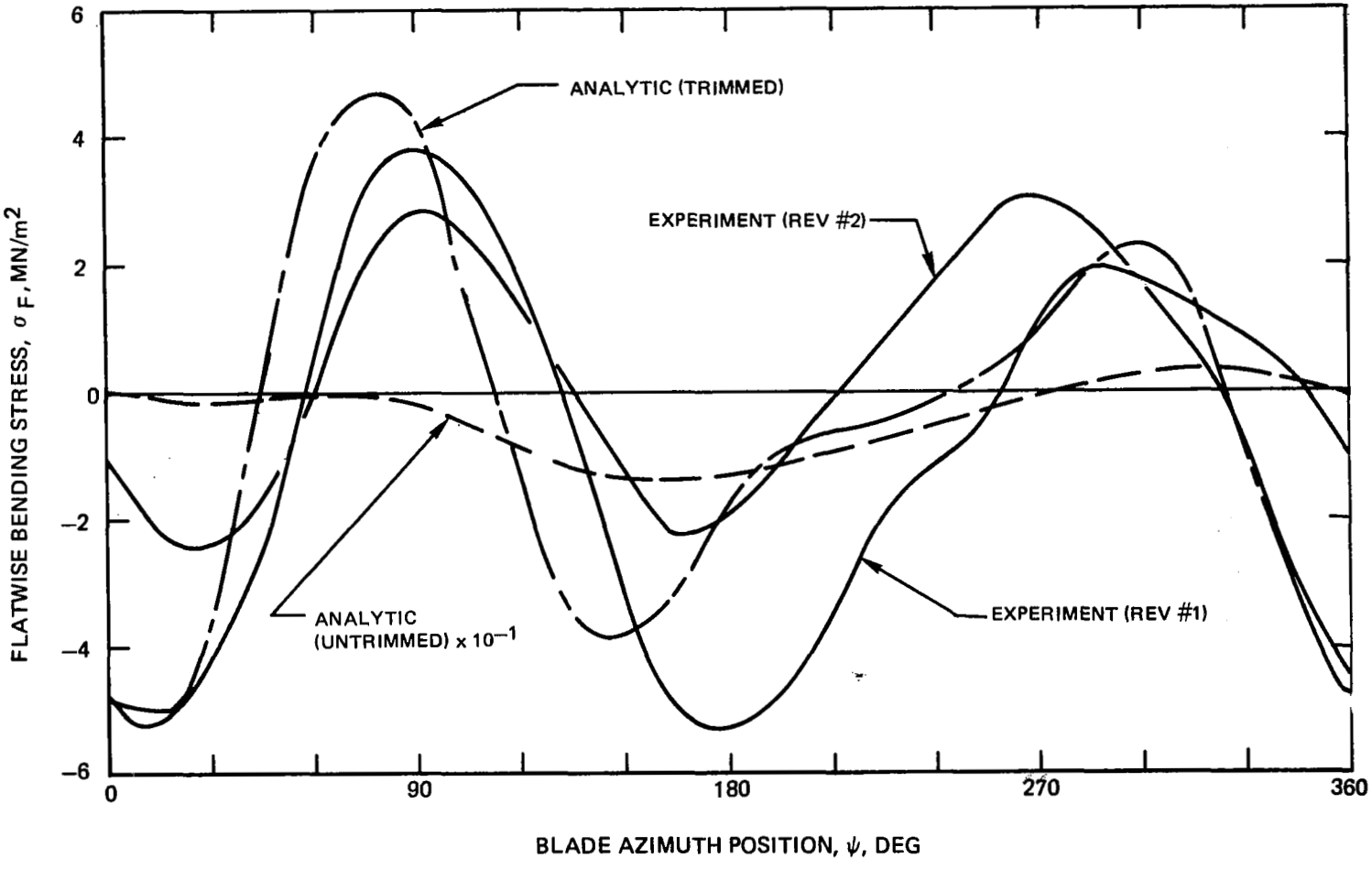

Figure 83. -Experimental and Analytic Time-Histories of Inboard Flatwise Bending Stresses, r = 0.06 R, Case 73.08, C_L/σ = 0.0412, μ = 0.47.

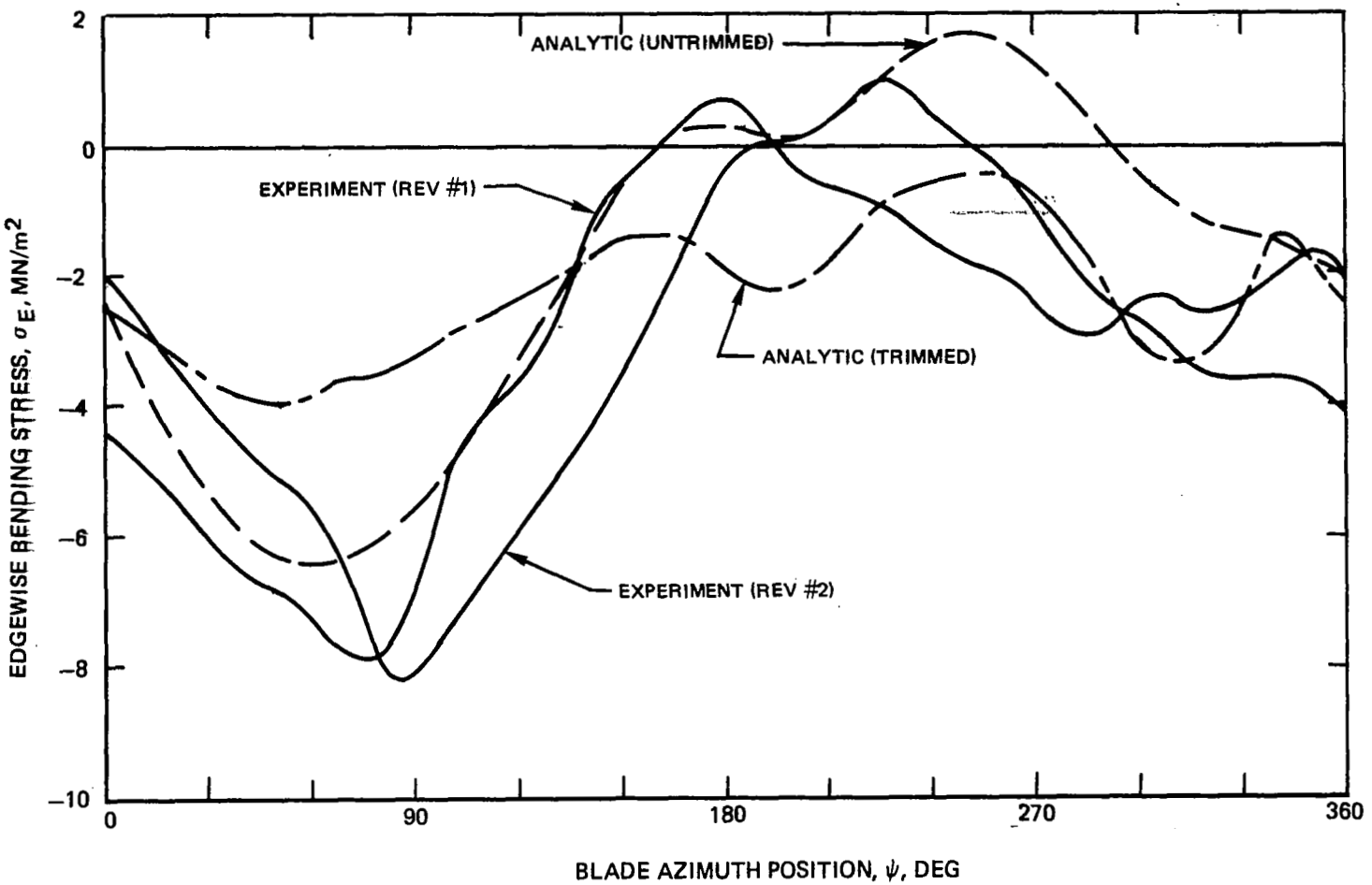

Figure 84. -Experimental and Analytic Time-Histories of Inboard Edgewise Bending Stresses, r = 0.06 R, Case 73.08, C_L/σ = 0.0412, μ = 0.47.

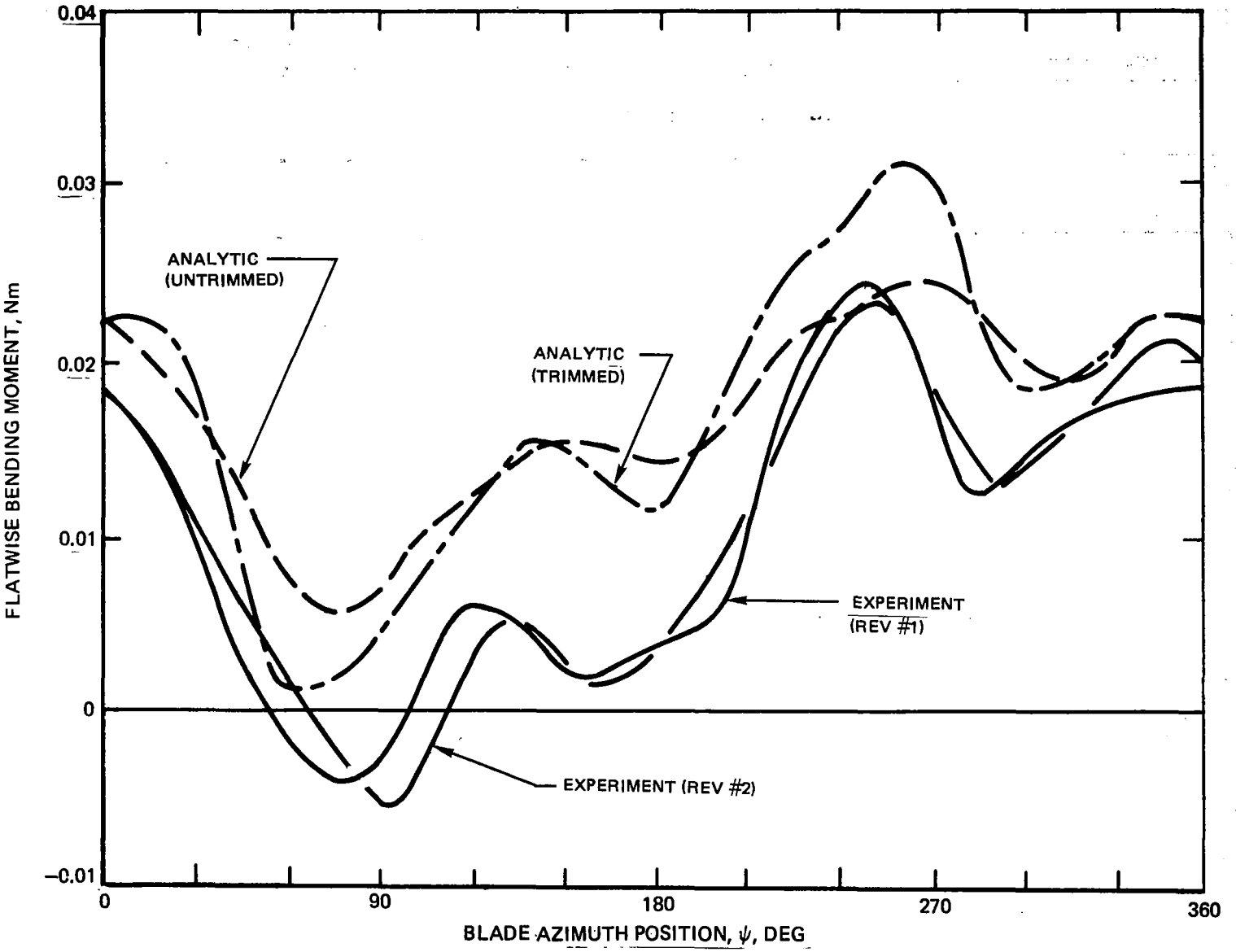

Figure 85. - Experimental and Analytic Time-Histories of Outboard Flatwise Bending Moments, r = 0.42 R, Case 73.08, C_L/σ = 0.0412, μ = 0.47.

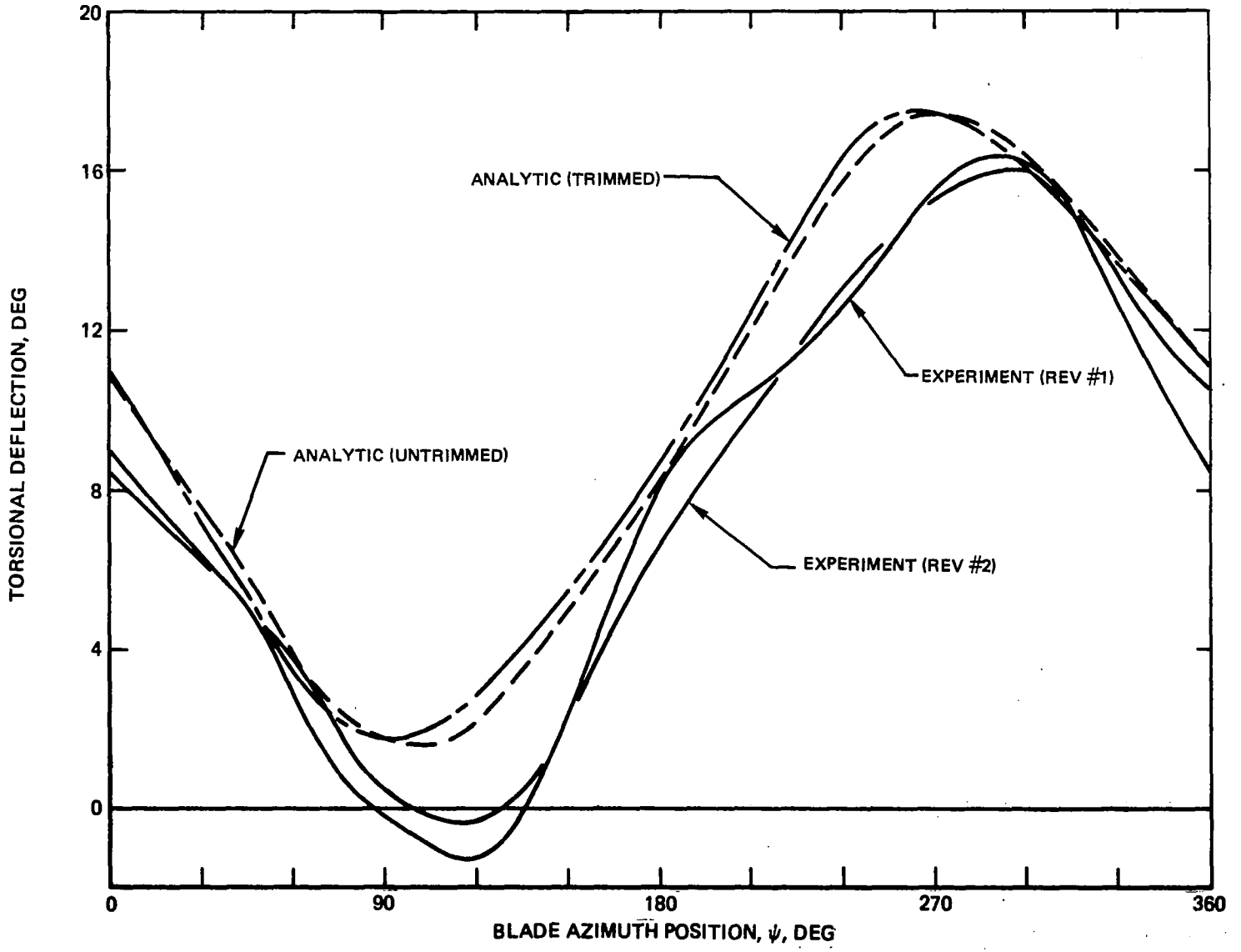

Figure 86. -Experimental and Analytic Time-Histories of Flexbeam Torsional Deflections, Case 73.08, C_L/σ = 0.0412, μ = 0.47.

Figure 87.—Layup of Cantilever Torque Tube Design

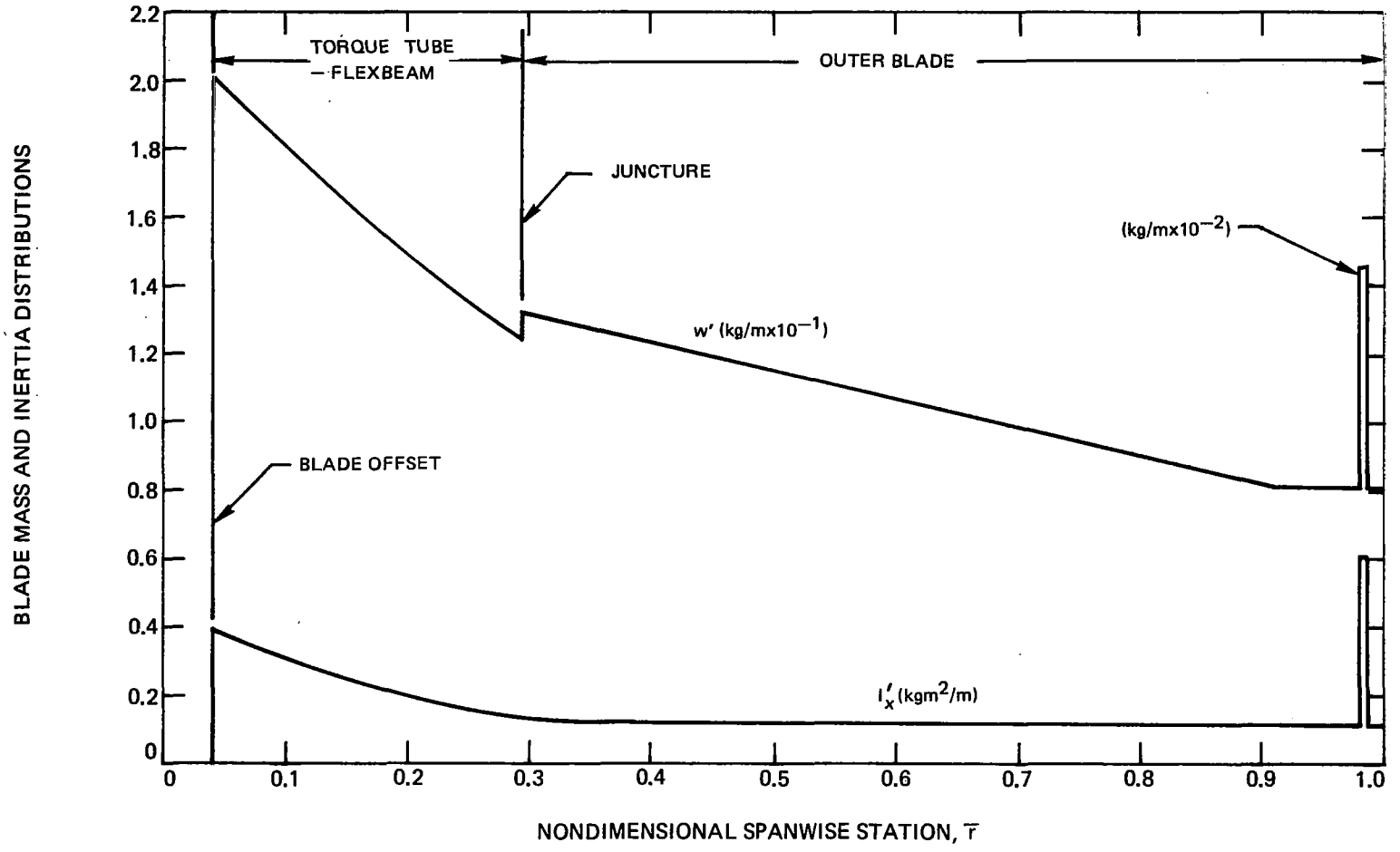

Figure 88. - Full Scale Weight and Inertia Distributions.

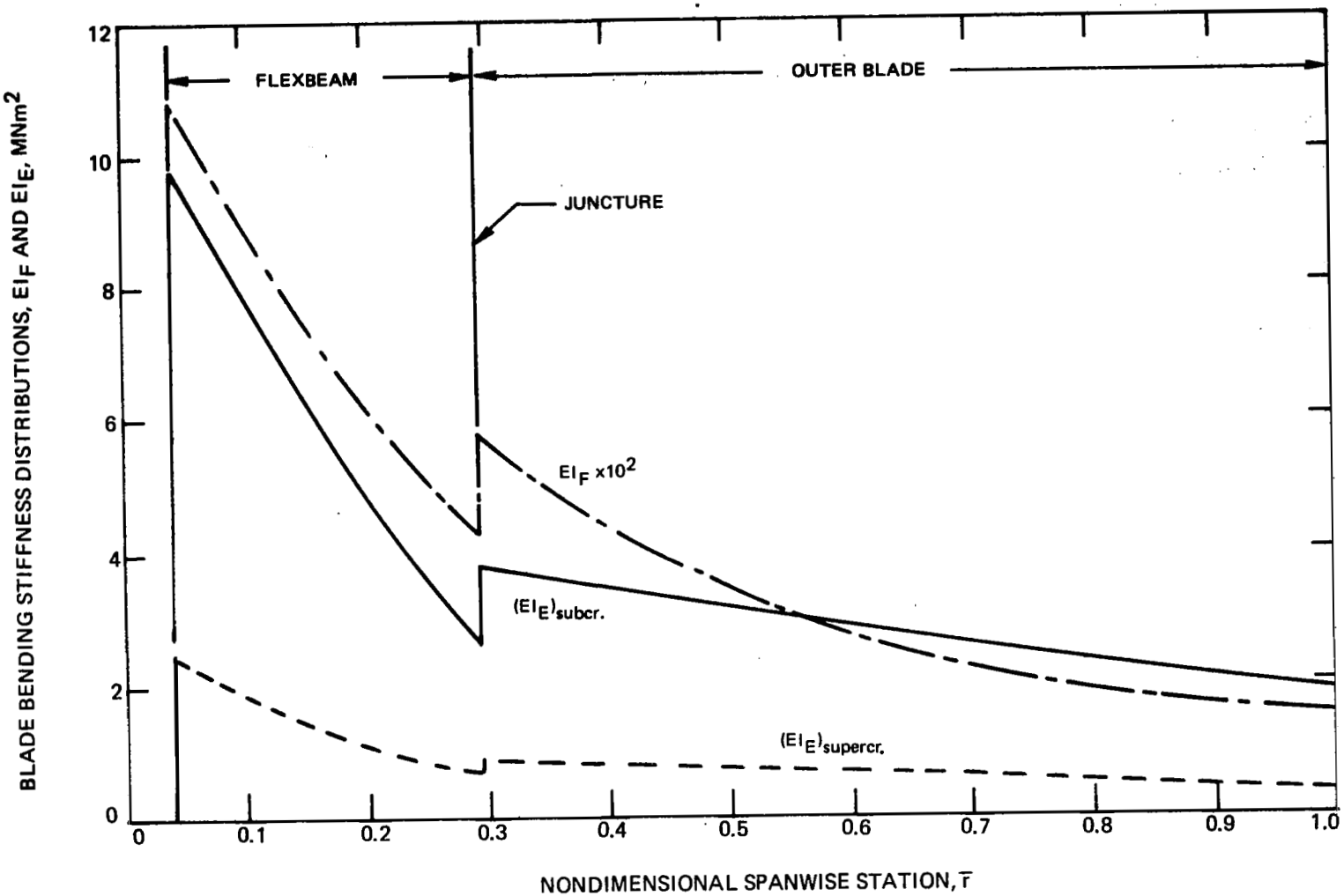

Figure 89. -Full Scale Bending Stiffness Distributions.

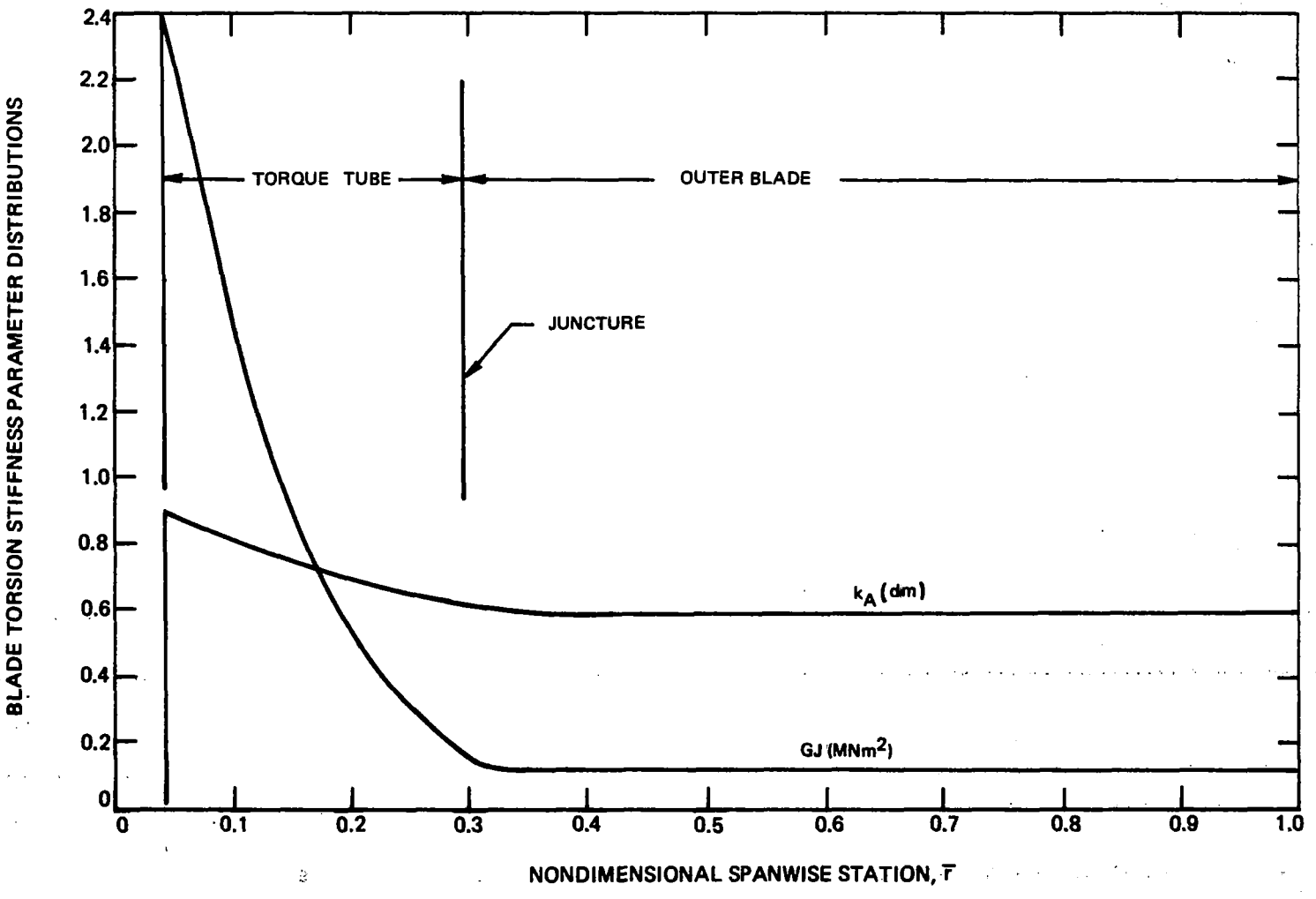

Figure 90. -Full Scale Torsion Stiffness Distributions.

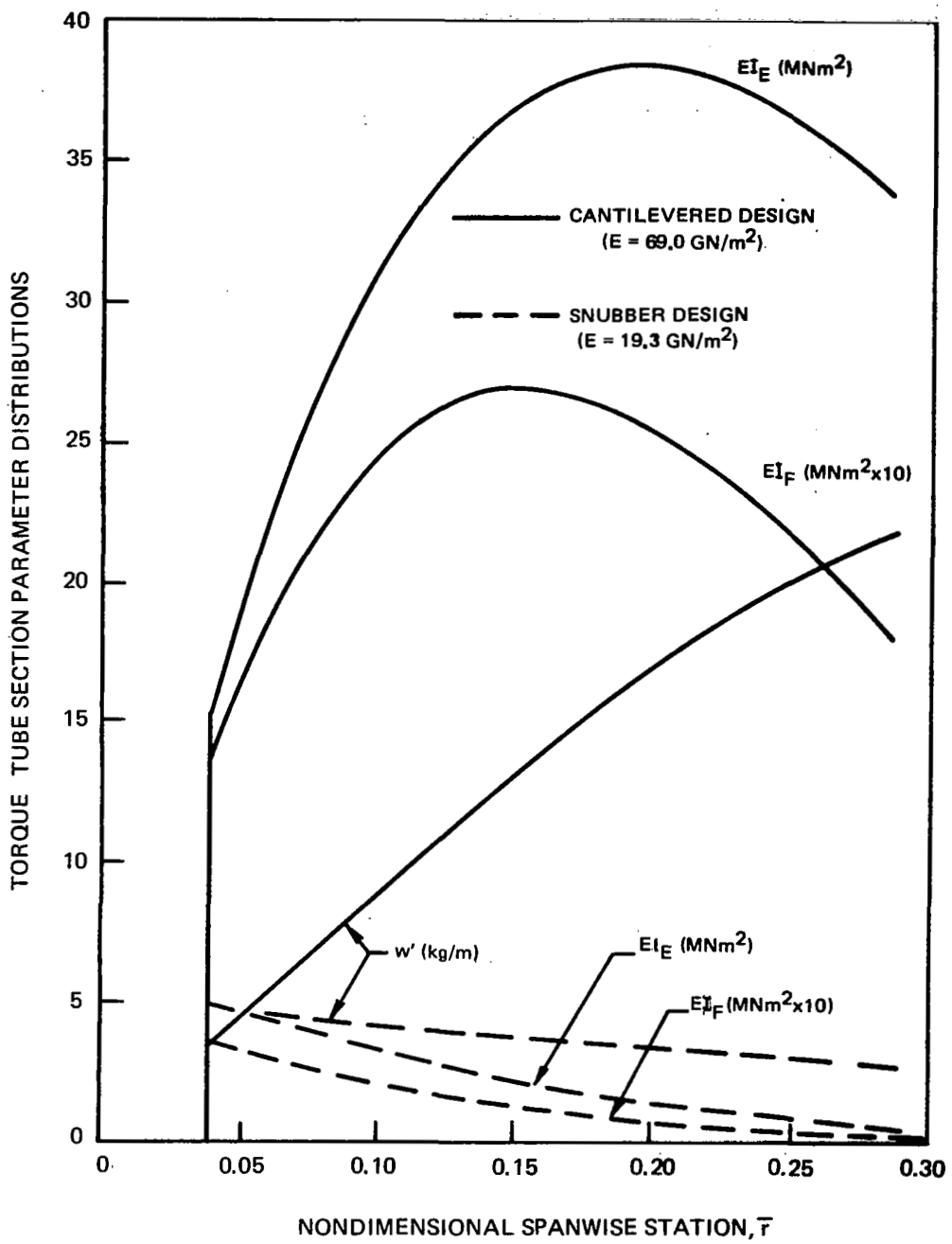

Figure 91. - Full Scale Torque Tube Characteristics, Cantilevered and Snubber Designs

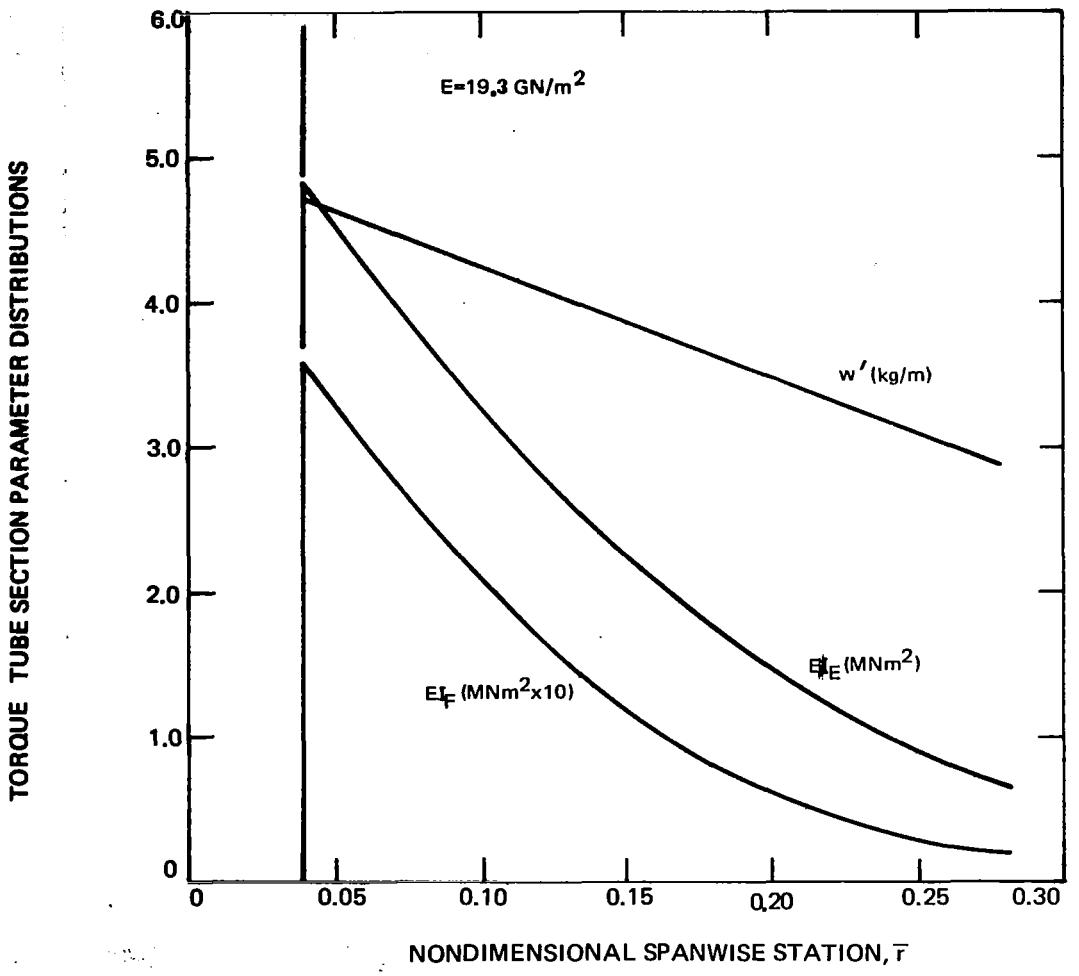

Figure 92. - Full Scale Torque Tube Characteristics, Snubber Design (Augmented Scale)

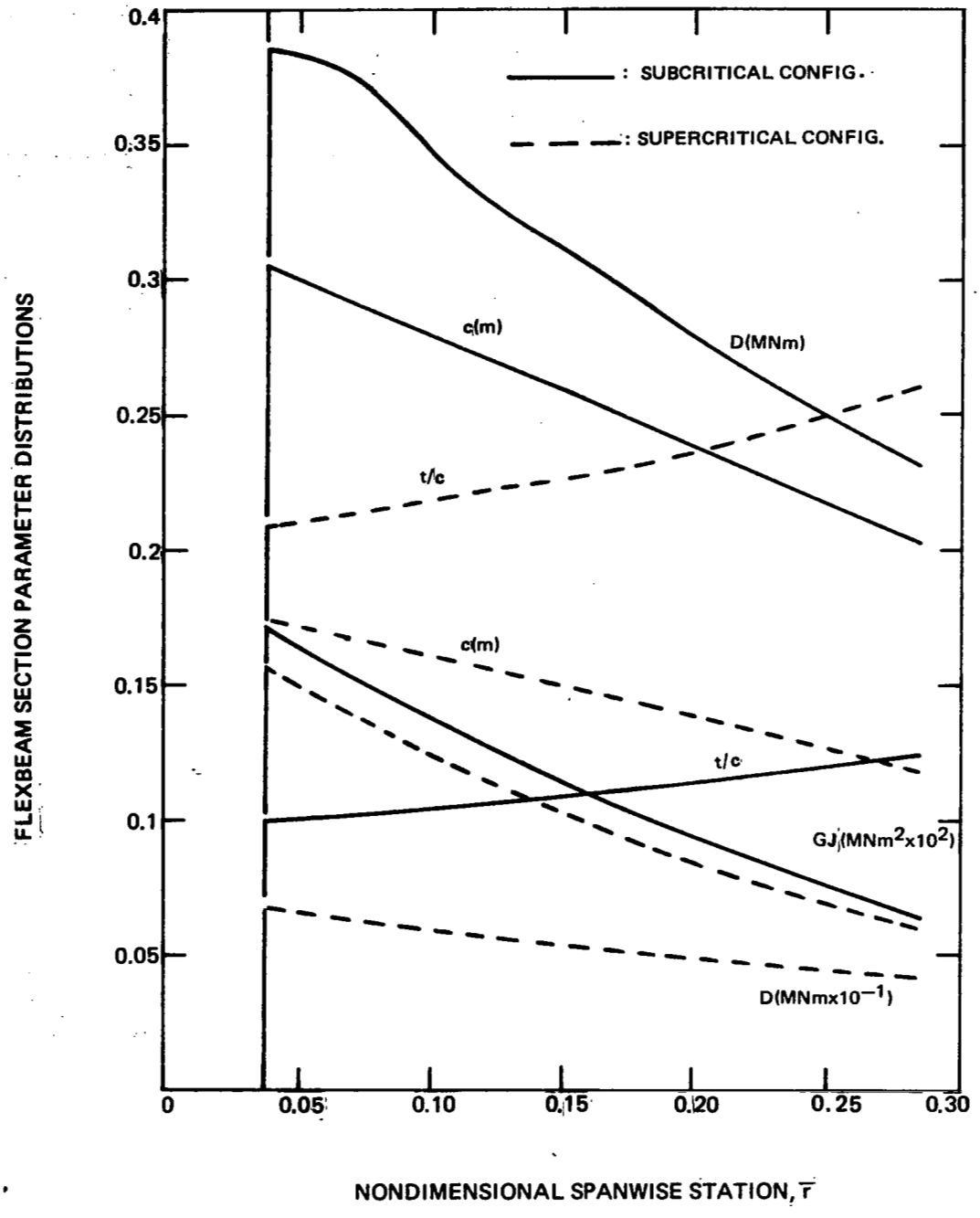

Figure 93. - Full Scale Flexbeam Characteristics

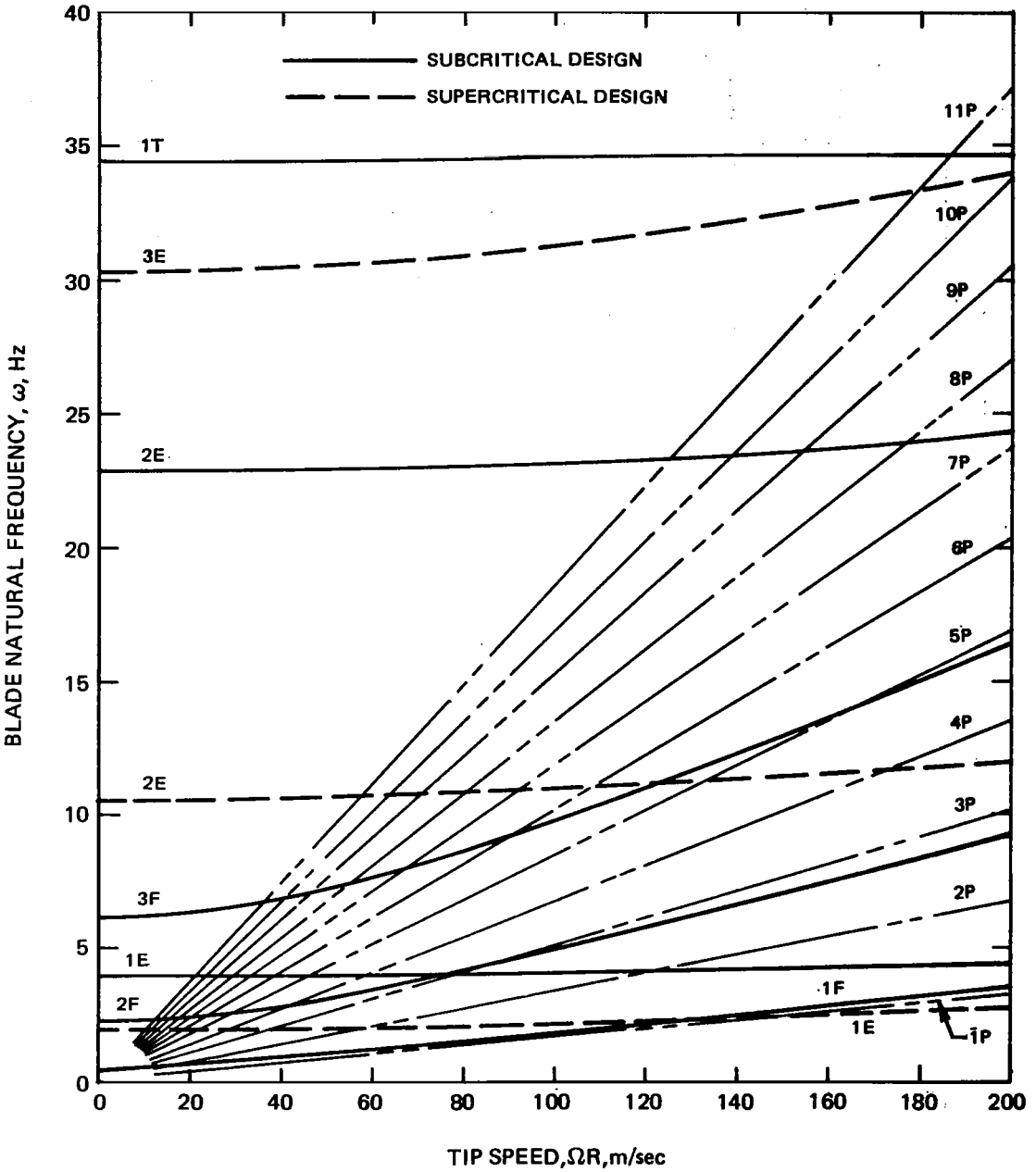

Figure 94. - Full Scale Blade Uncoupled Frequencies

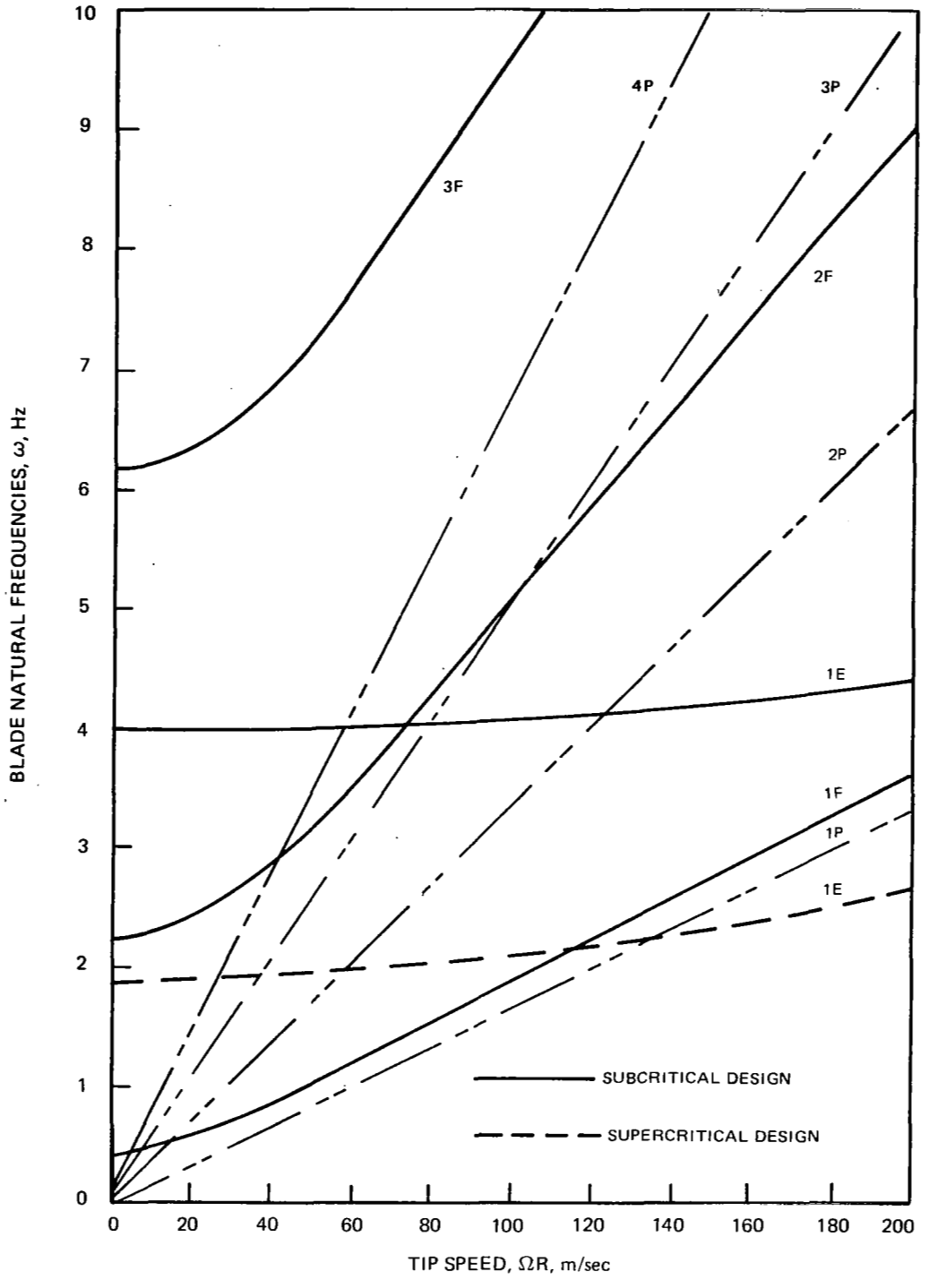

Figure 95.—Full Scale Blade Uncoupled Frequencies of Low Numbered Modes

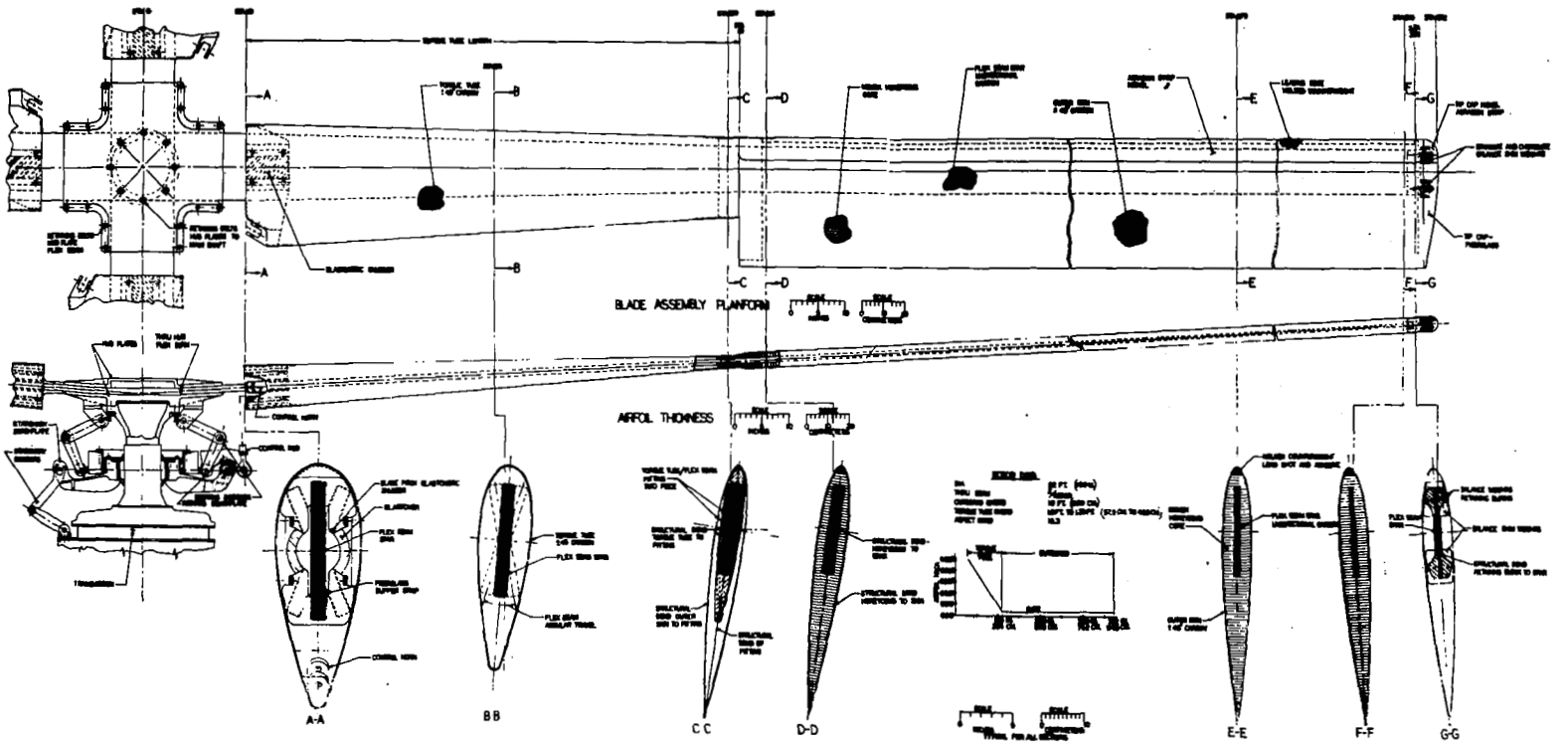

Figure 96.—Layup of Snubber Torque Tube Design

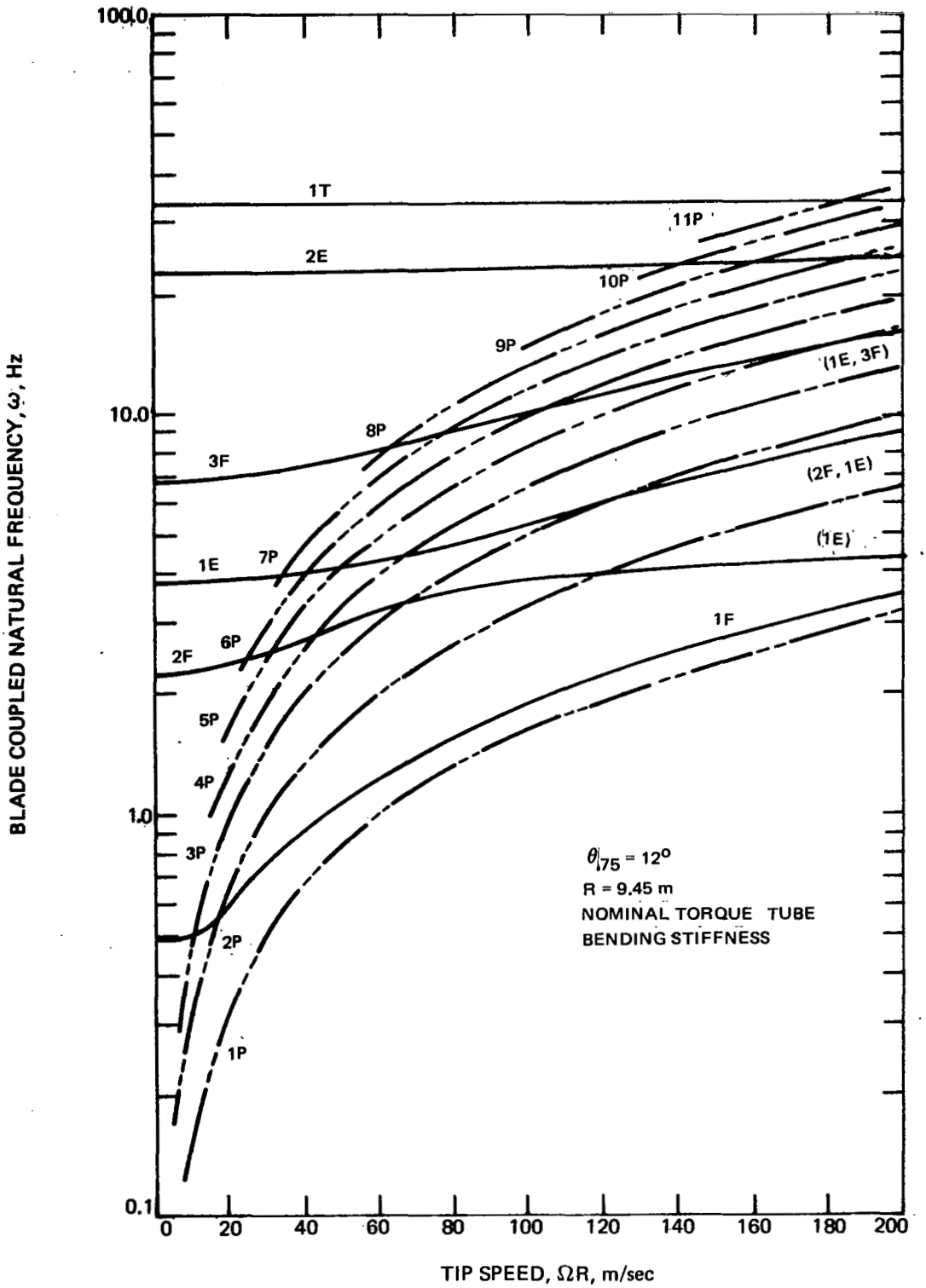

Figure 97. -Variation of Coupled Frequencies with Tip Speed, Subcritical Design

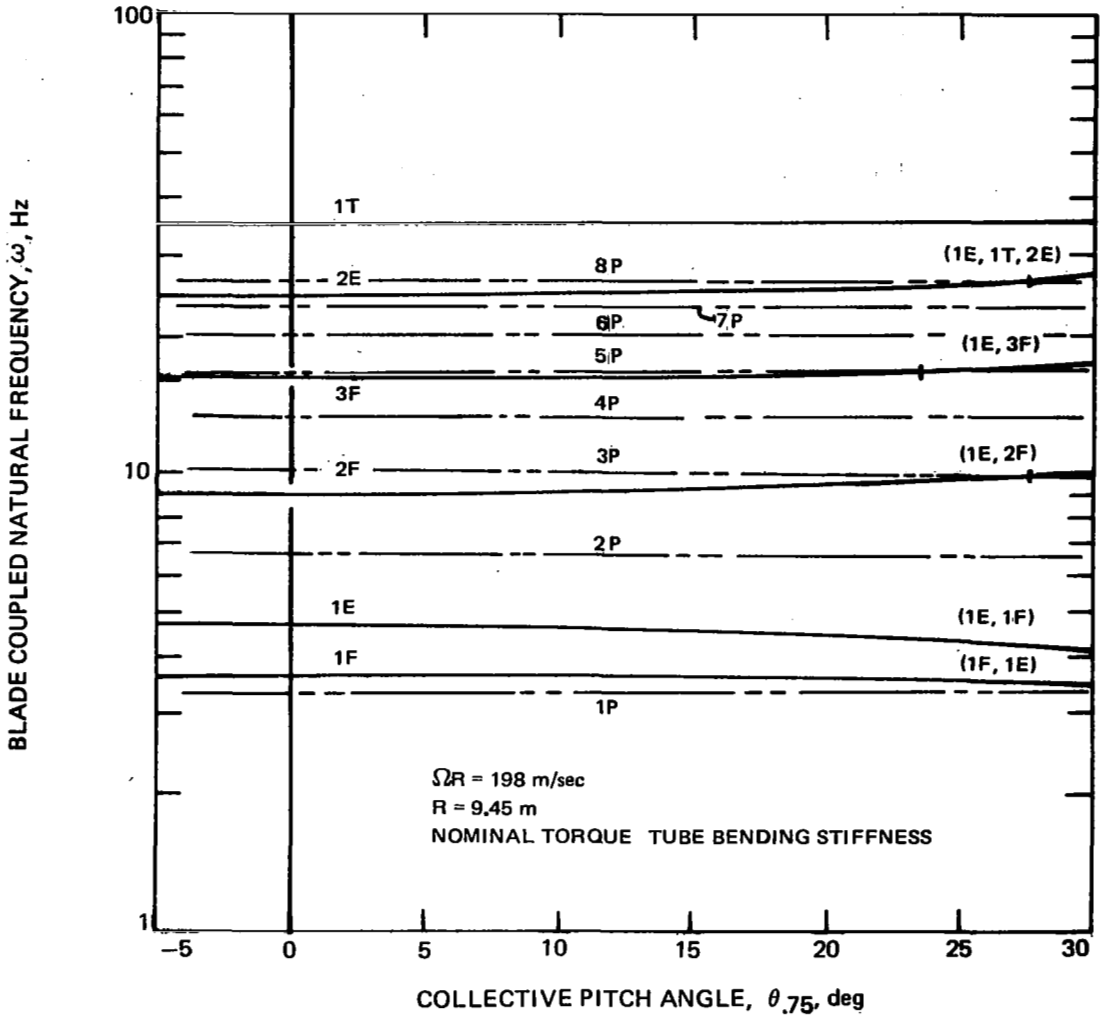

Figure 101. - Variation of Coupled Frequencies with Collective Pitch Angle, Supercritical Design

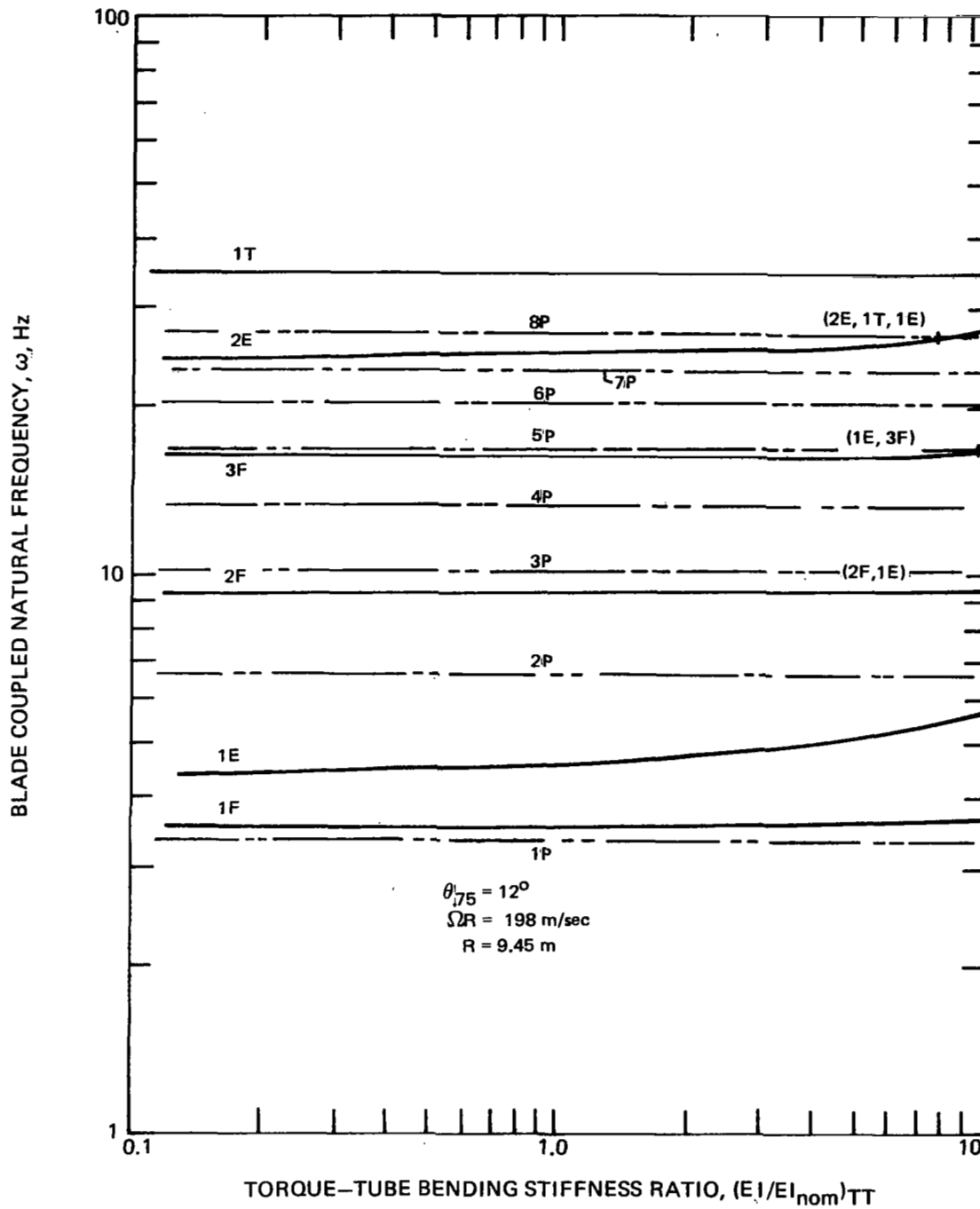

Figure 99. - Variation of Coupled Frequencies with Torque Tube Bending Stiffnesses, Subcritical Design

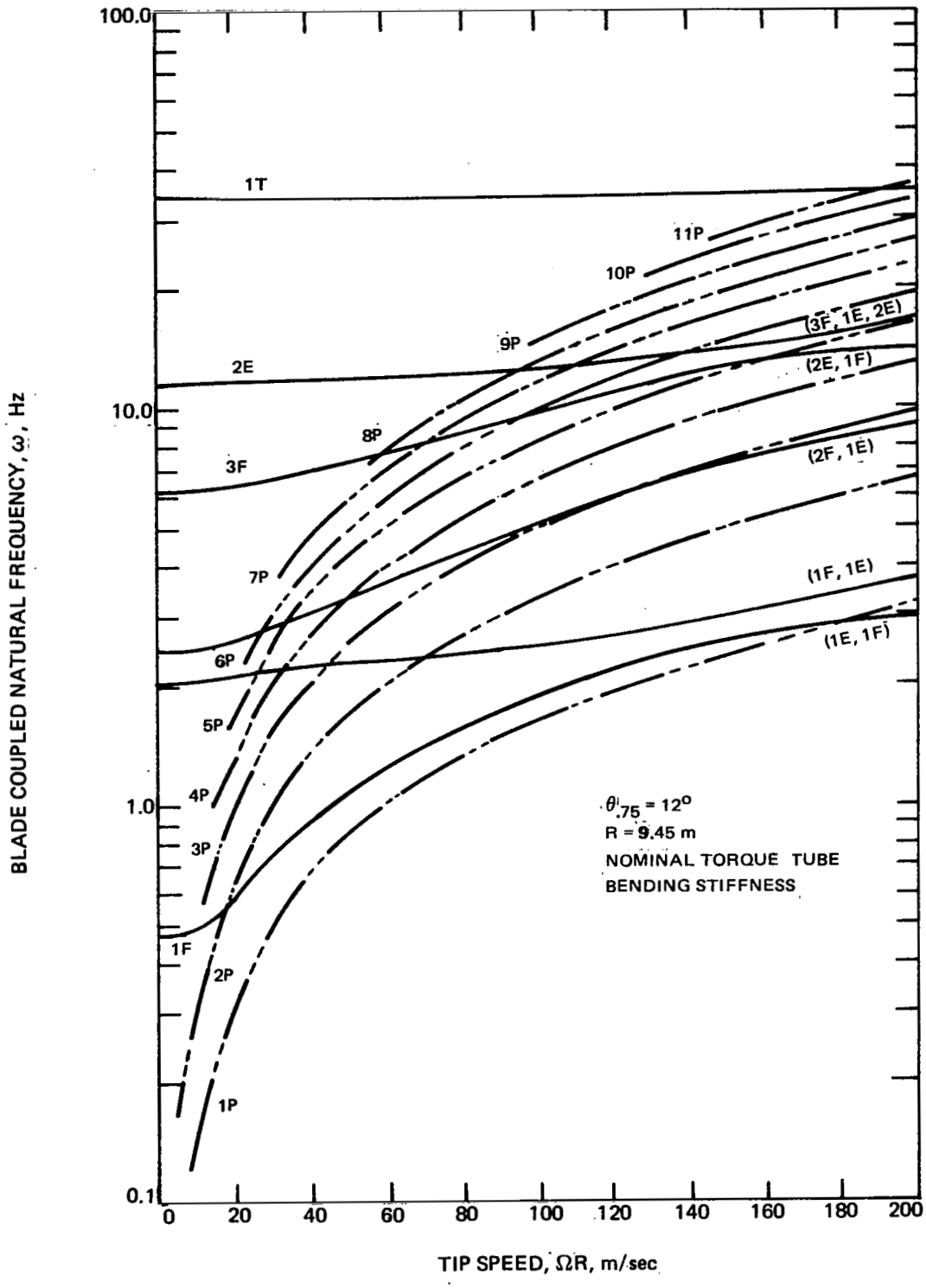

Figure 100. -Variation of Coupled Frequencies with Tip Speed, Supercritical Design

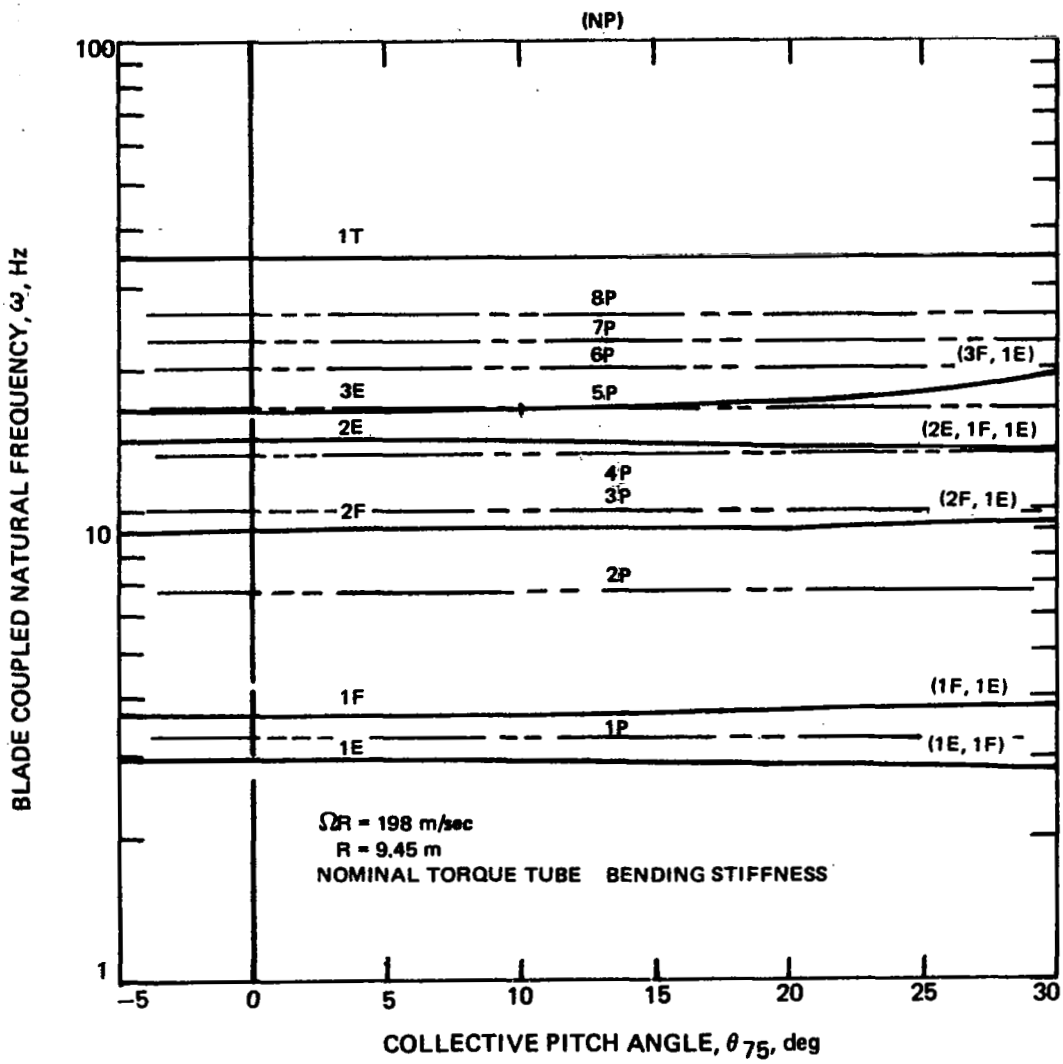

Figure 98. - Variation of Coupled Frequencies with Collective Pitch Angle, Subcritical Design

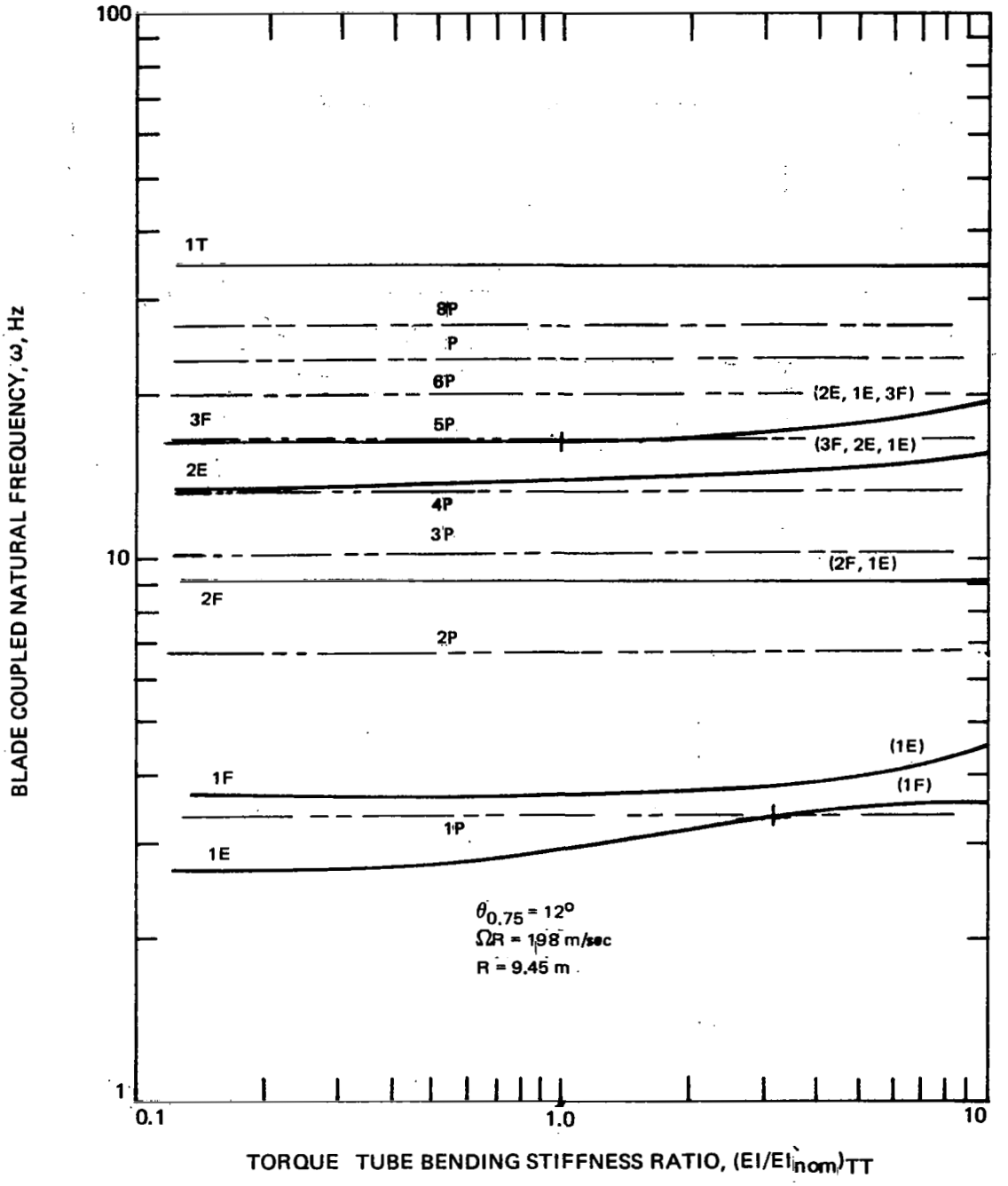

Figure 102. - Variation of Coupled Frequencies with Torque Tube Bending Stiffnesses, Supercritical Design

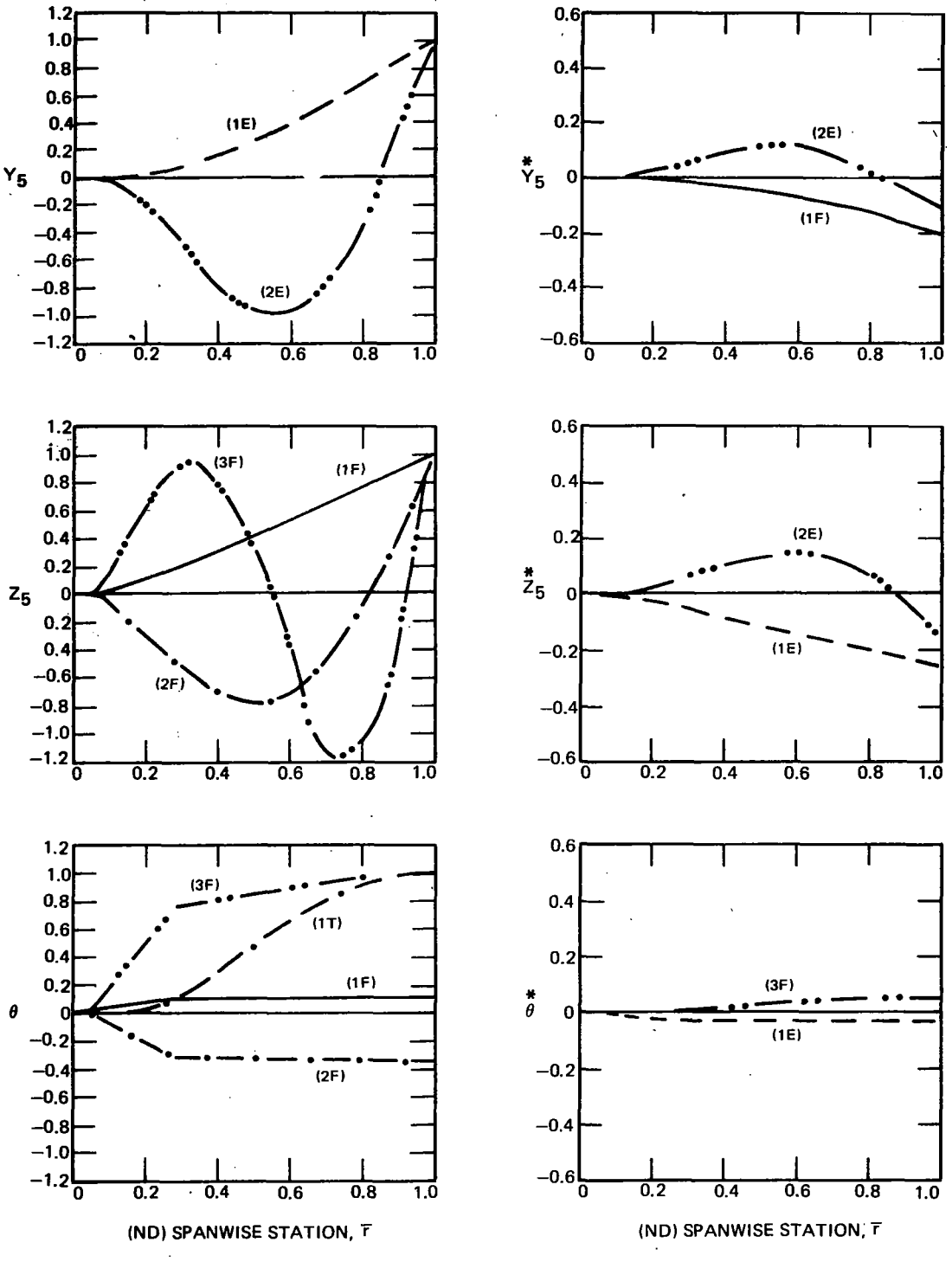

Figure 103.—Spanwise Variation of Coupled Mode Shape Components, $\theta_{.75R} = 0$, Subcritical Design

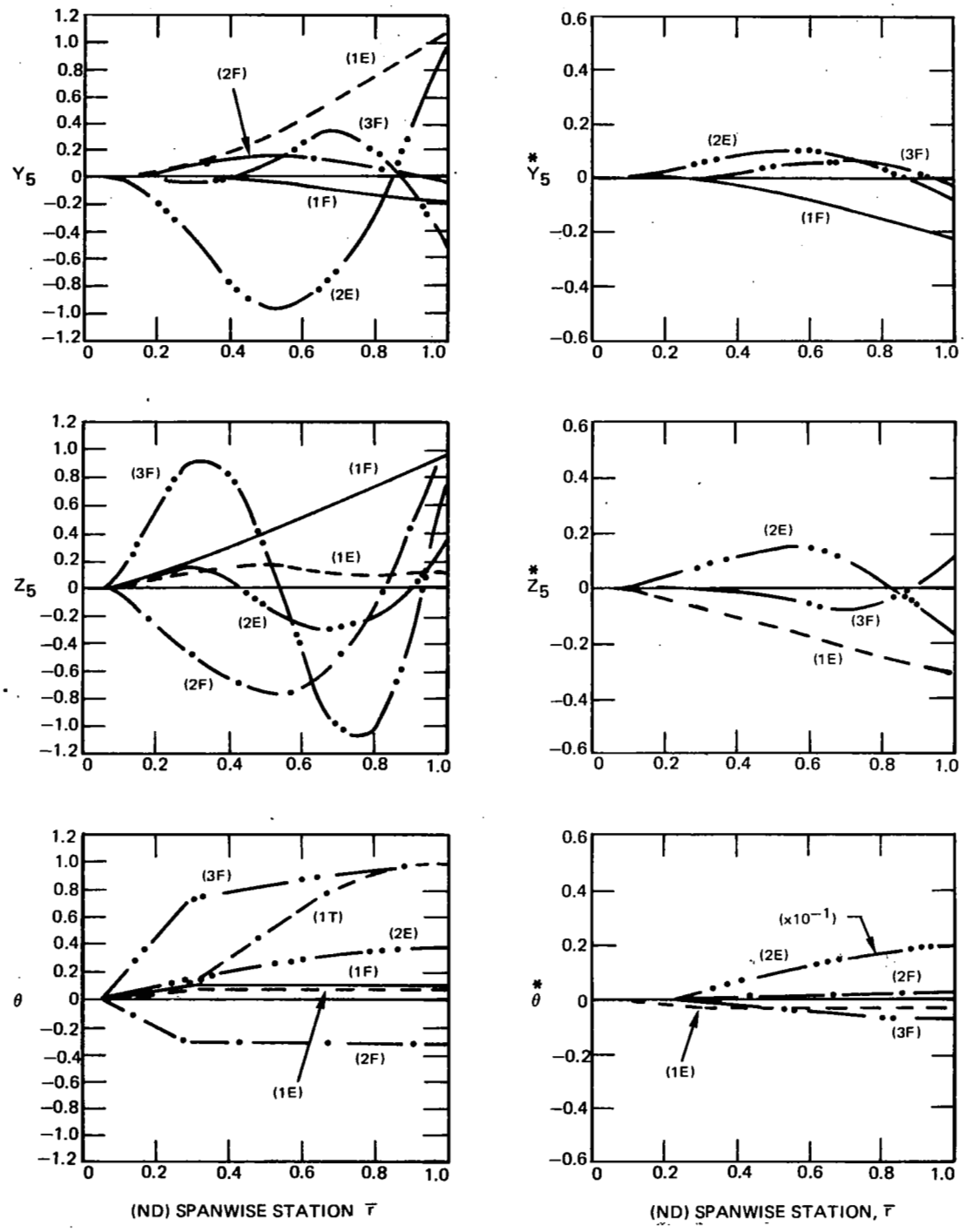

Figure 104.– Spanwise Variation of Coupled Mode Shape Components, $\theta_{.75R}$ = 12 deg, Subcritical Design

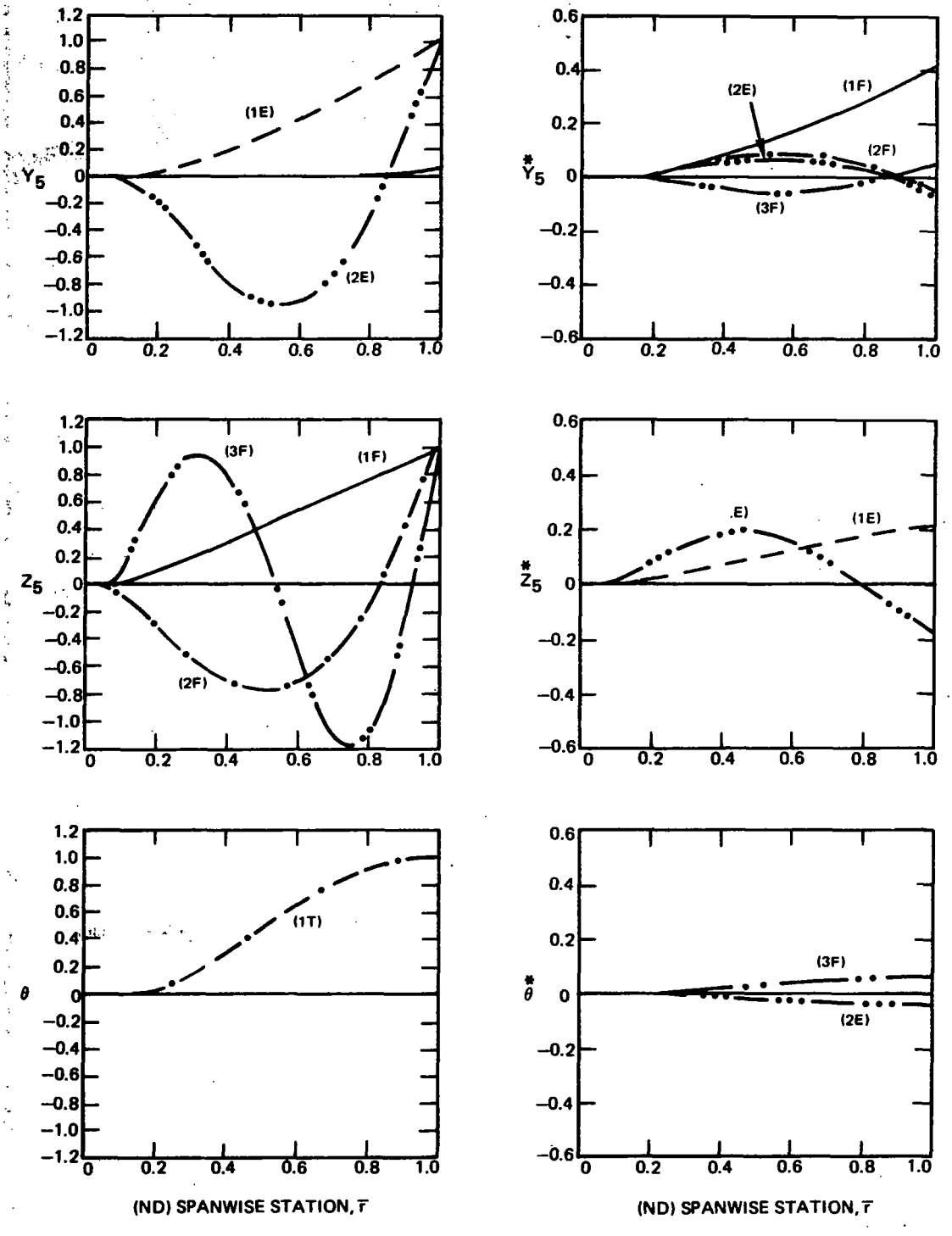

Figure 105.—Spanwise Variation of Coupled Mode Shape Components, $\theta_{.75R} = 0$, Supercritical Design

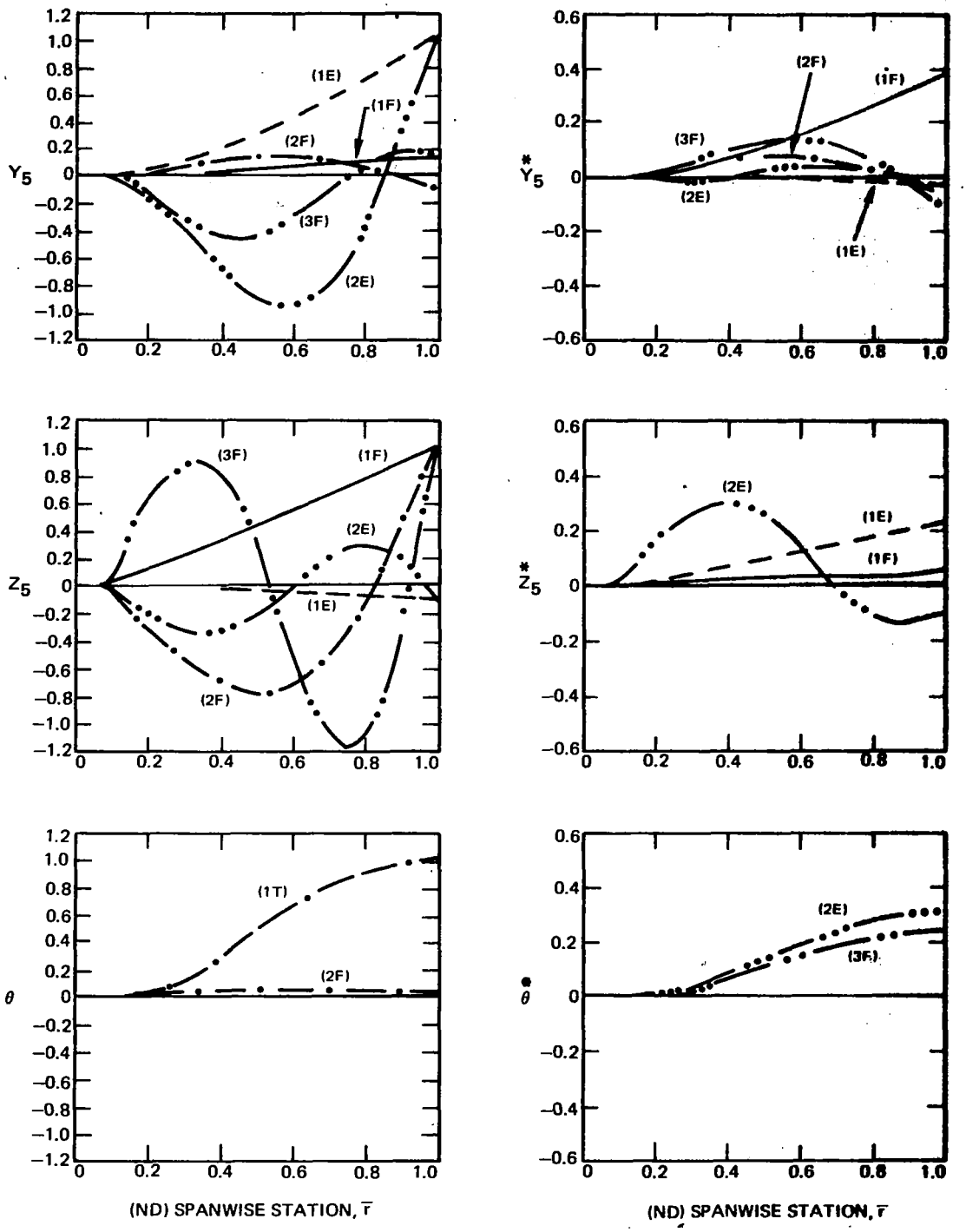

Figure 106.— Spanwise Variation of Coupled Mode Shape Components, $\theta_{.75R}$ = 12 deg, Supercritical Design

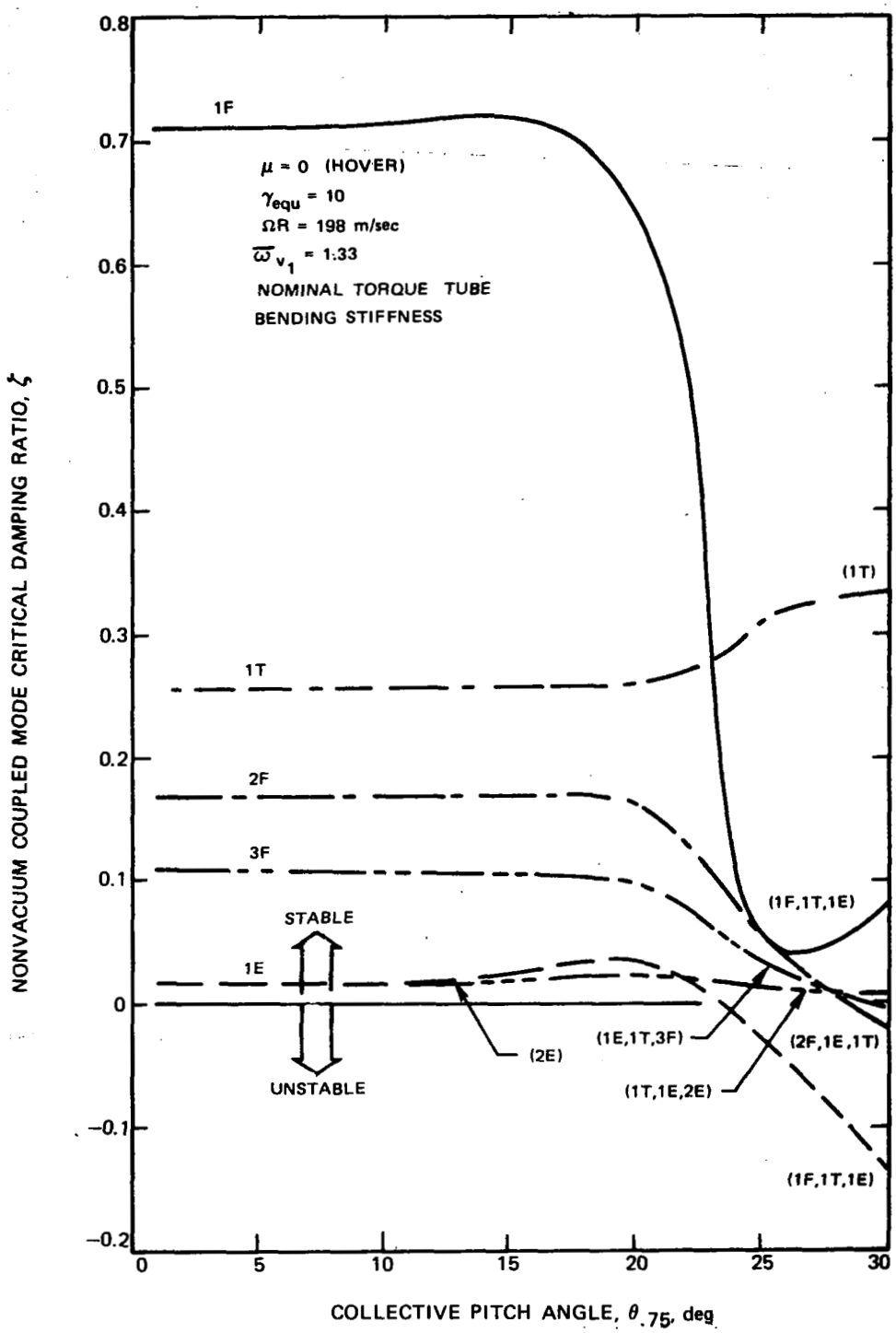

Figure 107.—Variation of Nonvacuum Coupled Mode Damping with Collective Angle, Nonstalled Aerodynamics, Subcritical Design

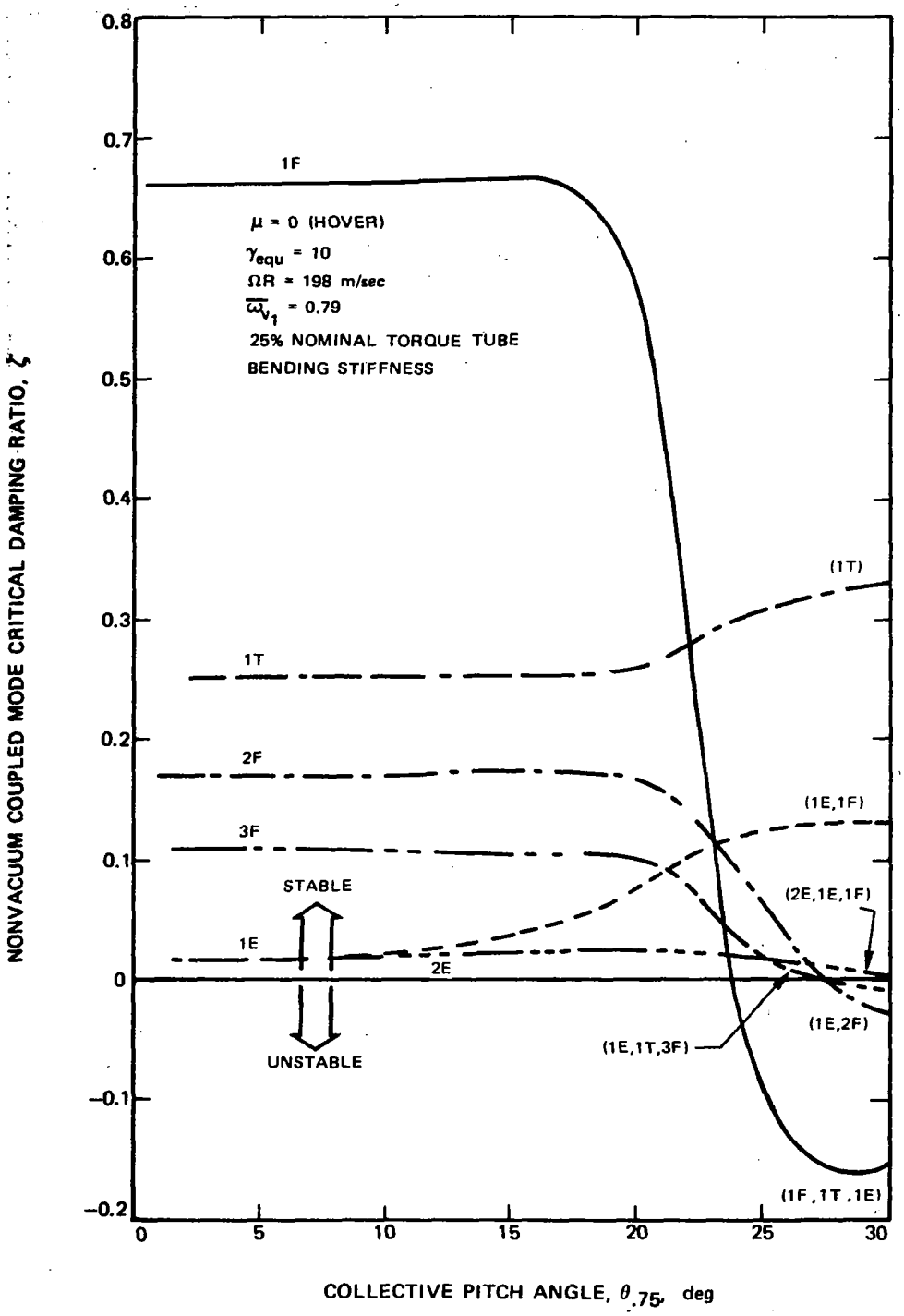

Figure 108.— Variation of Nonvacuum Coupled Mode Damping with Collective Angle, Nonstalled Aerodynamics, Supercritical Design

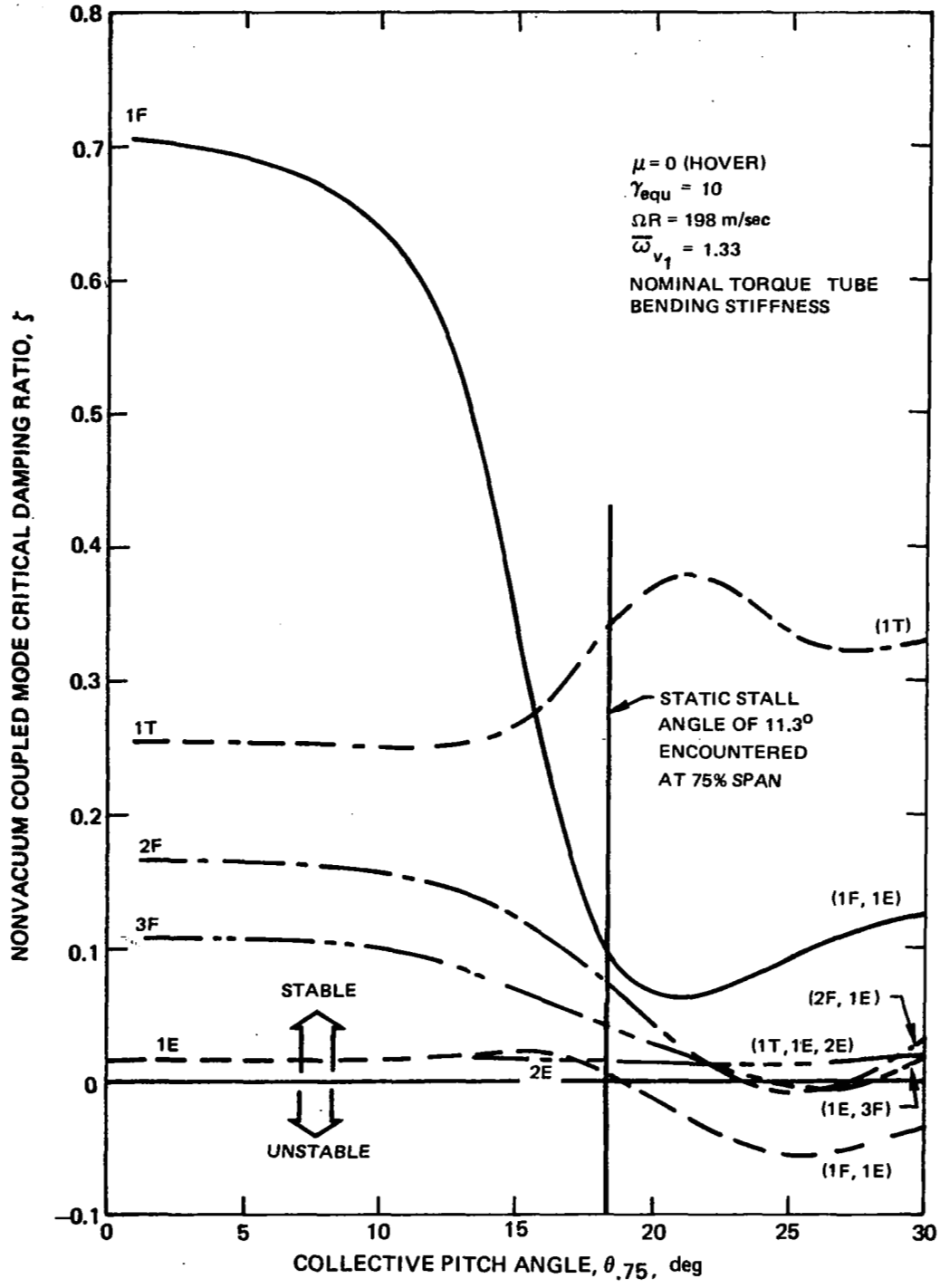

Figure 109. - Variation of Nonvacuum Coupled Mode Damping with Collective Angle, Including Stall Characteristics, Subcritical Design

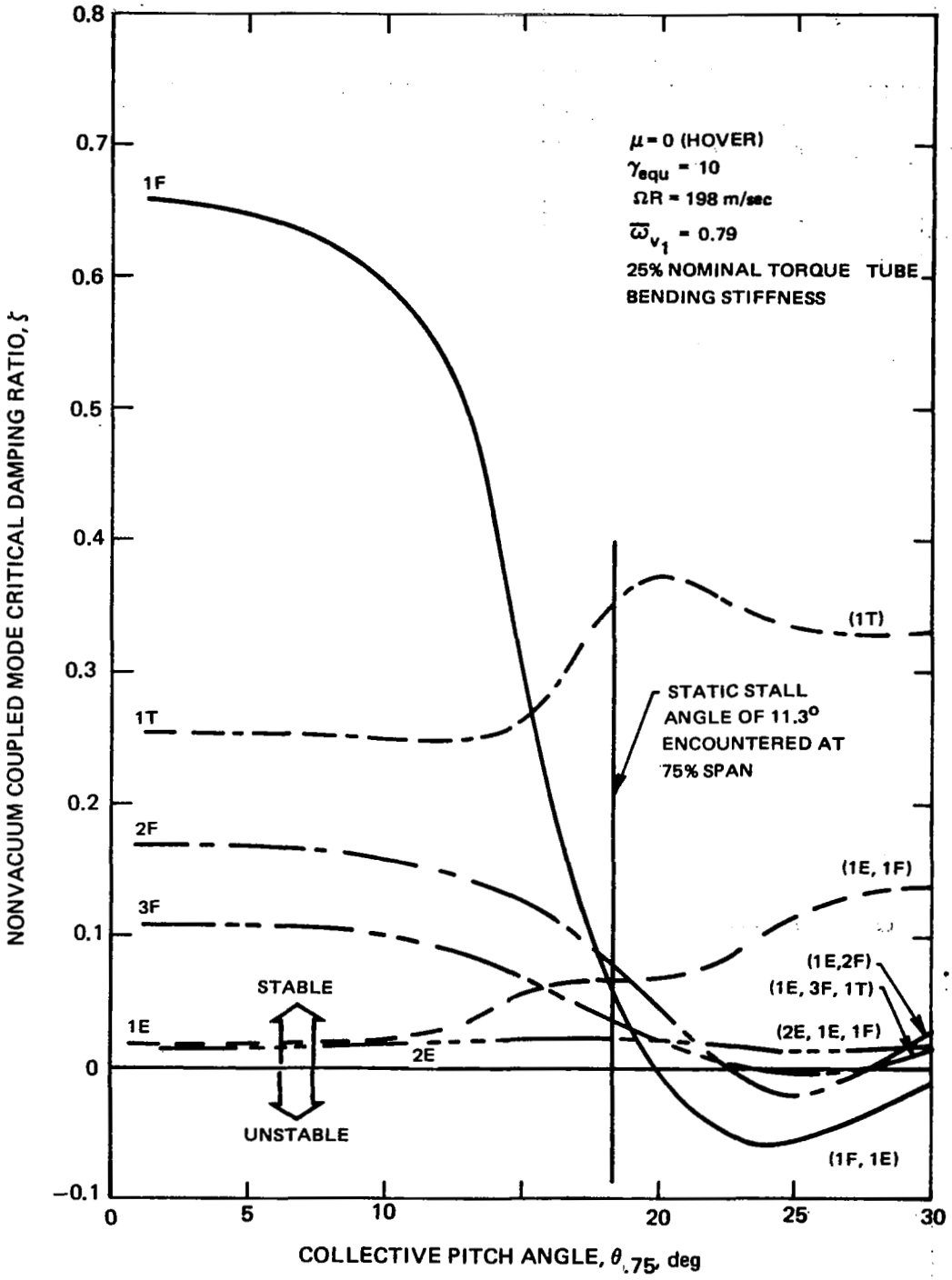

Figure 110. - Variation of Nonvacuum Coupled Mode Damping with Collective Angle, Including Stall Characteristics, Supercritical Design

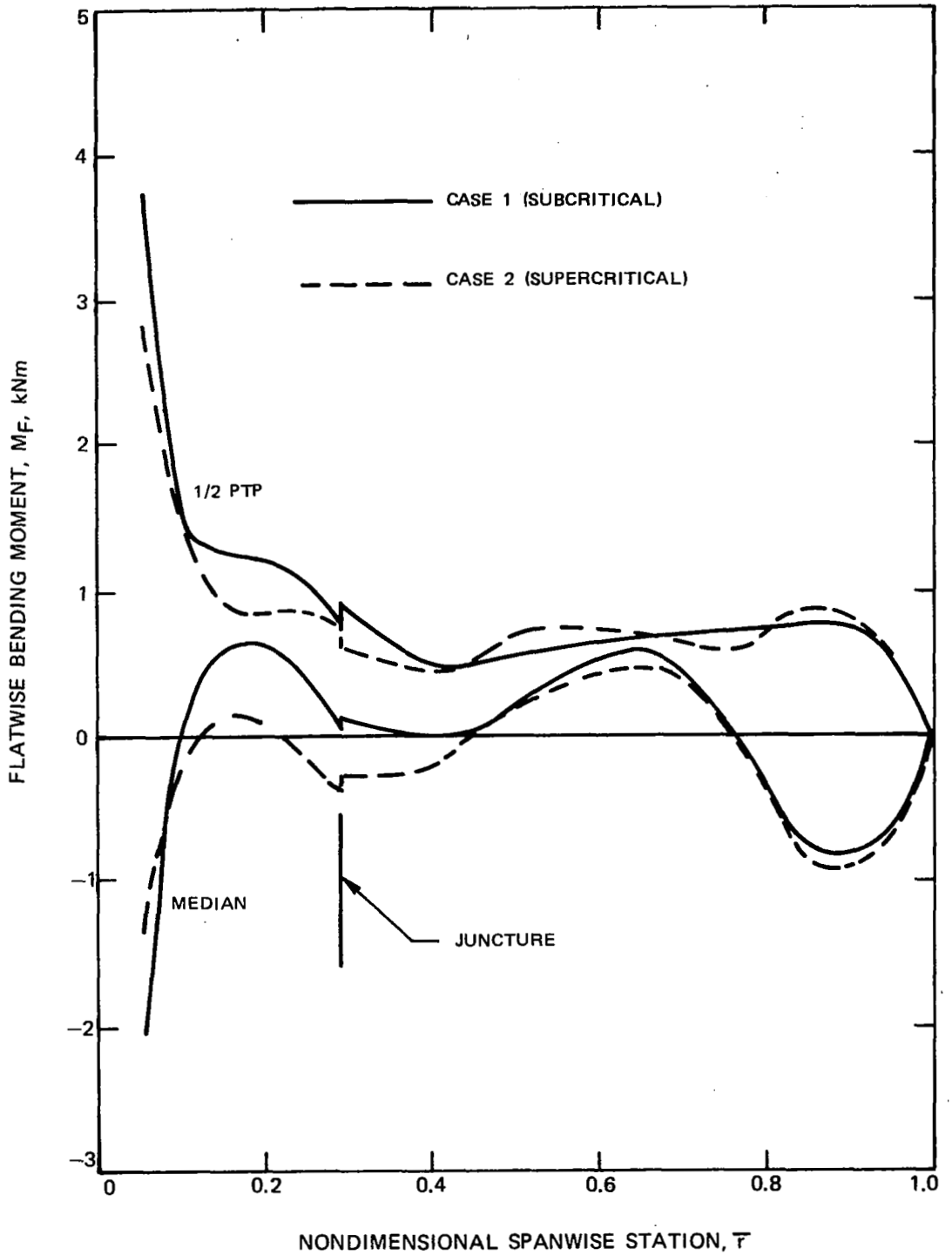

Figure 111. - Spanwise Variations of Flatwise Bending Moments, Trim Cases 1 and 2

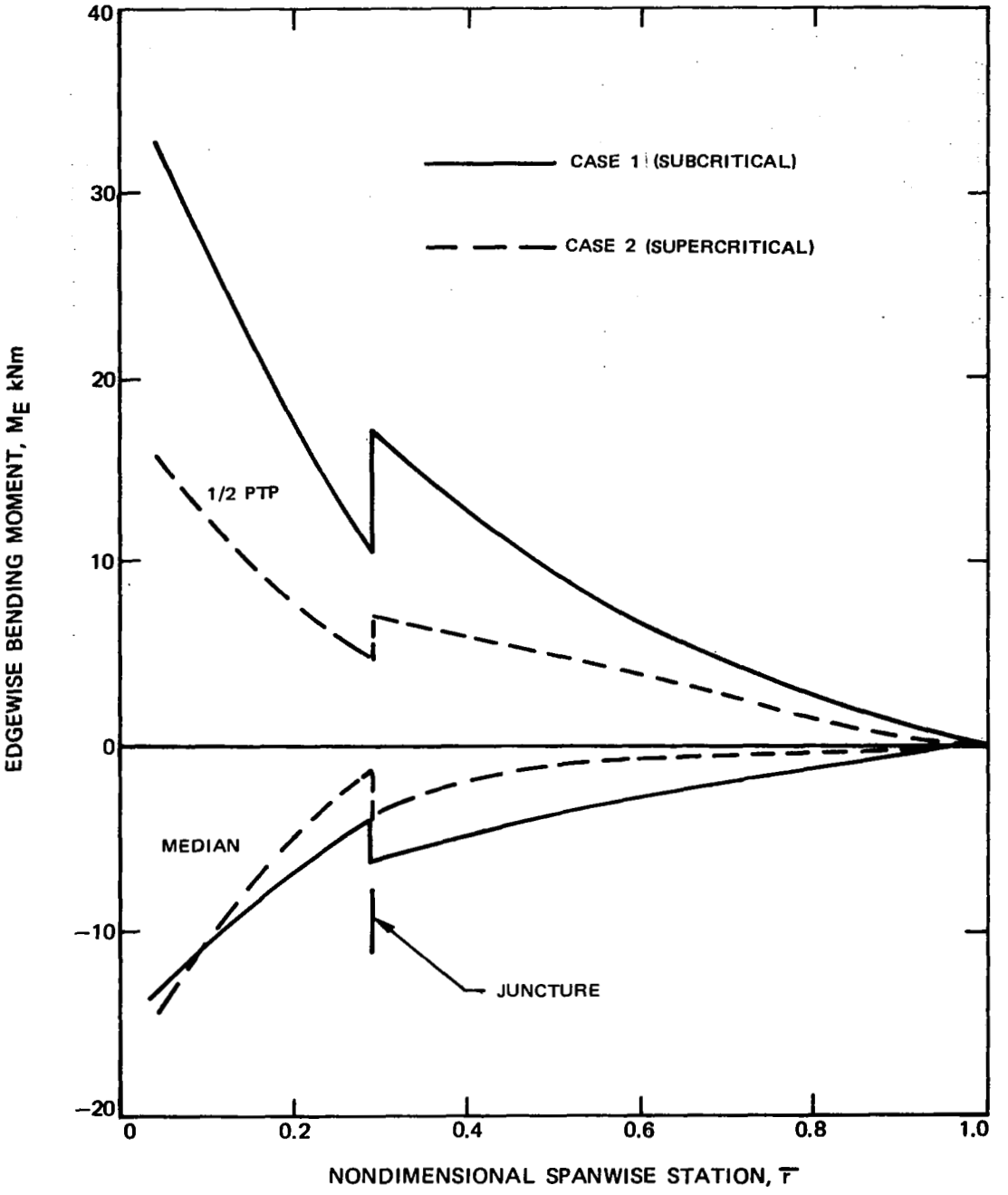

Figure 112. - Spanwise Variation of Edgewise Bending Moments, Trim Cases 1 and 2

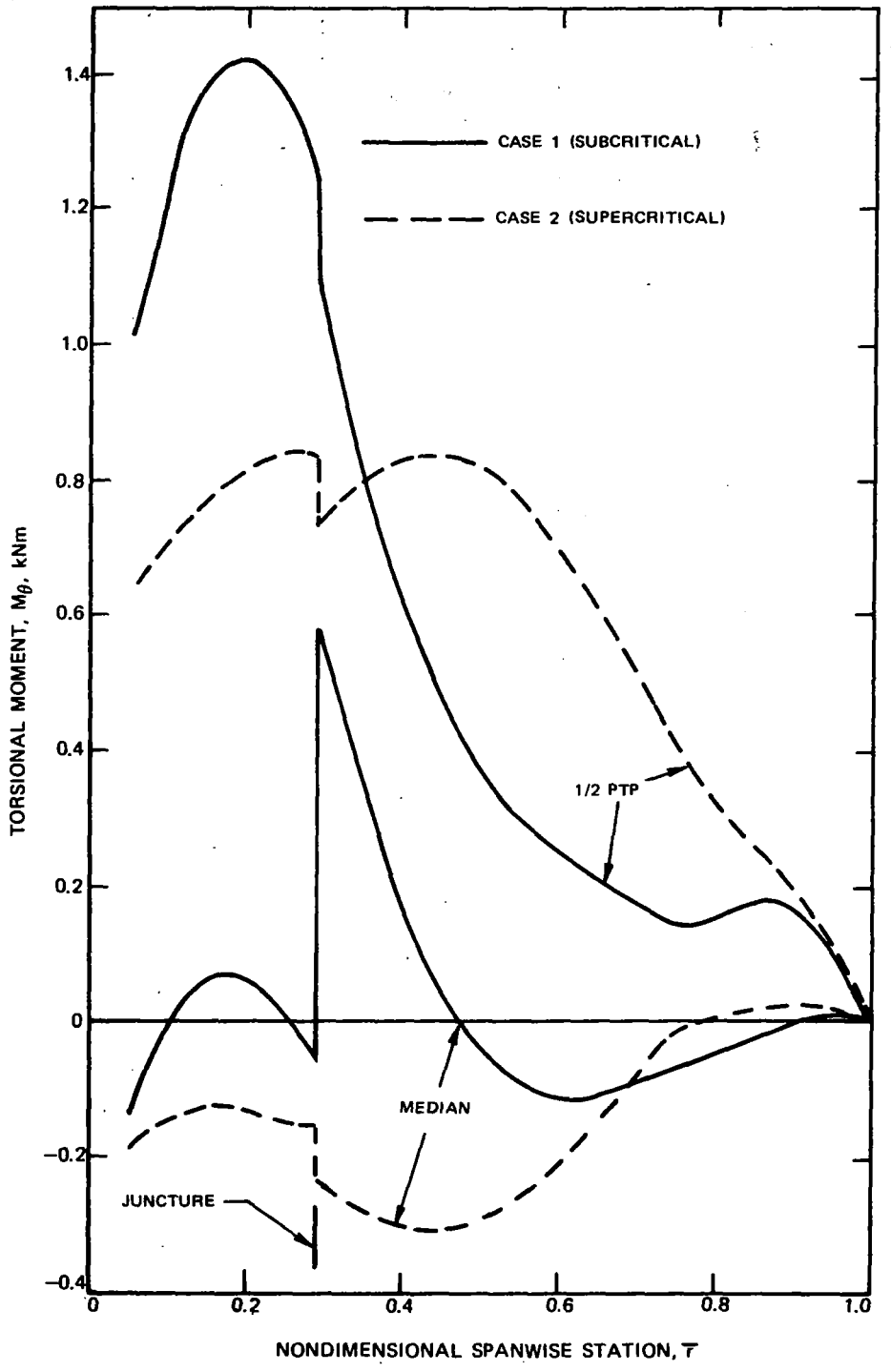

Figure 113.—Spanwise Variation of Torsion Moment, Trim Cases 1 and 2

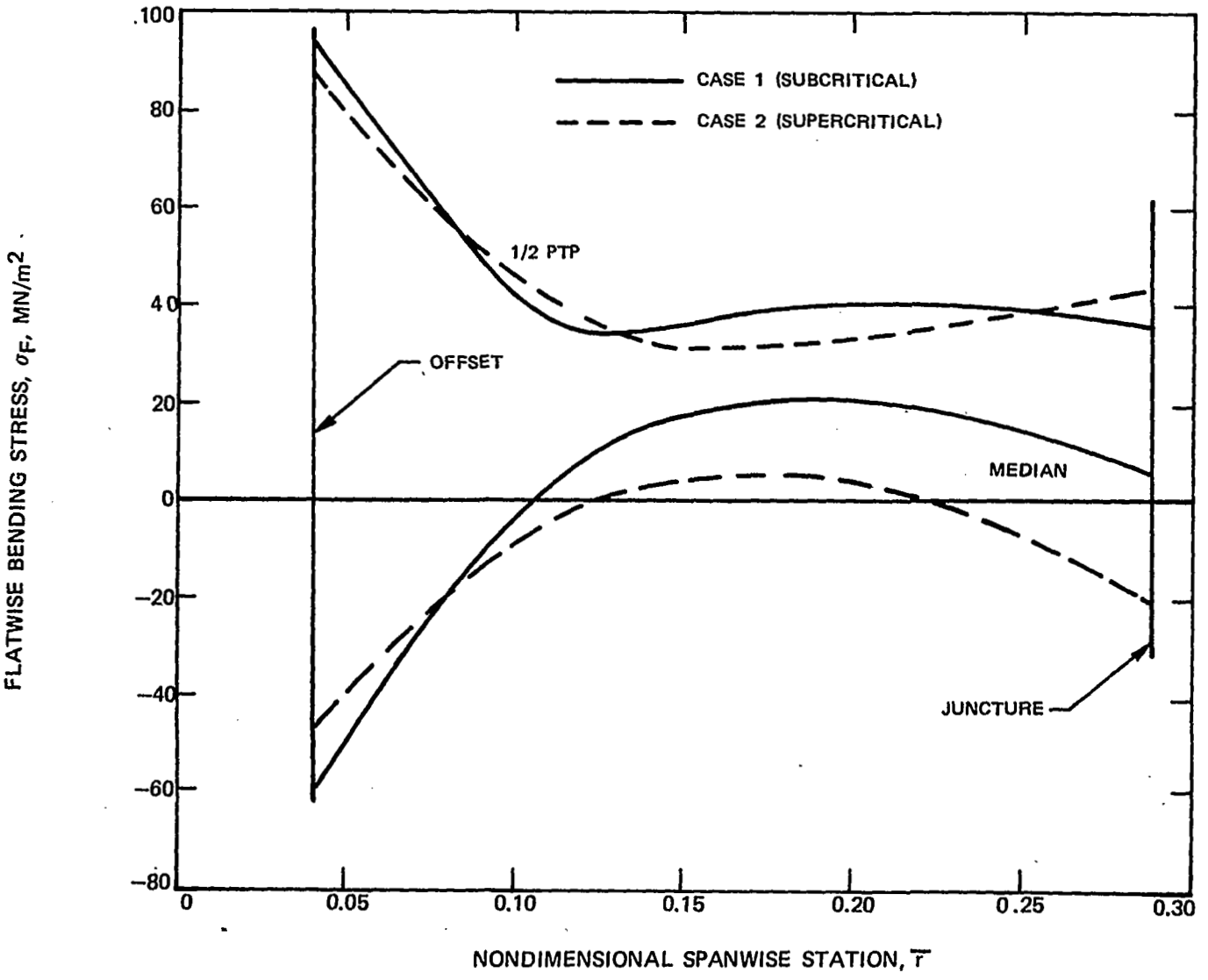

Figure 114. - Spanwise Variation of Flexbeam Flatwise Stresses, Trim Cases 1 and 2

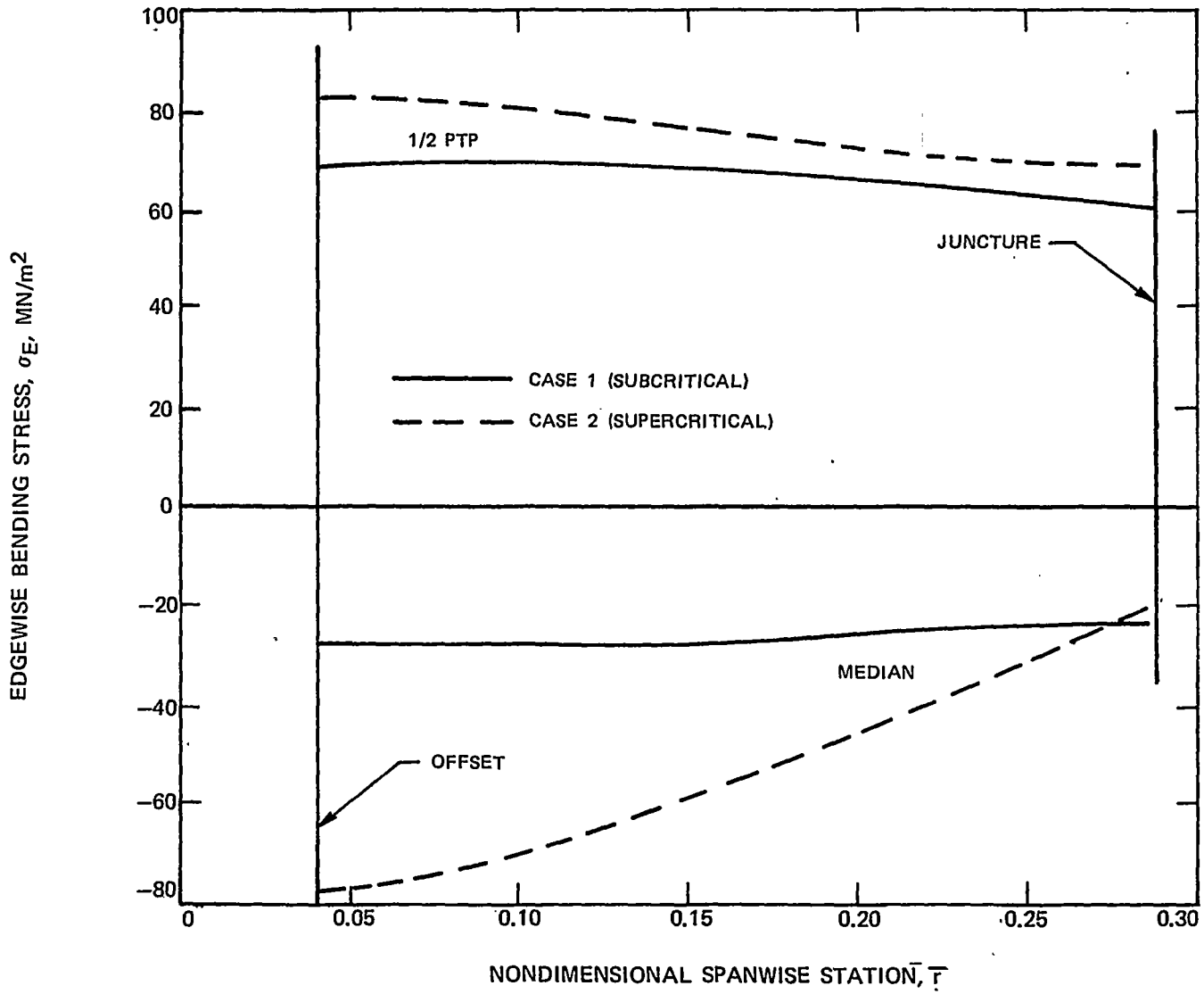

Figure 115. - Spanwise Variation of Flexbeam Edgewise Stresses, Trim Cases 1 and 2

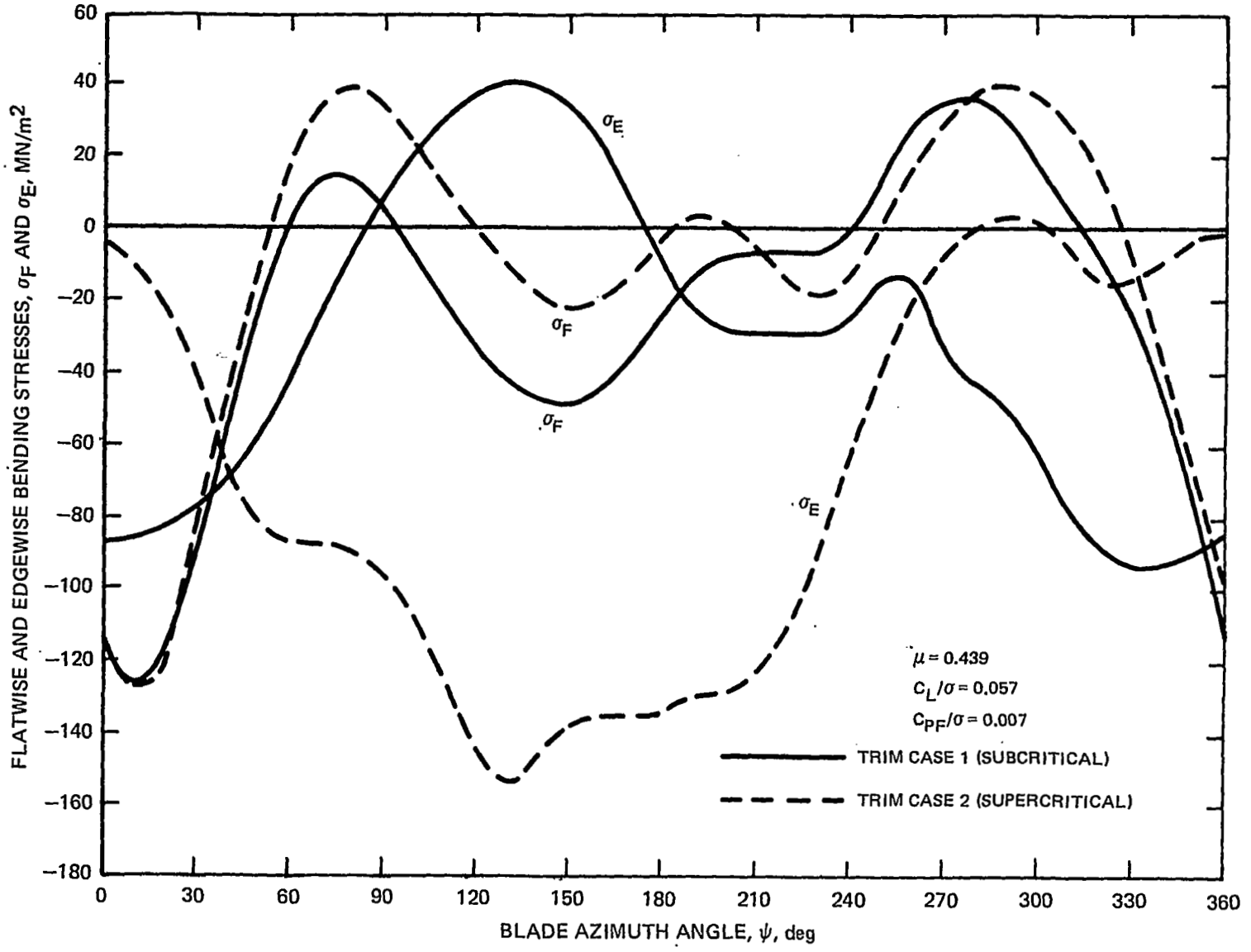

Figure 116. - Azimuthal Variation of Critical Bending Stresses, Trim Cases 1 and 2

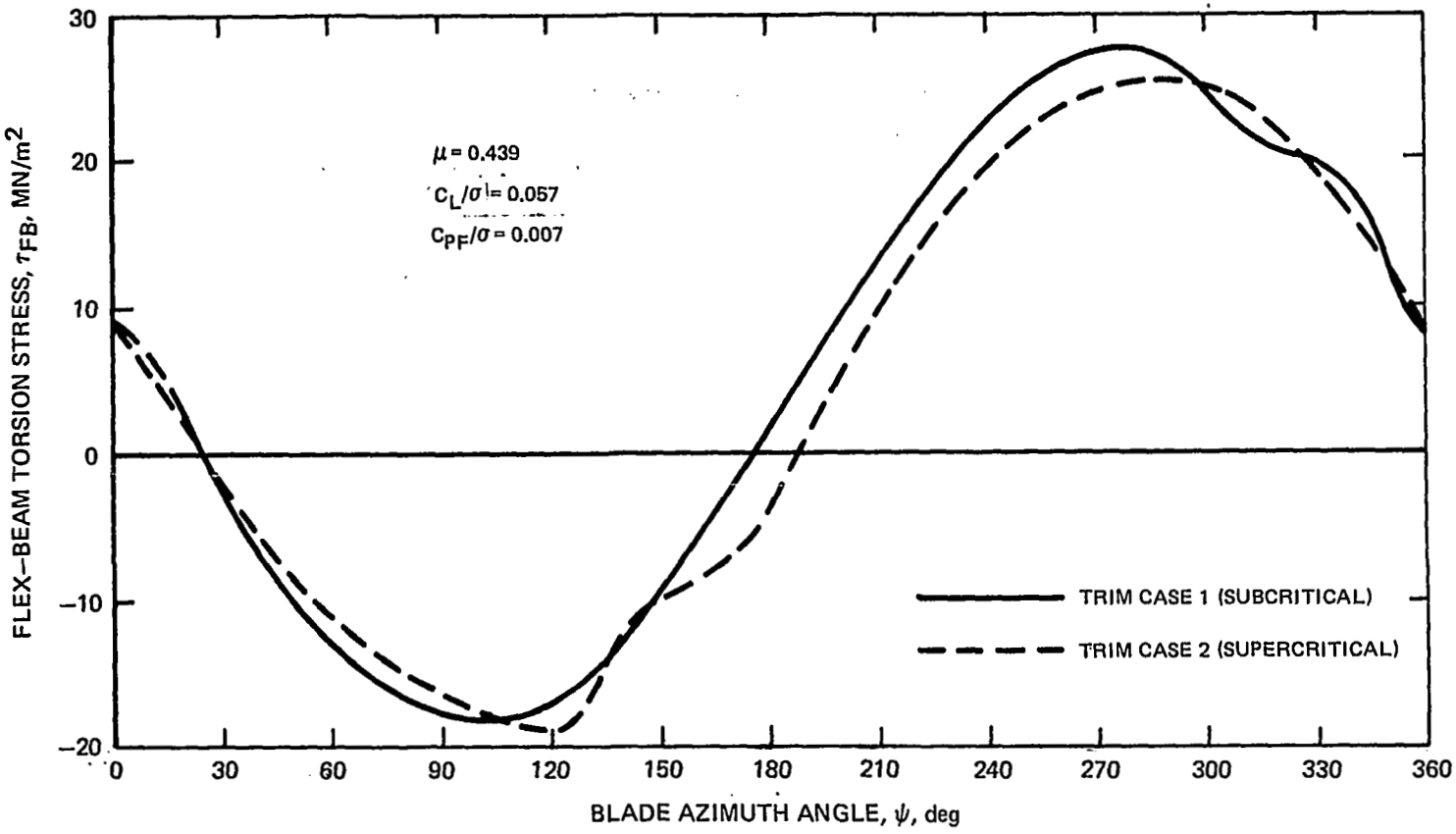

Figure 117. - Azimuthal Variation of Critical Flexbeam Torsion Stress, Trim Cases 1 and 2

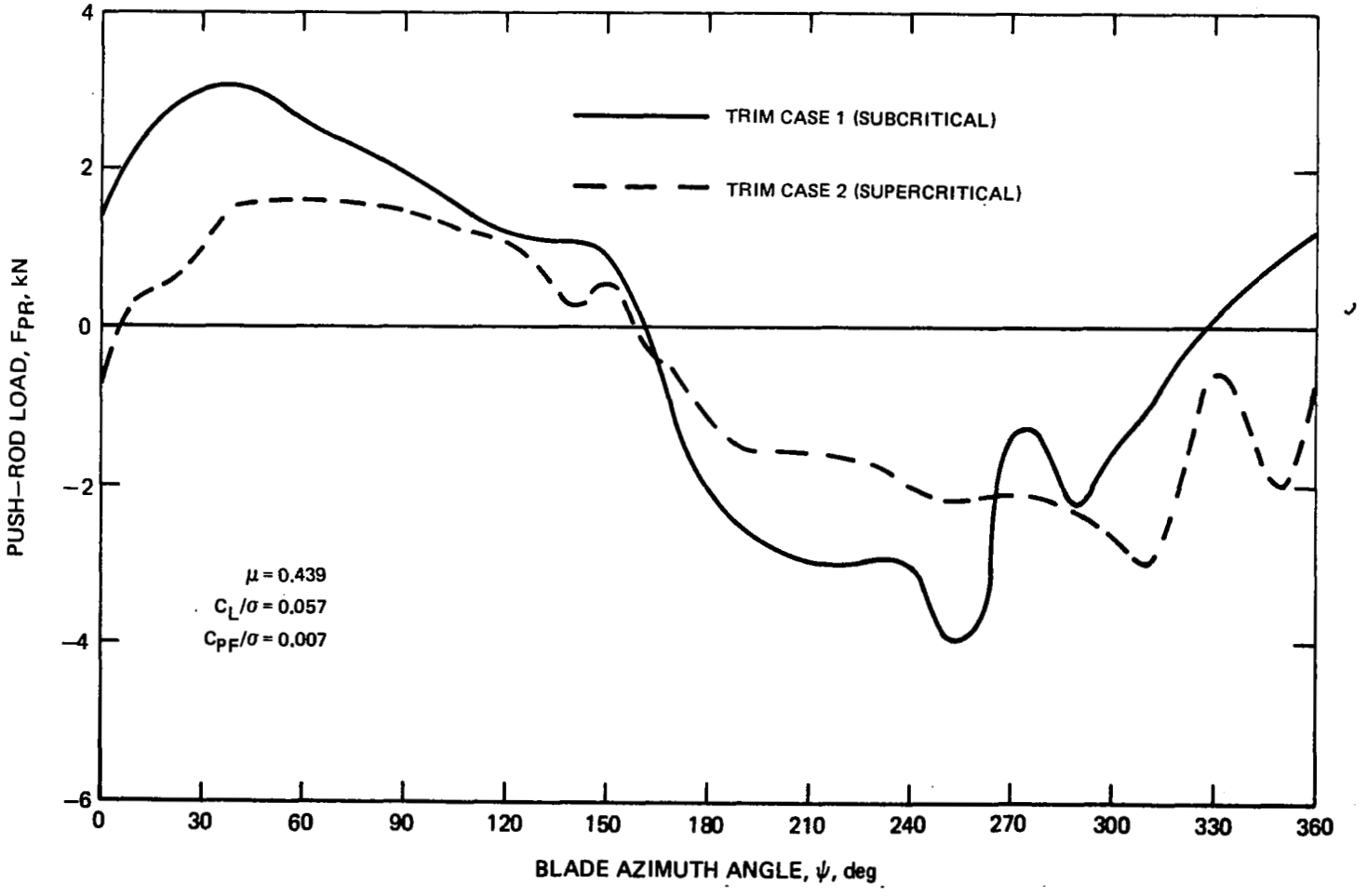

Figure 118. - Azimuthal Variation of Push-Rod Load, Trim Cases 1 and 2

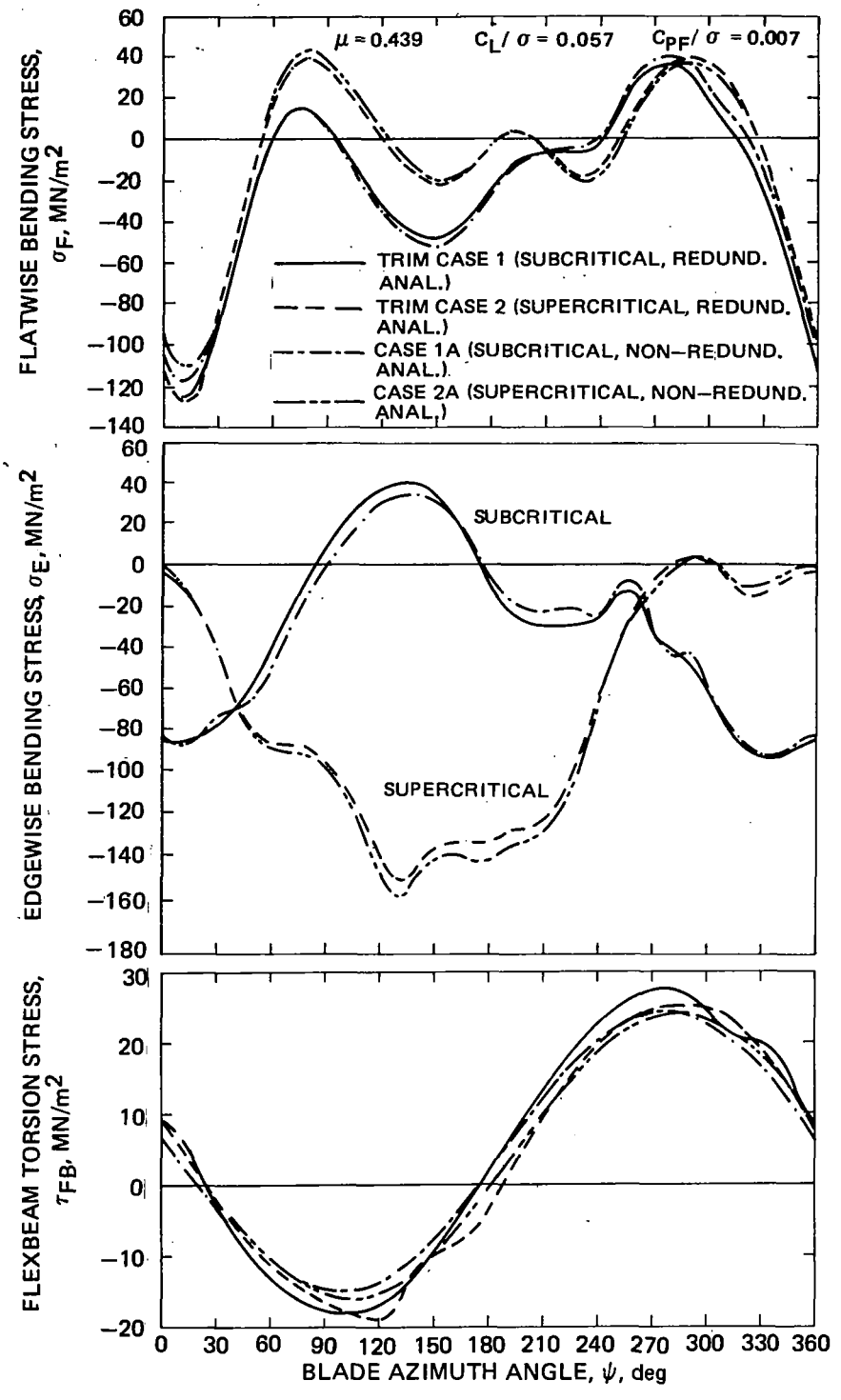

Figure 119a. - Effects of Complete Modelling of Structural Redundancy on Stresses

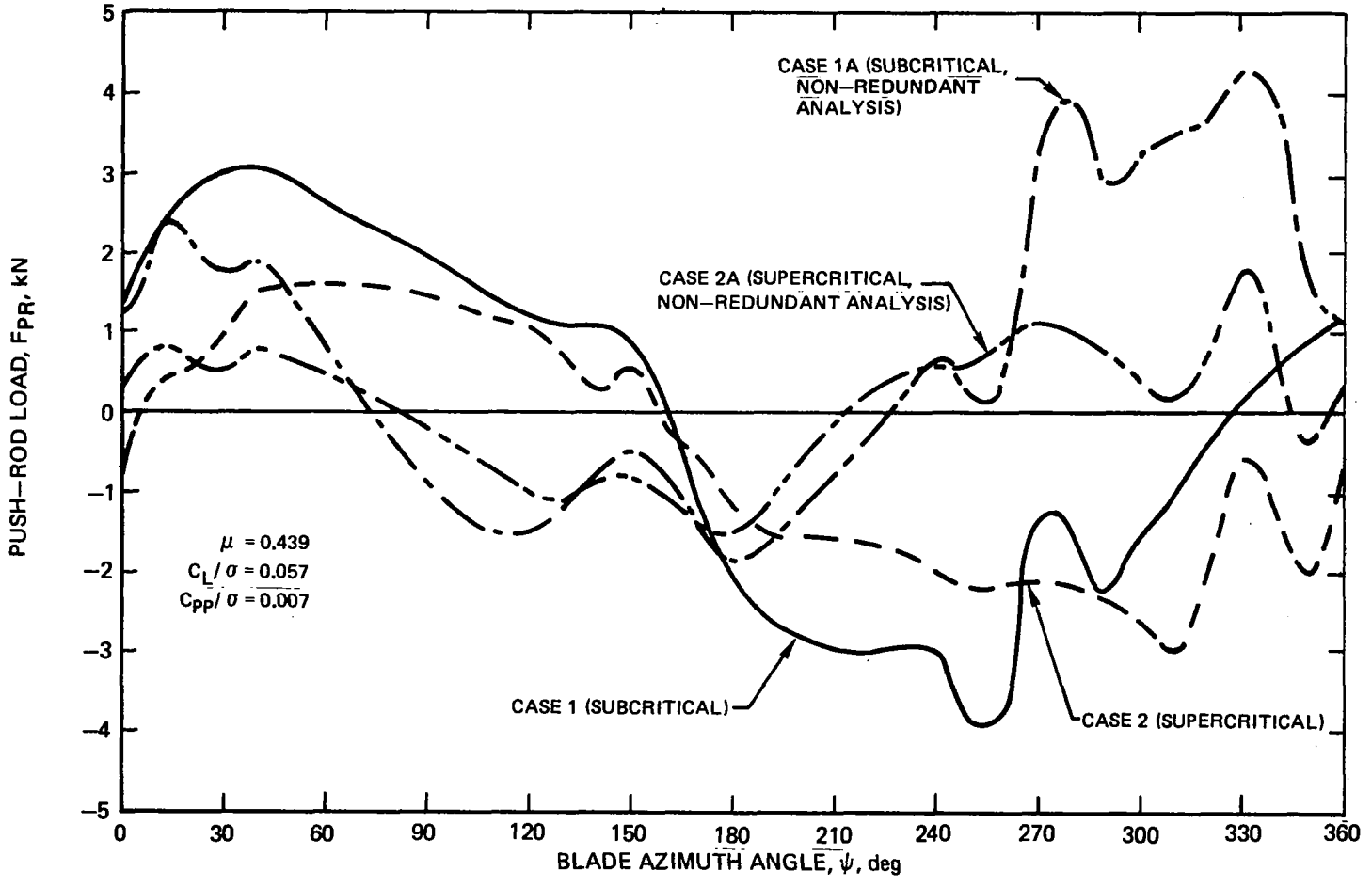

Figure 119b. - Effects of Complete Modelling of Structural Redundancy on Push-Rod Loads

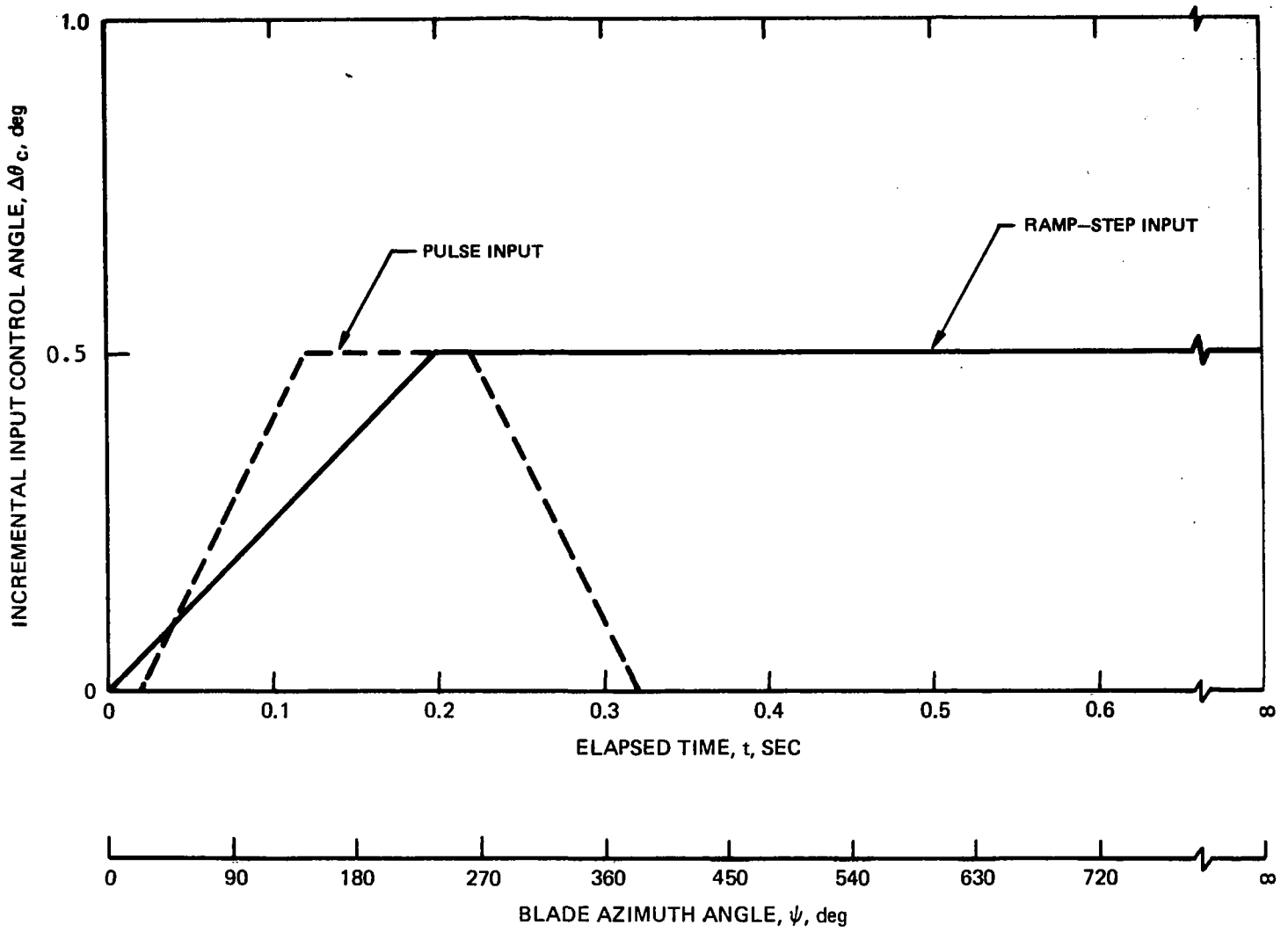

Figure 120. - Incremental Ramp-Step and Pulse Input Control Angle Time-Histories

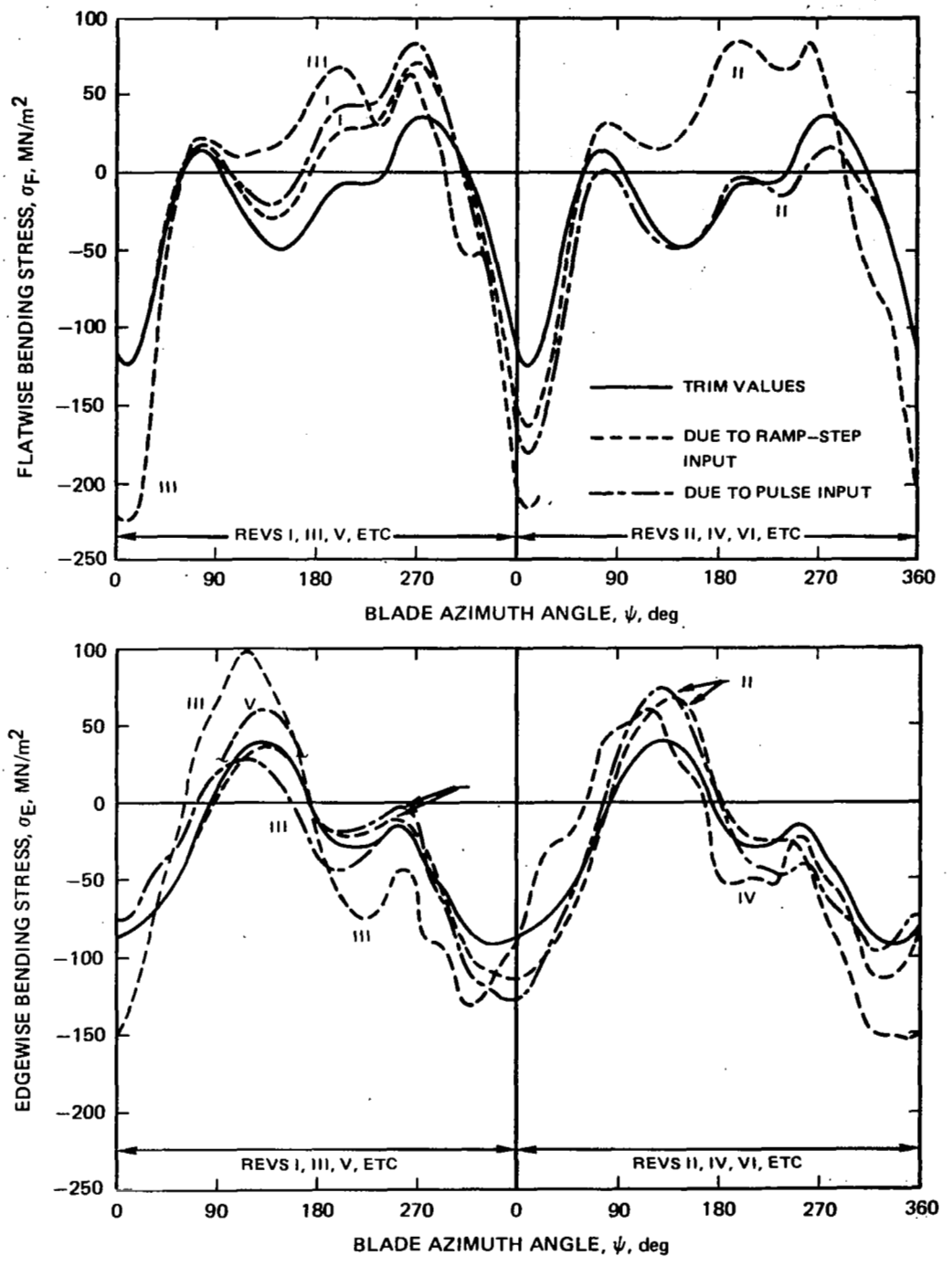

Figure 121a.—Transient Bending Stresses due to Collective Angle Inputs, Subcritical Design

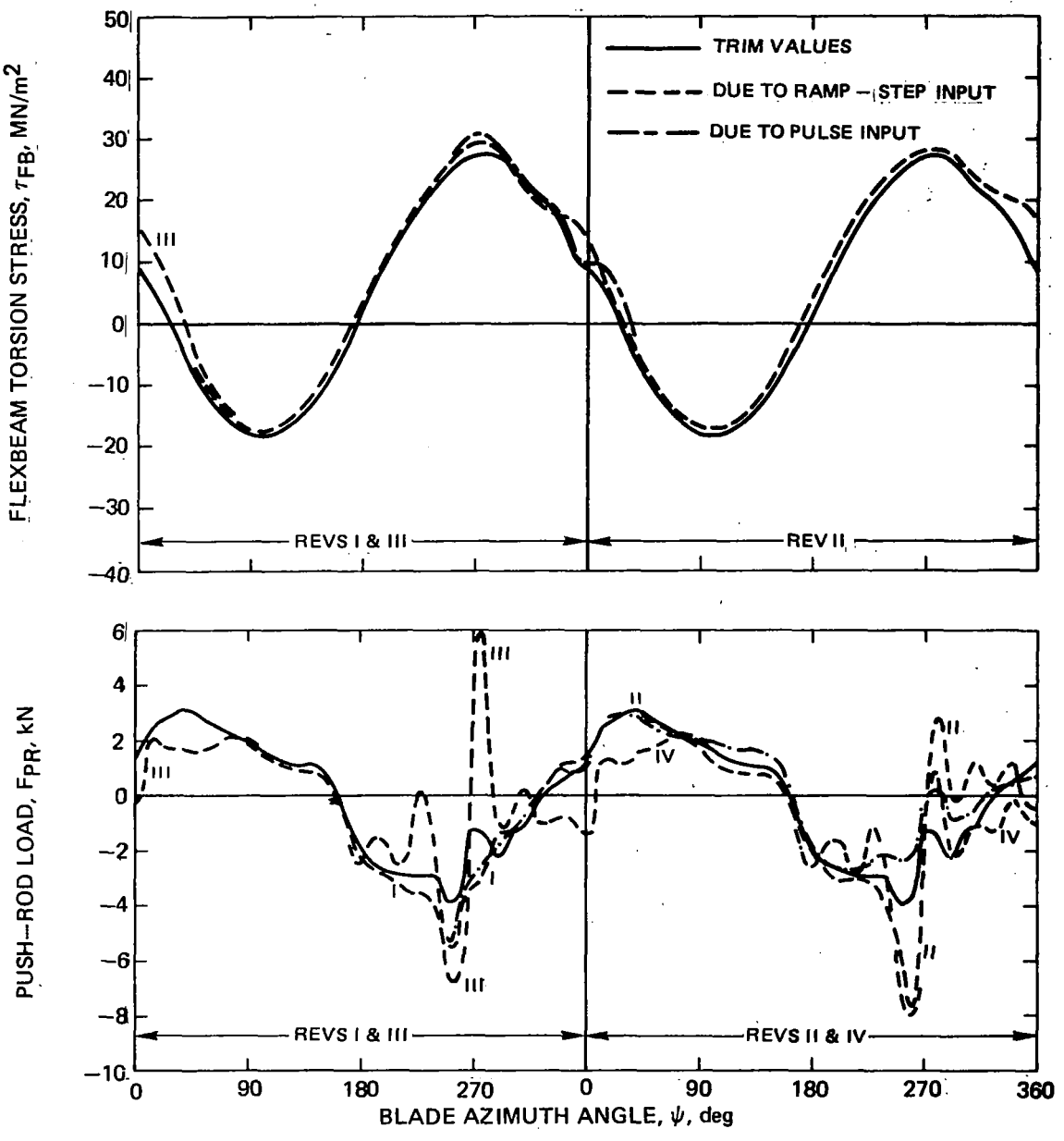

Figure 121b. - Transient Flexbeam Torsion Stresses and Push-Rod Loads due to Collective Angle Inputs, Subcritical Design

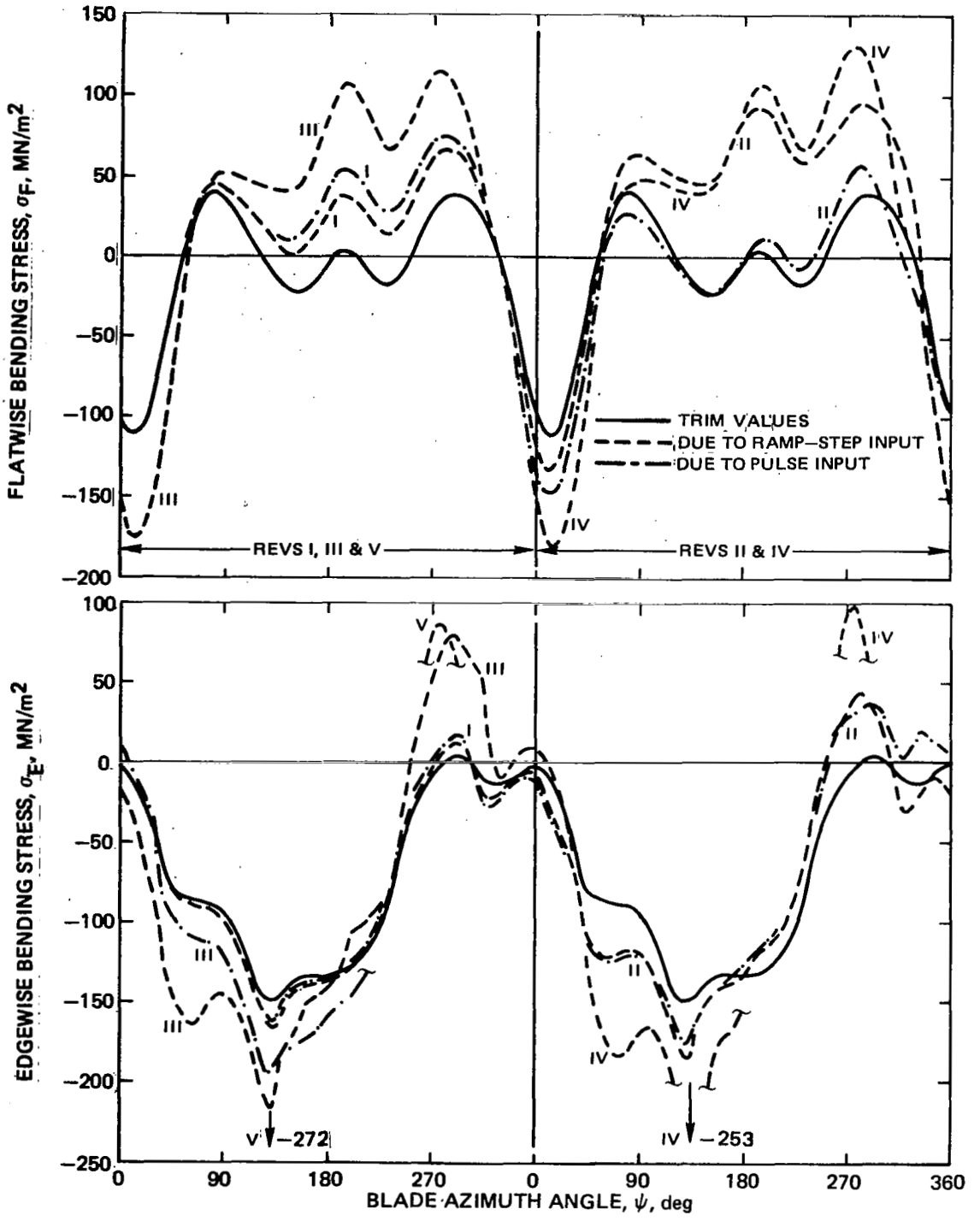

Figure 122a.- Transient Bending Stresses due to Collective Angle Inputs, Supercritical Design

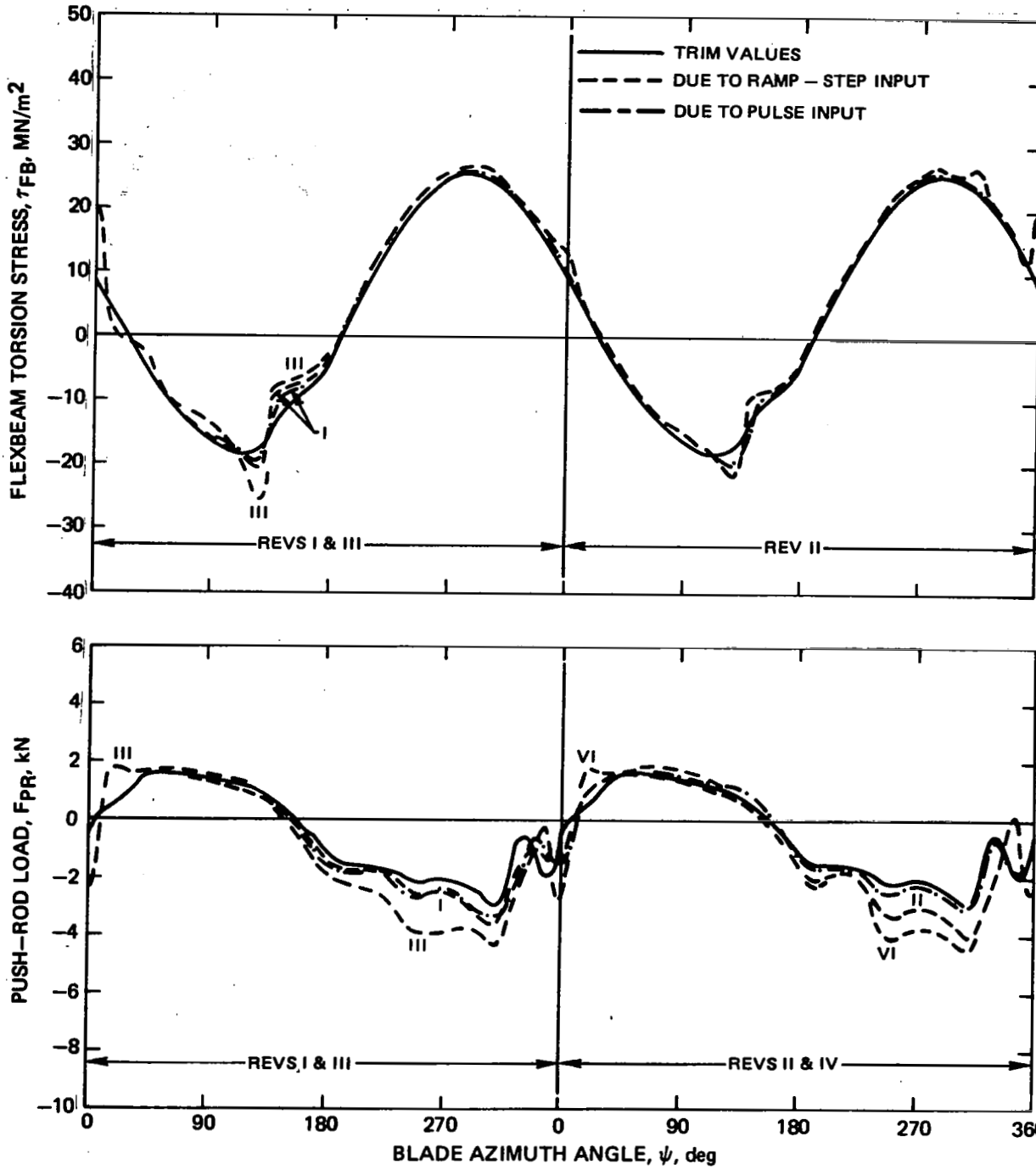

Figure 122b. - Transient Flexbeam Torsion Stresses and Push-Rod Loads due to Collective Angle Inputs, Supercritical Design

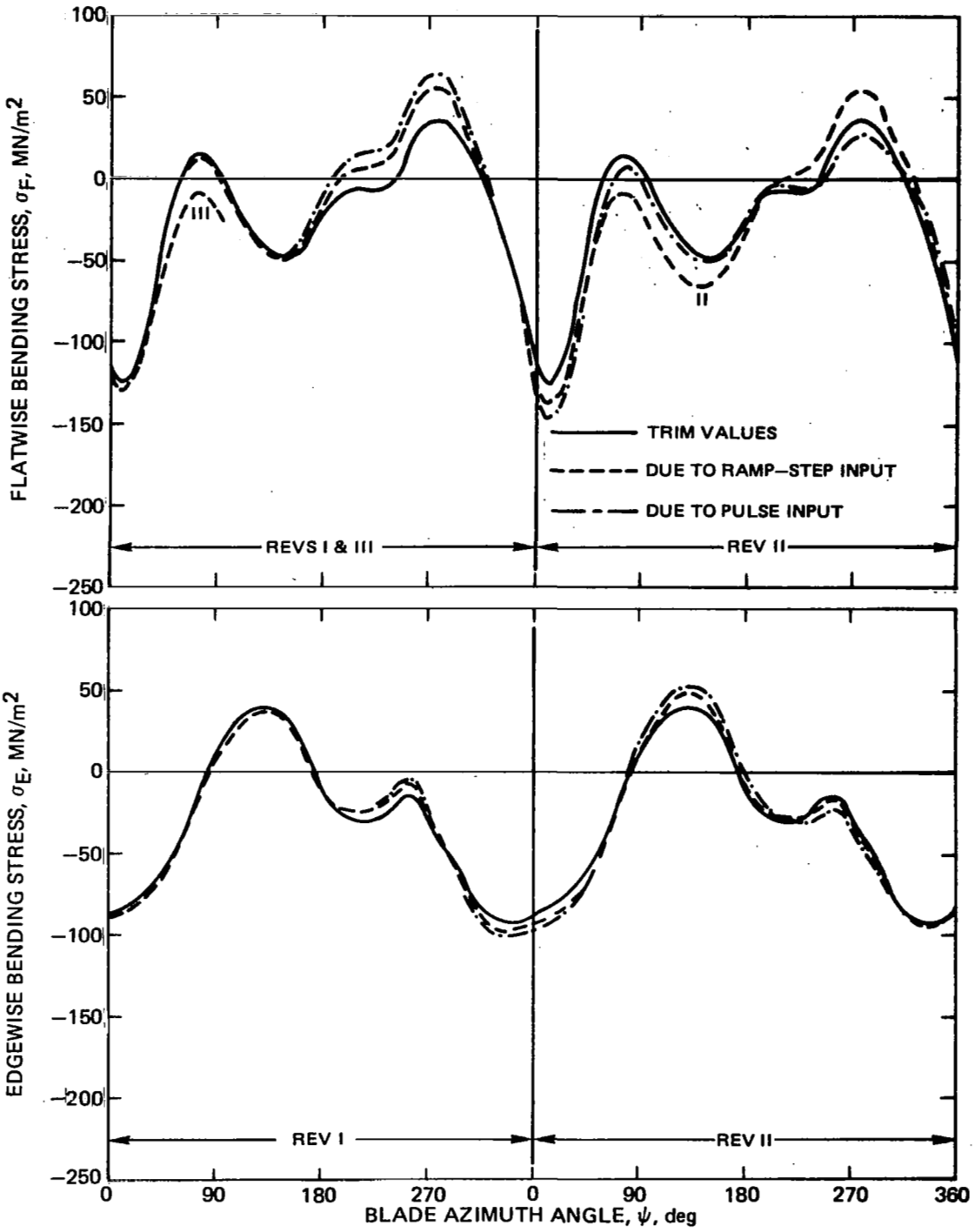

Figure 123a. - Transient Bending Stresses due to Longitudinal Cyclic Angle Inputs, Subcritical Design

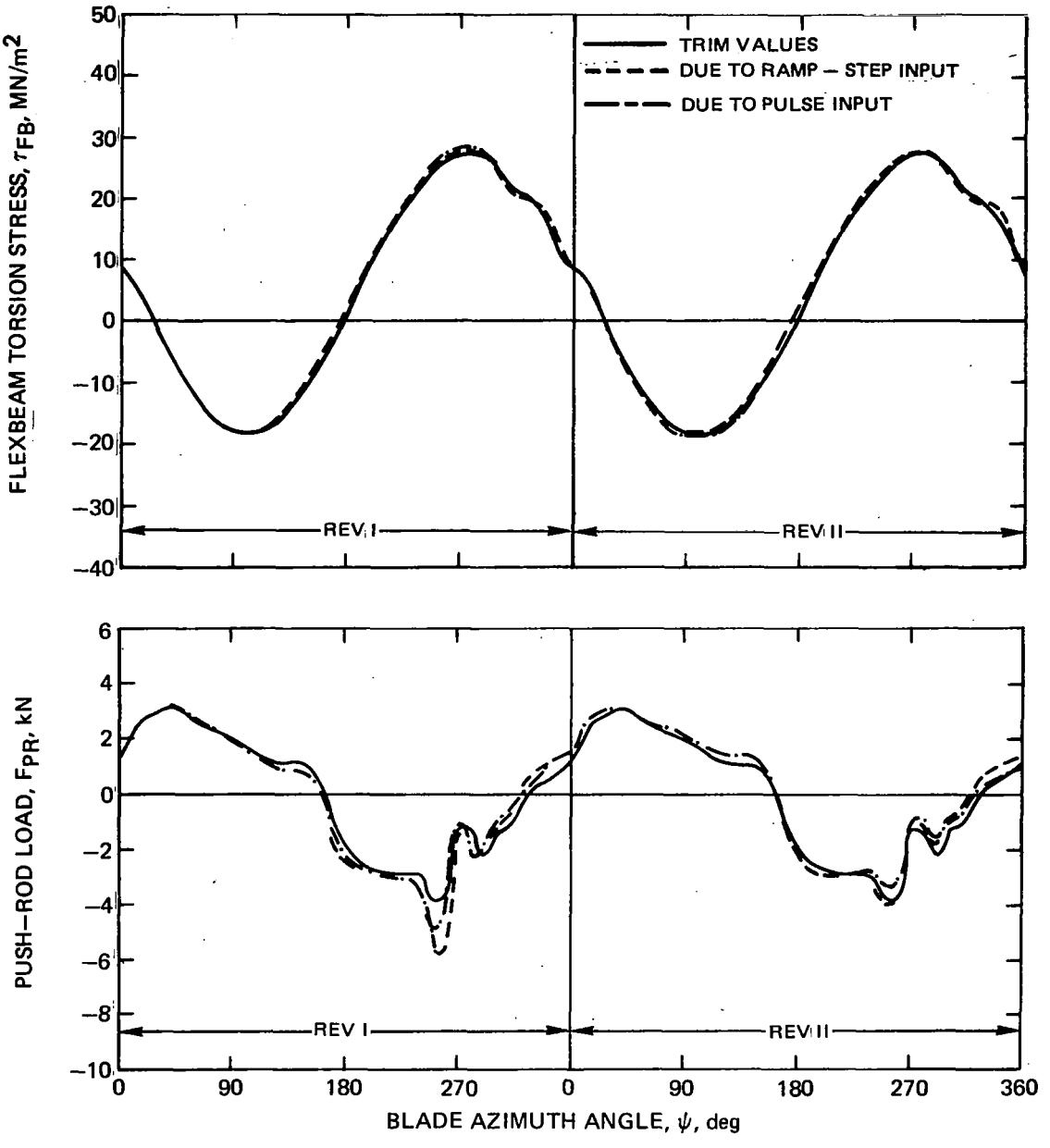

Figure 123b. - Transient Flexbeam Torsion Stresses and Push-Rod Loads due to Longitudinal Cyclic Angle Inputs, Subcritical Design

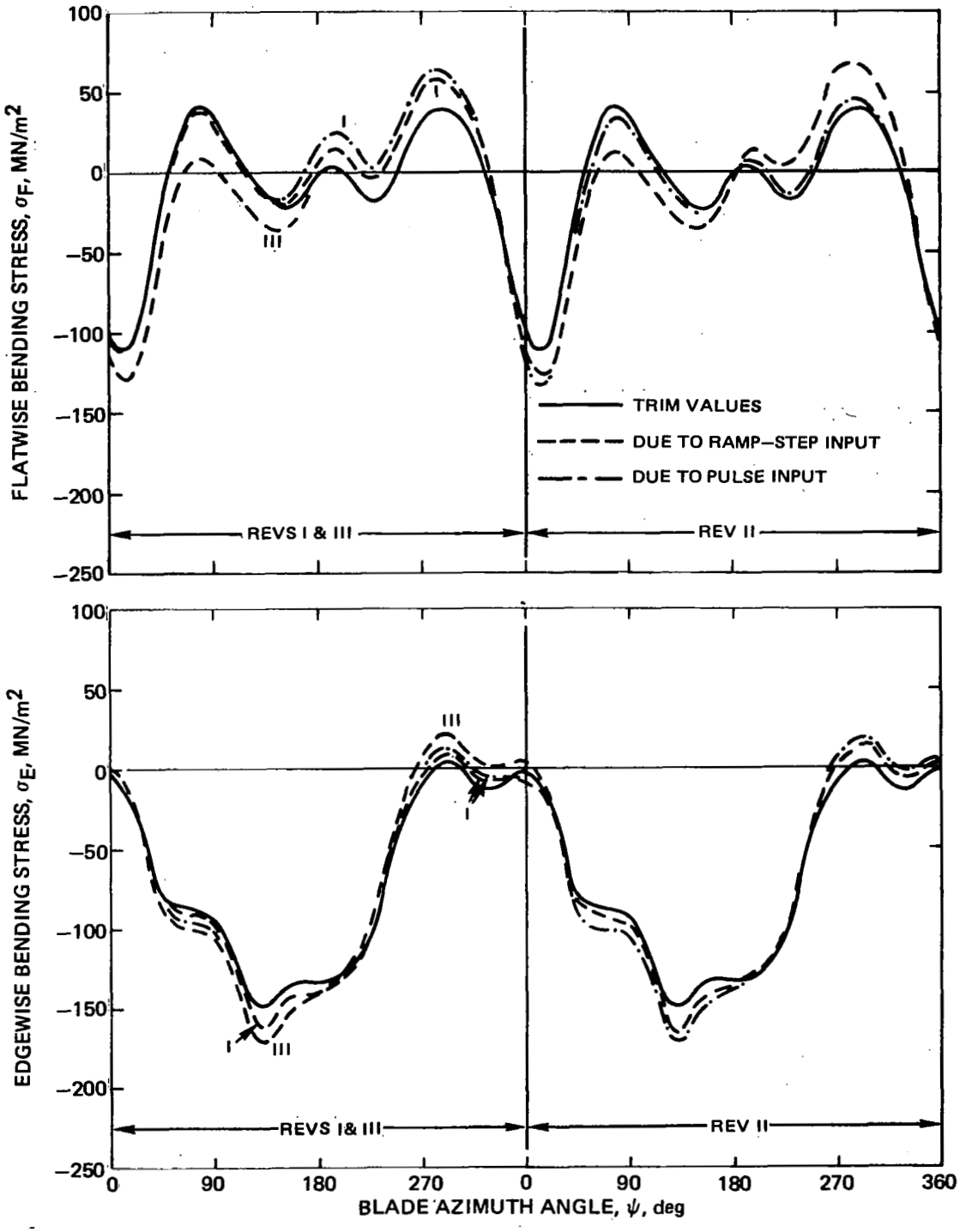

Figure 124a. - Transient Bending Stresses due to Longitudinal Cyclic Angle Inputs, Supercritical Design

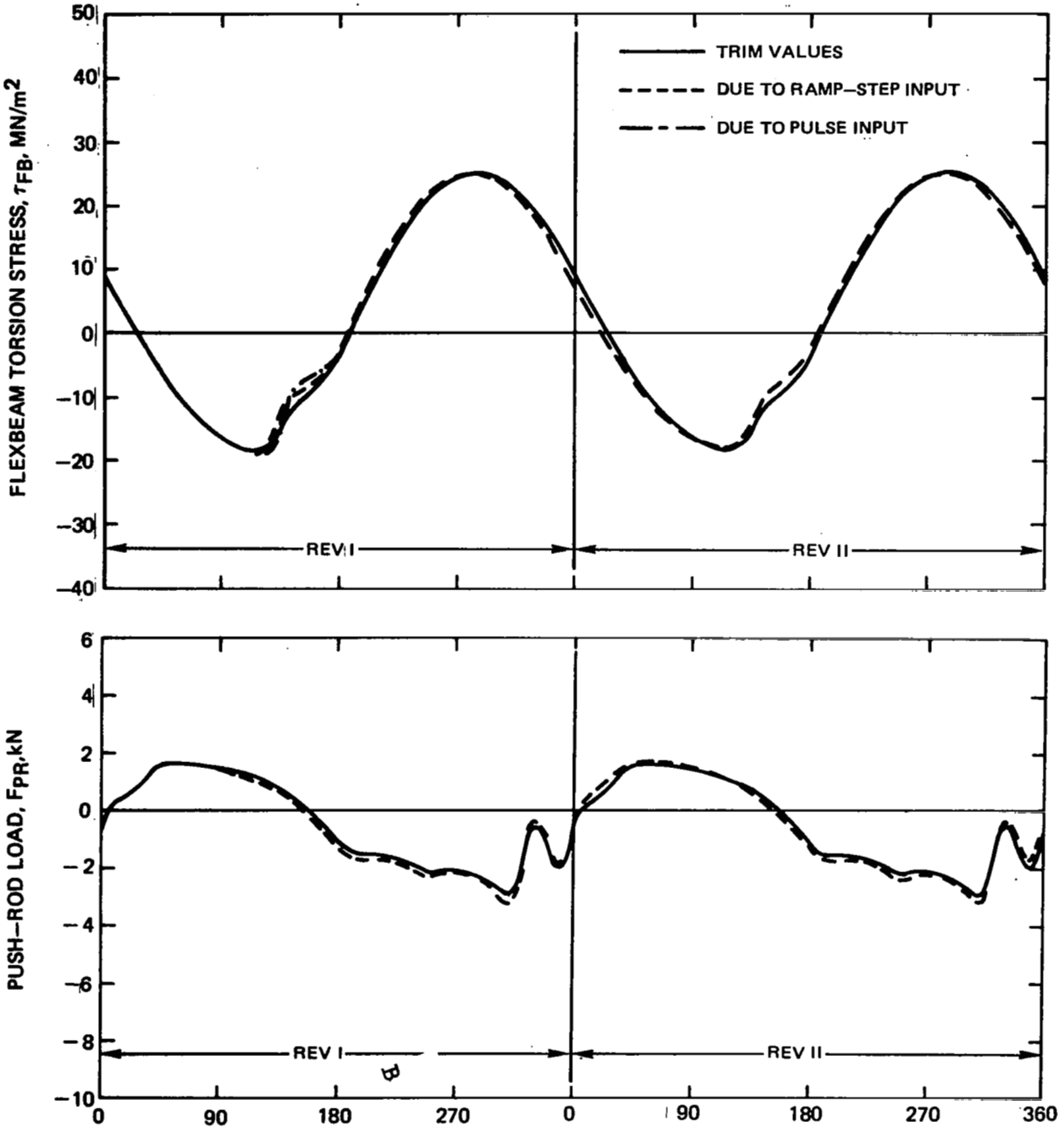

Figure 124b. - Transient Flexbeam Torsion Stresses and Push-Rod Loads due to Longitudinal Cyclic Angle Inputs, Supercritical Design

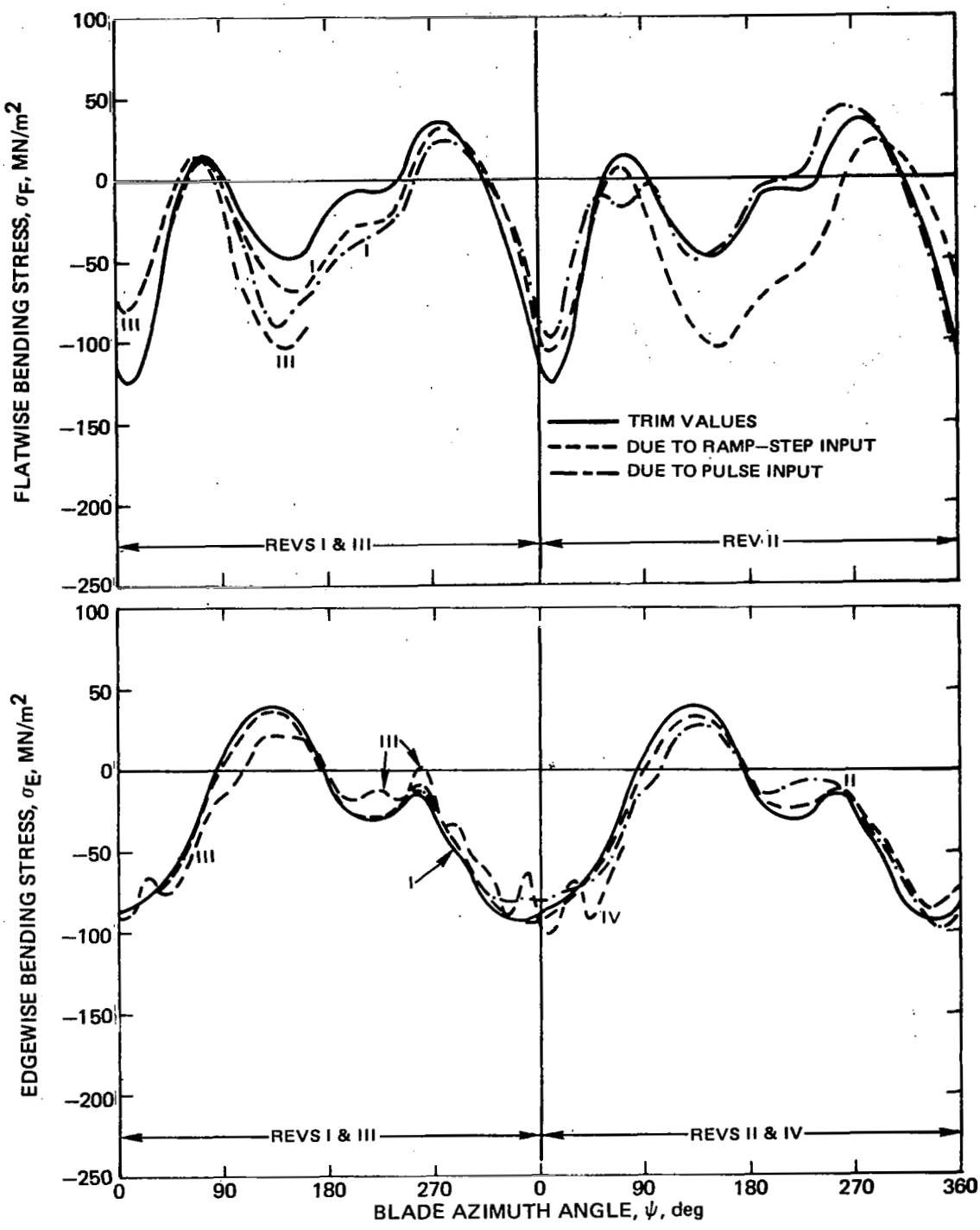

Figure 125a. - Transient Bending Stresses due to Lateral Cyclic Angle Inputs, Subcritical Design

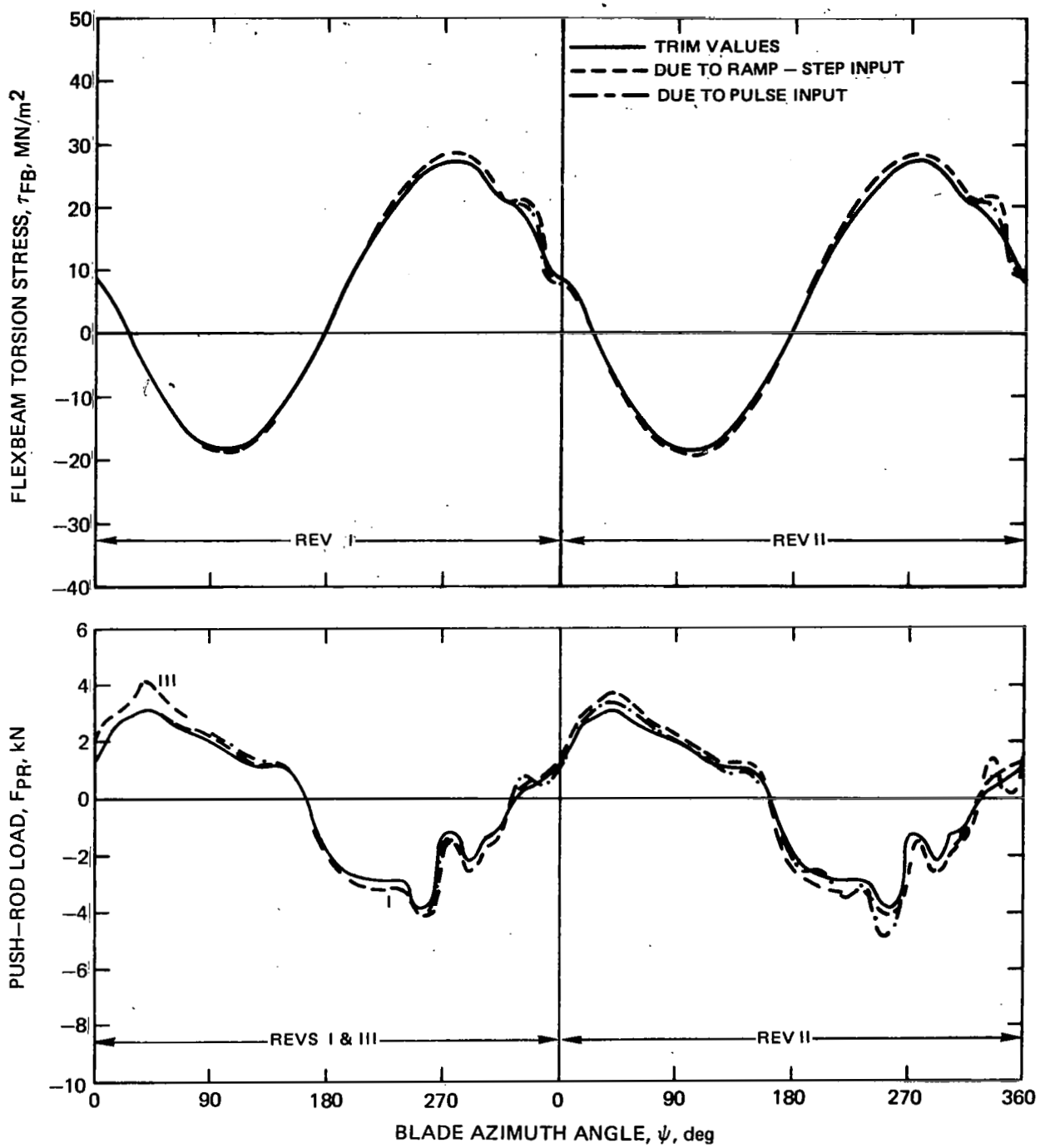

Figure 125b. - Transient Flexbeam Torsion Stresses and Push-Rod Loads due to Lateral Cyclic Angle Inputs, Subcritical Design

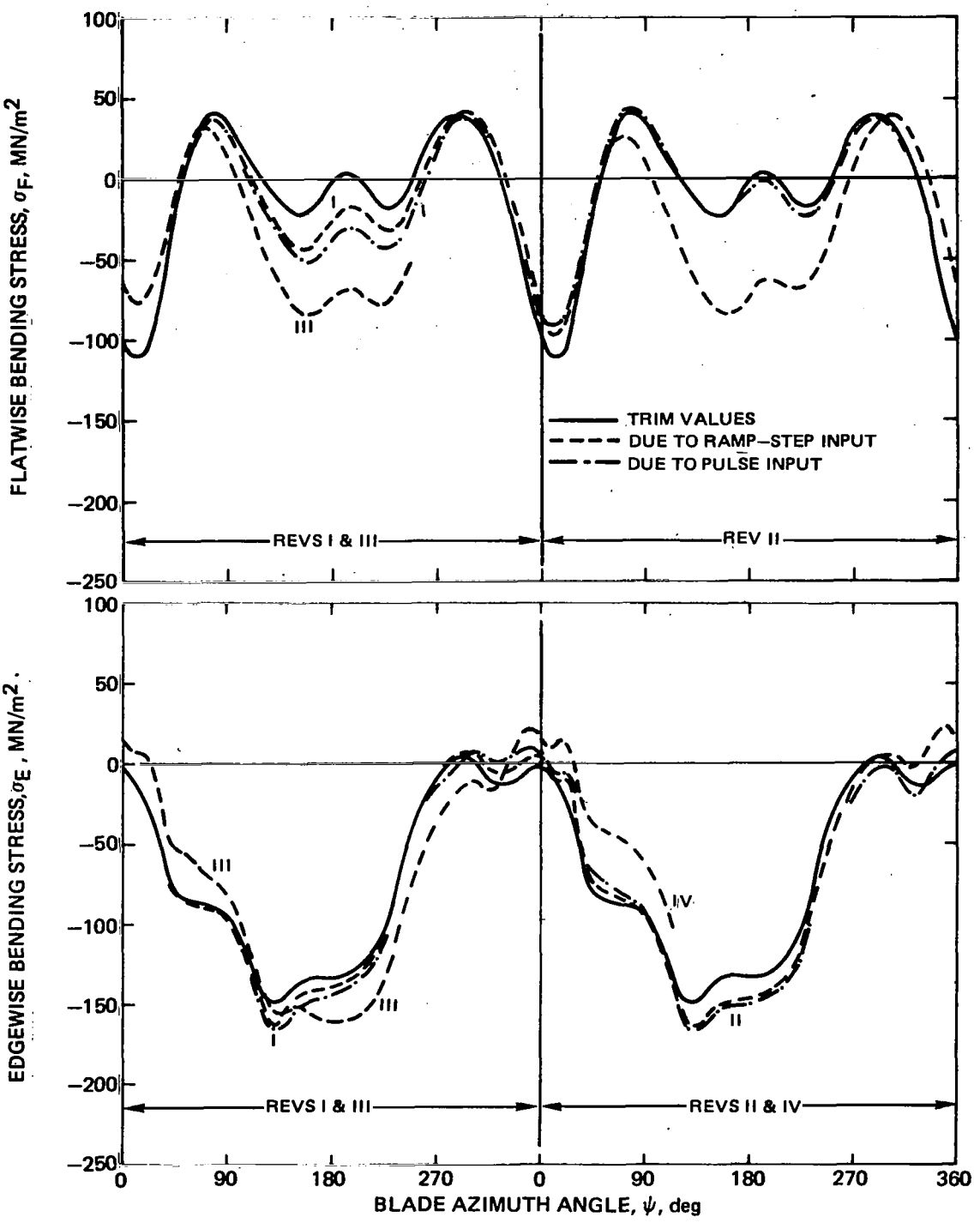

Figure 126a. - Transient Bending Stresses due to Lateral Cyclic Angle Inputs, Supercritical Design

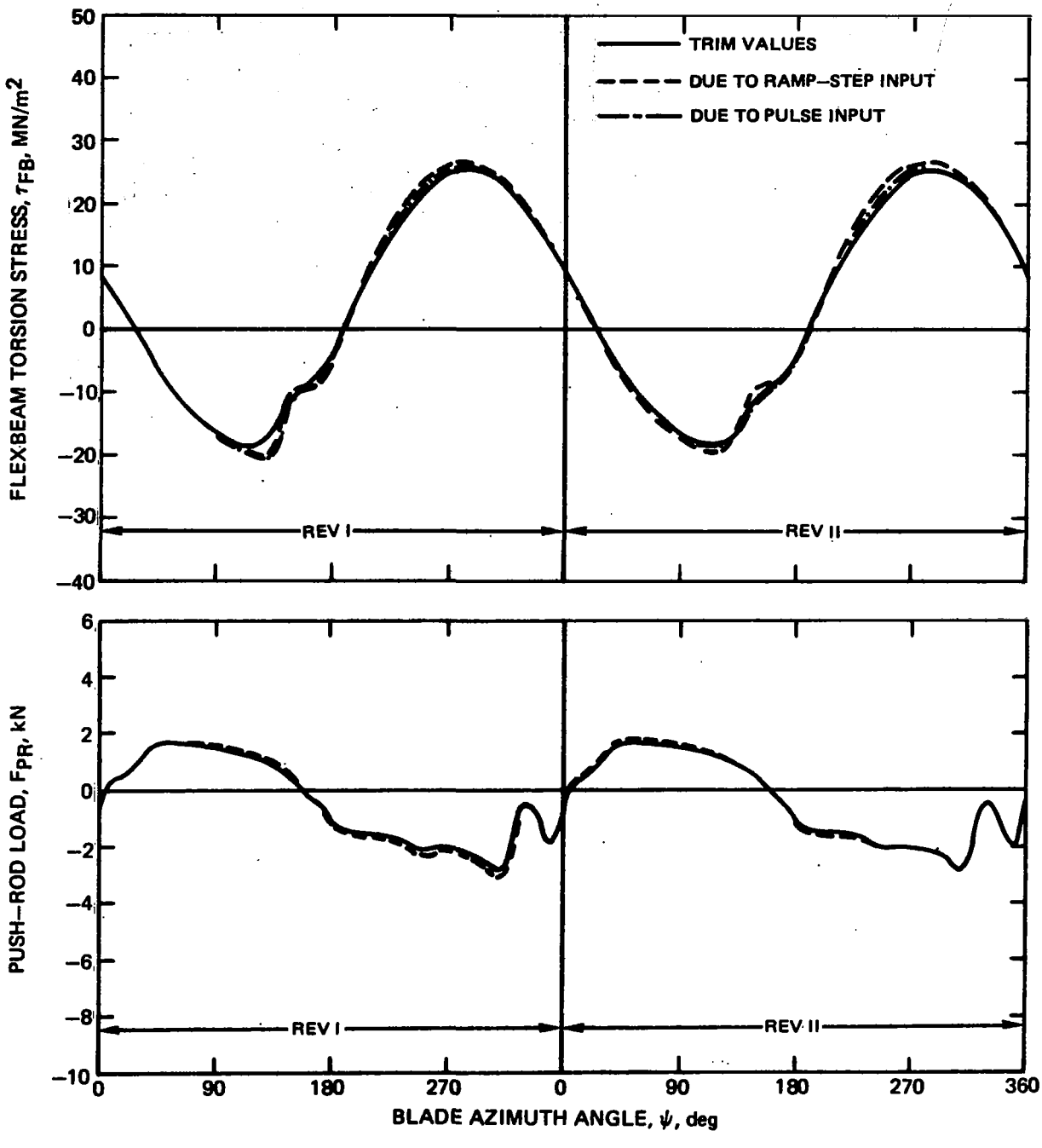

Figure 126b. - Transient Flexbeam Torsion Stresses and Push-Rod Loads due to Lateral Cyclic Angle Inputs, Supercritical Design

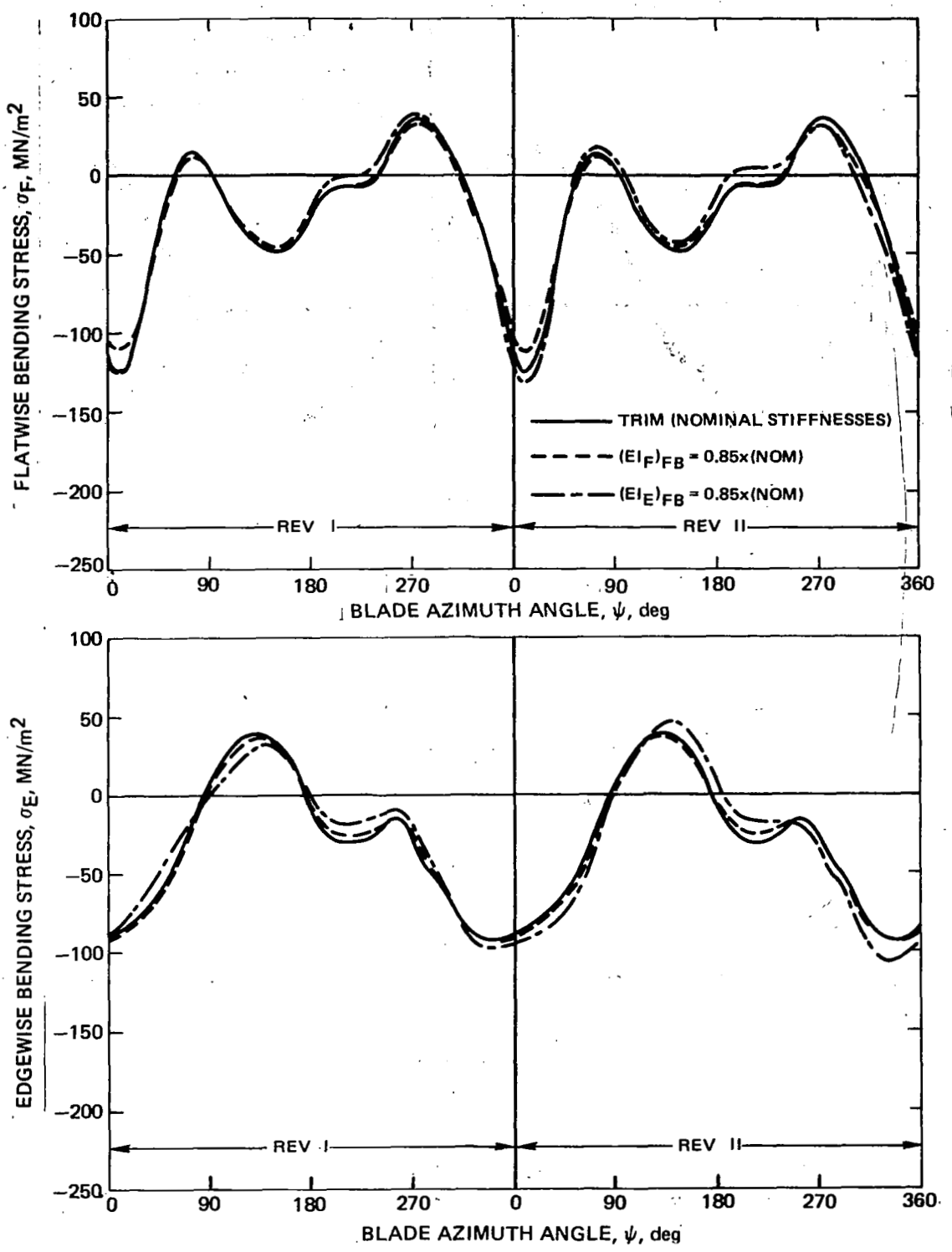

Figure 127. - Transient Bending Stresses due to Partial Flexbeam Material Failure, Subcritical Design

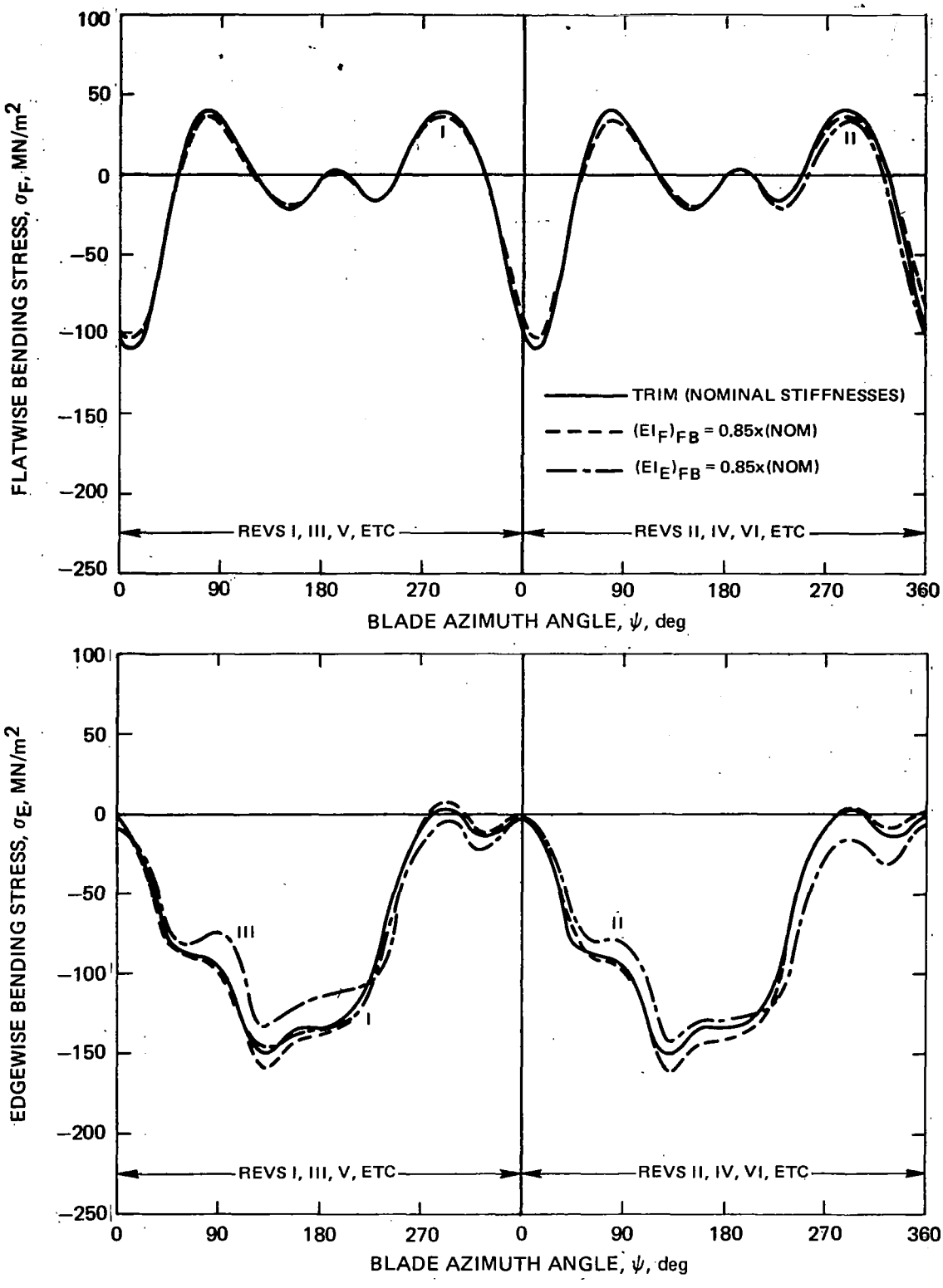

Figure 128. - Transient Bending Stresses due to Partial Flexbeam Material Failure, Supercritical Design

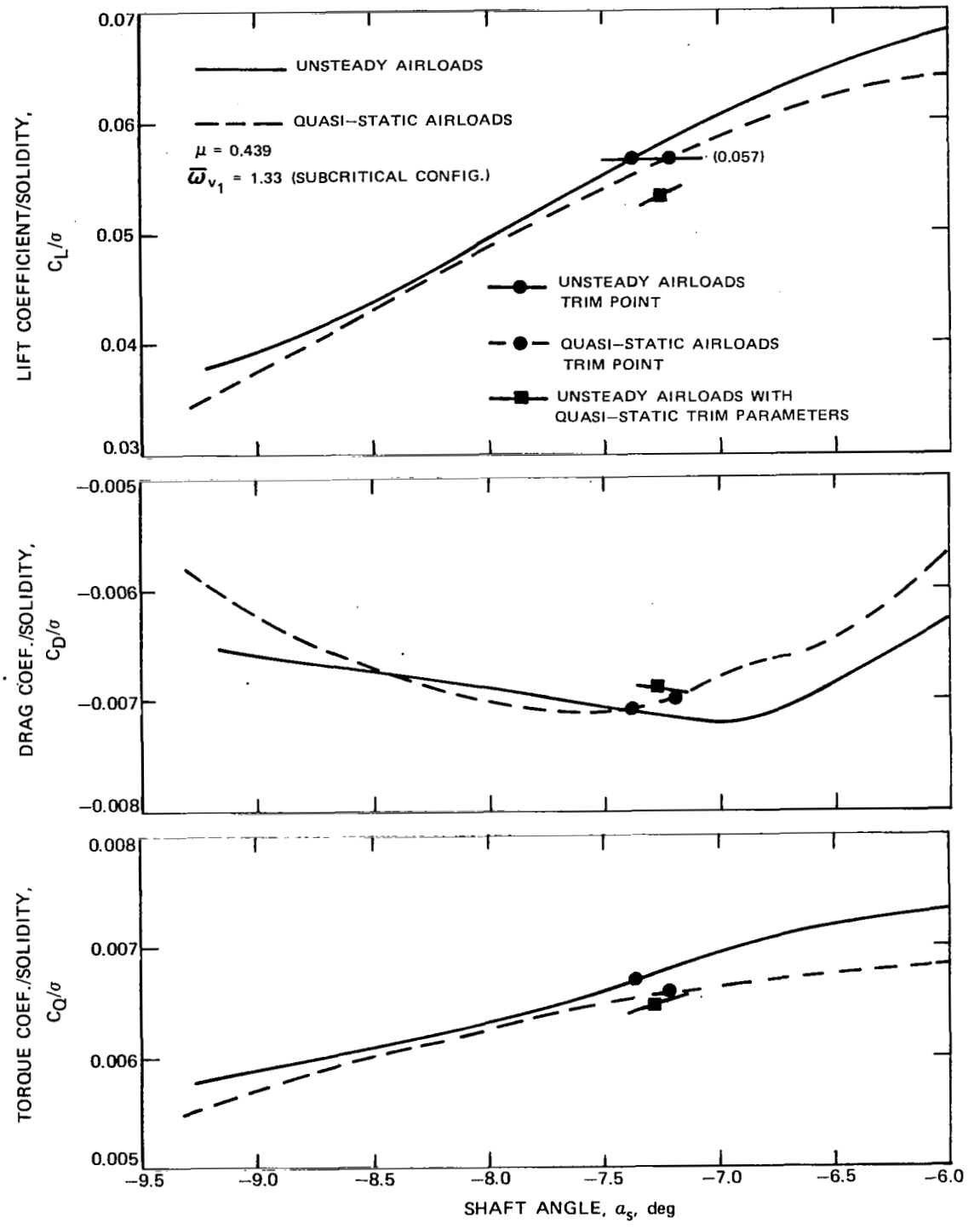

Figure 129. - Effects of Unsteady Airloads Formulation on Variation of Rotor Performance with Shaft Angle

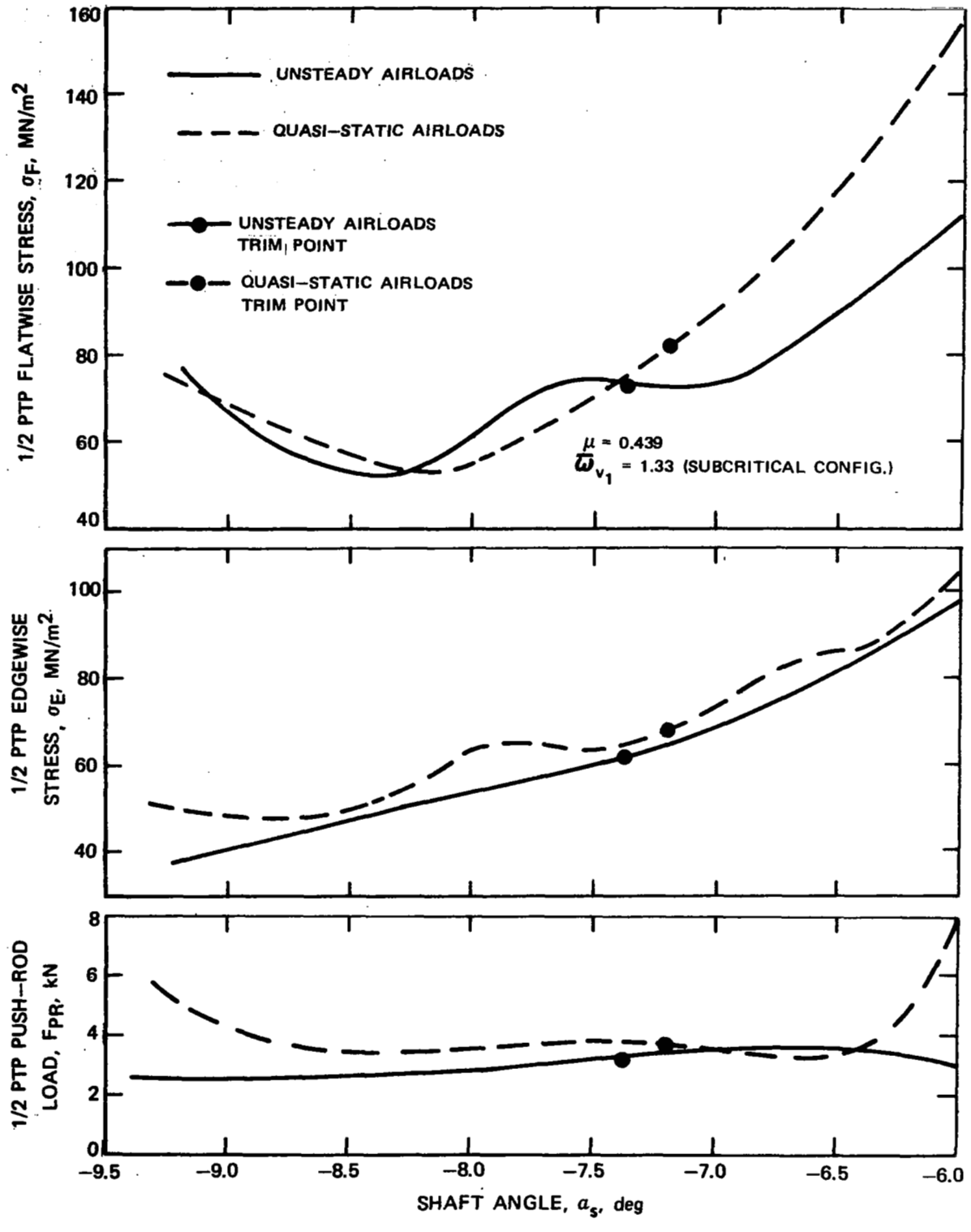

Figure 130. - Effects of Unsteady Airloads Formulation on Variations of Vibratory Bending Stresses and Push-Rod Load with Shaft Angle

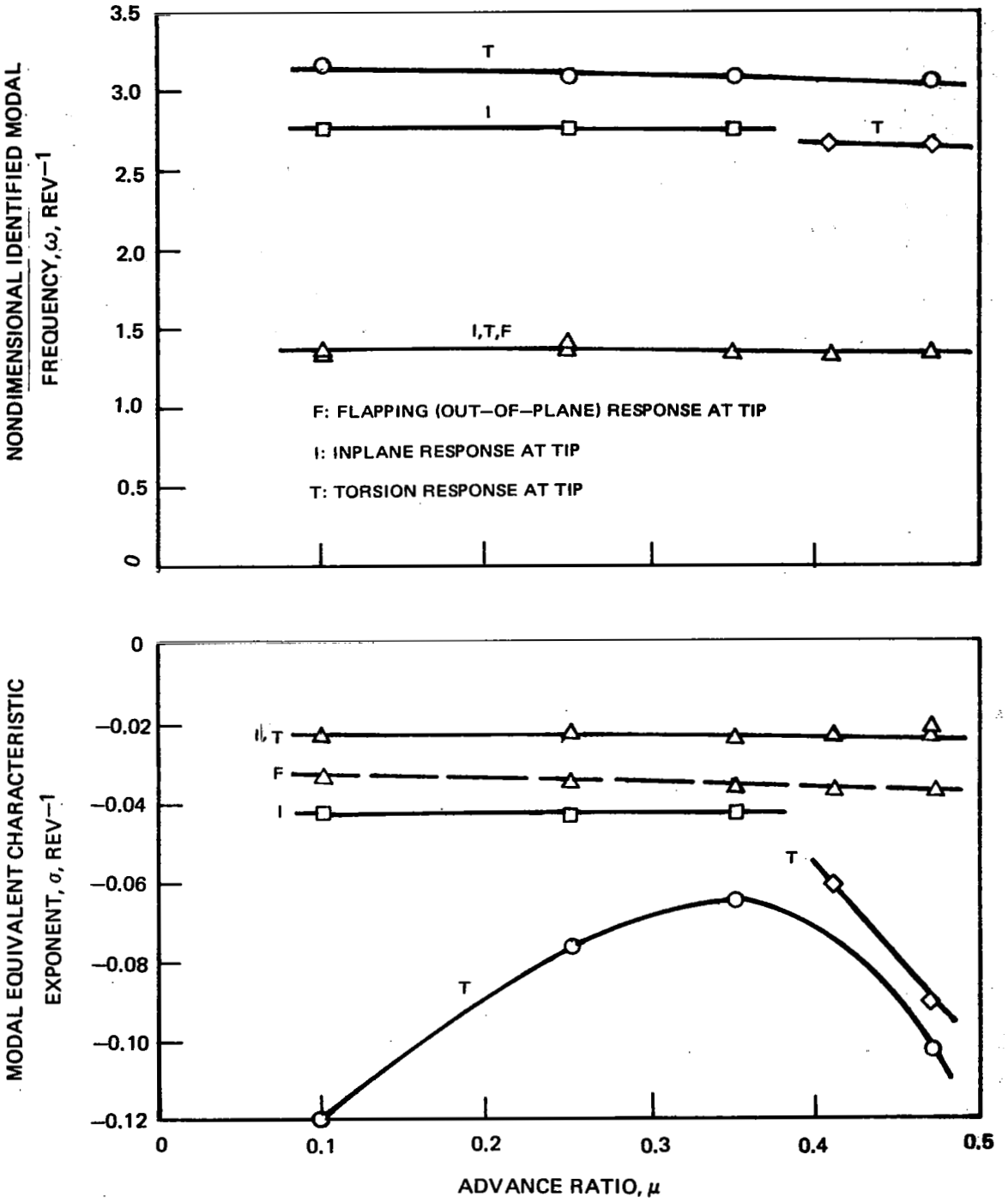

Figure 131. - Variation of Identified Modal Frequencies and Characteristic Exponents with Advance Ratio, Cantilevered Torque Tube Model Rotor, Trailing Edge Push-Rod Attachment at .080R

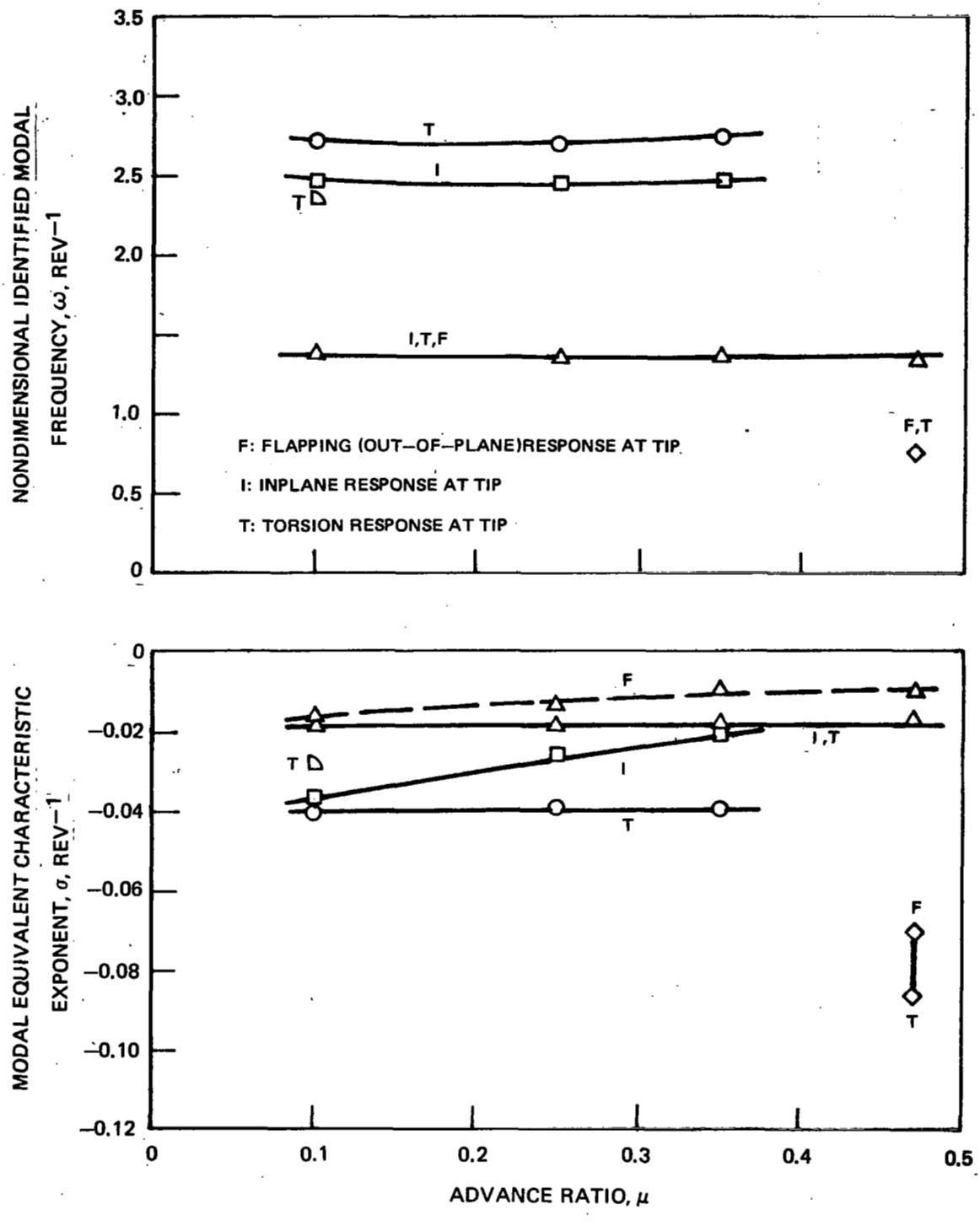

Figure 132. - Variation of Identified Modal Frequencies and Characteristic Exponents with Advance Ratio, Cantilevered Torque Tube Model Rotor, Leading Edge Push-Rod Attachment at .070R

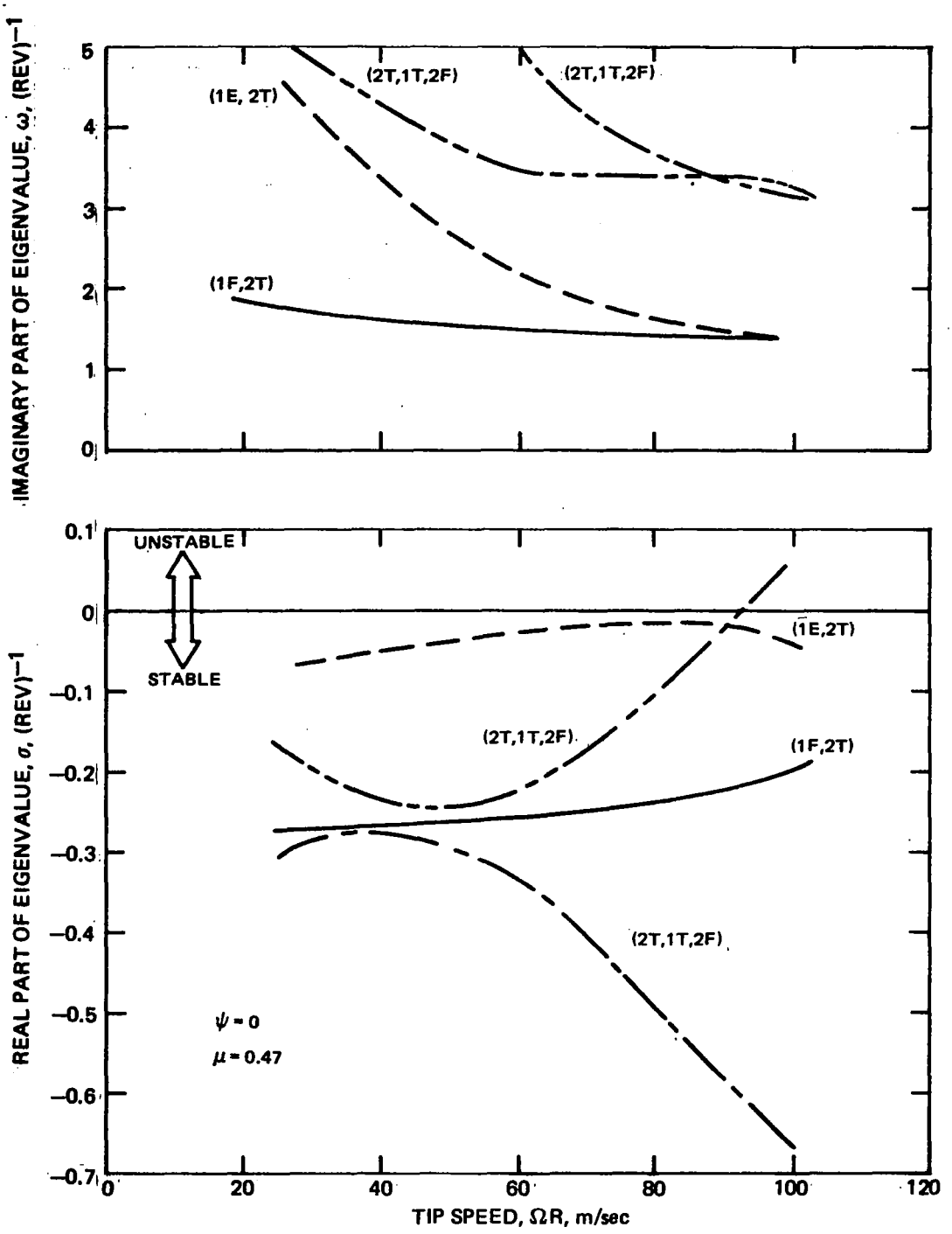

Figure 133. - Variation of Frozen Azimuth Eigenvalues with Tip Speed, Cantilevered Torque Tube Model Rotor, Trailing Edge Push-Rod Attachment at .080R

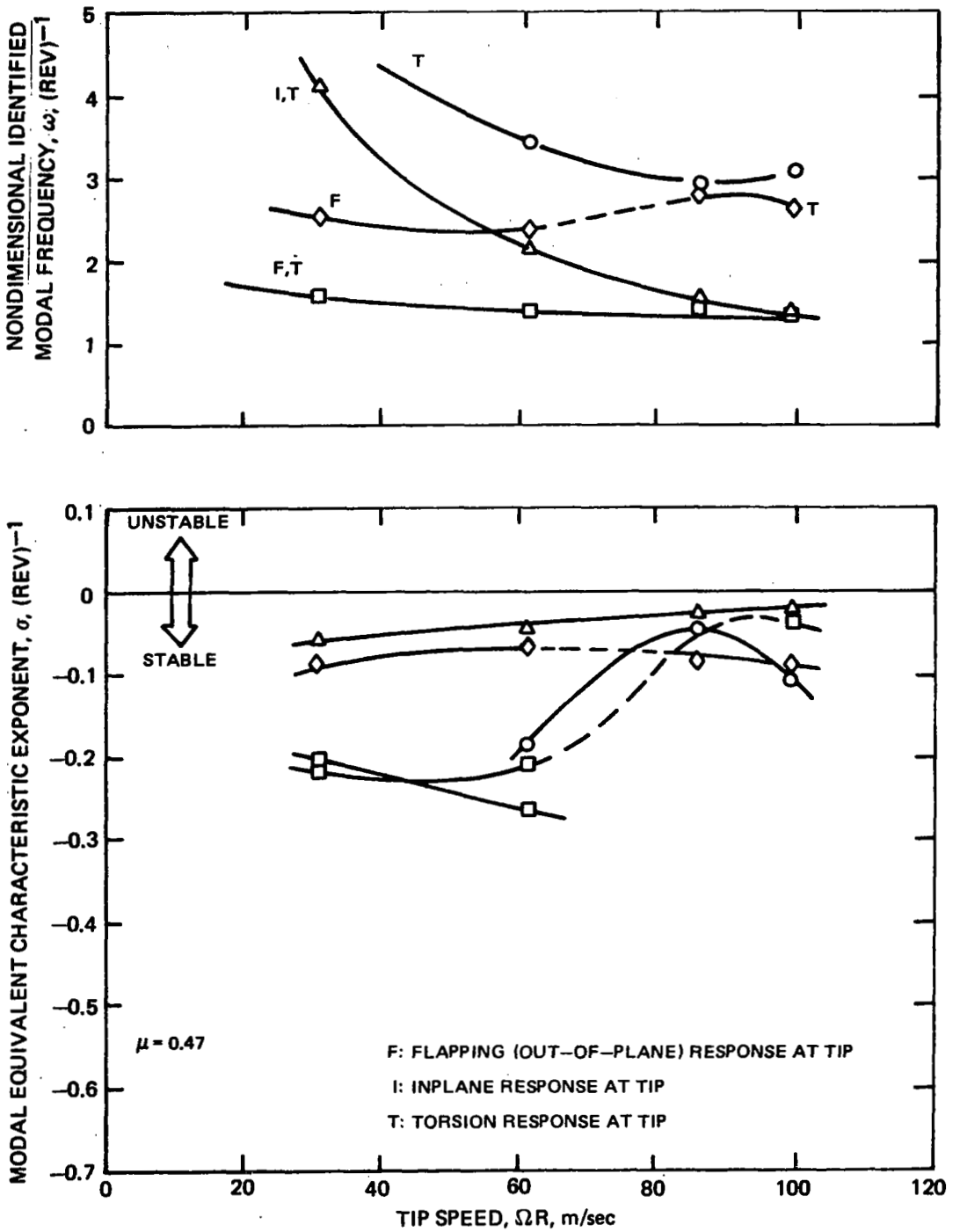

Figure 134. - Variation of Identified Modal Frequencies and Characteristic Exponents with Tip Speed, Cantilevered Torque Tube Model Rotor, Trailing Edge Push-Rod Attachment at .080R

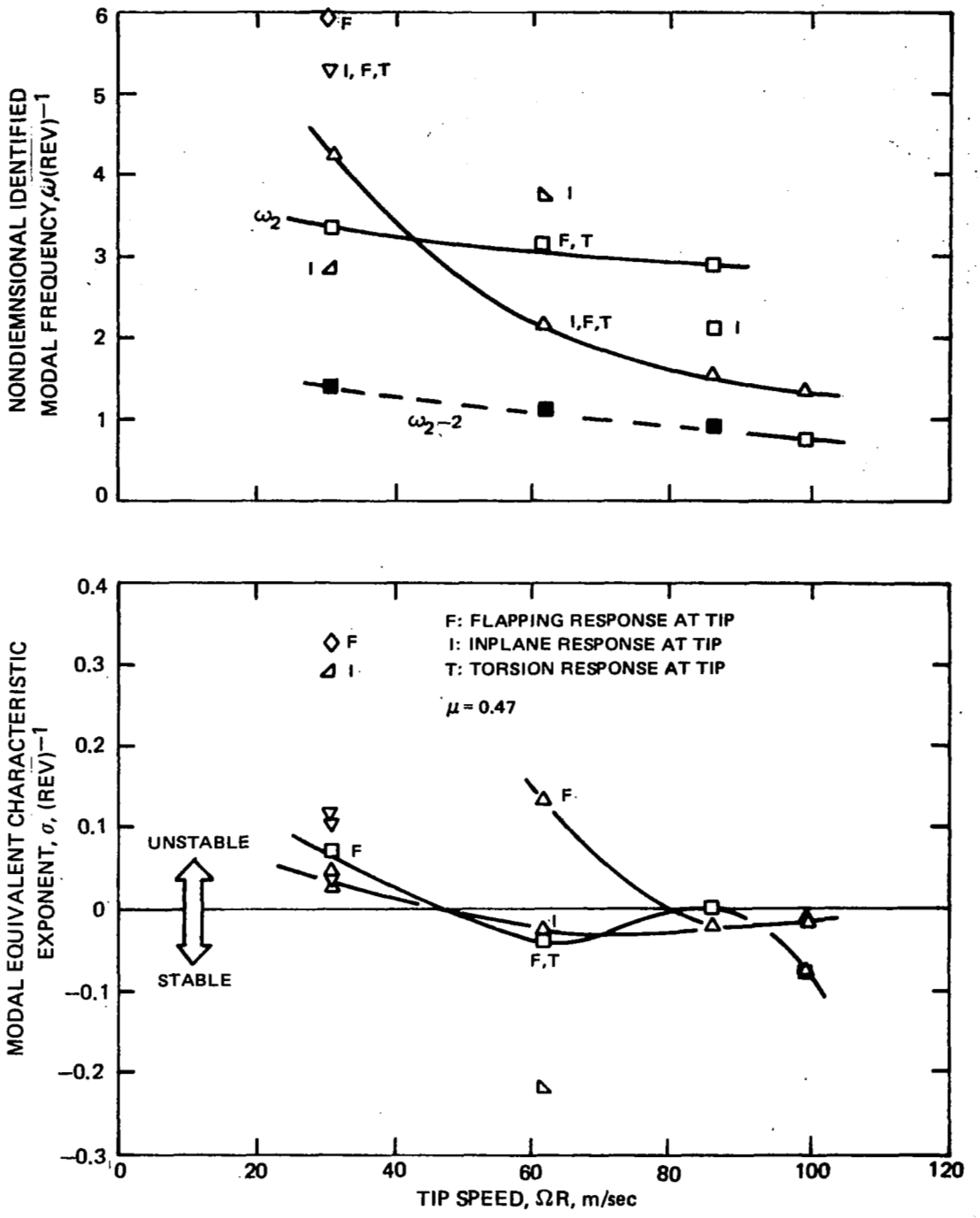

Figure 135. - Variation of Identified Modal Frequencies and Characteristic Exponents with Tip Speed, Cantilevered Torque Tube Model Rotor, Leading Edge Push-Rod Attachment at .070R

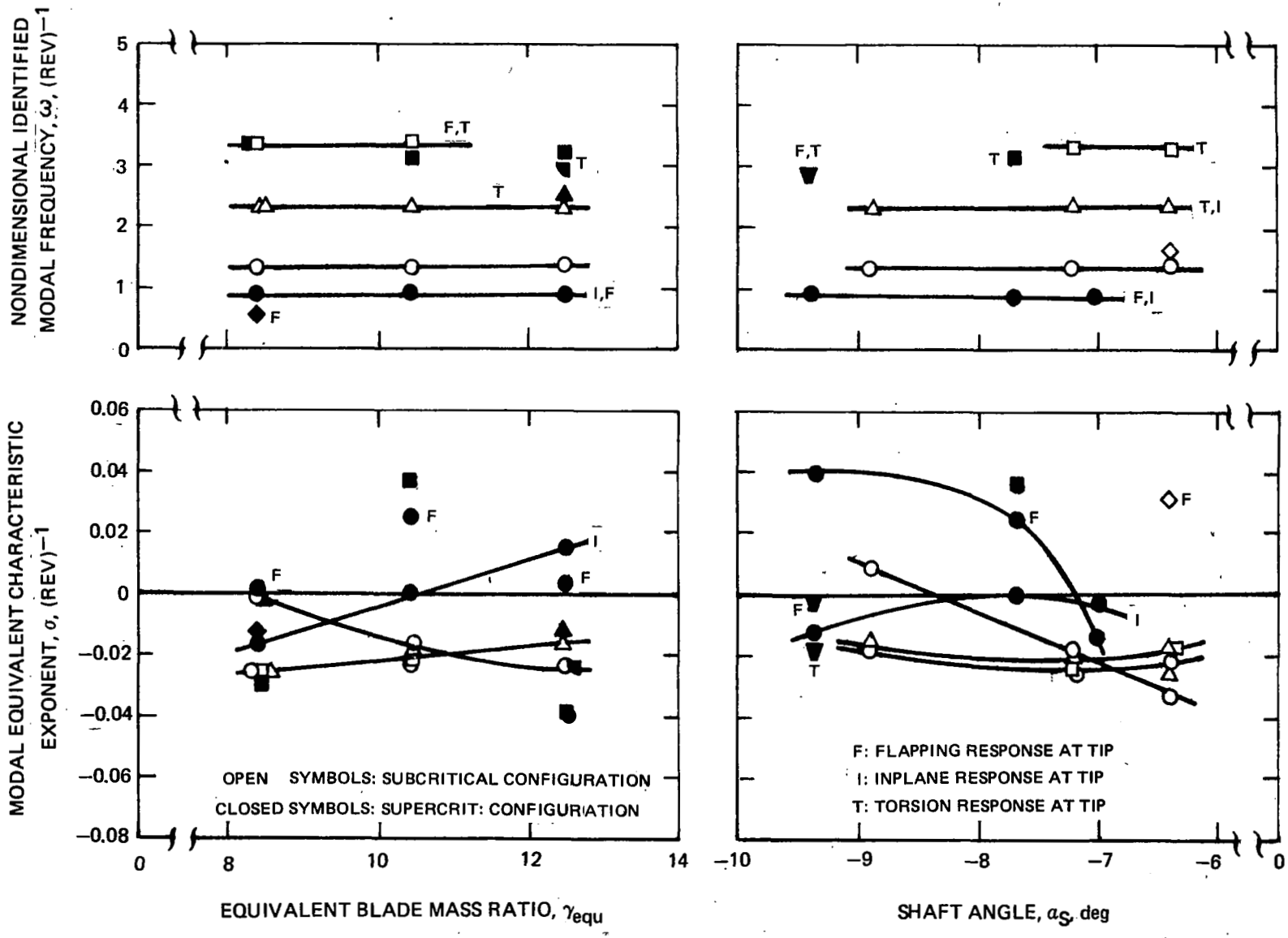

Figure 136. - Variations of Identified Modal Frequencies and Characteristic Exponents with Mass Ratio and Shaft Angle, Subcritical and Supercritical Full Scale Designs

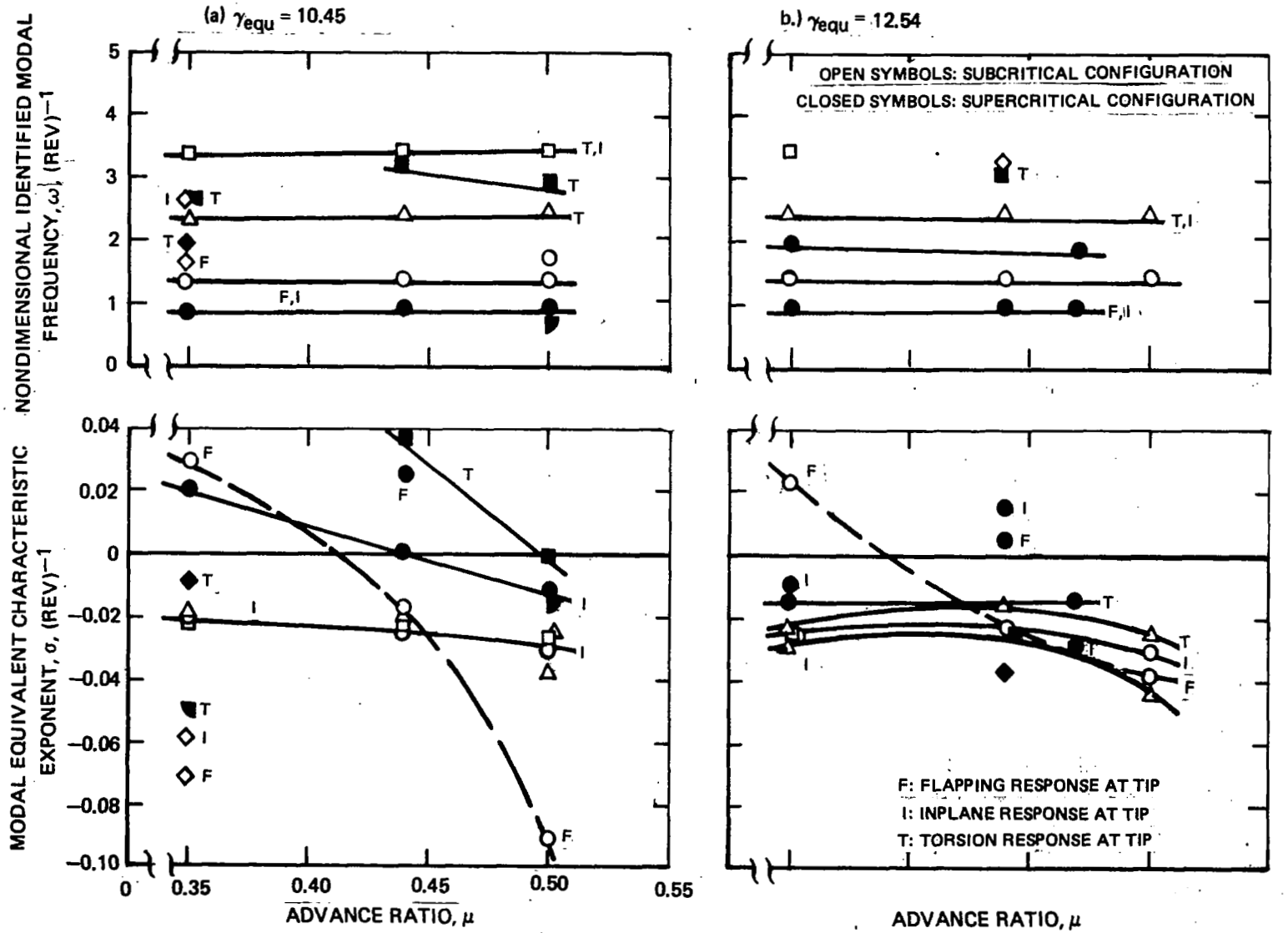

Figure 137. - Variation of Identified Modal Frequencies and Characteristic Exponents with Advance Ratio, Subcritical and Supercritical Full Scale Designs

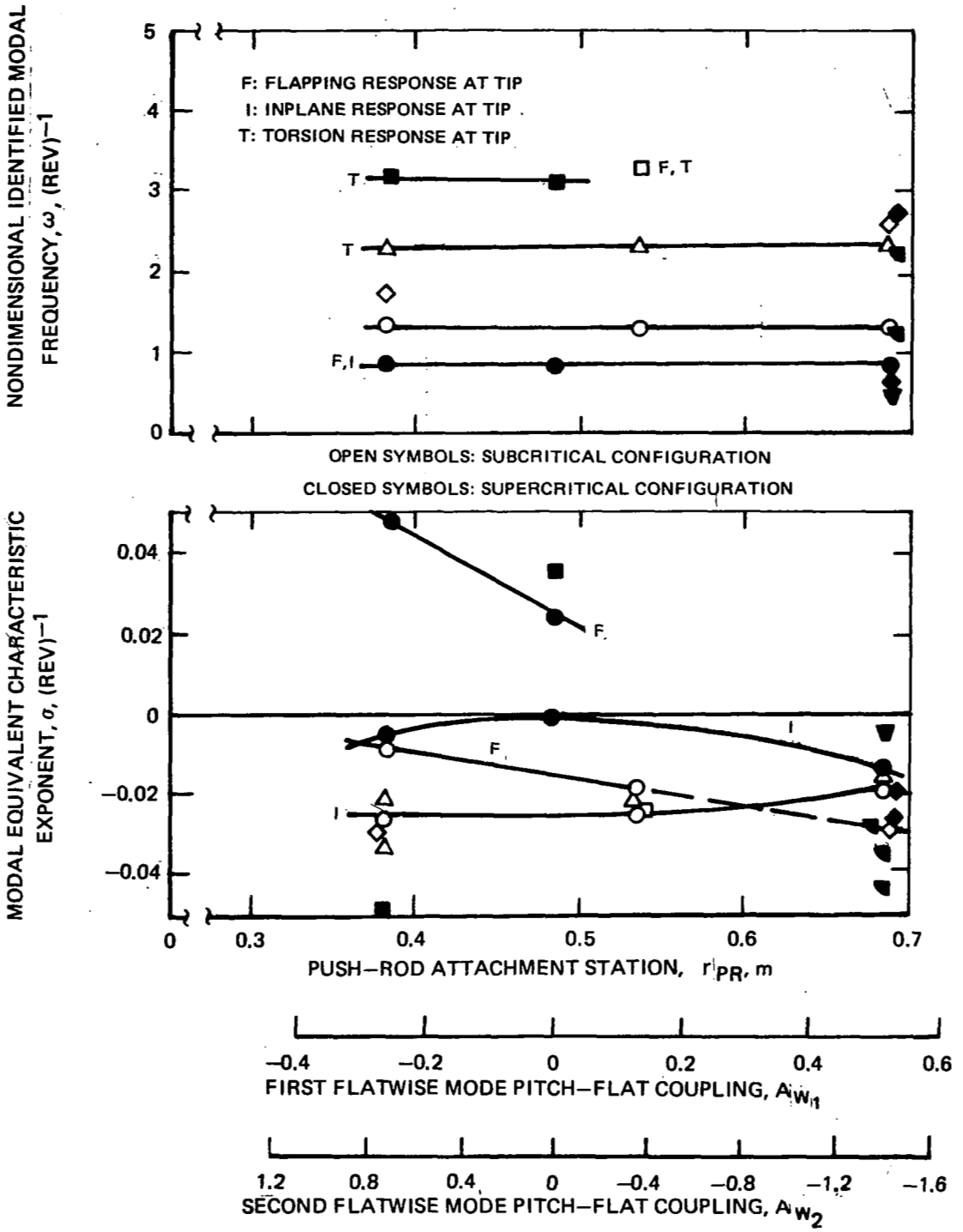

Figure 138. - Variation of Identified Modal Frequencies and Characteristic Exponents with Push-Rod Attachment Location, Subcritical and Supercritical Full Scale Designs

*U.S. GOVERNMENT PRINTING OFFICE: 1976 - 635-275/113